Resonance-Based Techniques for Microwave Breast Cancer Applications

Sun K. Hong

Dissertation submitted to the faculty of the Virginia Polytechnic Institute and State University in partial fulfillment of the requirements for the degree of

Doctor of Philosophy
In
Electrical Engineering

William A. Davis, Chair
Warren L. Stutzman
Ahmad Safaai-Jazi
Timothy Pratt
Slimane Adjerid

September 12, 2012
Blacksburg, VA

Keywords: natural resonance, microwave hyperthermia, breast cancer, singularity expansion method, pole, residue, ground penetrating radar

Resonance-based Techniques for Microwave Breast Cancer Applications

Sun K. Hong

ABSTRACT

It is well known that a finite-size scatterer has a set of natural resonances, which are uniquely determined by the physical properties of the scatterer. This is also the case for a breast tumor which can be regarded as a dielectric scatterer. Since the scatterer is naturally "tuned" at the resonances, it is expected that an increased electromagnetic coupling would take place at the resonance frequencies compared to other frequencies. For a breast tumor, this would mean a higher power absorption, indicating a faster temperature increase resulting in more efficient hyperthermia.

In this dissertation, an adaptive microwave concept is demonstrated for breast cancer applications. The general approach is to detect and identify the tumor-specific resonance, determine the electrical location of the tumor, and apply the focused microwave hyperthermia using the identified resonance and the electrical location. The natural resonances vary depending on the tumor size, shape, and breast tissue configuration. Therefore, an adaptive tuning of the microwave source to tumor-specific resonance frequencies could improve the overall efficiency of hyperthermia treatment by allowing for a faster and more effective heating to achieve a desired therapeutic temperature level.

Applying the singularity expansion method (SEM), both the resonances and the electrical location can be obtained from the poles and residues, respectively. This SEM-based approach is computationally inexpensive and can easily be implemented as a combination processing into emerging UWB microwave systems. Alternatively, a relatively simple microwave system based on this concept can potentially be used in conjunction with existing mammography.

ACKNOWLEDGEMENTS

I would like to thank my advisor, Dr. William A. Davis, for his support and guidance throughout this research. He has provided much advice not only for this dissertation, but also in many other technical aspects which helped expand my professional knowledge. I would also like to thank Dr. Warren L. Stutzman for his professional advice and serving on my committee. I also thank Dr. Ahmad Safaai-Jazi, Dr. Tim Pratt, and Dr. Slimane Adjerid for serving on my committee and their support in reviewing this dissertation.

I am also grateful for the support, advice and encouragement by Dr. Tim Andreadis. He has been a great mentor during my career at NRL. I would also like to thank Dr. Phil Girardi for his support and advice throughout my professional career since my first employment as an undergraduate intern. I would also like to give special thanks to Walter Wall, my good friend and colleague, who has provided me with great support, advice and ideas. My thanks also go to my other NRL colleagues for their help. I wish to express my thanks to Taeyoung Yang for much helpful advice and discussion during my time at VTAG. I would also like to express my thanks to other fellow graduate students during my stay at VTAG. I would also like to acknowledge NRL for the tuition support through the Edison Memorial Graduate Program.

Many thanks also go to my good friends Brandon Park, Sun "Edward Woo" Choi, Sungjae Cho, Timothy Kim, and the "Lee" brothers. My special thanks also go to Mr. John Wang, Mr. Han and the "Oikos" family for their support and prayers.

I would like to express my sincere gratitude to my parents, Byung and Moon, and my parents-in-law, Chaehun and Yeonhee, for their endless support, encouragement and prayers. I also thank my sister Eunice, brothers-in-law Ji-Hoon and Jaewon for their support. My love goes to my little nephew, Jayden, who always makes me smile.

My deepest gratitude and love goes to my wife, JaeHee. The love and support you have given me is indescribable. No words can express how much you mean to me. Above all, I would like to thank God for providing me with all of the exciting opportunities throughout these years and always guiding me to a better path in Christ Jesus.

TABLE OF CONTENTS

LIST OF FIGURES

Chapter 2

Chapter 3

Chapter 4

LIST OF TABLES

Chapter 4

Chapter 5

Chapter 6

Chapter 1 Introduction

Transient electromagnetic scattering in the resonance[1] region provides useful characteristic information about the scattering object. Of particular interest are the natural resonances, at which the object is uniquely "tuned" to oscillate when stimulated, even after the incident excitation pulse has passed the object. The natural resonances are determined based on the size, shape, material property, and the surrounding medium of a scattering object. Hence there exists a unique set of natural resonances for every different object, which can be used as distinctive characteristic features. For this reason, resonant scattering has been a subject of great interest over the past few decades in areas such as radar target identification, scatterer and antenna characterization [1-4].

Resonant scattering techniques could also be very useful for directing electromagnetic energy to a target. In order to effectively upset, damage, or destroy a target of interest, selection of source frequency is very important. For any given target, the incident field must interact well with the body or components in order to achieve most efficient and effective coupling of energy. It is intuitive that using the natural resonances could be very effective due to their inherent characteristics as the "tuned" frequencies of the target. Therefore, if the resonance frequencies of a target can be obtained from its transient scattering, it can be used as a source waveform to attack the target. An ideal scenario would involve three steps. First, ping the target of interest with a transient pulse. Second, the location and the resonance frequencies are identified from the scattered response of the target. Finally, the "kill" waveform is generated using the resonance

[1] Incident wavelength is on the order of the dimension of scattering object

frequencies and re-directed back to the target. This adaptive technique could potentially be used for various applications and scenarios.

One very significant and relevant area which this approach can be applied to is breast cancer. Detection and thermotherapy treatment of breast cancer using microwaves have been investigated by a number of researchers in the past decade. Use of microwaves for breast tumor detection has been of particular interest to researchers due to its non-ionizing nature [5-13]. The typical microwave frequency band used for UWB breast tumor detection (typically 0.5-20GHz) corresponds to the resonance region due to the effective electrical dimensions of breast tissue and tumor (lossy dielectric). Microwave thermotherapy has shown be a great potential alternative or combination treatment option, that it effectively ablates (heat-alone treatment) or causes the tumor to be more vulnerable (hyperthermia treatment) to chemotherapy or radiation therapy [14].

The ongoing interest in the use of microwaves to detect and treat breast tumors makes it a suitable application for the proposed resonance-based approach. Some previous detection efforts have demonstrated the use of natural resonances of breast tumor as features for distinguishing malignant tumors from benign mass [15, 16]. However, an adaptive use of resonant scattering for both detection and thermotherapy has not been investigated, although it was speculated by Rotman that the tumor resonance frequency would be best for hyperthermia [17]. Thus it was the motivation for the research presented in this dissertation. The general approach is to use the transient scattered response to 1) detect and identify the electrical location of the tumor, 2) determine the tumor-specific resonance frequency to be used for microwave treatment, and finally 3) focus the microwave signal at the location of the tumor.

The approach presented in this dissertation could potentially improve the overall efficiency and effectiveness of microwave detection and treatment of breast cancer. Here we focus on determining the electrical location of the tumor rather than physical location, since the objective is to extract the information needed for focusing the microwaves. This makes the proposed approach relatively simple and suitable technique that can easily be used in conjunction with other modalities such as mammography and other microwave-based imaging for determining the physical location of tumor. Non-invasive adaptive microwave focusing based on tumor-specific resonance could be a suitable alternative to current approach that uses a fixed frequency and invasive feedback probe to adjust focusing [10].

1.1 Research Objectives and Original Contribution

The goal of this research is to demonstrate the concept of an adaptive approach that utilizes resonant scattering parameters to detect the location of a tumor, identify the tumor-specific resonances, and use them for more efficient microwave treatment. More specifically the main objective is to investigate the Singularity Expansion Method (SEM) representation of tumor responses to identify the location and resonances, and demonstrate the performance of the focused microwave utilizing these parameters. Techniques for reducing clutter to extract tumor responses are also investigated. As previously mentioned, the focus of this research is to demonstrate the feasibility of an adaptive detection and treatment approach that does not necessarily require an image of the breast. However, it would make the most sense to use the proposed approach as a combination technique with an existing mammography or emerging microwave imaging. Original contributions in this research include:

- Introduction of an SEM-based adaptive concept for breast cancer applications
- Sliding-window Matrix Pencil approach for more robust resonance extraction
- Use of residue phase angle as electrical location of detected tumor
- Position-time plots for computationally inexpensive display of response data
- Investigation of simple clutter removal techniques for improved position-time plots
- Numerical and experimental demonstration of the effectiveness of tumor-specific resonances for microwave treatment

1.2 Dissertation Overview

The remaining chapters are organized as follows:

- In Chapter 2, a brief overview of breast cancer problem is provided followed by a summary of previous efforts and published work in microwave tumor detection (mostly imaging based) and thermotherapy treatment. Also discussed is currently used modalities for tumor detection/imaging and treatment.
- Chapter 3 discusses a general overview of the proposed concept. A simple flow diagram with brief description of each block is provided. Potential scenarios for the proposed approach as a stand-alone system or more preferably in conjunction with other modalities are also discussed.

- In Chapter 4, an overview of resonant scattering and the Singularity Expansion Method (SEM) is presented. SEM representation in a lossy medium is also briefly discussed. A technique for extracting SEM parameters (poles and residues), known as the Matrix Pencil Method (MPM), is described. A different way of applying MPM, i.e. Sliding-window Matrix Pencil, for more robust pole extraction is also presented.
- Chapter 5 discusses in detail the detection aspect of the proposed approach. The use of a relatively simple presentation of data using the position-time (or space-time) plot, widely used in ground penetrating radar (GPR) displays, are presented for identifying the tumor response. Possible scenarios for reducing clutter in the responses from dense breasts are also discussed. Determining the tumor electrical location and resonances from the extracted poles/residues is presented. These techniques are demonstrated through numerically simulated tumor responses of various two-dimensional breast models. An experimental demonstration is also presented using a simplified 2D-like measurement setup.
- In Chapter 6, focusing microwaves at the tumor using the extracted resonances is demonstrated through the same numerical models as well as the experimental setup used in Chapter 5. Effectiveness of tumor-specific resonances is evaluated by determining the power absorption distribution. The performance evaluation of tumor resonances in comparison to other frequencies is presented.
- Chapter 7 finally provides an overall summary of this dissertation research and conclusions. Original contributions made throughout this research are summarized followed by possible future work.

1.3 References

[1] C. Baum, "The singularity expansion method: Background and developments," *IEEE Antennas and Propagation Society Newsletter,* vol. 28, no. 4, pp. 14-23, Aug. 1986.

[2] C. Baum, E. J. Rothwell, K. M. Chen, and D. P. Nyquist, "The Singularity Expansion Method and its Applications to Target Identification," *Proceedings of the IEEE,* vol. 79, no. 10, pp. 1481-1492, Oct. 1991.

[3] G. Joshi, "Ultra-wideband Channel Modeling using Singularity Expansion Method," Ph.D. Dissertation, Virginia Tech, Blacksburg, VA, 2006.

[4] S. Licul and W. A. Davis, "Unified Frequency and Time-Domain Antenna Modeling and Characterization," *IEEE Transactions on Antennas and Propagation,* vol. 53, no. 9, pp. 2882-2888, Sept. 2005.

[5] P. M. Meaney, K. D. Paulsen, A. Hartov, and R. K. Crane, "MIcrowave imaging for tissue assessment: Initial evaluation in multitarget tissue equivalent phantoms," *IEEE Transactions on Biomedical Engineering,* vol. 43, no. 9, pp. 878-890, Sept. 1996.

[6] S. C. Hagness, A. Taflove, and J. E. Bridges, "Two-dimensional FDTD analysis of a pulsed microwave confical system for breast cancer detection: Fixed-focus and antenna-array sensors," *IEEE Transactions on Biomedical Engineering*, vol. 45, no. 12, pp. 1470-1479, Dec. 1998.

[7] P. M. Meaney, M. W. Fanning, D. Li, S. P. Poplack, and K. D. Paulsen, "A clinical prototype for active microwave imaging of the breast," *IEEE Transactions on Microwave Theory and Techniques*, vol. 48, no. 11, pp. 1841-1853, 2000.

[8] E. C. Fear, X. Li, and S. C. Hagness, "Confocal microwave imaging for breast tumor detection: localization of tumors in three dimensions," *IEEE Transactions on Biomedical Engineering*, vol. 49, no. 8, pp. 812-822, Aug. 2002.

[9] E. C. Fear, P. M. Meaney, and M. A. Stuchly, "Microwaves for breast tumor detection?," *IEEE Potentials*, vol. 22, no. 1, pp. 12-18, Feb.-Mar. 2003.

[10] A. J. Fenn, G. Wolf, and R. M. Fogle, "An adaptive microwave phased array for targeted heating of tumors in intact breast: Animal study results," *International Journal of Hyperthermia,* vol. 15, no. 1, pp. 45-61, Jan.-Feb. 1999.

[11] M. H. Falk and R. D. Issels, "Hyperthermia in onclolgy," *International Journal of Hyperthermia,* vol. 17, no. 1, pp. 1-18, Jan.-Feb. 2001.

[12] R. A. Gardner, H. I. Vargas, J. B. Block, C. L. Vogel, A. J. Fenn, G. V. Kuehl, and M. Doval, "Focused microwave phased array thermotherapy for primary breast cancer," *Annals of Surgical Oncology,* vol. 9, no. 4, pp. 326-332, May 2002.

[13] M. C. Converse, E. J. Bond, S. C. Hagness, and B. D. Van Veen, "Ultrawide-band microwave space-time beamforming for hyperthermia treatment of breast cancer. A computational feasibility study," *IEEE Transactions on Microwave Theory and Techniques,* vol. 52, no. 8, pp. 1876-1889, Aug. 2004.

[14] A. J. Fenn, *Breast Cancer Treatment by Focused Microwave Thermotherapy*. Sudbury, MA: Jones and Bartlett Publishers, 2007.

[15] Y. Chen, E. Gunawan, K. S. Low, S.-C. Wang, C. B. Soh, and T. Choudary, "Effect of Lesion Morphology on Microwave Signature in 2-D Ultra-Wideband Breast Imaging," *IEEE Transactions on Biomedical Engineering,* vol. 55, no. 8, pp. 2011-221, Aug. 2008.

[16] F. Yang and A. S. Mohan, "Complex natural resonances for breast tissues with complex morphology," in *2011 IEEE International Symposium on Antennas and Propagation (APSURSI)* 2011, pp. 699-702.

[17] R. Rotman, "Microwave Radiometry for Medical Diagnostics," Master's Thesis, Electrical Engineering and Computer Science, MIT, Cambridge, MA, 1985.

Chapter 2 Overview of Microwave Breast Tumor Detection and Treatment

Breast cancer is one of the most commonly diagnosed cancer and one of the leading causes of cancer deaths among women in the United States. The American Cancer Society estimates about 226,870 new cases of invasive breast cancer and about 39,510 deaths from the cancer for 2012 alone [1]. Hence, it still remains a significant problem, and the early-detection and effective treatment is very important.

2.1 Microwave Detection and Imaging

Currently, the most common and proven screening method for breast cancer is mammography, which generates images of a compressed breast, known as mammograms, by transmitting low-energy of x-rays from one side of the compressing plate to the opposing side. Mammograms have very high resolution arising from extremely short wavelengths. However, it is reported that 20 to 30 percent of breast cancers are not detected with the current mammography technology. Moreover, about 11 percent of mammograms are classified as non-normal that can include false positives, which require a follow-up action (i.e. additional imaging or biopsy) [2]. Some health issues due to the ionizing nature of x-rays are also of concern. Ultrasound is often used to determine whether a detected lesion is a liquid-based cyst or a solid tumor [3]. Magnetic resonance imaging (MRI) is also used for screening high-risk women or obtaining more information following a suspicious result from mammogram or ultrasound [4].

Over the past decade, there has been a considerable interest in the use of microwave technology as an alternative means of breast cancer screening, and numerous investigations have shown promising results [5-13]. Some of the prominent researchers who contributed to early development in this field of research include Hagness [7-10, 13], Meaney [5, 6] and Fear [3, 8]. Microwave systems proposed in the literature in general employ two main configurations that use the supine and prone positions of a patient. For the prone position system [11, 14, 15], the patient is lying face down and the breast is immersed into a tank surrounded by an antenna array. For the supine position system [7, 12, 13], the patient is lying down face up and the breast is scanned from an array placed above the breast. The two configurations are depicted in Figures 2.1a and 2.1b. The breast and antenna array are typically immersed in a matching medium to minimize the skin reflection. Both configurations do not involve compression plates used in mammography, which are found to be uncomfortable by many patients [3]. However, in this dissertation the compressed breast (Figure 2.1c) is also considered as a possible configuration, since it provides a good potential for combination use with mammography. It could also simplify the signal processing due to a two-dimensional like configuration (using a linear array), even when used as a stand-alone system. At the cost of comfortability, the compression plate approach could still be worthwhile if it could simplify the process and provide more robust detection performance. Moreover, there is also a good potential for implementation of an adaptive thermotherapy applicator using the same antenna elements used for detection.

2.1.1 Basic Principle

Microwave-based detection is made possible due to contrast in the dielectric properties between malignant tumors and normal breast tissues [16-22]. The fundamental principle is that the tumor is a lossy dielectric object surrounded by a different kind of lossy dielectric medium (normal breast tissues), which causes reflection and scattering due to the boundary condition. A normal breast consists of mainly fatty tissues and some fibroglandular tissues, which have different dielectric properties thereby creating boundary conditions. Therefore, typical transient response of the breast containing a tumor would primarily consist of the skin reflection, clutter, and the tumor response. Here, clutter basically represents the responses from tissues other than the tumor. The amount of fibroglandular tissues, which determines the clutter intensity in the response, varies from person to person. Figure 2.2 illustrates basic scattering mechanism in the breast for microwave detection.

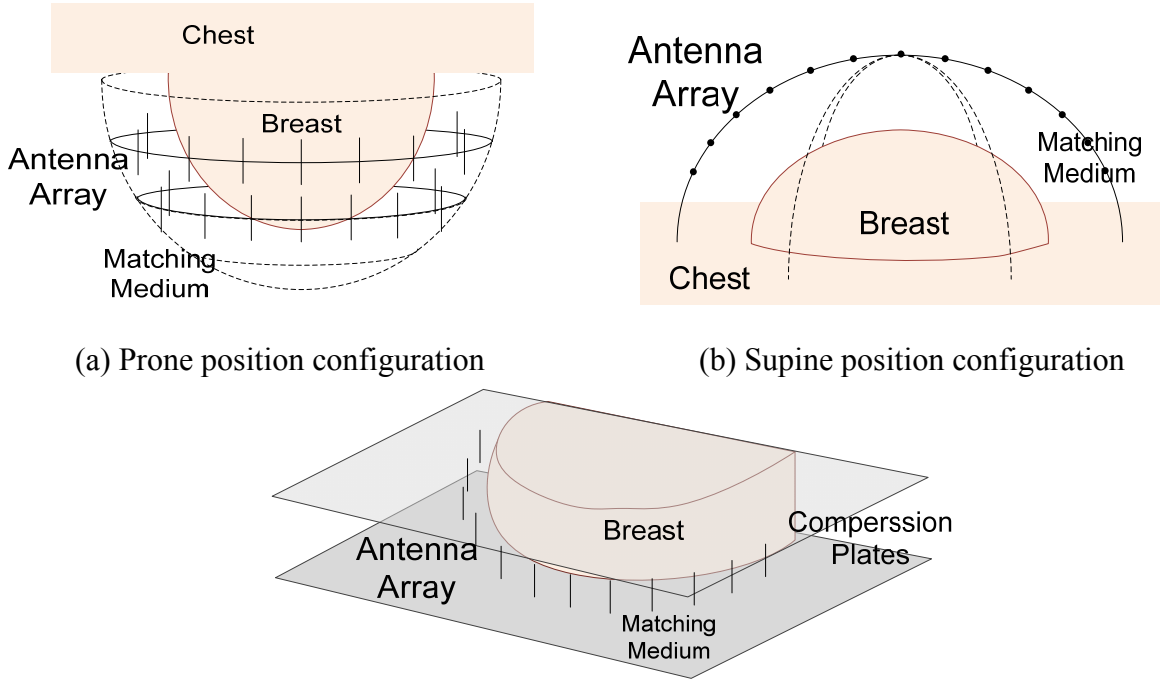

(a) Prone position configuration

(b) Supine position configuration

(c) Compression plate configuration

Figure 2.1 Various configurations for breast cancer detection using microwaves

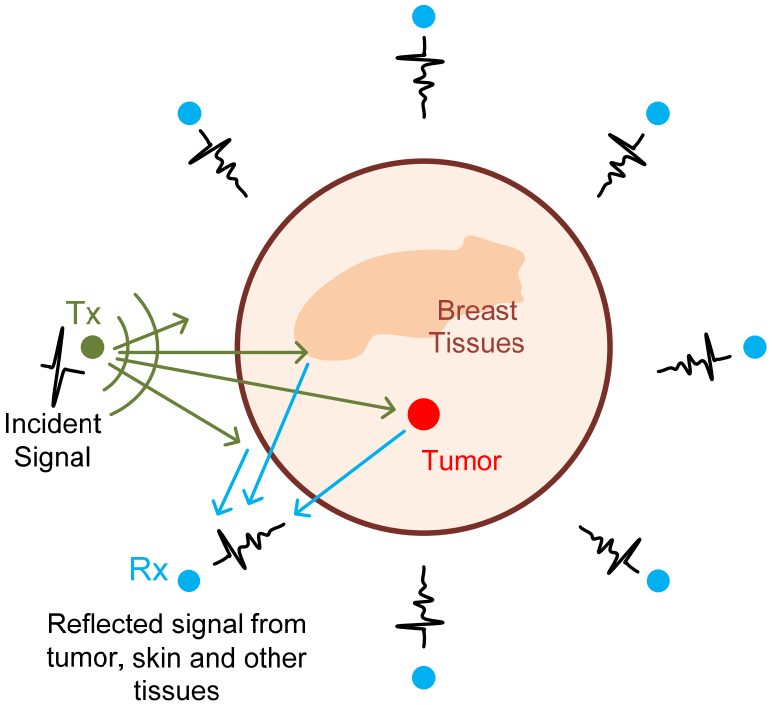

Figure 2.2 Illustration of basic scattering mechanism in breast and microwave detection approach

Dielectric property, or permittivity, of different tissues in the body is mainly determined by water content. The permittivity of a dielectric medium is expressed as a complex value:

$$\varepsilon = \varepsilon_o \left(\varepsilon_r^{'} - j\varepsilon_r^{''} \right) = \varepsilon_o \left(\varepsilon_r^{'} - j\frac{\sigma_{eff}}{\omega \varepsilon_o} \right), \tag{2.1}$$

where, ε_o is the permittivity in free space. The term in the parenthesis represents the relative permittivity, in which the real and imaginary parts represent the dielectric constant and loss term, respectively. The dielectric constant, $\varepsilon_r^{'}$, primarily determines the wavelength of electromagnetic waves in the medium. The loss term, $\varepsilon_r^{''}$, which includes the effective conductivity, σ_{eff}, primarily affects the electrical heating in the medium. Tissues with low water (e.g. fat, bone, and lung) content have lower permittivity values, in both real and imaginary, than those with high water content (e.g. muscle, brain, and internal organs) [3]. Past studies have suggested that typical dielectric properties of malignant tumors have permittivity values similar to that of muscles, providing a large dielectric contrast between the tumors and normal breast tissues consisting of mainly fatty and some fibroglandular tissues (low fat, higher water content). In the early studies, it was reported that the dielectric contrast could be up to 10:1 in a relatively homogeneous breast with mostly fatty tissues [13, 16-19], and most of early detection work [8-10, 12, 13] was based on these high contrast cases. However, a recent study by Lazebnik et al. [20-22] reports that some breasts could contain more fibroglandular tissues than previously assumed, indicating that the contrast could be lower depending on the heterogeneity of tissues surrounding the tumor. Lower dielectric contrast results in less scattering from tumor, thereby increasing the clutter to signal ratio. As a result, many recent efforts have investigated various approaches to improve signal to clutter ratio. Techniques for physically altering the dielectric contrast through infusion of contrast agents, such as conducting nanoparticles or microbubbles, have been investigated [23-25]. Other techniques based on signal processing have also been proposed [26]. More tissue heterogeneity in the breast makes it a challenging problem, but regardless of how high or low, as long as there exists some dielectric contrast, scattering from a tumor should be in the signal and it becomes a matter of how one can extract that information. Figure 2.3 shows the dielectric properties of different breast tissues based on the two-pole Debye model obtained from the experimental data reported in [22].

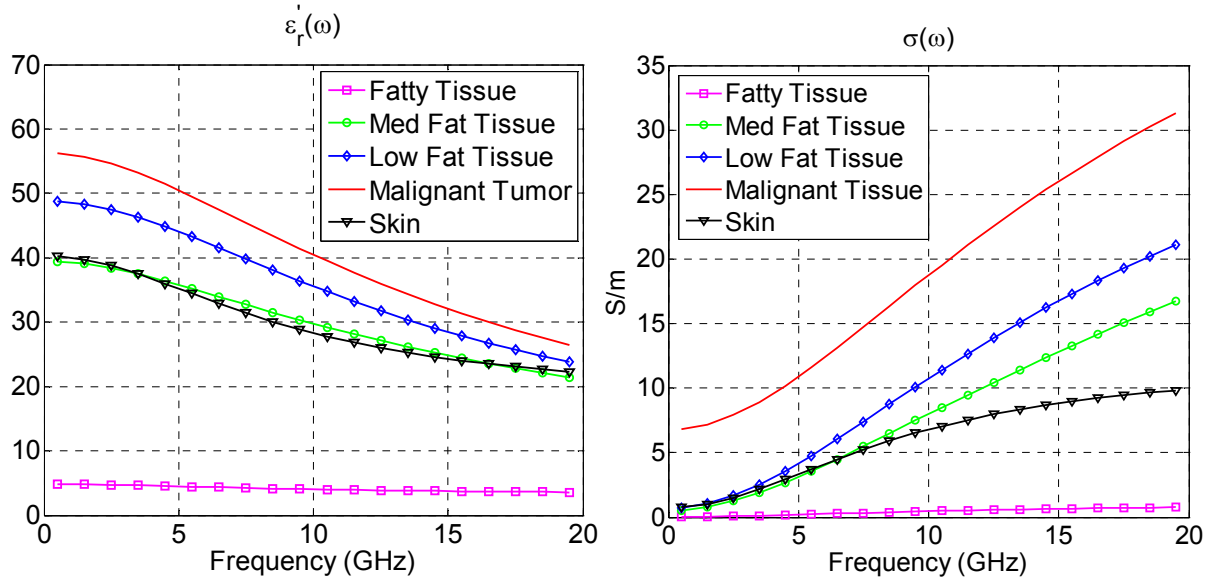

Figure 2.3 Dielectric properties of different tissue types in the breast [22]: Dielectric constant (real permittivity) is shown on the left, and the effective conductivity (obtained from imaginary permittivity) is shown on the right.

2.1.2 Overview of Microwave Detection/Imaging Techniques

Most of microwave tumor detection approaches proposed to date have been based on imaging of the physical breast. While there are two main microwave-based approaches to breast imaging, i.e. microwave tomography [5, 6] and UWB radar-based [7-13] imaging , the latter is of particular interest in this dissertation. Microwave tomography basically solves an inverse scattering problem with the measured responses from reflection and transmission to reconstruct the dielectric property profile of the measured breast. Radar-based imaging, which uses reflection-based responses, is more relevant topic for a discussion here, since this research is based on the same radar-based scattering principle and has the potential for a combination technique.

UWB radar-based techniques rely on the same principle as that in ground penetrating radar (GPR), which detects buried objects from their reflected backscatter. The breast is illuminated with an UWB pulse transmitted from an antenna or antenna array, and the backscattered response received through the same antenna or antenna array are processed and analyzed for detection and imaging. The UWB illumination of the breast can also be effectively performed through a stepped frequency sweep and converted into the time-domain through the

inverse Fourier Transform. Either through a monostatic/bistatic scan or multistatic responses, the scattered response of a tumor can be obtained from multiple aspect angles, providing information for imaging and determining the location of the tumor.

Based on this general concept, various imaging techniques have been investigated by a number of researchers, and encouraging results have been reported on such techniques [7, 8, 12, 13, 26-29]. In the delay-and-sum (DAS) technique used by Li et al. [8, 13], the backscattered signals received at different antenna locations are variably time-shifted and range-gated in the post-processing to achieve virtual scanning, and the coherent addition of the responses provides the image of the backscatter intensity in the breast. In other words, the focal point of the array is virtually varied in the post processing by adding the signals at different time steps corresponding to the estimated physical location. The basic principle is similar to that of synthetic aperture radar [30] in a sense that it uses different geometric positions of antenna elements (or bistatic antenna combinations) to synthetically create an aperture and focused imaging. The space-time beamforming by Bond et al. [7] is an improved version of the DAS technique, which compensates for the dielectric dispersion and removes artifacts using weighted finite impulse response filters. Other modifications have also been proposed to improve the performance of DAS-based techniques [11, 26]. In time-reversal (TR) based techniques proposed by Kosmas et al. [12, 29], the backscattered signals received through the antenna elements are time-reversed and re-transmitted into the virtual breast, that is, a numerical breast model created based on the patient-specific MRI image and *a priori* knowledge of general dielectric property of the breast. If the backscattered energy was dominantly from the tumor, then the waves converge back to the tumor location in the numerical breast, thereby constructing a bright focal spot in the image at the time of focus due to coherent addition of waves. Compensation of dispersion and loss in the breast medium in the processing for a better TR-based imaging was also discussed in the work by Kosmas et al. [12]. Other techniques such as time-of-arrival data fusion was proposed by Chen et al. [27] using the CLEAN deconvolution algorithm [31], and data-adaptive beamforming has also been proposed by Guo et al. [28] for detection processing. Most of these techniques require some *a priori* knowledge of the electrical property of the breast in order to generate an accurate image of the breast being tested.

2.1.3 SEM-based Techniques for Tumor Characterization and Discrimination

Techniques for characterizing tumors using the features based on their morphology from the UWB transient backscatter were also considered for the purpose of distinguishing between benign and malignant tumors. Davis et al. proposed a classification algorithm based on local discriminant bases and principal component analysis of the UWB backscatter from tumors [32]. The use of the natural resonances (SEM poles) as distinctive features between malignant tumor and benign tissue was proposed by Huo et al. in [33] as well as Chen et al. and Yang et al. [34, 35], which investigated the pole location change in the complex frequency (Laplace) domain as the tumor geometry varied. In these studies, it was reported that malignant tumors, which generally have more random, spiculated shapes, tend to have lower damping constants (real part of the pole), than benign tissues that are usually smooth and oval shaped. These results are encouraging because they demonstrate the applicability of the SEM-based characterization used in many other applications [36-39] for the beast tumor application. Furthermore, it makes the adaptive resonance-based thermotherapy approach proposed in this dissertation more relevant and attractive.

2.2 Microwave Thermotherapy

Breast cancer treatment using microwaves has received considerable interest in the past few decades and results from a number of studies have shown the effectiveness of thermotherapy using microwaves [40-42]. The goal of microwave thermotherapy is to raise the temperature of a tumor using microwaves to a level at which the cancer cell is killed or becomes more vulnerable to chemotherapy or ionizing radiation therapy. In order to achieve a tumor cell kill with microwave-only treatment, it is reported that the temperature range of 48-50^{o}C is required [40]. For mild thermotherapy, generally known as hyperthermia, since the purpose is just to cause the cancer cells to be more sensitive to other conventional treatments, a lower temperature range of 43-46^{o}C has shown to be sufficient [40]. Hyperthermia seems to be more desirable approach due to its lower temperature requirement. Clinical trials have shown the advantage of using hyperthermia as a combination treatment technique with chemotherapy and/or radiation therapy not only for breast cancers, but also for other types of cancer [43, 44]. Thermotherapy is a good example of microwave directed energy application and is very attractive due to its non-ionizing nature.

2.2.1 Basic Principle of Microwave Thermotherapy

Microwave thermotherapy is based on dielectric heating of the tumor. Dielectric heating takes place when there exists loss term (effective conductivity) in the complex permittivity as expressed in Equation (2.1). The basic mechanism of dielectric heating can be found from a time-varying electric field applying a force to dipole molecules and ions in the dielectric medium to rotate, move and collide with each other, producing heat energy, thereby causing an elevation in the temperature. The effective conductivity (imaginary part) can be considered as a measure of conversion of electromagnetic energy into heat. The same basic principle is used in microwave oven for heating food. The amount of dielectric heating increases as a function of the effective conductivity. This would mean that the same amount of microwave power can heat and damage tumors more than normal breast tissues, due to relatively higher conductivity values in malignant tumors than normal breast tissues. However, since there still exists conductivity in other breast tissues, particularly the low fat fibroglandular tissues, it is still important to avoid any hot spots other than at the tumor when applying the microwave thermotherapy. Hence, the key to an effective thermotherapy is to selectively focus microwave energy only at the tumor while not affecting the surrounding region in the breast. Selective focusing can be achieved using a multi-element antenna array by phasing each element (or applying equivalent time-delay), thereby creating a focal spot at a desired location through constructive interference. Since the location of the focal spot is determined by phasing of the array, it is important to acquire an accurate knowledge of the tumor electrical location. Figure 2.4 illustrates the general concept of microwave thermotherapy using a multi-element array.

An important practical consideration for thermotherapy is the monitoring of temperature at the tumor as well as throughout the breast. It is important to monitor temperature to ensure that the target temperature level is reached. Making sure that the other regions in the breast do not heat up above certain threshold is also important. Ensuring the minimum heating in the interior region of the breast is more essential, since the skin and the nearby tissues can be cooled via external air or liquid.

2.2.2 Overview of Microwave Thermotherapy Approaches for Breast Cancer

Most of the early investigations on microwave thermotherapy in general have focused on narrowband (fixed frequency) techniques using annular phased arrays (APAs). The work

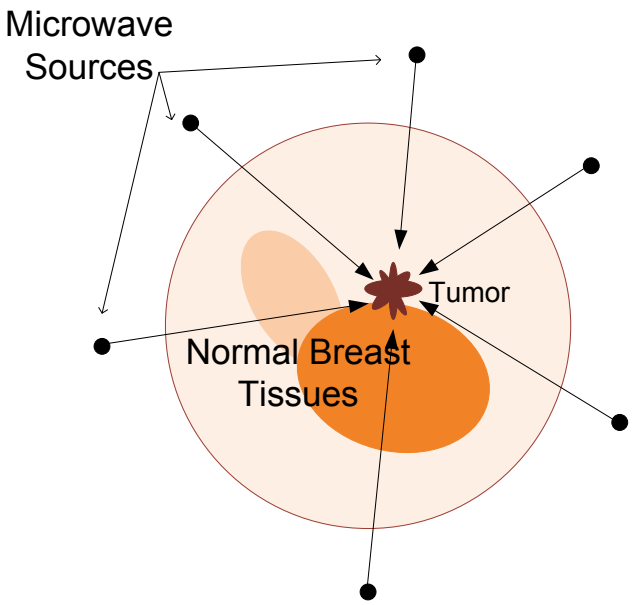

Figure 2.4 General concept of heating of breast tumor using multi-element microwave sources

proposed by Kowalski *et al.* [45] uses annular phased arrays with the aid of MRI for temperature estimation and monitoring. Using this type of configuration, a closed-loop temperature feedback control system was proposed [46]. Using multiple discrete frequencies over a narrow bandwidth (512MHz) in APA system was also investigated [47] and it was shown to have reduced number of hot spots in the volume illuminated with microwave.

Perhaps the most notable microwave breast cancer thermotherapy investigated to date is based on the use of narrowband phased array approach developed by Fenn *et al*. [40, 41], which employs an invasive electric field and temperature probes inserted into a breast to provide feedback for adaptive phasing as well as temperature monitoring as illustrated in Figure 2.5. The probes are placed at one or more positions including the predetermined tumor location from detection results (e.g. mammograms). Using a compression plate configuration similar to that used in mammography, narrowband microwave signals (915MHz) are transmitted from open-ended waveguides placed behind both compression plates. The feedback information from the probes is used for shifting phase at each feed in order to adjust the focus. While proven to be an effective technique for thermotherapy, possible limitations of this approach might come from

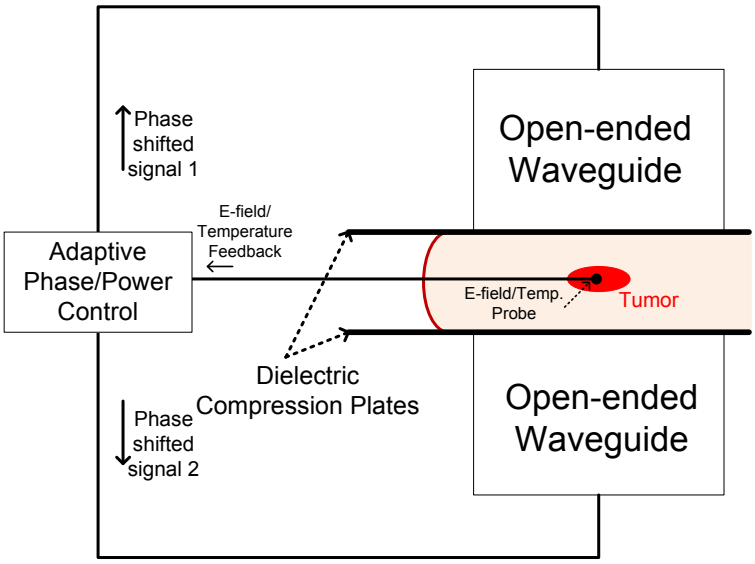

Figure 2.5 Narrowband (915MHz) adaptive phased array microwave thermotherapy approach developed by Fenn et al. [40].

the antenna configuration, which only allows the focus to be adjusted in vertical dimension and limits the focal resolution in horizontal plane.

More recently proposed techniques use UWB signals with the space-time beamforming [48] and time reversal (TR) techniques [49-51], both of which were also considered for the detection problem. These techniques propose to perform microwave focusing at the tumor without employing invasive probes, using only the predetermined information from the detection process or an additional processing. Focusing based on the space-time beamforming is essentially the "inverse" version of the detection process using the same technique [7]. In this method, once the breast is imaged using the DAS-based algorithm, the time delay, amplitude, and dispersion information of the detected tumor is obtained, which are then used to generate an UWB signal that will be amplified and fed into each antenna element to achieve focusing at the tumor for hyperthermia treatment. Non-invasive temperature monitoring schemes such as microwave [52] and ultrasound thermometry [53] were suggested as possible combination temperature monitoring techniques. TR-based focusing techniques are also applied in a similar manner, that is, the time-reversed waveforms are now transmitted into the patient's breast for microwave focusing instead of being transmitted numerically into a virtual breast for imaging. Two TR-based approaches were investigated, namely the measurement-based [54] and the

simulation-based methods [50, 51]. In the measurement-based method, it is suggested that the actual measured responses of the detected tumor to be time-reversed (after some post processing) and re-transmitted into the breast using the same antenna array used for detection. The waves transmitted from the antenna array will then converge back to the corresponding tumor location, thus creating a focal spot due to coherent addition of the waves. The simulation-based method shares the same TR principle, except that it uses numerically simulated time-reversed responses. A virtual source is placed at the location of the detected tumor in a patient-specific numerical breast created from an MRI image of the breast. The antenna array in the model records the signal emitted from the virtual source. The recorded signals are then time-reversed and fed into the array in the actual system for treatment.

Comparative studies of the effectiveness of hyperthermia using UWB signals versus narrowband signals were also conducted in [51, 55]. In the work by Converse et al. in [55], an UWB signal with the spectral content of 1-11GHz was compared with a set of discrete frequencies at 2, 4, 6 and 8 GHz. It was suggested that UWB signal provides tighter focusing and reduced hot spots in the breast for small tumors when applied with the space-time beamforming. In the work carried out by Trefina et al. in [51], a lower frequency band (0.434-1GHz) was investigated in the comparative study using a TR-based focusing scheme. Comparison between UWB signals versus a set of discrete frequencies in the same band at 0.1 GHz increment did not show a significant advantage of using UWB signals over narrowband signals. Since these studies considered only a limited number of "random" (i.e. not relating to resonance) discrete frequencies for comparison, it is not adequate to draw any hard conclusion about the advantage of using UWB signal in general. This paves a way for an investigation into using tumor-specific resonances for hyperthermia treatment, which is a major part of the original contribution in this dissertation.

2.3 References

[1] National Cancer Institute. Online. www.cancer.gov

[2] S. Grant and P. C. Oleson, "Breast Cancer Detection Research: Dual Use of Intelligence Technologies," *Studies in Intelligence,* vol. Semiannual Edition, no. 1, pp. 27-34, 1997.

[3] E. C. Fear, P. M. Meaney, and M. A. Stuchly, "Microwaves for breast tumor detection?," *IEEE Potentials,* vol. 22, no. 1, pp. 12-18, Feb.-Mar. 2003.

[4] American Cancer Society. Online. www.cancer.org

[5] P. M. Meaney, M. W. Fanning, D. Li, S. P. Poplack, and K. D. Paulsen, "A clinical prototype for active microwave imaging of the breast," *IEEE Transactions on Microwave Theory and Techniques,* vol. 48, no. 11, pp. 1841-1853, 2000.

[6] P. M. Meaney, K. D. Paulsen, A. Hartov, and R. K. Crane, "MIcrowave imaging for tissue assessment: Initial evaluation in multitarget tissue equivalent phantoms," *IEEE Transactions on Biomedical Engineering,* vol. 43, no. 9, pp. 878-890, Sept. 1996.

[7] E. J. Bond, X. Li, S. C. Hagness, and B. D. Van Veen, "Microwave imaging via space-time beamforming for early detection of breast cancer," *IEEE Transaction on Antennas and Propagation,* vol. 51, no. 8, pp. 1690-1705, Aug 2003.

[8] E. C. Fear, X. Li, and S. C. Hagness, "Confocal microwave imaging for breast tumor detection: localization of tumors in three dimensions," *IEEE Transactions on Biomedical Engineering,* vol. 49, no. 8, pp. 812-822, Aug. 2002.

[9] S. Hagness, A. Taflove, and J. Bridges, "Three-dimenstional FDTD analysis of a pulsed microwave confocal system for breast cancer detection: Design of antenna-array element," *IEEE Transaction on Antennas and Propagation,* vol. 47, pp. 782-791, May 1999.

[10] S. C. Hagness, A. Taflove, and J. E. Bridges, "FDTD modeling of a coherent-addition antenna array for early-stage detection of breast cancer," in *IEEE Antennas and Propagation Society International Symposium*, Atlanta, GA, 1998, pp. 1220-1223.

[11] M. Klemm, I. J. Craddock, A. Preece, J. Leendertz, and R. Benjamin, "Evaluation of a hemi-spherical wideband antenna array for breast cancer imaging " *Radio Science,* vol. 43, no. RS6S06, 2008.

[12] P. Kosmas and C. Rappaport, "Time Reversal With the FDTD Method for Microwave Breast Cancer Detection," *IEEE Transaction on Microwave Theory and Techniques,* vol. 53, no. 7, pp. 2317-2323, Jul. 2005.

[13] X. Li and S. Hagness, "A Confocal Microwave Imaging Algorithm for Breast Cancer Detection," *IEEE Microwave and Wireless Components Letters,* vol. 11, no. 3, pp. 130-132, Mar. 2001.

[14] S. M. Aguilar, M. A. Al-Joumayly, J. D. Shea, N. Behdad, and S. C. Hagness, "Design of a Microwave Breast Imaging Array Composed of Dual-Band Miniaturized Antennas," in *2011 XXXth URSI General Assembly and Scientific Symposium*, Istanbul, 2011.

[15] J. M. Sill and E. C. Fear, "Tissue Sensing Adaptive Radar for Breast Cancer Detection—Experimental Investigation of Simple Tumor Models," *IEEE Transaction on Microwave Theory and Techniques,* vol. 53, no. 11, pp. 3312-3319, Nov. 2005.

[16] S. S. Chaudhary, R. K. Mishra, A. Swarup, and J. M. Thomas, "Dielectric properties of normal and malignant human breast tissues at radiowave and microwave frequencies," *Indian Journal of Biochemistry and Biophysics,* vol. 21, pp. 76-79, 1984.

[17] C. Gabriel, S. Gabriel, and E. Corthout, "The dielectric properties of biological tissues: I. Literature survey," *Physics in Medicine and Biology,* vol. 41, pp. 2231-2249, Nov. 1996.

[18] S. Gabriel, R. W. Lau, and C. Gabriel, "The dielectric properties of biological tissues: II. Measurements on the frequency range 10Hz to 20GHz," *Physics in Medicine and Biology,* vol. 41, pp. 2251-2269, Nov. 1996.

[19] W. T. Joines, Y. Z. Dhenxing, and R. L. Jirtle, "The measured electrical properties of normal and malignant human tissues from 50 to 900 MHz," *Medical Physics,* vol. 21, pp. 547-550, 1994.

[20] M. Lazebnik, L. McCartney, D. Popovic, C. Watkin, M. Lindstrom, J. Harter, S. Sewall, A. Magliocco, J. Booske, M. Okoniewski, and S. Hagness, "A large-scale study of the ultrawideband microwave dielectric properties of normal breast tissue obtained from reduction surgeries," *Physics in Medicine and Biology,* vol. 52, pp. 2637-2656, 2007.

[21] M. Lazebnik, L. McCartney, D. Popovic, C. Watkin, M. Lindstrom, J. Harter, S. Sewall, A. Magliocco, J. Booske, M. Okoniewski, and S. Hagness, "A large-scale study of the ultrawideband microwave dielectric properties of normal, benign and malignant breast tissues obtained from cancer surgeries," *Physics in Medicine and Biology,* vol. 52, pp. 6093-6115, 2007.

[22] M. Lazebnik, M. Okoniewski, J. Booske, and S. C. Hagness, "Highly Accurate Debye Models for Normal and Malignant Breast Tissue Dielectric Properties at Microwave Frequencies," *IEEE Microwave and Wireless Components Letters,* vol. 17, no. 12, pp. 822-824, Dec. 2007.

[23] J. D. Shea, P. Kosmas, S. Hagness, and B. D. Van Veen, "Contrast-Enhanced Microwave Breast Imaging," in *13th International Symposium on Antenna Technology and Applied Electromagnetics and the Canadian Radio Sciences Meeting*, Toronto, ON, 2009.

[24] A. Mashal, B. Sitharaman, X. Li, P. K. Avti, A. V. Sahakian, J. H. Booske, and S. C. Hagness, "Toward Carbon-Nanotube-Based Theranostic Agents for Microwave Detection and Treatment of Breast Cancer: Enhanced Dielectric and Heating Response of Tissue-Mimicking Materials," *IEEE Transaction on Biomedical Engineering,* vol. 55, no. 8, pp. 1831-1834, Aug. 2010.

[25] Y. Chen, I. J. Craddock, and P. Kosmas, "Feasibility Study of Lesion Classification via Contrast-Agent-Aided UWB Breast Imaging," *IEEE Transaction on Biomedical Engineering,* vol. 57, no. 5, pp. 1003-1007, May 2010.

[26] F. Yang and A. S. Mohan, "EM techniques for the detection of breast cancer," in *IEEE Antennas and Propagation Society International Symposium (APSURSI)*, Toronto, ON, 2010.

[27] Y. Chen, E. Gunawan, K. S. Low, S.-C. Wang, C. B. Soh, and L. L. Thi, "Time of Arrival Data Fusion Method for Two-Dimensional Ultrawideband Breast Cancer Detection," *IEEE Transaction on Antennas and Propagation,* vol. 55, no. 10, pp. 2852-2865, Oct. 2007.

[28] B. Guo, Y. Yang, J. Li, P. Stoica, and R. Wu, "Microwave imaging via adaptive beamforming methods for breast cancer detection," *Journal of Electromagnetic Waves and Applications,* vol. 20, no. 1, pp. 53-63, 2006.

[29] M. Sajjadieh, F. Foroozan, and A. Asif, "Breast cancer detection using time reversal signal processing," in *Multitopic Conference, 2009. INMIC 2009. IEEE 13th International*, 2009.

[30] J. C. Curlander, *Synthetic Aperture Radar: Systems and Signal Processing*. New York: Wiley, 1991.

[31] R. Bose, A. Freedman, and B. D. Steinberg, "Sequence CLEAN: A modified deconvolution technique for microwave images of contiguous targets," *IEEE Transactions on Aerospace and Electronic Systems,* vol. 38, no. 1, pp. 89-96, 2002.

[32] S. K. Davis, B. D. Van Veen, S. C. Hagness, and F. Kelcz, "Breast Tumor Characterization Based on Ultrawideband Microwvave Backscatter," *IEEE Transaction on Biomedical Engineering,* vol. 55, no. 1, Jan. 2008.

[33] Y. Huo, R. Bansal, and Q. Zhu, "Breast tumor characterization via complex natural resonances," in *Microwave Symposium Digest, 2003 IEEE MTT-S International*, 2003, pp. 387-390.

[34] Y. Chen, E. Gunawan, K. S. Low, S. Wang, C. B. Soh, and T. C. Putti, "Effect of Lesion Morphology on Microwave Signature in 2-D Ultra-Wideband Breast Imaging," *IEEE Transaction on Biomedical Engineering,* vol. 55, no. 8, pp. 22011-2021, Aug. 2008.

[35] F. Yang and A. S. Mogan, "Complex natural resonances for breast tissues with complex morphology," in *IEEE International Symposium on Antennas and Propagation*, Spokane, WA, 2011, pp. 699-702.

[36] C. Baum, "The singularity expansion method: Background and developments," *IEEE Antennas and Propagation Society Newsletter,* vol. 28, no. 4, pp. 14-23, Aug. 1986.

[37] C. Baum, E. J. Rothwell, K. M. Chen, and D. P. Nyquist, "The Singularity Expansion Method and its Applications to Target Identification," *Proceedings of the IEEE,* vol. 79, no. 10, pp. 1481-1492, Oct. 1991.

[38] G. Joshi, "Ultra-wideband Channel Modeling using Singularity Expansion Method," Ph.D. Dissertation, Virginia Tech, Blacksburg, VA, 2006.

[39] S. Licul and W. A. Davis, "Unified Frequency and Time-Domain Antenna Modeling and Characterization," *IEEE Transactions on Antennas and Propagation,* vol. 53, no. 9, pp. 2882-2888, Sept. 2005.

[40] A. J. Fenn, *Breast Cancer Treatment by Focused Microwave Thermotherapy*. Sudbury, MA: Jones and Bartlett Publishers, 2007.

[41] A. J. Fenn, G. Wolf, and R. M. Fogle, "An adaptive microwave phased array for targeted heating of tumors in intact breast: Animal study results," *International Journal of Hyperthermia,* vol. 15, no. 1, pp. 45-61, Jan.-Feb. 1999.

[42] C. C. Vernon, J. W. Hand, S. B. Field, D. Machin, J. B. Whaley, J. van der Zee, van Putten, Wim L.J, G. C. van Rhoon, J. D. P. van Dijk, D. G. González, F.-F. Liu, P. Goodman, and M. Sherar, "Radiotherapy with or without hyperthermia in the treatment of superficial localized breast cancer: Results from five randomized controlled trials," *International Journal of Radiation Oncology*Biology*Physics,* vol. 35, pp. 731-744, 1996.

[43] R. Valdagni and M. Amichetti, "Report of long-term follow-up in a randomized trial comparing radiation therapy and radiation therapy plus hyperthermia to metastatic lymphnodes in stage IV head and neck patients," *International Journal of Radiation Oncology*Biology*Physics,* vol. 28, pp. 163-169, 1993.

[44] J. Van der Zee, D. G. González, G. C. van Rhoon, J. D. P. van Dijk, W. L. J. van Putten, and A. A. M. Hart, "Comparison of radiotherapy alone with radiotherapy plus hyperthermia

in locally advanced pelvic tumours: a prospective, randomised, multicentre trial," *Lancet,* vol. 355, pp. 1119-1125, 2000.

[45] M. E. Kowalski, B. Behnia, A. G. Webb, and J.-M. Jin, "Optimization of electromagnetic phased-arrays for hyperthermia via magnetic resonance temperature estimation," *IEEE Transaction on Biomedical Engineering,* vol. 49, no. 11, pp. 1229-1241, Nov. 2002.

[46] M. E. Kowalski and J.-M. Jin, "A temperature-based feedback control system for electromagnetic phased-array hyperthermia: Theory and simulation," *Physics in Medicine and Biology,* vol. 49, pp. 633-651, 2003.

[47] S. Jacobsen, "Reduction of hot spots in hyperthermia by means of broadband energy transmission," *Electronic Letters,* vol. 34, no. 20, pp. 1901-1902, Oct. 1998.

[48] M. C. Converse, E. J. Bond, S. C. Hagness, and B. D. Van Veen, "Ultrawide-band microwave space-time beamforming for hyperthermia treatment of breast cancer. A computational feasibility study," *IEEE Transactions on Microwave Theory and Techniques,* vol. 52, no. 8, pp. 1876-1889, Aug. 2004.

[49] B. Gou, L. Xu, and J. Li, "Time Reversal Based Microwave Hyperthermia Treatment of Breast Cancer," *Microwave and Optical Technology Letters,* vol. 47, no. 4, pp. 335-338, Nov. 2005.

[50] P. Kosmas, E. Zastrow, S. C. Hagness, and B. D. Van Veen, "A Computational Study of Time Reversal Techniques for Ultra-Wideband Microwave Hyperthermia Treatment of Breast Cancer," in *IEEE/SP 14th Workshop on Statistical Signal Processing. SSP '07.*, Madison, MI, 2007, pp. 312-316.

[51] H. D. Trefna, J. Vrba, and M. Persson, "Time-reversal focusing in microwave hyperthermia for deep-seated tumors," *Physics in Medicine and Biology,* vol. 55, pp. 2167-2185, 2010.

[52] S. Jacobsen and P. Stauffer, "Non-invasive temperature profile estimation in a lossy medium based on multi-band radiometric signals sensed by a microwave dual-purpose body-contacting antenna," *International Journal of Hyperthermia,* vol. 18, no. 2, pp. 86-103, 2002.

[53] R. M. Arthur, W. L. Straube, J. D. Starman, and E. G. Moros, "Noninvasive temperature estimation based on the energy of backscattered ultrasound," *Medical Physics,* vol. 30, no. 6, pp. 1021-1029, Jun. 2003.

[54] B. Guo, L. Xu, and J. Li, "Time Reversal Based Microwave Hyperthermia Treatment of Breast Cancer," *Microwave and Optical Technology Letters,* vol. 47, no. 4, pp. 335-338, Nov. 2005.

[55] M. C. Converse, E. J. Bond, B. D. Van Veen, and S. Hagness, "A Computational Study of Ultra-Wideband Versus Narrowband Microwave Hyperthermia for Breast Cancer Treatment," *IEEE Transaction on Microwave Theory and Techniques,* vol. 54, no. 5, pp. 2169-2180, May 2006.

.

This page intentionally left blank.

Chapter 3 Overview of Proposed Concept

This chapter presents the general overview of the proposed concept. As previously mentioned the objective is to introduce and demonstrate an adaptive approach that utilizes resonant scattering parameters to detect the location of a tumor, identify the tumor-specific resonances, and use them for microwave treatment. The feasibility of the concept is studied with the emphasis on the potential use as a combination technique with existing modalities or emerging microwave imaging techniques.

3.1 Overall Concept

The general concept is illustrated in the flow diagram shown in Figure 3.1. It is assumed that the breast is surrounded by an antenna array in either of the configurations (i.e. prone, supine, and compression plate) discussed in Chapter 2. The antenna array is also assumed to be in a matching medium. An UWB pulse is transmitted into the breast from one of the antennas and the response from the breast is received by all other elements in the array so as to generate multistatic response data. Depending on the detection processing scheme, the transmit antenna can be rotated to create a complete set of miltistatic antenna combinations. The antenna rotation can be performed either through electronic or mechanical scan. The responses are then processed for detection of tumor in the breast. This is the step at which various combinations of detection schemes can be applied to increase the robustness of detection. When used with other microwave imaging techniques mentioned in Chapter 2 [1-4], the same data can be applied for such algorithms, results from which can then be combined with those from the techniques investigated

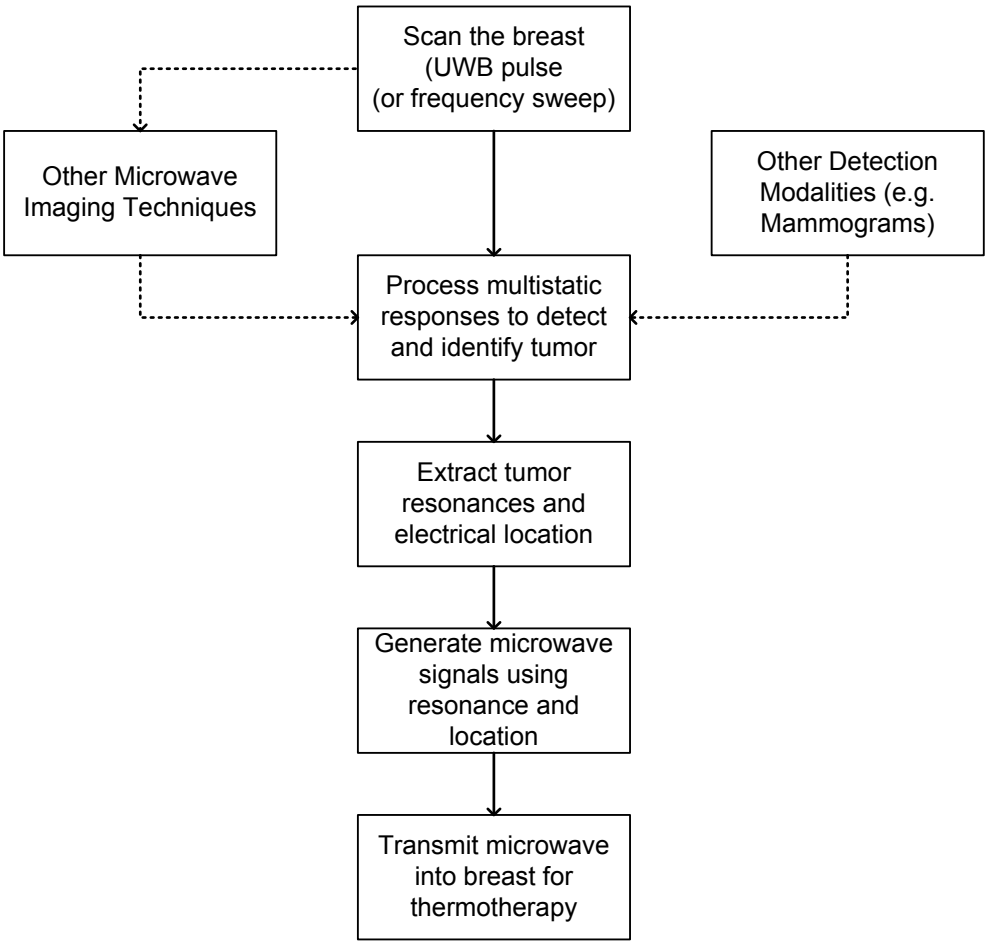

Figure 3.1 Flow diagram of the proposed concept of the resonance-based microwave breast tumor detection and treatment

in this dissertation (discussed in Chapter 5). When used with other modalities such as mammography, an additional algorithm would be needed in order to correlate the results. While the detailed discussion of how such combinations of detection techniques can be implemented is beyond the scope of this dissertation, it would become a significant topic for future work upon successful demonstration of the proposed concept. Therefore, a few possible combination scenarios are briefly discussed in the following section.

Once the potential tumor responses are identified and confirmed, the tumor resonance and the electrical location are determined. The resonance (pole) extraction algorithm is applied to each time-domain signal in the multistatic response data. The dominant resonance of the tumor is then determined from an ensemble of extracted poles from multistatic responses. The electrical location of the tumor basically represents the equivalent time-delay or phase angle with respect

to the location of the elements in the antenna array. The electrical location can be determined from the residue (complex amplitude) of the extracted poles or from the relative time delay between the peaks of the responses in the multistatic data. Chapters 4 and 5 discuss in more detail the background and the process of determining the tumor resonance and electrical location.

With the resonance frequency and the electrical location of the tumor identified, microwave signal is generated and fed into the array for non-ionizing microwave treatment. The focus should take place at the tumor location thereby heating the tumor while leaving other regions in the breast relatively unaffected. Adaptive tuning of the frequency of operation based on the tumor-specific resonance adds slight complexity to the system, but it could improve the overall efficiency due to the maximum energy coupling at the resonance frequency. Monitoring of the temperature is required to adjust the microwave power level to ensure the desired therapeutic temperature level in the tumor and a below-threshold temperature in the other regions in the breast. With the use of emerging non-invasive temperature monitoring techniques [5-7], the whole thermotherapy process could remain non-invasive.

3.2 Possible Scenarios

This section considers a few possible scenarios where the proposed concept can be applied, including the aforementioned combinations as well as a possible stand-alone use. It is to be noted that the potential scenarios are not limited to the ones discussed here.

3.2.1 Combination with Mammography

In this scenario, the best configuration may be to use the same compression plate configuration while applying the microwave antenna in between the plates to surround the breast in horizontal plane without affecting the mammography setup (see Figure 3.2). Moreover, the compressed breast provides a two-dimensional like configuration that could simplify the processing. Since the mammogram would provide a high resolution breast image with the physical location and features of the tumor and tissues, the microwave system may only need to provide the parameters corresponding to the electrical location and the resonance of the tumor. In case of no detection or non-normal detection from mammograms, microwave responses can act as a second check providing another level of detection confidence. The key to a robust detection depends on how well one can correlate the information obtained from the mammograms with those from

microwave data. This approach would allow for a relatively simple but robust combined system without significant extra cost or modification that could potentially enhance the early-stage breast cancer detection rate.

Using the same configuration, microwave focusing can be performed for hyperthermia treatment. Once the resonance and the electrical location of the tumor are determined, the same antenna array can be used to transmit microwaves into the breast. Since the antennas are located in front and around the breast in the horizontal plane, it can generate a tighter focus compared to the top/bottom approach by Fenn [8]. In the vertical plane the field distribution will be fixed with maximum intensity at the center in between the plates. However, since the compressed breast provides a relatively small vertical dimension, the tumor is less likely to be far off from the maximum in the vertical dimension. The antenna configuration could be more of a concern when applying thermotherapy since the microwaves are transmitted into the breast from the front into the back of the breast towards the chest where other organs are located. However, considering the attenuation that the waves will experience as they propagate in the breast tissue and the chest wall (bones), it is likely that the hyperthermia operation in such configuration would still be safe. Nevertheless, a thorough investigation would be needed to determine the safety of the approach.

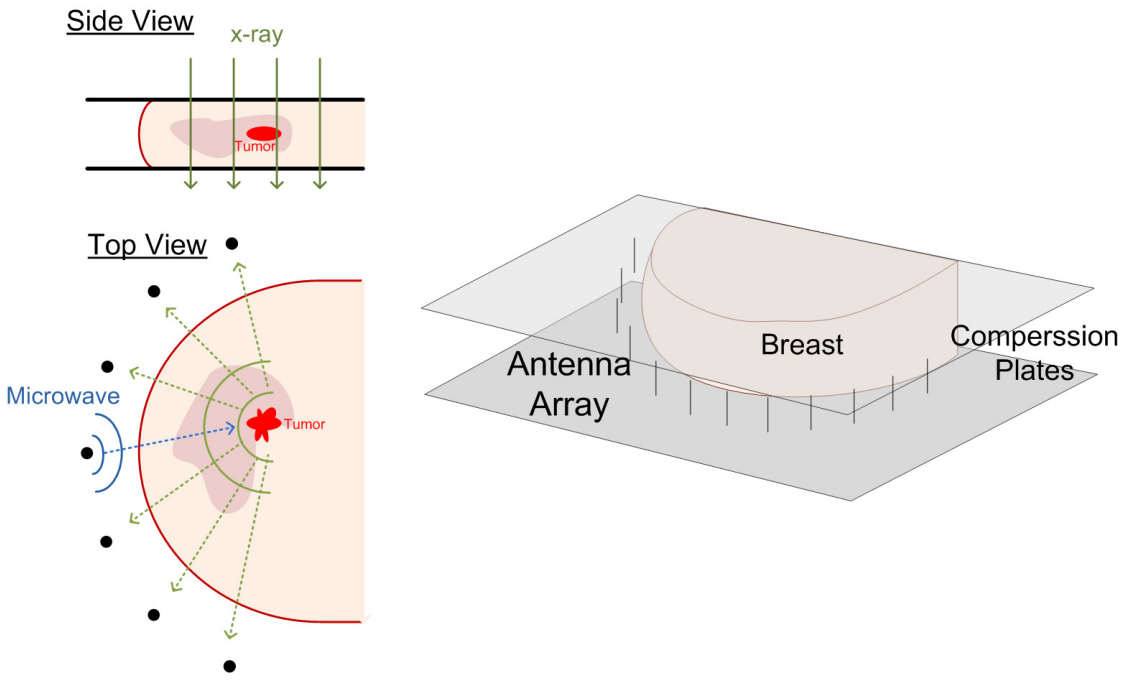

Figure 3.2 Illustration of microwave array used in compressing plate setup for use in conjunction with mammography.

3.2.2 Combination with Other Microwave Imaging Techniques

One advantage of applying the proposed concept in conjunction with other microwave imaging techniques [1-4] comes from the fact that it only requires a single microwave system, thus simplifying the system complexity. In this scenario, either of the configurations, i.e. prone or supine position (Figure 3.3), can be used. Recent trend in the literature has seen more use of the prone position configuration [2, 9, 10]. Since such systems already use ultra-wideband responses of the breast, it would only require a minimum extra processing for the resonance analysis for identification of tumor resonance and electrical location in addition to the physical location obtained from the imaging. The detection techniques discussed in Chapter 5 could also be used as a supplemental algorithm for enhanced detection. Once the potential tumor is identified and confirmed, its resonance and the electrical location can be extracted. Microwave focusing can then be performed for hyperthermia treatment by feeding the signals generated from the extracted information into the same antenna array.

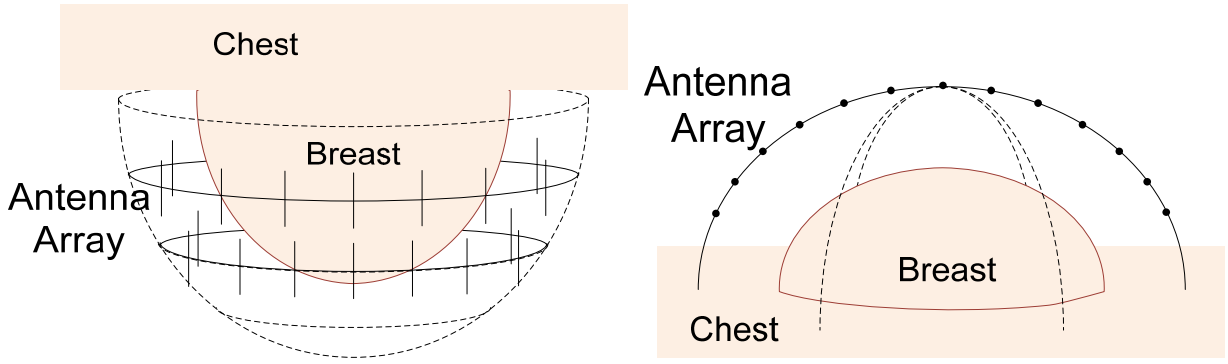

(a) Prone position configuration (b) Supine position configuration

Figure 3.3 Two common detection array configurations used in microwave-based systems.

3.2.3 Stand-alone System

In the case of a stand-alone resonance-based microwave system without imaging of the physical breast, the overall detection capability might be significantly limited. However, without requiring a computationally expensive processing, it could potentially become a low-cost precursory detection approach. One great potential application would be to implement a portable, low-cost

system that can be used for a routine screening for change detection. Since the focus is not to generate a high resolution image, a simpler array design can be used. The responses taken at different times can be compared for any changes. The processing algorithm discussed in Chapter 5, which are relatively "primitive" compared to the imaging algorithms, might be sufficient for change detection in the breast. Once a change in the breast response is detected, the abovementioned techniques can be applied for more thorough screening.

3.3 References

[1] E. J. Bond, X. Li, S. C. Hagness, and B. D. Van Veen, "Microwave imaging via space-time beamforming for early detection of breast cancer," *IEEE Transaction on Antennas and Propagation,* vol. 51, no. 8, pp. 1690-1705, Aug 2003.

[2] M. Klemm, I. J. Craddock, A. Preece, J. Leendertz, and R. Benjamin, "Evaluation of a hemi-spherical wideband antenna array for breast cancer imaging " *Radio Science,* vol. 43, no. RS6S06, 2008.

[3] P. Kosmas and C. Rappaport, "Time Reversal With the FDTD Method for Microwave Breast Cancer Detection," *IEEE Transaction on Microwave Theory and Techniques,* vol. 53, no. 7, pp. 2317-2323, Jul. 2005.

[4] X. Li and S. Hagness, "A Confocal Microwave Imaging Algorithm for Breast Cancer Detection," *IEEE Microwave and Wireless Components Letters,* vol. 11, no. 3, pp. 130-132, Mar. 2001.

[5] R. M. Arthur, W. L. Straube, J. D. Starman, and E. G. Moros, "Noninvasive temperature estimation based on the energy of backscattered ultrasound," *Medical Physics,* vol. 30, no. 6, pp. 1021-1029, Jun. 2003.

[6] H. Carlak, N. G. Gencer, and C. Besikei, "Thermal Images of Electrically Stimulated Breast: a simulation study," in *MEDICON, 2010 IFMBE Proceedings*, 2010, pp. 244-247.

[7] S. Jacobsen and P. Stauffer, "Non-invasive temperature profile estimation in a lossy medium based on multi-band radiometric signals sensed by a microwave dual-purpose body-contacting antenna," *International Journal of Hyperthermia,* vol. 18, no. 2, pp. 86-103, 2002.

[8] A. J. Fenn, *Breast Cancer Treatment by Focused Microwave Thermotherapy*. Sudbury, MA: Jones and Bartlett Publishers, 2007.

[9] S. M. Aguilar, M. A. Al-Joumayly, J. D. Shea, N. Behdad, and S. C. Hagness, "Design of a Microwave Breast Imaging Array Composed of Dual-Band Miniaturized Antennas," in *2011 XXXth URSI General Assembly and Scientific Symposium*, Istanbul, 2011.

[10] J. M. Sill and E. C. Fear, "Tissue Sensing Adaptive Radar for Breast Cancer Detection—Experimental Investigation of Simple Tumor Models," *IEEE Transaction on Microwave Theory and Techniques,* vol. 53, no. 11, pp. 3312-3319, Nov. 2005.

This page intentionally left blank.

Chapter 4 Improved Techniques for Pole Extraction and Scatterer Location Estimation from Complex Residues

The essence of the work presented in this dissertation is in the use of resonant scattering parameters for breast cancer applications. The typical microwave band used for breast applications is 0.5-20 GHz. At the corresponding wavelengths, typical dielectric properties of the tumor and surrounding tissues make the effective size on the order of the incident wavelengths, which makes the scattering problem in the resonance region. As previously mentioned, resonant scattering provides the information regarding the natural resonances of a scattering object. The singularity expansion method (SEM) [1] is an elegant way to represent the resonant scattering, since it directly uses complex natural resonances (i.e. poles and residues in the Laplace domain) as the key parameters in the representation. SEM is also a versatile representation since the resonance term is independent of incident waveform and aspect angle.

This chapter begins with a brief overview of resonant scattering and its SEM representation. Effects of lossy medium on the SEM parameters are also discussed. Techniques for estimating the SEM parameters from the time-domain response, namely Prony's [2] and the matrix pencil method (MPM) [3] are discussed. Then a new scheme of applying the MPM for improved pole estimation is presented. This approach helps better determine the poles corresponding to the actual scatterer resonance by providing a temporal presentation of the SEM representation. Finally the use of relative phase angles of complex residues as the electrical location of a scatter is introduced.

4.1 Electromagnetic Scattering

Here we would like to discuss the general field representation of electromagnetic scattering. When an electric field, $\vec{E}^i$, is incident on an object, the scattered field, $\vec{E}^s$, can be expressed as an integral equation in terms of the equivalent induced current, $\vec{J}$, as

$$\vec{E}^s(\bar{r},s) = \int_v \bar{\bar{G}}(\bar{r},\bar{r}',s)\cdot\vec{J}(\bar{r}',s)\,dv', \tag{4.1}$$

Where $\bar{\bar{G}}$ represents dyadic Green's function. The above equation is the frequency-domain representation with $s = j\omega$, and the spatial variables, $\bar{r}'$ and $\bar{r}$, respectively denote the points in the volume of the scattering object and the observation point of the scattered field. Figure 4.1 illustrates this general electromagnetic scattering. Note that there are magnetic field counterparts, namely $\vec{H}^i$ and $\vec{H}^s$, which are related to the electric fields by the Maxwell's equation. Only the electric fields are mentioned here for the brevity of discussion. The induced current, $\vec{J}$, can be treated as volume density, surface density, or line current, depending on the problem. The characteristics of $\vec{J}$ depend on the properties of the incident field (i.e. amplitude, phase and polarization) as well as the boundary condition, which is governed by the properties of both the scattering object ($\varepsilon_2, \mu_2, \sigma_{c2}$) and the surrounding medium ($\varepsilon_1, \mu_1, \sigma_{c1}$). $\bar{\bar{G}}$ is determined by the properties of both media. For far field scattering, $\bar{\bar{G}}$ is dominated by the first order term, i.e. $e^{-\gamma R}/4\pi R$, where γ is the propagation constant and $R = |\bar{r} - \bar{r}'|$ is the distance between the observation point $\bar{r}$ and the evaluation point $\bar{r}'$ in the volume integral over the scatterer geometry. The propagation constant is a complex value expressed as

$$\gamma = \alpha + j\beta = \sqrt{j\omega\mu(\sigma_c + j\omega\varepsilon)}, \tag{4.2}$$

where α is the attenuation constant and β is the phase constant. For a lossless medium, α becomes zero, which means the only loss the scattered field experiences is due to $1/4\pi R$ spherical spread of the electromagnetic wave. If the medium is lossy as in the case of breast tissues, the scattered field will experience an additional loss due to a nonzero value of α.

The time-domain equivalent expression of the scattered field in Equation 4.1 is

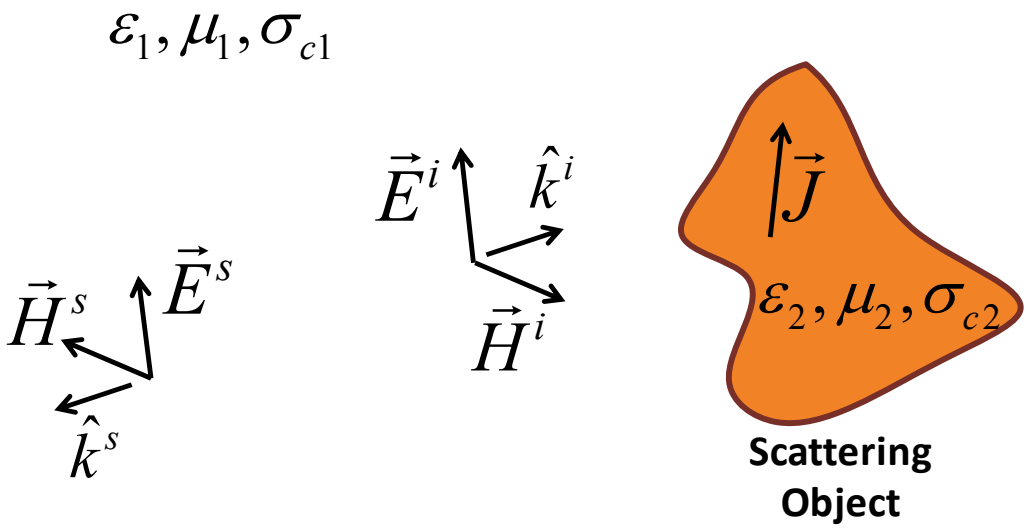

Figure 4.1 Illustration of electromagnetic scattering in general

$$\vec{E}^s(\bar{r},t) = \int_v \bar{\bar{G}}(\bar{r},\bar{r}',t-R/v) \dot{\otimes} \vec{J}(\bar{r}',t) dv', \tag{4.3}$$

Where $v = \omega/\beta$ is the speed of propagation in the medium, and $\otimes$ denotes temporal convolution. Here the phase term is basically converted into time delay.

The general representation of electromagnetic scattering above provides a good starting point for a discussion of scattering in the resonance region, or simply resonant scattering, which is presented in the following section.

4.2 Scattering in the Resonance Region

Electromagnetic scattering in general can be divided into three regions, namely the Rayleigh, resonance and optical regions. These three regions are defined using relative scatterer size to the incident wavelength. In the Rayleigh region, the incident wavelength is large compared to the object dimensions ($D/\lambda << 1$, where D is the maximum object dimension). In the resonance region, the incident wavelength is on the same order as the object dimensions ($0.5 < D/\lambda < 10$). In the optical region, the incident wavelength is much smaller than the object ($D/\lambda > 10$) [4].

As a simple demonstration of the three different regions in the scattering, we consider the canonical case of scattering from a conducting sphere in free space. Figure 4.2 shows the

normalized backscattering amplitude, also known as the radar cross section (RCS), of a conducting sphere as a function of its radius, a, in terms of the wavelength scale ($2\pi a/\lambda = \beta a$) and the three regions as defined above are highlighted. The RCS represents the relative amplitude level of the far field scattered electric field with respect to the incident field:

$$\lim_{r\to\infty}\left(4\pi r^2\left|\frac{E^s}{E^i}\right|^2\right). \tag{4.4}$$

The plot in Figure 4.2 is generated from the analytic formulation using spherical Bessel functions [4]. As shown in the figure, the scattering amplitude in the Rayleigh region simply increases as a function of frequency ($\sim\lambda^{-1}$) until the resonance region, where it starts to vary having several peaks occur, until it converges asymptotically in the optical region to a value that corresponds to the physical cross section, becoming frequency (or wavelength) independent.

The increase in amplitude as a function of frequency in the Rayleigh region is due to the object being much smaller than the incident wavelength, such that the whole object body is exposed to the same incident field level. For this reason, the Rayleigh region scattering is often analyzed using quasi-static approximation, where one uses a static problem except for the time-varying part [5].

The leveling of the scattering amplitude in the optical region is due to the target size being much larger than the incident wavelength, where most of the scattering contribution comes from specular reflections from the illuminated surface of the target, which results in the amplitude converging to the physical area of the cross section. Scattering in the optical region are typically treated using classical geometrical optics (GO) combined with the geometrical theory of diffraction, which extends GO to include diffractions from edges, corners, and points [6, 7]. Physical optics (PO) is another technique, where the approximate currents predicted from GO are used in the exact integral equation representation of the scattered field [4].

In the resonance region, since the incident wavelength is on the order of the size of the scattering object, it is primarily the global body features that affect the scattering characteristics as in the Rayleigh region. However, the fluctuation in the scattering amplitude as a function of wavelength comes from the same fact that the incident wavelength being on the order of the object size, which allows for the induced current on the object to behave in a resonant manner. In other words, the induced current on the body has a modal distribution with “standing wave” pattern [5]. Due to such modal behavior of the induced current, the scattered fields have the same

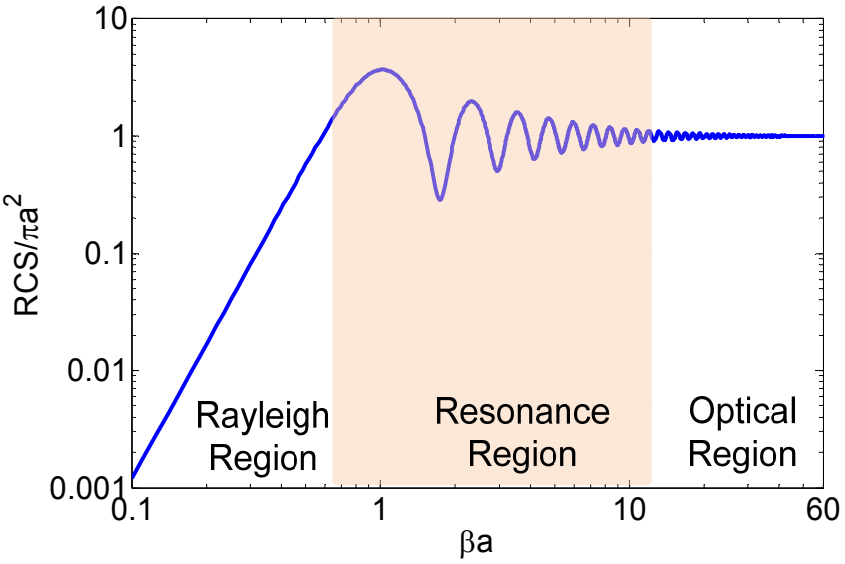

Figure 4.2 Normalized monostatic scattering amplitude or radar cross section (RCS) of a perfectly conducting sphere as a function of its circumference in terms of wavelengths ($2\pi a/\lambda = \omega a/c = \beta a$).

resonant characteristics. Such modes represent the natural resonances of the object that can be regarded as the frequencies at which the object is naturally "tuned" to resonate. For accurate analysis in the resonant scattering, the problem needs to be treated in a full-wave aspect. The problem can formulated into integral (similar to Equation 4.1) or differential equation forms, and the solutions can be obtained by either analytically (in a few limited cases) or numerically using techniques such as Method of Moments [8] and Finite Element Methods [9] in both frequency and time domains. Solutions can also be obtained by directly solving discretized Maxwell's equations in time-domain via Finite Difference Time Domain (FDTD) method [10, 11]. The SEM representation can be formulated into the integral equation in both the frequency [1, 12] and time domain [13] to solve for the natural resonances, or can be used directly with the solutions (i.e. scattered field or induced currents) to the numerical problem or measured responses to extract the natural resonances [2, 3]. More detailed discussion on the SEM and extracting the natural resonances are presented in the following section.

Figure 4.3 shows the transient backscatter response of a conducting sphere, which is basically the time-domain equivalent of the RCS plot in Figure 4.2. Transient response is in essence the impulse response of a scattering object. The plot in Figure 4.3 is generated using the same bandwidth from the RCS plot in Figure 4.2 to include all three regions in the incident spectrum. In this time-domain plot, temporal interaction of the incident pulse with the sphere is

evident. First, the specular reflection is observed, followed by the creeping wave and then comes the resonant response in the later time as the induced current on the sphere starts to behave in a resonant manner after the incident pulse has passed. Relating this transient phenomenon back to the frequency domain, the specular part is mainly due to the interaction in the optical region, where the scattering amplitude is flat across the frequencies, which in turn produces a sharp peak in the time-domain. The effect of the interaction in the Rayleigh region is not clearly observed in the transient response due to the rapid fall off in the scattering amplitude, which only results in a small perturbation in the response. The creeping wave and the resonant response in the later time are due to the interaction in the resonance region where the scattering amplitude varies across the band with several peaks corresponding to the resonance modes.

The basic scattering mechanism presented in this section for a conducting sphere in free space should in general apply to any scattering object. While the same basic principle applies, the change in detailed interaction is governed by the physical properties of the scattering object and the propagation medium, giving rise to different transient responses (or resonance modes) for different objects and scattering environments. In the case of a breast tumor, where the problem is modeled as dielectric (lossy) scattering in a lossy propagation medium, the internal modes may give rise to another class of natural resonances.

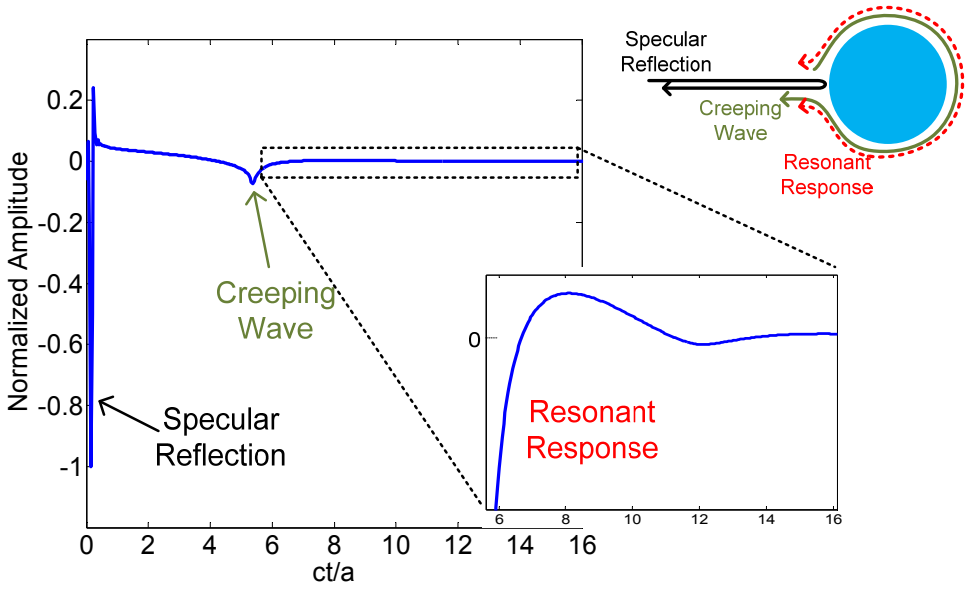

Figure 4.3 Transient monostatic scattered response of a perfectly conducting sphere as a function of normalized time (*ct/a*).

4.3 Singularity Expansion Method

The singularity expansion method (SEM) is a mathematical representation of transient scattering. The SEM was originally introduced by Baum in 1971 after observing exponentially decaying sinusoids in typical electromagnetic scattered responses from finite-size objects excited by a short, impulse-like incident signal [1]. Such phenomenon comes from the modes generated by the induced current (natural resonances) on the object as previously mentioned.

In efforts to represent this resonance phenomenon and characterize such electromagnetic interaction more efficiently, Baum developed a representation of transient scattering in terms of series expansion of Laplace domain singularities, i.e. poles and residues. Consider a conducting object in free space for the simplicity of expression as the SEM representation is derived here. For the present consideration of scattering, it is appropriate to start from the expression in Equation 4.1. The SEM representation of induced current (by incident field $\bar{E}^i$), $\vec{J}$, is [12]

$$\vec{J}\left(\bar{r}',s\right)=\sum_{n=1}\frac{E^i\left(s_n\right)\eta_n\left(\hat{k}^i,\hat{e}^i\right)\nu_n\left(\bar{r}'\right)}{s-s_n}e^{-(s-s_n)t_L}+\bar{F}\left(\hat{k}^i,\hat{e}^i,s\right), \tag{4.5}$$

where $s_n=\sigma_n+j\omega_n$ is the pole representing the natural resonance, ν_n is the natural mode that describes the modal structure at the natural resonances, and η_n is the coupling coefficient that determines the strength of natural mode induced by the incident field. Note that the coupling coefficient depends on the direction and polarization of incidence. The first term is referred to as the late-time term. The second term, $\bar{F}$, is an entire function representing the early-time response, which is the response while the incident pulse is still passing the object [12]. The scattered electric field can be obtained by substituting Equation 4.5 into Equation 4.1 as

$$\vec{E}^s\left(\bar{r},s\right)=\sum_{n=1}\frac{e^{-(s-s_n)t_L}\int_v\bar{\bar{G}}\left(\bar{r},\bar{r}',s_n\right)\cdot E^i\left(s_n\right)\eta_n\left(\hat{k}^i,\hat{e}^i\right)\bar{\nu}_n\left(\bar{r}'\right)dv'}{s-s_n}+\int_v\bar{\bar{G}}\left(\bar{r},\bar{r}',s\right)\cdot\bar{F}\left(\hat{k}^i,\hat{e}^i,s\right)dv'. \tag{4.6}$$

Combining some terms, the above expression can be reduced to,

$$\vec{E}^s\left(\bar{r},s\right)=\sum_{n=1}\frac{\bar{R}_n'\left(\hat{k}^i,\hat{e}^i,\bar{r}\right)}{s-s_n}e^{-(s-s_n)t_L}+\bar{W}\left(\hat{k}^i,\hat{e}^i,\bar{r},s\right), \tag{4.7}$$

where R_n' represents the complex residue of the n^{th} pole, and the second term still remains as an entire function describing the early-time scattered electric field. An entire function is needed for

the early-time response to ensure the convergence of the representation [12]. The residue in this expression can be considered as the resulting amplitude (and phase) of the scattered field at the resonance frequency depending on the direction/polarization of incidence ($\hat{k}^i$ and $\hat{e}^i$), and the direction of scattering and observation distance ($\bar{r}$). Through the Laplace transform, the time-domain representation of the expression in Equation 4.7 becomes

$$\vec{E}^s\left(\bar{r},t\right)=\sum_{n=1}\bar{R}_n'\left(\hat{k}^i,\hat{e}^i,\bar{r}\right)e^{s_n t}u\left(t-t_L\right)+\bar{W}_e\left(\hat{k}^i,\hat{e}^i,\bar{r},t\right), \tag{4.8}$$

which is now clear that the first term is a sum of exponentially decaying sinusoids, representing Baum's observation in [1]. In the above equation, $u(t)$ is a unit step function, and t_L, is the resonance "turn on" time, which can be regarded as the time after which the incident pulse had passed the target and only the resonant behavior remains [12]. The poles are in complex conjugate pairs for $\vec{E}^s\left(\bar{r},t\right)$ to be real-valued. The first term is typically defined as the late-time response and the second term as the early-time response. As suggested above, the late-time response is the source free oscillation at the natural resonances of the object after the incident pulse has passed (after t_L). Since the early-time response is generated while the incident pulse is still interacting with the object, it generally contains specular reflections from different scattering centers of the object as well as the forced oscillation due to the traveling wave on the object. The early-time response is represented with a continuous function that rapidly decays after t_L.

Figure 4.4 shows the poles of a conducting sphere obtained from an analytic solution (Mie series [14]) and from the late-time SEM representation of the response in Figure 4.3 using the matrix-pencil method (MPM) [3], which will be discussed in the following section. Notice that the poles in the first layer are accurately estimated by the MPM while none of the poles in the second layer are estimated. This is due to high decay constants that make such poles hardly present in the simulated or measured responses.

It is clear from the above equations that the poles (natural resonances) are independent of aspect (i.e. polarization/angle of incidence or scattering). They are determined only by the physical properties of the target (shape, size, and material composition). The residues, however, are aspect-dependent and related to the scattering pattern of the object. This means that the scattered response measured at any aspect angle and distance should contain the same poles, but at different amplitudes and phases.

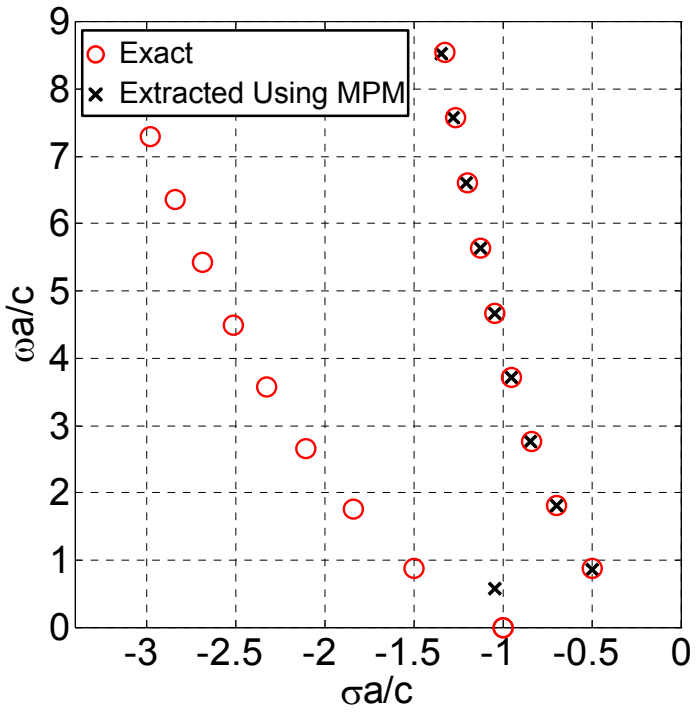

Figure 4.4 Poles of a perfectly conducting sphere (a=15cm): Analytically determined vs. estimated using the matrix-pencil method.

4.3.1 SEM parameters of Objects Immersed in Lossy Dielectrics

For the breast tumor problem, the general SEM representation discussed above still applies. However, the resonance mechanism is slightly more involved since the problem now consists of dielectric scatterer buried in another dielectric propagation medium, which could be inhomogeneous. For dielectric scattering, there exist external and internal modes. The external modes are determined by the boundary condition and the parameters of the propagation medium in the same way as a conducting scatterer. The internal modes are determined by the parameters of the scatter since they are in essence lossy cavity modes [15]. Heterogeneity in the breast also adds more complexity into the resonance phenomena. Moreover, since both media (i.e. breast tissue and tumor) are lossy, the resonant oscillation decays faster than it would in the case of lossless dielectrics, which results in higher damping constants ($\sigma_n = \mathrm{Re}\{s_n\}$) in the poles. Due to relatively high conductivity of tumors, the resonances from the internal modes may not be

apparent in the scattered response and thus may not be as significant as it would be in the low-loss or lossless case.

It is helpful to briefly discuss how the SEM parameters for buried objects scale to the SEM parameters of the same in free space. This scaling relationship provides an insight into the region in the incident spectrum where the resonances might occur given an estimate of the propagation medium and scatterer parameters. For the simplicity of discussion, we limit the case to a scatterer in homogeneous medium with constant (frequency independent) permittivity and conductivity, without loss of generality. Using the constitutive parameters defined in Figure 4.1, we start with a conducting object in a lossy dielectric propagation medium, where only the external (surface) resonances exist, the scaling is only determined by the properties of the propagation medium as [15]

$$s_n = -\frac{\sigma_{c1}}{2\varepsilon_1} + \sqrt{\left(\frac{\sigma_{c1}}{2\varepsilon_1}\right)^2 + \frac{\left(s_n^{fs}\right)^2}{\varepsilon_{r1}}} \tag{4.9}$$

where $\varepsilon_1 = \varepsilon_{r1}\varepsilon_o$, $s_n = \sigma_n + j\omega_n$ are the poles of the object in the medium (i.e. $\varepsilon_{r1} > 1$ and $\sigma_{c1} > 0$), and $s_n^{fs} = \sigma_n^{fs} + j\omega_n^{fs}$ are the poles of the same object in free space (i.e. $\varepsilon_r = 1$ and $\sigma_{c1} = 0$). For scatterers whose natural resonances are significantly larger in magnitude than the relaxation frequency of propagation medium (i.e. $|s_n| \gg \sigma_{c1}/\varepsilon_1$), the scaling can be reduced to [15]

$$s_n \approx \frac{s_n^{fs}}{\sqrt{\varepsilon_{r1}}} - \frac{\sigma_{c1}}{2\varepsilon_1} + O\left(1/s_n^{fs}\right). \tag{4.10}$$

For a dielectric scattering object (i.e. $\varepsilon_{r1} \neq \varepsilon_{r2} > 1$ and $\sigma_{c1} \neq \sigma_{c2} > 0$), where both external and internal resonances exist, the same scaling relationship as in Equation 4.9 can be used for the external modes, while there is no scaling in internal modes as they remain relatively unaffected by the surrounding medium. However, the poles for the internal modes will shift depending on the surface boundary condition, as it determines the damping of the internal resonances in the scattered response [15].

Consider for example a conducting sphere with the radius of 1cm in a simple lossy dielectric medium with $\varepsilon_{r1} = 4$ and $\sigma_{c1} = 0.25$ S/m. The size and the material properties are chosen to approximately match those in the breast tumor problem. Using the scaling relationship in Equation 4.9, one can obtain the scaled poles corresponding to the natural resonances of the

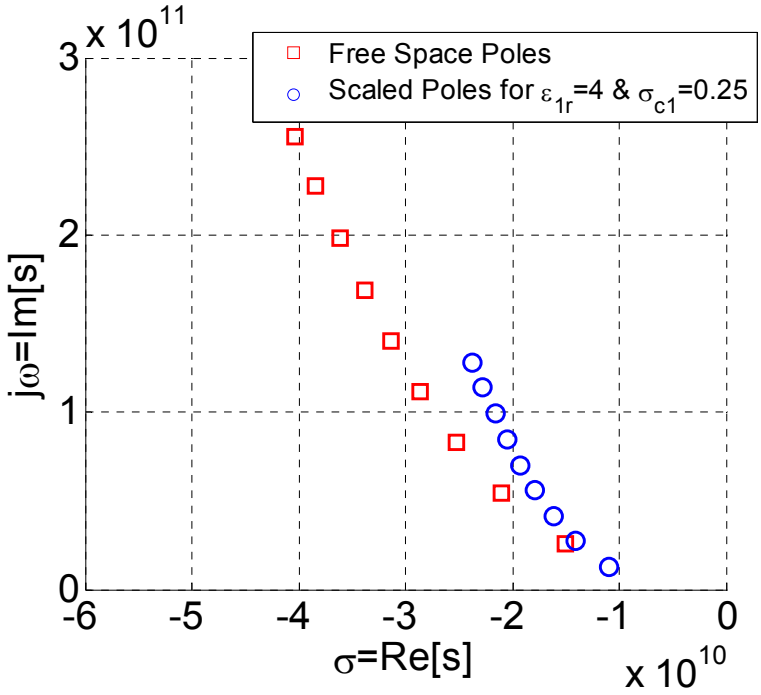

Figure 4.5 Scaled poles of a conducting sphere of 1cm radius in simple lossy dielectric medium ($\varepsilon_{r1} = 4$ and $\sigma_{c1} = 0.25$ S/m) using Equation 4.9.

sphere in the lossy medium (see Figure 4.5). These scaled poles are what one would expect to obtain when processing the actual response of the sphere in the specified medium.

To investigate the utility of the scaling equation, the poles estimated from a numerically simulated response of the same sphere were compared with the scaled poles. The simulation is done using SEMCAD X®, a finite difference time domain (FDTD) code. The responses are obtained by exciting the sphere with a plane wave of differentiated Gaussian pulse with the equivalent bandwidth of 10GHz, and the backscattered response is recorded at 10cm away from the sphere. The poles from the backscattered responses are obtained using the matrix-pencil method. In Figure 4.6 the extracted poles from the simulated response are compared with the scaled poles. The poles in general seem to be in good agreement (fist three poles as indicated by dashed circles) although some extraneous poles (that occur at higher frequencies and typically low in residue amplitude) seem to have been extracted. It should be noted that the error could have come from relatively coarse rectangular FDTD grid (~$0.1\lambda_{high}$) used in the model and imperfect absorbing boundary condition, which could possibly have introduced some artifact in

the response. Since the purpose of the simulation was to provide the basic insight into pole scaling, a rather coarser gridding would be sufficient. The poles obtained from the simulated response of a lossy dielectric sphere ($\varepsilon_{r2} = 20$ and $\sigma_{c2} = 4$ S/m) of the same size is also plotted in Figure 4.6. A pole can be found that matches with the first pole of the PEC sphere, which corresponds to the fundamental external resonance. Due to relatively high conductivity in the dielectric sphere, it is not likely to see much of the internal resonances except for the first few modes. Hence it can be speculated that some of the low frequency (ω) poles are likely from the internal resonances. The other poles in the higher frequency region seem to loosely match those of conducting sphere, indicating that they could as well be the result of numerical error. In general the simulated poles from both conducting and dielectric spheres seem to agree with those estimated using the scaling relations, providing a general estimate of the parameters to expect when applying the SEM-based techniques in breast tumor problem.

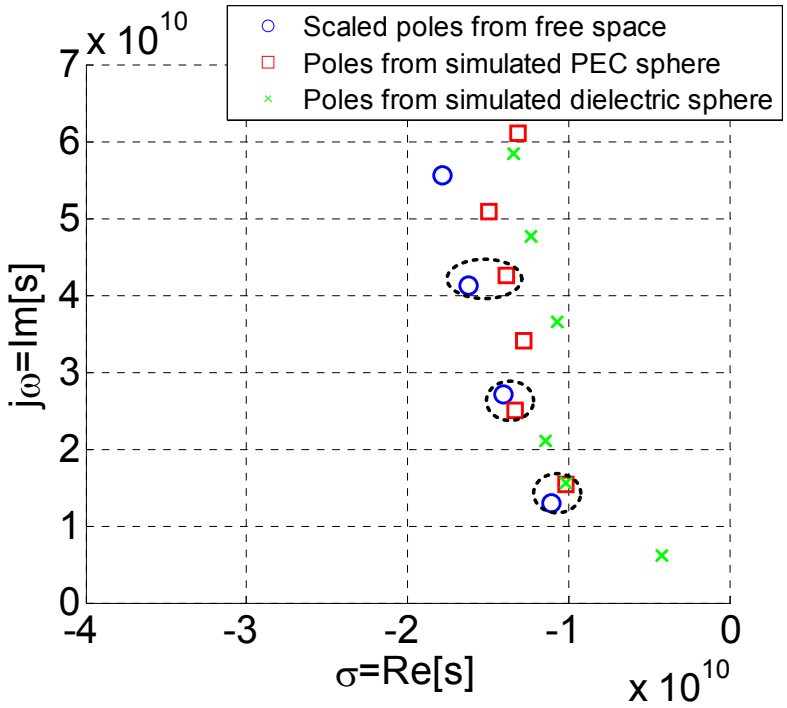

Figure 4.6 Poles extracted from numerically simulated responses of conducting ($\sigma_{c2} = \infty$) and lossy dielectric ($\varepsilon_{r2} = 20$ and $\sigma_{c2} = 4$ S/m) spheres in simple lossy dielectric medium ($\varepsilon_{r1} = 4$ and $\sigma_{c1} = 0.25$ S/m) compared with the scaled poles.

4.4 Estimating the SEM parameters from Transient Backscatter

Here the late-time response is of particular interest since the SEM parameters, i.e. poles and resides, are contained in the late-time response. In principle, there are an infinite number of natural modes (resonances) in a scattering object, which means that if the object is excited by a true impulse, the late-time term should have an infinite series expansion. However, in practice the excitation is bandwidth limited, so too should the transient scattered response, limiting the number of poles in the series. The late-time scattered response measured by an antenna can be expressed as

$$x_{LT}\left(\bar{r},t\right)=\sum_{n=1}^{N}R_n\left(\hat{k}^i,\hat{e}^i,\bar{r},\hat{e}^m\right)e^{s_n t}u\left(t-t_L\right) \qquad (4.11)$$

where N is the number of poles available or dominant in the response. Note that the residue, R_n, in this expression is different from $\bar{R}'_n$ in Equation 4.8, since the antenna effective length and polarization need to be taken into account. The subscript $_{LT}$ denotes the late-time.

From the late-time transient scattered response, the poles and residues can be extracted in essence by fitting the signal as a sum of complex exponentials [2, 3]. The sampled late-time response in Equation 4.11 can be represented as

$$x_{LT}\left(m\Delta_t+t_L\right)=x_m\approx\sum_{n=1}^{N}R_n e^{s_n(m\Delta_t)}=\sum_{n=1}^{N}R_n z_n^m,\quad \text{for}\quad m=0,\ 1,\ \ldots,\ M-1 \qquad (4.12)$$

where M is the total number of samples in the signal and Δ_t is the sampling interval. For the sampled signal, the maximum number of poles that can be extracted, N, is limited by the number of samples and the Nyquist sampling limit, i.e. $s_N=\sigma_N\pm j\omega_N=\sigma_N\pm j2\pi f_N\ \rightarrow f_N=1/2\Delta_t$ and $M=2N$. Noise in the response could set additional constraints to the maximum number of true poles (that correspond to natural resonance) that can be extracted from the signal. The problem is now reduced to estimating the poles (s_n) and residues (R_n) by essentially fitting the response into the expression in Equation 4.12. In the following subsections, two prominent methods for extracting poles from the time-domain response, namely Prony's method and the Matrix Pencil Method (MPM), are briefly discussed.

4.4.1 Prony's Method

Prony's method was originally developed by Prony in 1795 for solving the problems in thermal expansion of gases by representing the time-sampled data using a weighted sum of exponentials [16]. The use of Prony's method for extracting the SEM parameters in electromagnetic radiation and scattering was first demonstrated by VanBlaricum in [2] using the transient response of a dipole antenna. Prony's method bases its approach in formulating the transient response into a polynomial expression and finding its roots to obtain poles.

Prony's method involves a three-step procedure for extracting the poles and residues. The first step is to solve for the coefficients, c_i, in the following expression, which was shown to satisfy the expression in Equation 4.12 [2],

$$\sum_{i=0}^{N} c_i x_{i+p} = 0, \quad \text{for } i+p = m = 0,\ 1,\ \ldots,\ M-1. \tag{4.13}$$

where M is the total number of samples in the signal, N is the number of assumed poles in the signal, and x_{i+p} are the sampled data points of the transient response. If we set $c_N = 1$, then the above equation becomes

$$\sum_{i=0}^{N-1} c_i x_{i+p} = -x_{N+p}, \quad \text{for } i+p = m = 0,\ 1,\ \ldots,\ M-1, \tag{4.14}$$

and the matrix form is

$$\begin{bmatrix} x_0 & x_1 & \cdots & x_{N-1} \\ x_1 & x_2 & \cdots & x_N \\ \vdots & \vdots & \ddots & \vdots \\ x_{M-N-1} & x_{M-N} & \cdots & x_{M-2} \end{bmatrix}_{(M-N)\times N} \begin{bmatrix} c_0 \\ c_1 \\ \vdots \\ c_{N-1} \end{bmatrix}_{N\times 1} = -\begin{bmatrix} x_N \\ x_{N+1} \\ \vdots \\ x_{M-1} \end{bmatrix}_{N\times 1}, \tag{4.15}$$

or simply

$$\mathbf{X}\,\mathbf{c} = \mathbf{x}. \tag{4.16}$$

With this matrix formulation the coefficient matrix, $\mathbf{c}$, can be solved. If $M=2N$, then $\mathbf{X}$ becomes a square matrix, allowing for the solution to be obtained using the exact inverse matrix. If $M > 2N$, then $\mathbf{X}$ is a non-square matrix, requiring a least-square type approach using the pseudoinverse to obtain the solution. Once the coefficients are obtained by solving Equation

4.16, the next step is to find the poles. Substituting Equation 4.12 into Equation 4.13 and after some algebraic manipulation, the following equation is obtained [2]:

$$\sum_{i=0}^{N} c_i z_n^i = 0, \quad \text{for n=1, } \ldots \text{ , } N \tag{4.17}$$

which is an N^{th} polynomial with the roots z_n. Once the roots are found, the poles can be extracted,

$$s_n = \frac{\ln z_n}{\Delta_t}. \tag{4.18}$$

The last step then is to obtain the residues, R_n, by solving Equation 4.12 in the following matrix form using the least squares approach,

$$\begin{bmatrix} 1 & 1 & \cdots & 1 \\ z_1 & z_2 & \cdots & z_N \\ \vdots & \vdots & \ddots & \vdots \\ z_1^{M-1} & z_2^{M-1} & \cdots & z_N^{M-1} \end{bmatrix}_{M\times N} \begin{bmatrix} R_1 \\ R_2 \\ \vdots \\ R_N \end{bmatrix}_{N\times 1} = \begin{bmatrix} x_0 \\ x_1 \\ \vdots \\ x_{M-1} \end{bmatrix}_{M\times 1}. \tag{4.19}$$

While the original Prony's method has shown to be effective in extracting poles in the early investigation which only consisted of relatively clean signals [2], there are some significant limitations in its performance [3]. It has been known for being sensitive to noise in the signal. It can also become computationally inefficient when the number of poles to extract, N, is high, since it is difficult to find the roots as the order increases. Moreover, it is difficult to estimate N accurately unless *a priori* information is given. If N is larger than the exact number of poles contained in the signal, then the set of extracted poles will contain spurious poles along with the actual poles. On the other hand, if N is smaller than the exact number of poles contained in the response, then the extracted pole values may significantly deviate from the actual pole values.

To overcome some the limitations of original Prony's method, various modifications have been introduced by various authors [17-20]. Notable approaches include the Kumaresan-Prony [17] and TLS-Prony methods [19], which attempt to improve the performance of pole estimation in a noisy signal by applying singular value decomposition (SVD) of $\mathbf{X}$ (Kumaresan-Prony) or to $[\mathbf{X}\ \mathbf{x}]$ (TLS-Prony) to retain only the significant singular values thereby reducing the order of the matrix before applying Prony's method. Such modifications have shown improvement over the original Prony's method for noise-prone data. These approaches should also help in terms of estimating N.

4.4.2 Matrix Pencil Method

The matrix-pencil method (MPM) [3, 21, 22] has shown to be more robust method for extracting the SEM parameters. The main advantage of MPM is in its computational efficiency, which comes from the single-step process (as opposed to two-step in Prony's method) for extracting poles, which reduces round-off error problems. MPM is also known to be less sensitive to noise in the signal. MPM bases its approach on formulating the sampled response into a generalized eigenvalue problem [3, 21]. The name Matrix-Pencil originated from the matrix formulation of the pencil-of-functions, *p*, defined as

$$p(t,\lambda) = g(t) + \lambda f(t), \tag{4.20}$$

which is a linear combination of two functions *g* and *f* with a scalar parameter λ.

MPM consists of two-step overall procedure for obtaining the poles and residues. The first step is the pole extraction process, where one starts by rearranging the sampled data in Equation 4.12 into two matrices as follows [3]:

$$\mathbf{X}_0 = \begin{bmatrix} x_0 & x_1 & \cdots & x_{L-1} \\ x_1 & x_2 & \cdots & x_L \\ \vdots & \vdots & \ddots & \vdots \\ x_{M-L-1} & x_{M-L} & \cdots & x_{M-2} \end{bmatrix}_{(M-L)\times L} = \begin{bmatrix} \sum_{n=1}^{N} R_n z_n^0 & \cdots & \sum_{n=1}^{N} R_n z_n^{L-1} \\ \vdots & \ddots & \vdots \\ \sum_{n=1}^{N} R_n z_n^{M-L-1} & \cdots & \sum_{n=1}^{N} R_n z_n^{M-2} \end{bmatrix}_{(M-L)\times L} \tag{4.21}$$

and

$$\mathbf{X}_1 = \begin{bmatrix} x_1 & x_2 & \cdots & x_L \\ x_2 & x_3 & \cdots & x_{L+1} \\ \vdots & \vdots & \ddots & \vdots \\ x_{M-L} & x_{M-L+1} & \cdots & x_{M-1} \end{bmatrix}_{(M-L)\times L} = \begin{bmatrix} \sum_{n=1}^{N} R_n z_n^1 & \cdots & \sum_{n=1}^{N} R_n z_n^L \\ \vdots & \ddots & \vdots \\ \sum_{n=1}^{N} R_n z_n^{M-L} & \cdots & \sum_{n=1}^{N} R_n z_n^{M-1} \end{bmatrix}_{(M-L)\times L} \tag{4.22}$$

where *M* is the total number of samples in the signal, *N* is the number of assumed poles in the signal, and *L* is the number of samples in the data window chosen for generating the matrices above, also known as the matrix pencil parameter [3, 21]. Note that the elements in $\mathbf{X}_1$ are shifted by one index (Δ_t in time scale) relative to their counterparts in $\mathbf{X}_0$. The mutual constraints for *L* and *N* can be found by looking into the underlying structure of the above matrices by decomposing them in the following manner:

$$\mathbf{X}_0 = \mathbf{Z}_0 \mathbf{R} \mathbf{Z}_1 \tag{4.23}$$

and

$$\mathbf{X}_1 = \mathbf{Z}_0 \mathbf{R} \mathbf{Z}_z \mathbf{Z}_1 \tag{4.24}$$

where

$$\mathbf{Z}_0 = \begin{bmatrix} 1 & 1 & \cdots & 1 \\ z_1 & z_2 & \cdots & z_N \\ \vdots & \vdots & \ddots & \vdots \\ z_1^{M-L-1} & z_2^{M-L} & \cdots & z \end{bmatrix}_{(M-L)\times N}, \tag{4.25}$$

$$\mathbf{Z}_1 = \begin{bmatrix} 1 & z_1 & \cdots & z_1^{L-1} \\ 1 & z_2 & \cdots & z_2^{L-1} \\ \vdots & \vdots & \ddots & \vdots \\ 1 & z_N & \cdots & z_N^{L-1} \end{bmatrix}_{N\times L}, \tag{4.26}$$

$$\mathbf{R} = \begin{bmatrix} R_1 & 0 & \cdots & 0 \\ 0 & R_2 & \cdots & 0 \\ \vdots & \vdots & \ddots & \vdots \\ 0 & 0 & \cdots & R_N \end{bmatrix}_{N\times N}, \text{ and} \tag{4.27}$$

and

$$\mathbf{Z}_z = \begin{bmatrix} z_1 & 0 & \cdots & 0 \\ 0 & z_2 & \cdots & 0 \\ \vdots & \vdots & \ddots & \vdots \\ 0 & 0 & \cdots & z_N \end{bmatrix}_{N\times N}. \tag{4.28}$$

Now putting the matrices into the form of pencil-of-functions, we have

$$\begin{aligned} \mathbf{X}_1 - \lambda \mathbf{X}_0 &= \mathbf{Z}_0 \mathbf{R} \mathbf{Z}_z \mathbf{Z}_1 - \lambda \mathbf{Z}_0 \mathbf{R} \mathbf{Z}_1 \\ &= \mathbf{Z}_0 \mathbf{R} \left[\mathbf{Z}_z - \lambda \mathbf{I} \right] \mathbf{Z}_1 \end{aligned} \tag{4.29}$$

where $\mathbf{I}$ is the M x M identity matrix. The matrix pencil, $\mathbf{X}_1 - \lambda \mathbf{X}_0$, in general should have the rank of N, if $N \le L \le M - N$, which sets up a general relationship on N and L that result in the pole extraction performance. If we consider $\lambda = z_n$ (n = 1, 2, …, N), the rank of the matrix pencil

reduces to M-1, and λ are the eigenvalues of the matrix pencil, which can be solved by formulating into the generalized eigenvalue problem,

$$\mathbf{X}_1\mathbf{v}_n = z_n\mathbf{X}_0\mathbf{v}_n \qquad \text{or} \qquad \left(\mathbf{X}_0^{+}\mathbf{X}_1 - \lambda\mathbf{I}\right)\mathbf{v}_n = 0 \tag{4.30}$$

where $\mathbf{v}_n$ are the corresponding eigenvectors and the superscript, $(\cdot)^{+}$, denotes the pseudoinverse. Once the eigenvalues (z_n) are obtained, the poles can be extracted using Equation 4.18.

To improve the performance limited by noise in the signal, a modified version of the MPM was developed [3, 22], which uses the singular value decomposition (SVD) to determine the essential number of poles and thus reducing the rank of the matrix. This approach is similar to those modifications made to Prony's method [17, 19] in a sense that SVD is applied to reduce the order of data matrix based on the number of significant singular values. We start by creating a new form of data matrix by combining $\mathbf{X}_0$ and $\mathbf{X}_1$ as follows:

$$\mathbf{X}=\begin{bmatrix} x_0 & x_1 & \cdots & x_L \\ x_1 & x_2 & \cdots & x_{L+1} \\ \vdots & \vdots & \ddots & \vdots \\ x_{M-L-1} & x_{M-L} & \cdots & x_{M-1} \end{bmatrix}_{(M-L)\times L+1} \tag{4.31}$$

Note that the signal is now assumed to have noise content. Then, SVD of $\mathbf{X}$ is performed, such that

$$\mathbf{X}=\mathbf{U}\boldsymbol{\Sigma}\mathbf{V} \tag{4.32}$$

where $\mathbf{U}$ and $\mathbf{V}$ are unitary matrices in column and row composed of eigenvectors of $\mathbf{X}\mathbf{X}^{\mathbf{H}}$, and $\boldsymbol{\Sigma}$ is a diagonal matrix containing the singular values of $\mathbf{X}$. Now the number of dominant poles can be estimated by determining the number of significant singular values in $\boldsymbol{\Sigma}$. One way to do so is to look at the ratio between the maximum singular values (normalized amplitude) and the other singular values in the matrix. After discarding the singular values that are below some threshold ratio, P significant singular values (above threshold) are retained. Following the reduced matrix formulation from [23, 24], the truncation of matrices can be carried out as follows:

$$\mathbf{W}=\mathbf{U}'\boldsymbol{\Sigma}' \tag{4.33}$$

where $(\cdot)'$ denotes the retention of only the P significant terms. Relating the truncated form above back to the original sequential matrices, $\mathbf{W_0}$ and $\mathbf{W}_1$ are defined as

$$\mathbf{W_0} = \mathbf{W}\left(1:M-L-1,1:P\right) = \begin{bmatrix} w_{1,1} & w_{1,2} & \cdots & w_{1,P} \\ w_{2,1} & w_{2,2} & \cdots & w_{2,P} \\ \vdots & \vdots & \ddots & \vdots \\ w_{M-L-1,1} & w_{M-L-1,2} & \cdots & w_{M-L-1,P} \end{bmatrix}_{(M-L-1)\times P} , \tag{4.34}$$

and

$$\mathbf{W}_1 = \mathbf{W}\left(2:M-L,1:P\right) = \begin{bmatrix} w_{2,1} & w_{2,2} & \cdots & w_{2,P} \\ w_{3,1} & w_{3,2} & \cdots & w_{3,P} \\ \vdots & \vdots & \ddots & \vdots \\ w_{M-L,1} & w_{M-L,2} & \cdots & w_{M-L,P} \end{bmatrix}_{(M-L-1)\times P} . \tag{4.35}$$

The problem can now be reduced to solving eigenvalues (z_n) of the matrix pencil

$$\mathbf{W}_1\mathbf{v}_n = z_n\mathbf{W}_0\mathbf{v}_n \quad \Rightarrow \quad \left(\mathbf{W}_0^H\mathbf{W}_1\right)\mathbf{v}_n = z_n\left(\mathbf{W}_0^H\mathbf{W}_0\right) . \tag{4.36}$$

With a smaller rank matrix, reduced number of eigenvalues is obtained, representing the true poles in the signal more accurately. These eigenvalues obtained using the form in Equation 4.33 yield the same set of eigenvalues obtained using the truncated $\mathbf{v}$ matrices as in [3].

Once the poles are obtained from the eigenvalues, the corresponding residues can be found by solving the least squares problem of the following representation:

$$\begin{bmatrix} 1 & 1 & \cdots & 1 \\ z_1 & z_2 & \cdots & z_P \\ \vdots & \vdots & \ddots & \vdots \\ z_1^{M-1} & z_2^{M-1} & \cdots & z_P^{M-1} \end{bmatrix}_{M\times P} \begin{bmatrix} R_1 \\ R_2 \\ \vdots \\ R_P \end{bmatrix}_{P\times 1} = \begin{bmatrix} x_0 \\ x_1 \\ \vdots \\ x_{M-1} \end{bmatrix}_{M\times 1} , \tag{4.37}$$

which is essentially the same formulation as Equation 4.19 except for a different maximum number of poles.

The MPM approach presented above has shown to be more robust in noise-prone signals than Prony's method [3]. It was shown that the statistical variance of the estimated poles from noisy signals using the MPM with SVD is less than that obtained using Prony's method with SVD [3]. Moreover, implementation of the MPM algorithm can be carried out in a simpler way

due to a single step eigenvalue formulation for the pole estimation. For this reason we use the MPM for resonance extraction in this dissertation. To improve the robustness of the pole extraction, a new way of applying the MPM is be introduced in the following section (4.4) and utilized in the following chapters for breast tumor models.

4.4.2.1 MPM Performance with Noisy Signals

In a practical measurement environment, scatterer responses will always contain some noise and it is important to minimize the effect of noise in the pole extraction process. As previously mentioned above the matrix-pencil method (MPM) applied with SVD have shown to perform quite well with noisy signal. Here the utility of the MPM is verified using a simulated signal which contains two conjugate pole pairs with as the signal-to-noise ratio (SNR) is varied.

Consider a signal *y(t)* defined as

$$y(t) \approx y(m\Delta_t) = \sum_{n=1}^{N=2} R_n e^{s_n m\Delta_t} + n_m \qquad m = 0\ ,\ \ldots,\ M \tag{4.38}$$

where $s_1 = -0.5\times10^9 \pm j2\pi\left(1\times10^9\right)$, $s_2 = -1\times10^9 \pm j2\pi\left(1.7\times10^9\right)$, $R_1 = 0.5$ and $R_2 = 0.5e^{\pm j(\pi/6)}$. The signal is truncated at $t = 8\times10^{-9}$ s with $\Delta_t = 0.05\times10^9$, such that $M = 160$. The second term represents the noise in the signal, which is generated numerically using a Gaussian distribution. Signals containing the noise at various SNR values are put in the form of matrix **X** as in Equation 4.31 and the SVD is obtained to observe the effect of SNR on the singular values. As shown in Figure 4.7, for the signals with SNR values of 15dB or higher, it is pretty clear that there are four dominant singular values corresponding to the actual poles. The reduced form matrix in Equation 4.33 can be truncated as such and the poles and residues can be calculated with fairly small error as shown in Table 4.1. At lower SNR values the number of dominant singular values is difficult to determine as the other singular values increase in relative amplitude. Moreover, the extracted poles and residues seem to deviate further from the original values. The estimated poles and residues shown in Table 4.1 are all calculated from the truncated matrix with using *P*=4. It should be noted, however, that the deviation in the estimated poles take place more in the damping constant, $\mathrm{Re}\{s_n\} = \sigma_n$, than in the oscillating frequency, $\mathrm{Im}\{s_n\} = \omega_n$ (see Figure 4.8), which gives more tolerance to error when one is only interested in the oscillating frequency part of the complex resonance. The estimated residues seem to be

reasonably close to the actual values for the signal with SNR=5dB, but significantly off when SNR is 0dB.

In general, the pole estimation using MPM-SVD seems to work fairly well when SNR is above 15-20dB. This observation is consistent with that made in [3, 25]. For the breast tumor application, even with a controlled measurement environment with a reasonable output power level and a good dynamic range, achieving the SNR of 15dB in a single tumor response could be a challenge. However, the limitations can be overcome with processing gain, particularly from averaging. Averaging multiple shots of received signal improves the SNR significantly since the noise with random distribution will average to zero while the signal remains unchanged. Figure 4.9 shows the averaging of 100 shots of the signal with SNR of 0dB. A much cleaner signal that is very close to the original response is observed after 100-shot averaging (the SNR seems to have improved to about 15dB). As a result, the estimated poles and residues are significantly closer to the actual values.

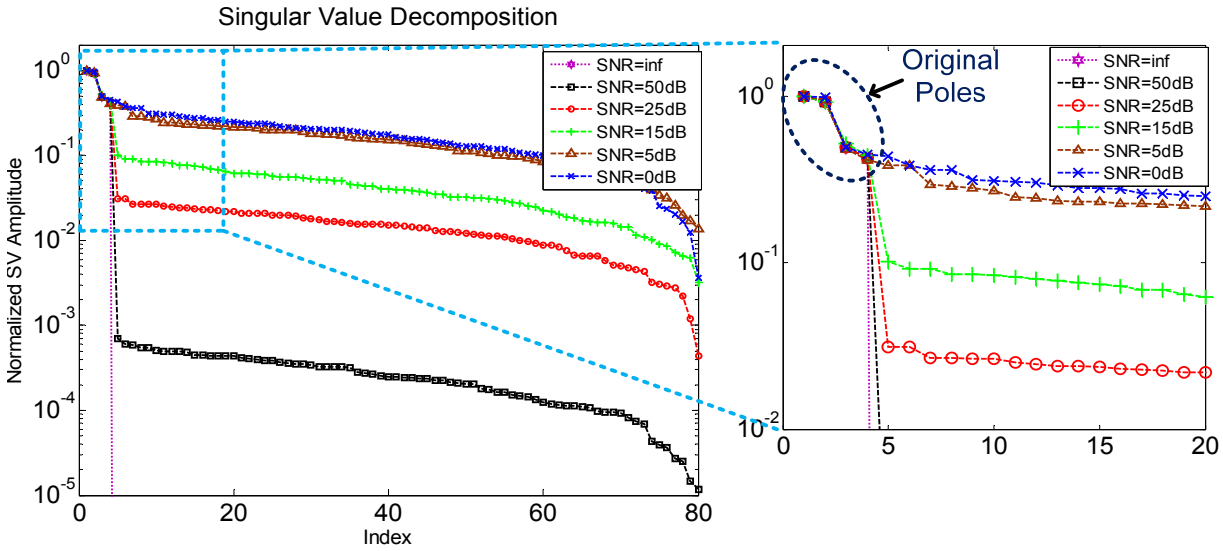

Figure 4.7 Singular value decomposition of the matrix **X** generated from the signal *y(t)* with various signal-to-noise ratio.

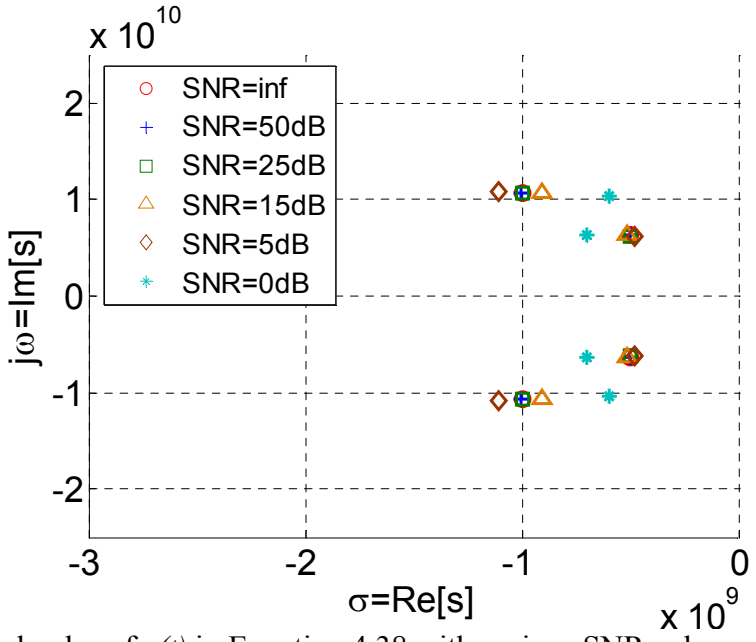

Figure 4.8 Estimated poles of *y(t)* in Equation 4.38 with various SNR values.

Table 4.1 Estimated poles and residues from *y(t)* with various SNR values.

SNR	Extracted Poles s_n $(\times 10^9)$	Poles % error $(\mathrm{Re}\{s_n\}/\mathrm{Im}\{s_n\})$	Extracted Residues R_n	Residues error $\lvert R_n\rvert$ % *error*/$\Delta\phi_n$ deg
∞	$s_1 = -0.5 \pm j2\pi(1)$	s_1 : 0 / 0	$R_1 = 0.5$	R_1 : 0 / 0
	$s_2 = -1 \pm j2\pi(1.7)$	s_2 : 0 / 0	$R_2 = 0.5e^{\pm j0.5236}$	R_2 : 0 / 0
50dB	$s_1 = -0.5 \pm j2\pi(1)$	s_1 : 0 / 0	$R_1 = 0.5$	R_1 : 0 / 0
	$s_2 = -1 \pm j2\pi(1.7)$	s_2 : 0 / 0	$R_2 = 0.5e^{\pm j0.5236}$	R_2 : 0 / 0
25dB	$s_1 = -0.503 \pm j2\pi(0.998)$	s_1 : 0.7 / 0.2	$R_1 = 0.499e^{\pm j0.023}$	R_1 : 0.3 / 1.3°
	$s_2 = -0.996 \pm j2\pi(1.705)$	s_2 : 0.4 / 0.3	$R_2 = 0.499e^{\pm j0.505}$	R_2 : 0.1 / 1.0°
15dB	$s_1 = -0.517 \pm j2\pi(1.001)$	s_1 : 3.3 / 0.1	$R_1 = 0.505e^{\pm j0.012}$	R_1 : 1.0 / 0.7°
	$s_2 = -0.906 \pm j2\pi(1.704)$	s_2 : 9.4 / 0.3	$R_2 = 0.479e^{\pm j0.523}$	R_2 : 4.2 / 0.0°
5dB	$s_1 = -0.479 \pm j2\pi(0.985)$	s_1 : 4.2 / 1.5	$R_1 = 0.460e^{\pm j0.1}$	R_1 : 7.9 / 5.8°
	$s_2 = -1.109 \pm j2\pi(1.731)$	s_2 : 10.9 / 1.8	$R_2 = 0.471e^{\pm j0.548}$	R_2 : 5.8 / 1.4°
0dB	$s_1 = -0.698 \pm j2\pi(0.999)$	s_1 : 39.6 / 0	$R_1 = 0.629e^{\pm j0.111}$	R_1 : 25.9 / 6.4°
	$s_2 = -0.595 \pm j2\pi(1.653)$	s_2 : 40.5 / 2.8	$R_2 = 0.392e^{\pm j0.877}$	R_2 : 21.6 / 20.3°

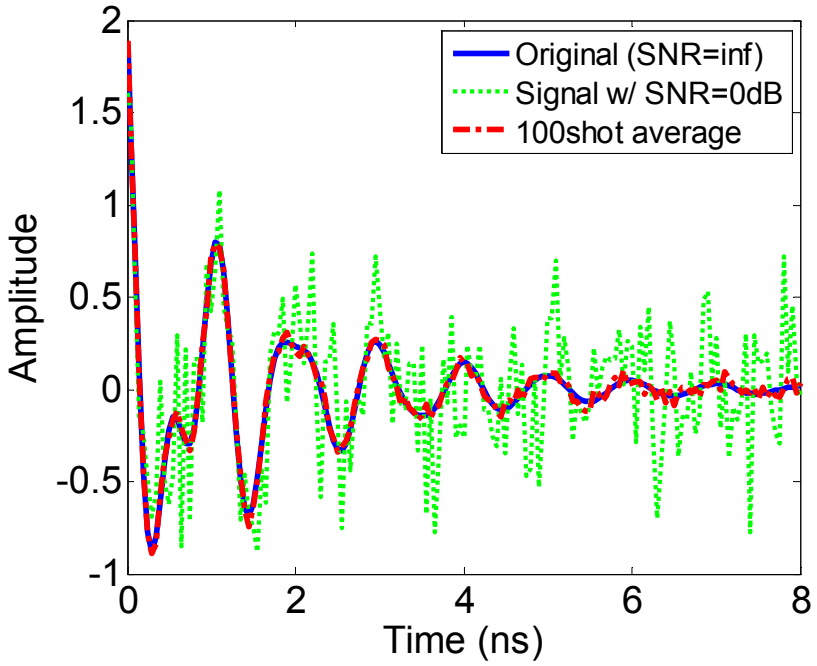

Figure 4.9 100-shot average of signals with SNR=0dB compared with the original signal.

Table 4.2 Estimated poles and residues from 100-shot average of *y(t)* with 0dB SNR.

SNR	Extracted Poles s_n $(\times 10^9)$	Poles % error $(\mathrm{Re}\{s_n\}/\mathrm{Im}\{s_n\})$	Extracted Residues R_n	Residues error $\lvert R_n\rvert$ % *error*$/\Delta\phi_n$ deg
100shot average of SNR 0dB signals	$s_1 = \begin{cases} -0.505 + j2\pi(1.002) \\ -0.505 - j2\pi(1.002) \end{cases}$ $s_2 = \begin{cases} -0.973 + j2\pi(1.697) \\ -0.973 - j2\pi(1.697) \end{cases}$	$s_1 : \begin{cases} 0.9/0.2 \\ 0.9/0.2 \end{cases}$ $s_2 : \begin{cases} 2.7/0.2 \\ 2.7/0.2 \end{cases}$	$R_1 = \begin{cases} 0.504e^{-j0.006} \\ 0.504e^{j0.006} \end{cases}$ $R_2 = \begin{cases} 0.502e^{j0.531} \\ 0.502e^{-j0.531} \end{cases}$	$R_1 : \begin{cases} 0.84/0.3^\circ \\ 0.84/0.3^\circ \end{cases}$ $R_2 : \begin{cases} 0.4/0.4^\circ \\ 0.4/0.4^\circ \end{cases}$

If one can only achieve no more than low SNR values, i.e. 5dB or below, a way to improve the performance of SEM parameter estimation is to overestimate the number of poles, *P,* and then sorting the dominant poles using the residue energy level [25]. Consider for example the signal with SNR of 3dB (Figure 4.10a). As its SVD plot shows (Figure 4.10b), it is difficult to exactly determine the number of dominant poles. A line can be drawn at a point where the

slope seems to "level off", above which are the values to keep in the truncated matrix. In this example there are 8 singular values above threshold, such that $P = 8$. Now the poles are extracted from the truncated matrix and plotted I Figure 4.11. Note that the first pole pair is very close to the actual value while the second pole pair is off from the actual value in terms of decay constant. There are also two extra pairs of poles extracted due to the overestimated P. Assuming that the actual poles are not known, one can look at the energy content of the corresponding residues in order to determine the dominance of the extracted poles in the signal [25]:

$$E_{R_n} = \int_{t=0}^{T} \left| R_n e^{s_n t} + R_n^* e^{s_n^* t} \right|^2 dt \ . \qquad (4.39)$$

Figure 4.12 shows the residue energy content obtained using the above Equation. In the figure the dominant poles in terms of E_{R_n} are the estimates for the actual poles. Hence the other non-significant poles can be discarded to retain only the dominant ones, which are reasonably close to the actual poles. Another option is to go back to the reduced matrix pencil form and re-estimate the poles using the number of final dominant poles, i.e. $P = 4$. The re-estimated poles are shown in Figure 4.13 and compared with the poles extracted using P=8 and the actual poles. It is observed that while the first pole pair is reasonably close to the actual values, the second pair does not seem to have been estimated correctly. This implies that more robust pole estimation take place when the number of poles is overestimated for noisy signals.

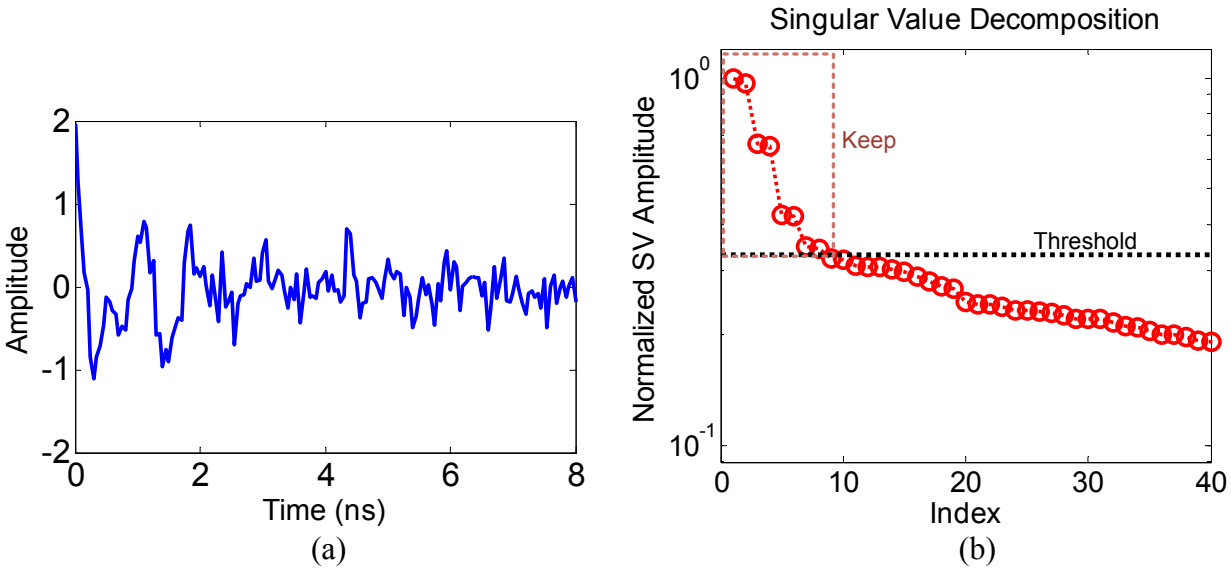

Figure 4.10 (a) Plot of *y(t)* with SNR=3dB and (b) SVD of **X** generated from *y(t)*.

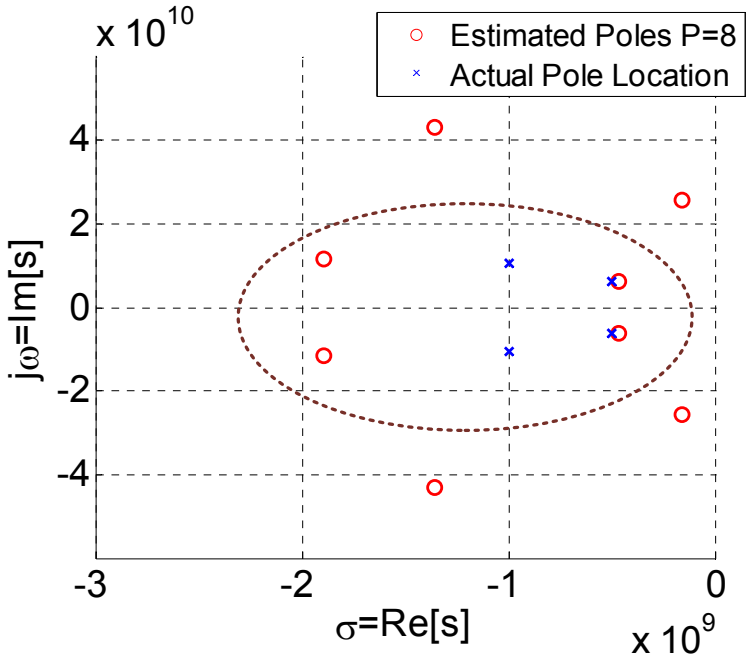

Figure 4.11 Estimated poles from *y(t)* with SNR=3dB using *P*=8 compared with the actual poles.

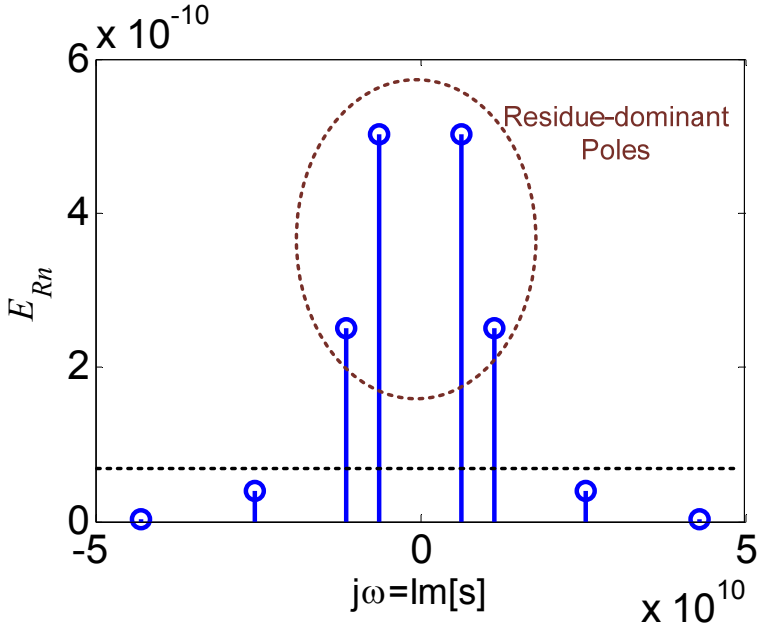

Figure 4.12 Energy content of the residues corresponding to the poles in Figure 4.11.

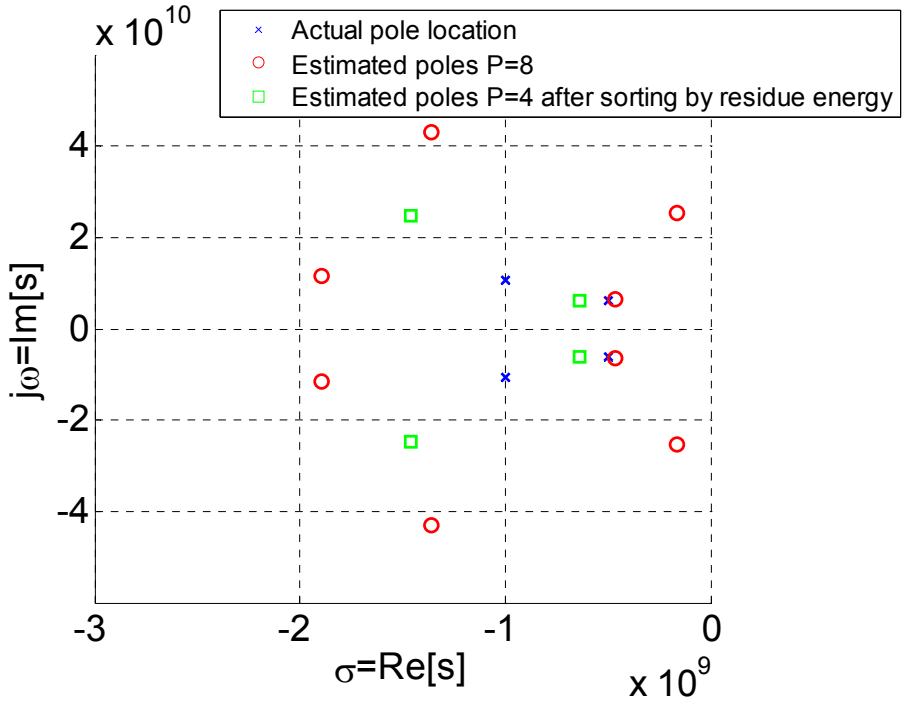

Figure 4.13 Re-estimated poles of *y(t)* with SNR=3dB after obtaining *P*=4 from residue energy comparison. Comparison with the actual poles and the poles obtained with *P*=8 is shown.

The abovementioned approaches are useful for more accurate pole extraction from noise-prone transient responses. As discussed, the key is to ensure a reasonable signal-to-noise ratio such that the poles are estimated with minimal error. Using SVD of the response data enhances the performance as well as the efficiency of MPM. While the residue amplitude approach seems to filter out non-significant false poles when *P* is overestimated for noisy data, it might require some additional processing for more robust estimation. A statistical approach was proposed to mitigate the effects of noise in the estimated poles and demonstrated an improved performance in the extraction of poles from noisy data [25].

An important parameter to consider when estimating poles is the time window of the samples. The window size determines the number of samples (*M*) given the sampling interval (Δ_t). The window size needs to include a sufficient length of signal (at lease a period) at the corresponding pole ($j\omega$ part) in order to correctly estimate it. Many times it would be desirable to have a longer time window, but due to noise in the signal spurious poles can be extracted when the window size is large. Multipath and clutter could also be limiting factors for the sample

window size. Processing techniques such as time-gating can be applied to sort out the desired response from the multipath and cluttered signal, but if the location of the target is unknown, it may require more processing to gain information on the target location. For the breast tumor problem, removal of clutter (reflections from skin and other tissues in the breast) is an essential step in the detection process. Techniques for such process including a new simplified technique are discussed in the next chapter.

Location of the sample window is essential since the poles are estimated based on the assumption that the signal represents only the late-time (i.e. sum of decaying sinusoids). Estimating the start of the late-time can be challenging, especially when there is no *a priori* information about the scattering object. If the sample window is not completely in the late-time, spurious poles will be extracted to represent the non-resonant part of the response (entire-function), some of which could have relatively large residue amplitudes and appear as one of the significant singular values in SVD, which could be problematic. To overcome such problems, a new way of applying the MPM to gain additional information, that is, a temporal progression of pole series representation, is presented in the next section.

4.5 Sliding-window MPM Approach for More Robust Pole Extraction

As mentioned previously, an accurate pole extraction requires that the time window of the sampled data should be in the late-time. In the analytical work carried out in [26], the time after which the pole series is guaranteed to converge, which we refer to as the start of the late-time, t_L, is defined as (considering the case of backscattering, i.e. $\hat{k}^i = -\hat{k}^s$)

$$t_L \geq 2t_A + 2t_{\mathrm{Lmax}} + t_{PW} = 2R/v + 2L_{\max}/v + t_{PW} \qquad (4.40)$$

where R is the distance between the scatterer and the transmit/receive location, $L_{\max}$ is the maximum linear dimension of scatterer, v is the propagation speed, and t_{PW} is the incident pulsewidth. Although there are cases where the pole series can converge before t_L depending on the orientation of scatter, Equation 4.40 provides a general definition of the late-time starting point, which means that in principle a complete pole series representation is valid after the whole body is illuminated by the incident pulse. If the sample window starts before t_L, which indicates

that some of the early-time response is included, spurious poles may be extracted since the MPM will only try to "fit" the data into a sum of damping sinusoids (pole series). Such extraneous poles are the ones that do not contribute to the convergent pole series, but rather represent the non-resonant part (impulsive peaks) in the early-time response. Therefore they could have relatively large residue amplitudes and appear as one of the significant singular values in SVD, which could be problematic. Spurious poles are extracted not only due to misestimation of the late-time, but also due to noise, clutter and many other possible sources of error in the signal even when the sample window is in the late-time.

To overcome this problem, one can take advantage of the fact that these "non-converging" poles are inconsistently extracted when the sample window location is changed, e.g. shifted by a few indices. Therefore, by extracting poles in a sliding-window manner, a temporal progression of estimated poles series representation can be observed, providing more accurate information regarding the late-time and convergent poles that correspond to the natural resonances [27]. With this sliding-window approach the estimated pole series representation can be written as

$$x_{w_i,m} \approx \sum_{n=1}^{P} R_n e^{s_n (w_i+m)\Delta_t} \quad \text{for } m = 0,\cdots,M \text{ and } w_i = w_0, w_1, \cdots, w_f \tag{4.41}$$

where w_0 and w_f are the initial and final time window locations, respectively. This temporal presentation of estimated pole series is in a sense analogous to time-frequency representation of the response, which in general can be written as

$$X_{m,\omega} = \sum_n x_n h[n-m] e^{j\omega n} \tag{4.42}$$

where $h[n]$ represents a window function or other specified functions depending on the type of TF transform used [28]. A work carried out separately by Manteghi uses a similar approach for improved estimation of the poles for chipless RFID applications [29].

To demonstrate this approach, numerically simulated backscattered response of a thin conducting wire in free space is considered as an example [27]. An FDTD model of a 15cm long thin wire is simulated with a plane wave excitation (130ps Gaussian[1] pulse) via SEMCAD X®. The wire is parallel to the incident polarization as shown in Figure 4.14. The backscattered

[1] It is practically impossible to radiate a Gaussian pulse due to its DC component. Nevertheless, it is used in the simulation to yield a response that is close to an impulse response of the object.

response at a distance of 2.1 meters from the wire is plotted in Figure 4.15. Also indicated in Figure 4.15 are the locations of the initial and final time windows, i.e. $t_0 = w_0\Delta_t = 14.4\,\text{ns}$ and $t_f = w_f\Delta_t = 17.8\,\text{ns}$. The width of the time window, $M\Delta_t$, is chosen to be 5ns to include at least a few cycles of the fundamental resonance. At an increment of 0.1 ns, a total of 34 different sets of pole series are estimated between the initial and final time windows. The maximum number of estimated poles, *P*, is purposely overestimated to represent the general case where the response may be noisy, and the residue energy threshold of 1% of the maximum residue energy value is used. Figure 4.16a shows a temporal progression of the estimated poles ($\text{Im}\{s_n\}/2\pi$) as a function of $t_i = w_i\Delta_t$, which is the starting point of each time window, plotted on the top of the original response. In Figure 4.16b, all of the estimated poles are plotted in the Laplace domain. The poles seem to converge to a stable set of locations after t_L, which is calculated to be 15.6ns in this case, showing a good agreement with the analytically determined definition of the late-time starting point. Moreover, the locations of "non-converging" poles estimated when time window starts in the early-time are inconsistent as expected. It is quite clear now which poles are the ones that represent the natural resonances of the wire.

Another interesting observation is made in Figure 4.17, which shows a temporal progression of the poles in terms of their corresponding residue magnitude in log scale. In this plot, the inconsistency in the residue magnitudes of the non-converging poles is observed while the residue magnitudes of the converging poles stay constant. This is also expected since the residues of inconsistent poles are the result of rather "curve fitting", as opposed to providing parameters associated to the actual resonance.

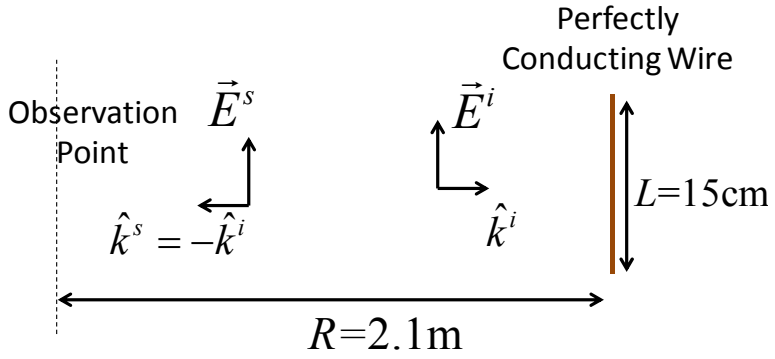

Figure 4.14 Thin-wire simulation setup

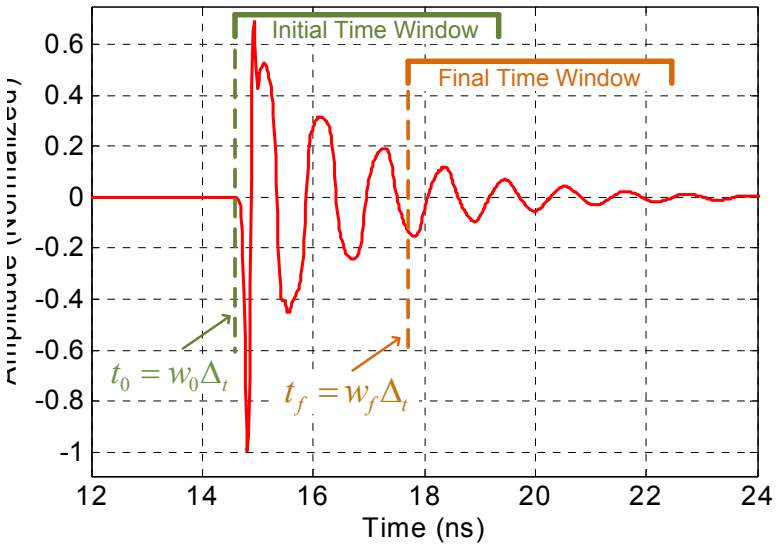

Figure 4.15 Simulated transient backscattered response. The initial and final time window location is shown.

This approach seems to be an effective way to improve pole estimation accuracy without requiring an *a priori* or initial guess for the early/late-time boundary for an unknown scatterer. This new way of presenting the SEM parameters in the data, hereafter referred to as the Sliding-window MPM approach, will be used throughout the remainder of this dissertation for extracting poles from the responses of breast tumor models.

4.5.1 Observation Regarding Early-time

Another interesting observation is an approximate representation of entire function (early-time response) by non-converging poles [27]. Although this representation is not directly used in the breast tumor problem considered in this work, it is still worthwhile discussing since there could be a potential use in other types of target characterization and identification applications.

Consider a set of poles extracted when the time window starts in the early-time, say at $t_i = 14.7$ ns, as shown in Figure 4.18. From the temporal pole plot in Figure 4.16a, it is possible to distinguish between the converging poles from non-converging poles based on the consistency of their occurrences. Now the pole series representation can be separated into two different sums, namely *np* series and *p* series, respectively corresponding to the non-converging and converging poles as follows:

$$x(t;t_i) \approx \sum_{np} R_{np} e^{s_{np}(t-t_i)} u(t-t_i) + \sum_{p} R_p e^{s_p(t-t_i)} u(t-t_i). \qquad (4.43)$$

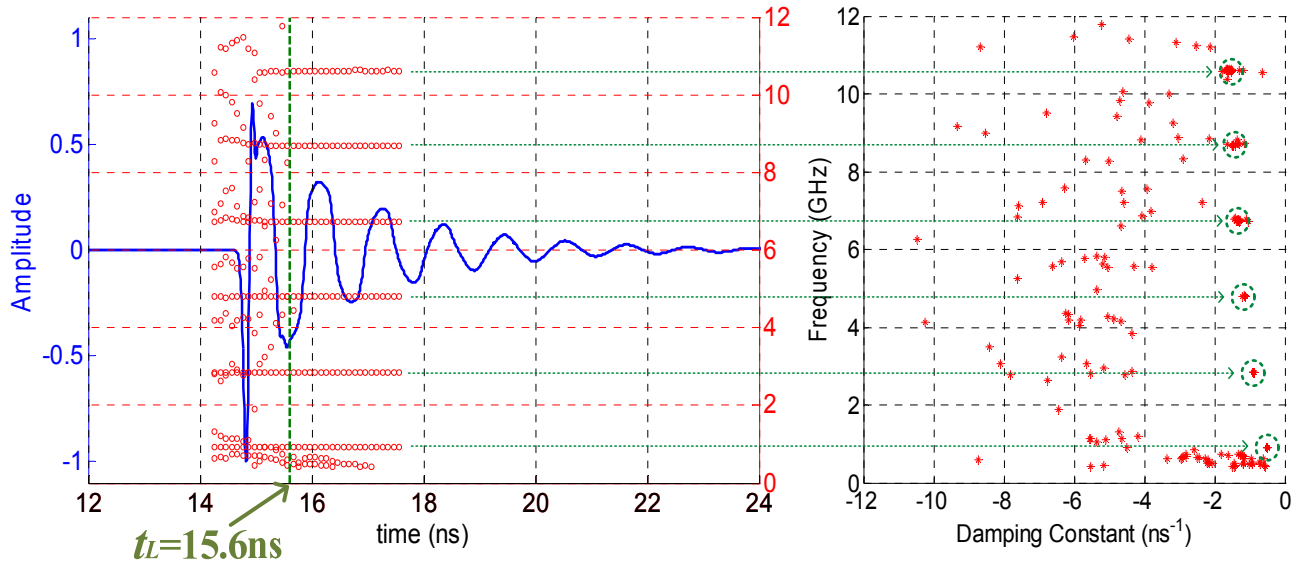

Figure 4.16 Estimated poles via sliding-window MPM [27]: a) Temporal progression of the estimated poles ($\mathrm{Im}\{s_n\}/2\pi$) plotted with the response. b) S-plane plot of the estimated poles .

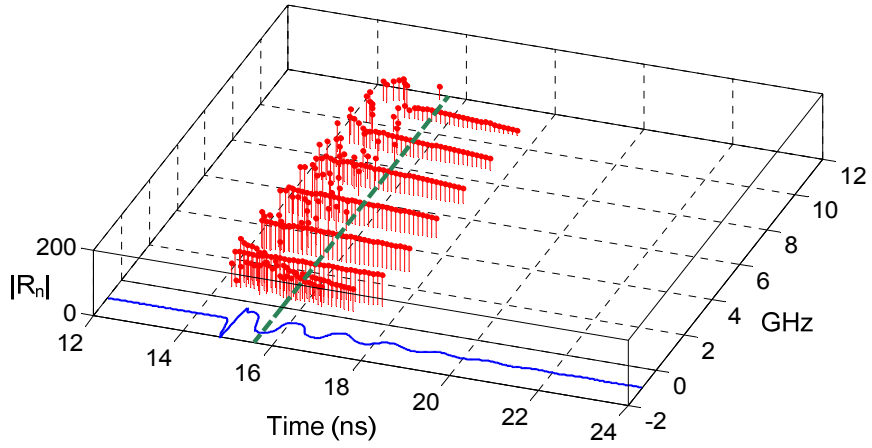

Figure 4.17 Estimated poles and the corresponding residue amplitude (log scale) as a function of time [27].

Using this equation, the response is reconstructed into two different signals as shown in Figure 4.19. The reconstructed signal from *p* series corresponds to the slowly-varying part in the early-time and continues into the late-time, closely matching the original response. The signal reconstructed from *np* series is more impulsive than that reconstructed from *p* series and quickly vanishes after t_L, which indicates that *np* series contributes to the early-time forced response.

In the Laplace domain Equation 4.43 is expressed as

$$\tilde{\mathrm{E}}_{\mathrm{r}}^{\mathrm{bs}}(s)=\sum_{np}\frac{R_{np}}{s-s_{np}}e^{-(s-s_{np})t_i}+\sum_{p}\frac{R_{p}}{s-s_{p}}e^{-(s-s_{p})t_i} \tag{4.44}$$

According to the SEM framework, the early-time representation should be an entire function, which means that the first term in Equation 4.44 is not a valid representation. However, we can relate the term to the generalized representation of an entire function in the left-half plane using the Cauchy integral [30], which is

$$\tilde{x}_{entire}(s)=\frac{1}{2\pi j}\int_{c_\infty}\frac{R(s')}{s-s'}ds' \text{ , where } c_\infty=\lim_{\Delta\to\infty} c \text{ (left-plane contour).} \tag{4.45}$$

This Cauchy integral representation can be considered as consisting of poles with continuous residue distribution $R(s')$ at $s\to\infty$, suggesting that an entire function can be regarded as a function with the singularities at infinity [30]. Therefore, from this perspective the poles (singularities) in the first term of equation 4.45 can be approximately represents an "entire function" to describe the early-time forced response, as a reduced parameter form, which could potentially be used as another form of characteristic features of scatterer.

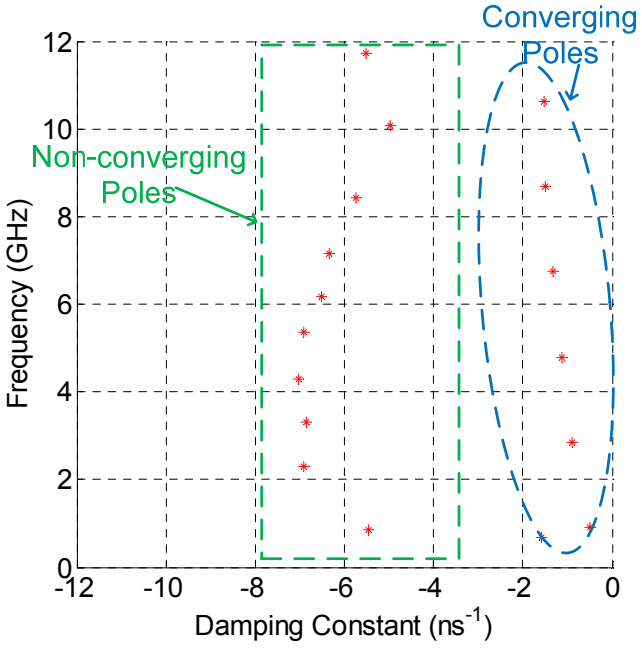

Figure 4.18 Estimated poles when $t_i=14.7$ ns [27].

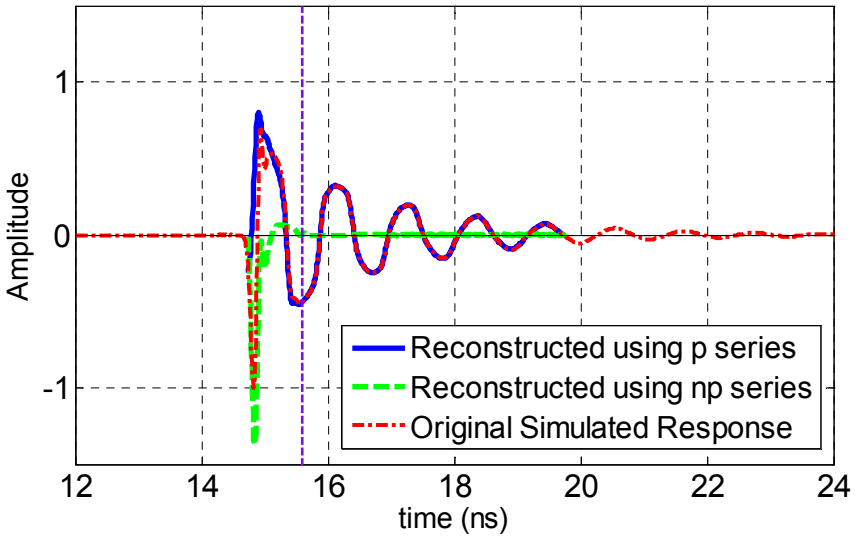

Figure 4.19 Reconstructed responses from two separate pole series [27]: converging poles (solid blue) and non-converging poles (dashed green). Original response is shown in dotted red.

4.6 Determining the Electrical Location of the Scatterer from Complex Residues

As indicated in Equation 4.8 the residues in the SEM representation of transient scattering is a function of $\bar{r}$, the observation point. In a multistatic array setup, it means that the complex residues estimated from received signals would vary with the receiver location. Relating back to the integral equation form of scattering in Equation 4.3, the retarded time R/v and the spherical spread in the Green's function are the factors, along with the coupling coefficients (Equation 4.6), that determine the values of complex residues in received signals. Here we are primarily interested in obtaining the scatterer location relative to the receiver, which is determined by the retarded time R/v that translates to relative phase angle in the frequency domain.

Considering a measurement setup involving multi-element array as shown in Figure 4.20, a multistatic data of received scatterer response is

$$\mathbf{X}_i(t) = \begin{bmatrix} x_{i1}(t) \\ x_{i2}(t) \\ \vdots \\ x_{iK}(t) \end{bmatrix} \qquad i = 1, 2, ..., K \tag{4.46}$$

where i is the transmit element number, K is the total number of elements in the array. $\mathbf{X}_i(t)$ consists of the scatterer responses received by all elements when i^{th} element is transmitting. Note

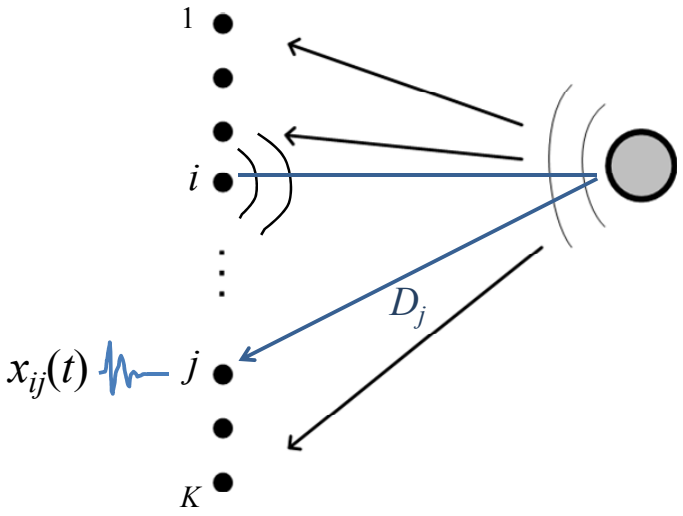

Figure 4.20 General setup of multi-element scattering measurement

that cross-coupling between the elements are assumed to be removed. The response received by each antenna element, $x_{ij}(t)$, is related to the scattered field in Equation 4.3 as

$$x_{ij}(t) \sim \bar{E}_i^s(\bar{r}_j, t) = \int_v \bar{J}_i(\bar{r}', t) \otimes \bar{G}(\bar{r}_j, \bar{r}', t - D_j/v)\, dv', \tag{4.47}$$

where $\bar{J}_i(\bar{r}', t)$ represents the current induced by an incident field transmitted from i^{th} element and D_j is the distance between the scatterer and j^{th} receiving element. The SEM representation of $x_{ij}(t)$ can be written as

$$x_{ij}(t) = \sum_{n=1}^{N} R_{ij,n} e^{s_n t} u\left(t - t_{L_j}\right) + x_{ij}^e(t). \tag{4.48}$$

where $t_{L_j} = 2R_j/v + 2L_{\max}/v + t_{PW}$, the late-time start point or convergence time, depends on the receiving element location. The early-time component in the second term is also delayed by D_j/v. The late-time term can be decomposed into following:

$$x_{LT\_ij}(t) = \sum_n \left|R_{ij,n}\right| e^{j(\phi_n + \phi_j)} e^{s_n t} = \sum_n \left|R_{ij,n}\right| e^{j\phi_n} e^{\sigma_n t} e^{j\omega_n\left(t - \frac{D_j}{v}\right)}, \tag{4.49}$$

where the phase term in complex residue is separated into two terms, namely ϕ_n and ϕ_j, which respectively represent the phase determined by coupling at the scatterer and the phase

determined by the time-delay D_j/v. Since ϕ_n is not a function of receiver location, the relative phase differences in residues of n^{th} pole obtained at different receiver locations should correspond to the relative distances of array elements with respect to the scatter. We refer to this relative phase shift or time-delay as the "electrical location" of the target. This suggests that a multistatic SEM analysis of scattering response could provide the necessary information to perform adaptive resonance-based focusing (i.e. to identify the resonance, location of target, and then to focus the energy) more efficiently.

To demonstrate this approach, simulated multistatic scattered responses from a thin wire embedded in a simple lossy dielectric medium is considered. In the numerical model, the length of wire is 1.6cm and the dielectric property of the medium is set up to have $\varepsilon_{r1} = 40$ and $\sigma_{c1} = 0.3$ S/m. A lossy dielectric medium was chosen to loosely resemble a breast tumor problem. A 20-element circular array was placed on a plane intersecting the center point of wire (z=0) around a perimeter with 8.4cm radius. The setup is shown in Figure 4.21. The wire is parallel to z-axis and placed at (x=2cm, y=1cm) from the center (0, 0). An infinitesimal dipole source is used as array element to minimize the effect of antenna. Using a 75ps Gaussian pulse as excitation transmitted from element 1, multistatic responses, i.e. $\mathbf{X}_1(t)$, are simulated with FDTD via SEMCAD X®. After time-gating the antenna cross-coupling, the scattered responses from the wire were obtained. In Figure 4.22a, $\mathbf{X}_1(t)$ containing all 20 responses collected by the antenna array is shown, while Figure 4.22b shows $x_{1,2}(t)$ and $x_{1,18}(t)$ for a better look at the transient response. As expected the specular peaks occur at different times since the relative distances between the elements and scatterer are different. The relative delay between the specular peaks should correspond to the relative distances (D_j) of elements from the scatter. The peak amplitudes also vary, which in this case should strictly depend on the distance, since both the scatterer and antennas have azimuth independent pattern.

The SEM parameters are estimated from each response using the Sliding-window MPM. Based on SVD of sampled data, *P*=6 was used and only dominant poles are obtained after residue energy filtering. Figure 4.23 shows the extracted poles from $\mathbf{X}_1(t)$. In the plot, clustering of poles at two distinct locations that correspond to the fundamental and second order modes can be observed. A mean taken at the cluster of fundamental poles seem to be in a good

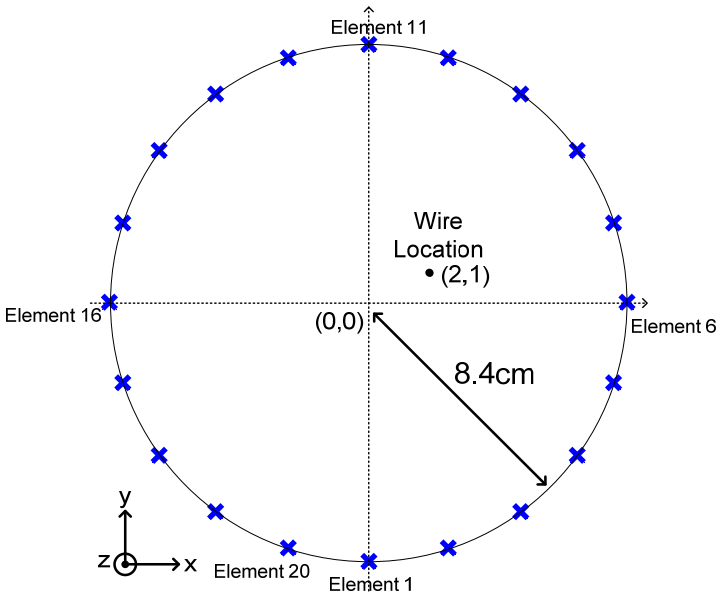

Figure 4.21 Simulation setup (top view) of multistatic scattered response of a thin wire (1.6cm) in a simple lossy dielectric medium using 20-element circular array. An infinitesimal dipole-like source was used as an element.

agreement with the scaled analytically determined pole using [12, 13] Equation 4.10 indicated by the red circle.

Now we want to look at the phase angle of the complex residues ($R_{1j,1}$) of the fundamental pole (s_1). Figure 4.24 shows the unwrapped relative phase angles with respect to the minimum phase angle that occurs at element 7. This is in good agreement with the physical distance, where the scatting path between element 1 (Tx) and element 7 (Rx) is the shortest, which should provide minimum unwrapped phase angle due to the term, $\phi_j = \omega_n \left(D_j / v \right)$, in Equation 4.49. By simply dividing by $\omega_n = \mathrm{Im}\{s_n\}$, the phase angles can be translated into relative time delays, which should match with those of specular peaks. Figure 4.25 shows the relative time delays obtained from residue phase angles in comparison with the relative delay between specular peaks, which indeed show a good agreement. This suggests that a multistatic SEM analysis could be an efficient way to obtain necessary information to perform adaptive resonance-based focusing for breast tumor applications. In the following chapters we demonstrate the use of this approach for breast tumor problem.

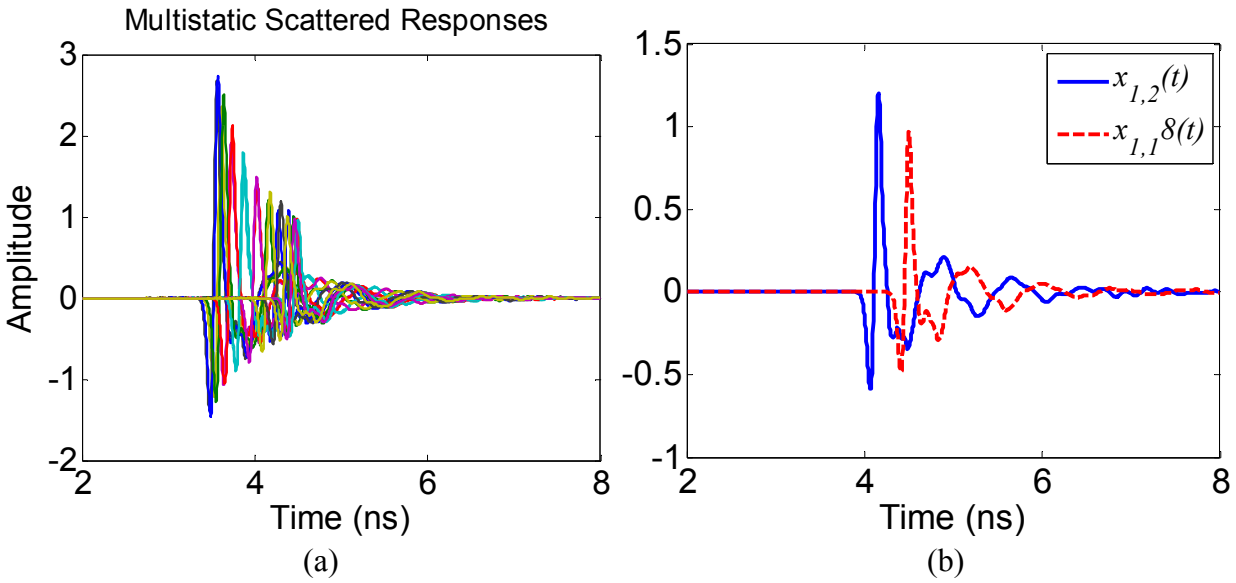

Figure 4.22 Simulated scattered responses of a thin wire (1.6cm) in a simple lossy dielectric medium ($\varepsilon_{r1} = 40$ and $\sigma_{c1} = 0.3$ S/m): a) Responses received by all 20 elements, $\mathbf{X}_1(t)$ and b) $x_{1,2}(t)$ and $x_{1,18}(t)$

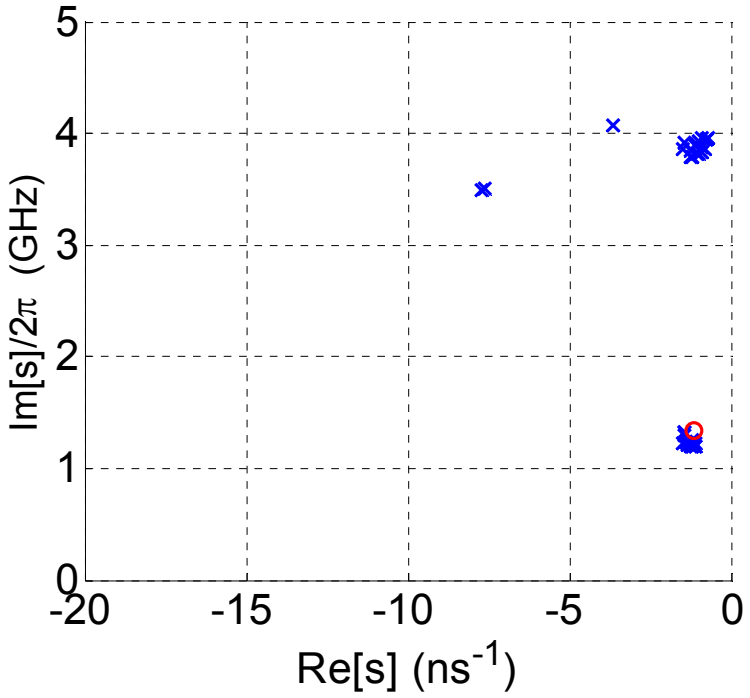

Figure 4.23 Extracted poles (blue) from 20 multistatic responses $\mathbf{X}_1(t)$. The fundamental pole is in good agreement with the scaled pole (red) analytically obtained.

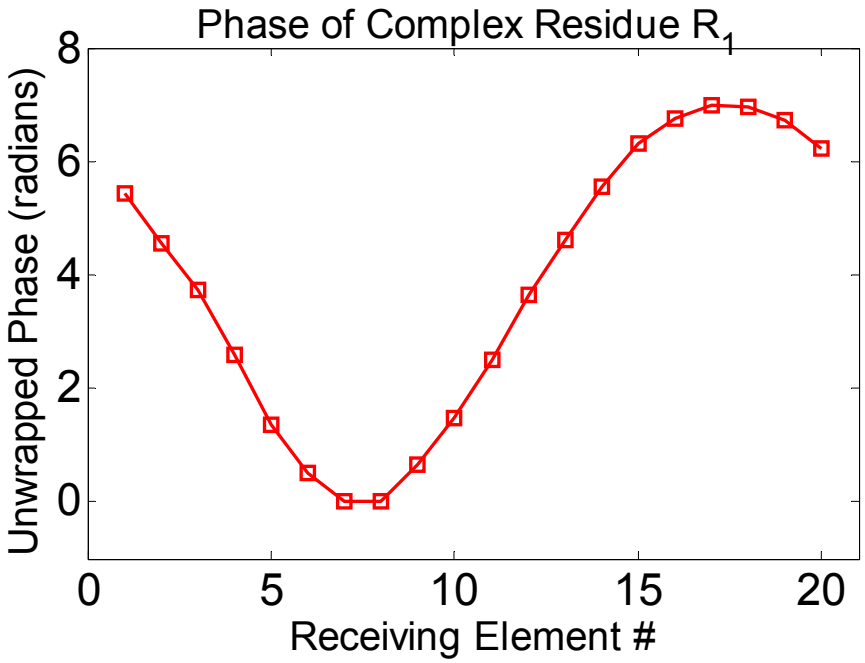

Figure 4.24 Unwrapped relative phase angles obtained from complex residues of the fundamental pole.

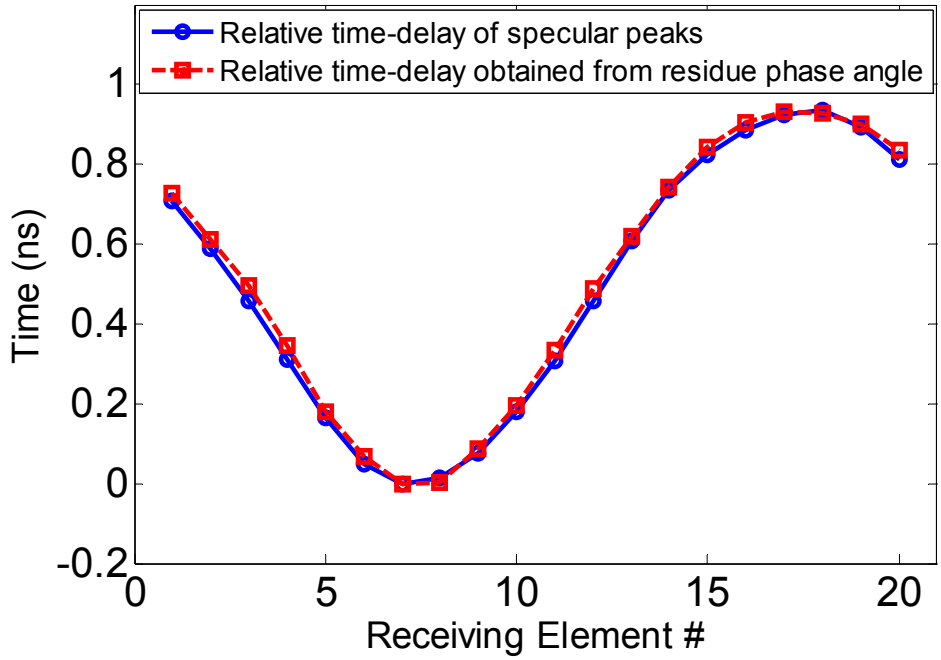

Figure 4.25 Relative time delays obtained from residue phase angles for s_1 in comparison with the relative delay between specular peaks.

4.6.1 Relevance to the Time-Reversal Technique

Using the parameters obtained above, microwave focusing is achieved by feeding the signal (with frequency corresponding to ω_n) into array elements with conjugated phase (or reversed time delay). An analogy can be made between this process and time reversal (TR) operation, which in essence shares a similar principle.

The basic principle of the time-reversal technique is in the time-reversal invariance in the wave equation [31]. For example, the wave equation in a lossless homogeneous medium,

$$\frac{1}{v^2}\frac{\partial^2 \overline{E}(\vec{r},t)}{\partial t^2} + \nabla^2 \overline{E}(\vec{r},t) = F(t)\delta(\overline{r} - \overline{r}_o), \tag{4.50}$$

gives both $\overline{E}(\vec{r},t)$ and $\overline{E}(\vec{r},-t)$ are the solutions since $\partial^2 E(\vec{r},t)/\partial t^2 = \partial^2 E(\vec{r},-t)/\partial t^2$. Consider an ideal scenario where a continuous array completely encloses a volume over a surface *S*, in which a point source (or scatterer) is located as illustrated in Figure 4.26. A signal emitted from the source seen by each point element in the array can be expressed as (far-field scattering assumed)

$$\begin{aligned} \overline{E}(\overline{r}_i,t) &= G(\overline{r}_i,\overline{r}_o,t-D_i/v)\otimes \overline{F}(t) \\ &= G(\overline{r}_i,\overline{r}_o,t)\otimes \overline{F}(t-D_i/v) \end{aligned} \quad i = 1, \cdots, \infty \tag{4.51}$$

where $G(\overline{r}_i,\overline{r}_o,t)$ is the Green's function, $\overline{F}(t)$ is the source waveform (assume short pulse), $D_i = |\overline{r}_i - \overline{r}_o|$ is the distance between an element in the array and the source (scatterer). An integral equation form is not needed here since a point source is used for the simplicity of derivation. By reversing the time variable in $\overline{E}(\overline{r},t)$, we have $\overline{E}(\overline{r},-t)$, which represents the field propagating backwards in time converging back to the source point. Using Fourier Transform properties, we can observe that a time-reversed function is equivalent to phase conjugation, i.e.

$$\overline{E}(\overline{r},-t) \xrightarrow{F} \overline{E}^*(\overline{r},\omega) \tag{4.52}$$

where the superscript * denotes phase conjugation.

With this basic principle, if the wave recorded through the infinite array for duration *T* (long enough to record the signal at all points on the surface) is time reversed and re-transmitted into the enclosed volume, the field can be effectively expresses as,

$$\overline{E}_{TR}(\overline{r},t) = G(\overline{r}_i,\overline{r}_o,-t)\otimes \overline{F}(T-t) \tag{4.53}$$

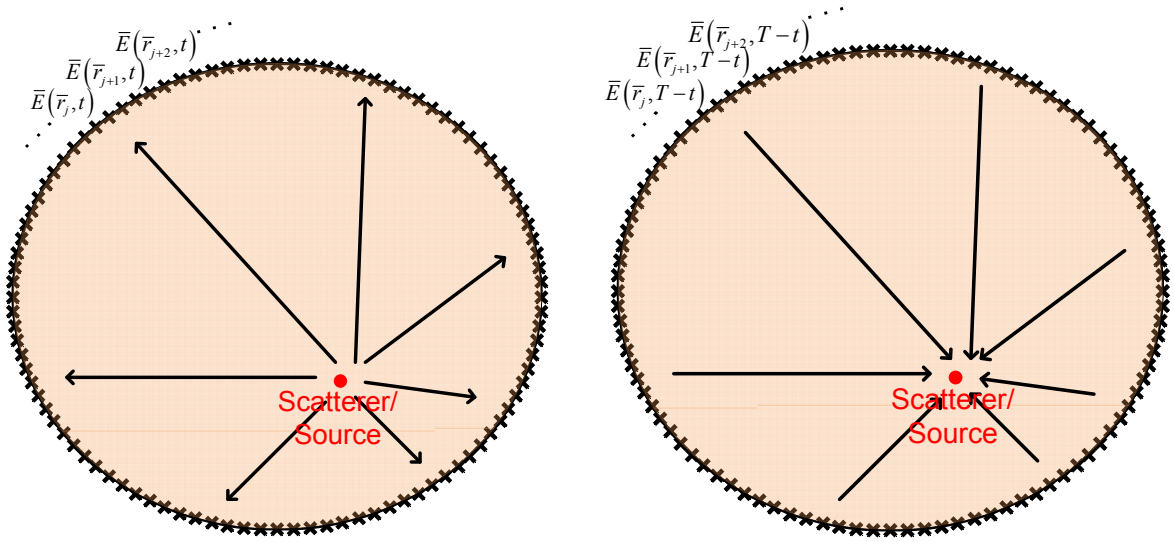

(a) (b)

Figure 4.26 Illustration of the basic principle of time-reversal based focusing.

which will coherently add at $t = T$ to create a focus back at the original source location $\bar{r}_o$.

The expression in Equation 4.53, however, should be valid only up to $t = T$ since the wave starts to propagate forward (diverge) once a focus takes place at the source. Hence, to accommodate this, one needs to include a time-forward Green's function term [31, 32], such that

$$\bar{E}_{TR}(\bar{r},t) = \left[G(\bar{r}_i,\bar{r}_o,-t) - G(\bar{r}_i,\bar{r}_o,t)\right] \otimes \bar{F}(T-t). \tag{4.54}$$

Considering an impulse excitation, i.e. $F(t) = \delta(t)$, the above expression reduces to

$$E_{TR}(\bar{r},t) = \frac{1}{4\pi D}\left[\delta(t + D/v) - \delta(t - D/v)\right], \tag{4.55}$$

which is clear that there are two points of nonzero E field in space at a particular time instance due to converging and diverging waves. Through Fourier Transform a frequency domain representation of the above expression can be obtained as

$$E_{TR}(\bar{r},\omega) = \frac{e^{j\omega(D/v)} - e^{-j\omega(D/v)}}{4\pi D} = \frac{1}{j\lambda}\frac{\sin(2\pi D/\lambda)}{2\pi D/\lambda}, \tag{4.56}$$

which becomes a spatial sinc function with the width of the main peak basically representing the spatial focusing resolution of the time-reversed waves at a particular frequency. This resolution

limit is closely related to classical diffraction limit. Note that this is an ideal case where all of the emitted (or scattered) energy is collected over a closed surface and used for TR operation. The degradation in the focusing quality will occur as information is collected over a finite number of points in space over as finite amount of time. Moreover, complexity (e.g. heterogeneity, lossiness) of propagating medium and scatterer also affects the time-reversal operation. However, discussion presented here should provide a qualitative representation of TR without loss of generality.

It should be quite evident now that the focusing approach discussed in the previous subsection using conjugated phase from residues or reversed equivalent time-delay is closely related to time reversal operaton. By conjugating the relative phase (or reversing the equivalent relative time-delays) between the array elements, one is effectively performing a time reversal operation in a limited sense since we want to use a different signal retransmitted into the medium than the original transient response. However, since the medium characteristics remains the same (i.e. same Green's function), using the conjugated phase on a different signal (resonant frequency) would simply mean that $\overline{F}(T-t)$ in Equation 4.54 is replaced with a different signal, e.g. a sinusoid. Hence the time reversal operation still applies and the focusing field resolution limit can be determined using Equation 4.56.

4.7 Chapter Summary

Following a brief introduction of resonant scattering, the singularity expansion method with Prony's and the matrix-pencil method, this chapter presented a different way of applying matrix-pencil method for improved pole estimation performance for an unknown target. The sliding-window MPM provides a temporal progression of the estimated poles, allowing one to determine the actual poles without requiring *a priori* knowledge or an initial guess about the late-time. Spurious poles extracted in the early-time were also investigated for a potential use in other types of target characterization and identification applications.

The use of residue phase angles as electrical location of scatterer was also introduced in this chapter. Through a simple example it was shown that relative phase between the complex residues of a pole obtained from receiving element locations accurately represents the retarded-time delay in the transient response, which directly corresponds to the relative location

of scatter with respect to array. This suggests that the SEM analysis of multistatic scattering data can efficiently provide necessary information (electrical location and resonance) to perform an adaptive focusing proposed in this dissertation. Relevance of conjugated residue phase approach to time reversal operation was discussed.

In the next chapter, the techniques presented in this chapter are applied for breast tumor problem through two-dimensional numerical breast models of various configurations. Techniques to reduce clutter, which is an essential step before applying the SEM analysis, are also discussed.

4.8 References

[1] C. E. Baum, "On the Singularity Expansion Method for the Solution of Electromagnetic Interaction Problems," *AFWL Interaction Notes*, 88, Dec. 1971.

[2] M. V. VanBlaricum and R. MIttra, "A Technique for Extracting the Poles and Residues of a System Directly from Its Transient Response," *IEEE Transactions on Antennas and Propagation,* vol. 23, no. 6, pp. 777-781, Nov. 1975.

[3] T. K. Sarkar and O. Pereira, "Using the Matrix Pencil Method to Estimate the Parameters of a Sum of Complex Exponentials," *IEEE Antennas & Propagation Magazine,* vol. 37, no. 1, pp. 48-55, Feb. 1995.

[4] C. A. Balanis, *Advanced Engineering Electromagnetics*: John Wiley & Sons, 1989.

[5] M. V. VanBlaricum, "Radar Cross Section and Target Scattering," in *Introduction to Ultra-Wideband Radar Systems*, J. D. Taylor, Ed., CRC Press, 1995.

[6] J. B. Keller, "Geometrical Theory of Diffraction," *Journal of Optical Society of America* vol. 52, no. 2, pp. 116-130, Feb. 1962.

[7] R. G. Kouyoumjian and P. H. Pathak, "A uniform geometrical theory of diffraction for an edge in a perfectly conducting surface," *Proceedings of IEEE,* vol. 62, no. 11, pp. 1448-1461, Nov. 1974.

[8] R. F. Harrington, *Field Computation by Moment Methods*. New York, NY: Wiley-IEEE Press, 1993.

[9] J. L. Volakis, A. Chatterjee, and L. C. Kempel, *Finite Element Method for Electromagnetics*. New York, NY: Wiley-IEEE Press, 1998.

[10] K. S. Yee, "Numerical solution of initial boundary value problems involving Maxwell's equations in isotropic media," *IEEE Transactions on Antennas and Propagation,* vol. 14, no. 3, pp. 302-307, May 1966.

[11] A. Taflove and S. Hagness, Eds., *Computational Electrodynamics: The Finite Difference Time Domain Method*. Artech House, 2005.

[12] C. E. Baum, "The Singularity Expansion Method," in *Transient Elecromagnetic Fields*, L. B. Felsen, Ed., Springer-Verlag, 1976.

[13] J. T. Cordaro and W. A. Davis, "Time-Domain Techniques in the Singularity Expansion Method," *IEEE Transactions on Antennas and Propagation,* vol. 29, no. 3, pp. 534-538, May 1981.

[14] K. Chen and D. Westmoreland, "Impulse Response of a Conducting Sphere Based on Singularity Expansion Method," *Proceedings of IEEE,* vol. 69, no. 6, pp. 747-750, Jun. 1981.

[15] C. E. Baum, Ed., *Detection and Identification of Visually Obscured Targets*. Taylor & Francis, 1997.

[16] R. Prony, "Essai experimental et analytique sur les lois de la dilatabilite de fluids elastiques et sur celles de la force expansion de la vapour e I'alkool, a differents temperatures," *Journale L'Ecole Polytech,* vol. 1, pp. 24-76, 1795.

[17] R. Kumaresan and D. W. Tufts, "Estimating the Parameters of Exponentially Damped Sinusoids and Pole-Zero Modeling in Noise," *IEEE Transactions on Acoustics, Speech, and Signal Processing,* vol. 30, no. 6, pp. 833-840, Dec. 1982.

[18] D. W. Tufts and R. Kumaresan, "Estimation of Frequencies of Multiple Sinusoids: Making Linear Prediction Perform Like Maximum Likelihood," *Proceedings of IEEE,* vol. 70, no. 9, pp. 975-989, Sep. 1982.

[19] M. A. Rahman and K. B. Yu, "Total Least Squares Approach for Frequency Estimation Using Linear Prediction," *IEEE Transactions on Acoustics, Speech, and Signal Processing,* vol. 35, no. 10, pp. 1440-1454, Oct. 1987.

[20] E. M. Dowling, R. D. DeGroat, and D. A. Linebarger, "Exponential parameter estimation in the presence of known components and noise," *IEEE Transactions on Antennas and Propagation,* vol. 42, no. 5, pp. 590-599, May 1994.

[21] Y. Hua and T. K. Sarkar, "Generalized pencil-of-function method for extracting poles of an EM system from its transient response," *IEEE Transactions on Antennas and Propagation,* vol. 37, no. 2, pp. 229-234, Feb. 1989.

[22] Y. Hua and T. K. Sarkar, "On SVD for estimating generalized eigenvalues of singular matrix pencil in noise," *IEEE Transactions on Signal Processing,* vol. 39, no. 4, pp. 892-900, Apr. 1991.

[23] S. Licul, "Ultra-Wideband Antenna Characterization and Measurements," Ph.D. Dissertation, Electrical Engineering, Virginia Polytechnic Institute and State University, Blacksburg, VA, 2004.

[24] W. A. Davis, "Prony, Matrix Pencil & Antennas," Electomagnetics Seminar, Virginia Tech, Blacksburg, VA2008.

[25] G. Joshi, "Ultra-wideband Channel Modeling using Singularity Expansion Method," Ph.D. Dissertation, Virginia Tech, Blacksburg, VA, 2006.

[26] C. E. Baum, "Representation of Surface Current Density and Far Scattering in EEM and SEM with Entire Functions," *Interaction Notes*, 486, Feb. 1992.

[27] S. K. Hong, W. S. Wall, T. D. Andreadis, and W. A. Davis, "Practical Implications of Pole Series Convergence and the Early-time in Transient Backscatter," *NRL Memorandum Report*, NRL/MR/5740--12-9411, Apr. 2012.

[28] S. Qian and D. Chen, *Joint Time-Frequency Analysis: Methods and Applications*. Upper Saddle River, NJ: Prentice Hall, 1996.

[29] M. Manteghi, "A space-time-frequency target identification technique for chipless RFID applications," in *the Proceedings of IEEE International Symposium on Antennas and Propagation (APSURSI)*, Spokane, WA, 2011, pp. 3350-3351.

[30] C. E. Baum, "Towards an Engineering Theory of Electromagnetic Scattering: The Singularity Expansion and Eigenmode Expansion Methods," in *Electromagnetic Scattering*, Academic Press, 1978.

[31] M. Fink, D. Cassereau, A. Derode, C. Prada, P. Roux, M. Tanter, J. Thomas, and F. Wu, "Time-reversed Acoustics," *Reports on Progress in Physics,* vol. 63, pp. 1933-1995, 2000.

[32] H. D. Trefna, J. Vrba, and M. Persson, "Time-reversal focusing in microwave hyperthermia for deep-seated tumors," *Physics in Medicine and Biology,* vol. 55, pp. 2167-2185, 2010.

This page intentionally left blank.

Chapter 5 Identifying Tumor Response, Electrical Location and Resonances

An important step before identifying the tumor resonance and electrical location is to accurately detect and extract the tumor response from the multistatic data. While there are many approaches proposed [1-4] based on generating a focused image to locate the physical position of a tumor, here we would like to focus on acquiring the information sufficient to extract the tumor resonance and electrical location. To this end, a relatively simple technique using the GPR-inspired position-time plot to detect the tumor response is presented. Change detection and the use of contrast enhancing agents are also discussed as schemes to improve detection for heavily cluttered breasts. Two-dimensional FDTD simulation of numerical breast models with various tissue and tumor configurations are used to demonstrate the technique. As it was mentioned earlier, this approach could potentially be used as a combination technique with other imaging modalities or as a computationally efficient processing algorithm for a possible stand-alone system discussed in Chapter 3.

Techniques presented in the previous chapter, i.e. the sliding-window MPM for resonance extraction and the use of residue phase angles as the tumor electrical location, are then applied to the simulated responses from the aforementioned numerical models, as well as the measured responses from a simplified experiment with 2D-like apparatus.

5.1 Numerical Breast Models used for Simulation

To demonstrate the utility of the overall approach, two-dimensional (2D) numerical breast models with different tissue configurations are constructed and simulated with SEMCAD X®, a FDTD based numerical solver [5]. 2D models provide a qualitative insight into how the proposed approach would work without loss of generality while reducing the computation time significantly. Moreover, 2D models provide flexibility in terms of varying the configuration or parameters in the model. Hence it is suitable to utilize 2D models for the study performed in this dissertation, which is in a concept demonstration stage. The proposed approach should in general be applicable to 3D cases, possibly with some additional processing.

5.1.1 Finite Difference Time-Domain (FDTD) Method

Here we briefly discuss the FDTD method, a numerical computation technique for solving electromagnetic problem employed by SEMCAD X®, which is used in this study to simulate breast models. An FDTD solver was chosen because of its direct-solve process in time domain and differential equation-based operation which solves for the field solutions at all points in the computation domain. FDTD is also known to work well in solving inhomogeneous and dispersive media. For this reason, FDTD is well suited for simulating breast models, which involve short pulse excitation and inhomogeneous media.

The FDTD method is a differential equation and time-domain technique, which provides solutions in discrete space and time. It uses the concept of finite differencing, where the partial differential operator is approximated with finite difference equations. Finite differencing scheme is also used by other numerical techniques, i.e. Finite Element Methods [6] and Method of Moments [7]. However, unlike such methods that involve matrix formulation from the integral or differential form of the solutions to the wave equation, FDTD directly applies the finite differencing to the time-domain form of the Maxwell's curl equations. Originally proposed by Yee for solving electromagnetic problems in 1966, FDTD divides the computation domain into Cartesian grid cells [8]. The field values in the Maxwell's equations are then decomposed into rectangular components, resulting in six scalar equations. Each component is then placed at the nodes of two interlocking grids in a unit cell, such that every electric component is surrounded by four circulating magnetic field components and every magnetic field components is surrounded by four circulating electric field components [9]. The electric fields are evaluated at

every $(n+1/2)^{th}$ time step, and the time derivatives of magnetic fields are evaluated at every n^{th} time step from the discretized Maxwell's equations. The solution process is known as a *leapfrog* arrangement, in which the electric field components in the computation space are solved at a particular time step using the calculated magnetic field data computed from the most recent time step and stored in the memory. As the time step is incremented, the magnetic field data can now be computed using the electric field data from the previous time-step. This mechanism is repeated for the duration of the solution process defined by the user. The rectangular discretization and solution process discussed above is known as the Yee algorithm [8, 9]. Other dicretization techniques have been proposed using non-rectangular grids for more conformal meshing of structures and can be found in more detail in [9]. The simulated breast models in this dissertation use Yee's rectangular grid.

The time and spatial steps are carefully chosen to minimize numerical dispersion, where the velocity of the numerical wave modes differs from the actual physical velocity. This numerical error is caused by the accumulated phase/delay errors that may arise from the relative grid size respect to the wavelength and the direction of wave propagation in the grid.

When solving a scattering problem using FDTD method, one can utilize absorbing boundary conditions (ABCs) to effectively simulate the scattered fields as if it is propagating into an infinite space beyond the computation domain. The basic mechanism of an ABC is to minimize reflection at the boundary so as to keep the waves from going back into the computation domain and interact with the scattered fields. Of particular interest is the perfectly matched layer (PML) ABCs, which are utilized by SEMCAD X®. The PML ABCs are created by extending computational domain with layers of perfectly matched lossy material so that the incoming waves propagate without reflection while the amplitude is attenuated through lossy layers. This mechanism is analogous to that of absorbers used in an anechoic chamber. The PML was originally introduced by Berenger [10]. The uniaxial PML (UPML) [11] and convolutional PML (CPML) [12] are improved versions of the original PML. The UMPL formulation uses permittivity and permeability tensors to represent the layers as artificial anisotropic material, which is a physical-model based approach, as opposed to the original PML formulation, which represent the layers as hypothetical medium based on a mathematical model by splitting the electromagnetic fields into non-physical values in the layers [11]. The CPML was later proposed to reduce reflection errors for highly evanescent waves, sharp corners, or low frequency

excitations by using the complex frequency shifted tensor coefficients and recursive convolution technique [12]. An extensive detail on these PML-type ABCs can be found in [9-12]. The simulations carried out in this work typically used 20-25 layers of UPML ABCs.

5.1.2 Creating 2D Models in SEMCAD X®

A two dimensional model can be generated assuming that there is no variation in one of the axis, say *z*-direction, and FDTD can be formulated into a reduced form by setting all partial derivatives with respect to *z* equal to zero. This reduced formulation, however, is not explicitly provided in SEMCAD X®, which means that it only considers a full 3D model. However, one can effectively create a 2D model in SEMCAD X® from a 3D geometry by imposing a condition such that all partial derivatives with respect *z* will go to zero. This can be done by using a very small vertical dimension ($<< \lambda_{high}$) in *z*-axis and choosing appropriate *z*-axis boundary conditions (*xy*-plane) depending on the mode of propagation. In order to create TM_z mode, which involves only E_z, H_x and H_y, a perfect electric conductor (PEC) boundary should be used. For TE_z mode, which involves only H_z, E_x, and E_y, a perfect magnetic conductor (PMC) should be used. The models simulated in this work are configured to have TM_z mode.

To validate this approach, a simple TM_z mode configuration involving a point source (current) in a homogeneous medium as shown in Figure 5.1 is considered. A Gaussian modulated pulse of 100ps pulsewidth is used as a source waveform in the simulation. A vertical dimension of 0.5mm (much less than the wavelength at the highest frequency in the incident spectrum) is chosen as depicted in Figure 5.2. After obtaining the time-domain field solution, the Fourier Transform is performed to extract the time harmonic solution, which are then compared with the analytic solution represented by the Hankel function [13],

$$E_z = \left(-k^2 I / 4\omega\varepsilon\right) H_0^{(2)}\left(k\rho\right), \qquad (5.1)$$

where $\rho = \sqrt{x^2 + y^2}$, and k is the propagation constant, which can be complex if the medium is lossy. Figure 5.2 shows $\left|E_z\right|$ extracted from SEMCAD X® simulation at 5GHz compared with the analytic solution obtained from Equation 5.1 for: a) free space ($\varepsilon_r = 1$ and $\sigma_{eff} = 0$), and b) lossy dielectric ($\varepsilon_r = 5$ and $\sigma_{eff} = 0.2$ S/m). The current *I* at the source is normalized to 1A. The solutions obtained from the SEMCAD X® simulations for both cases match very closely with that obtained from the analytic formulation from Equation 5.1, demonstrating the validity of

effective 2D models used in SEMCAD X®. The average percentage errors between the simulated and analytical values are 0.27% and 0.18% for the free space and lossy dielectric cases, respectively.

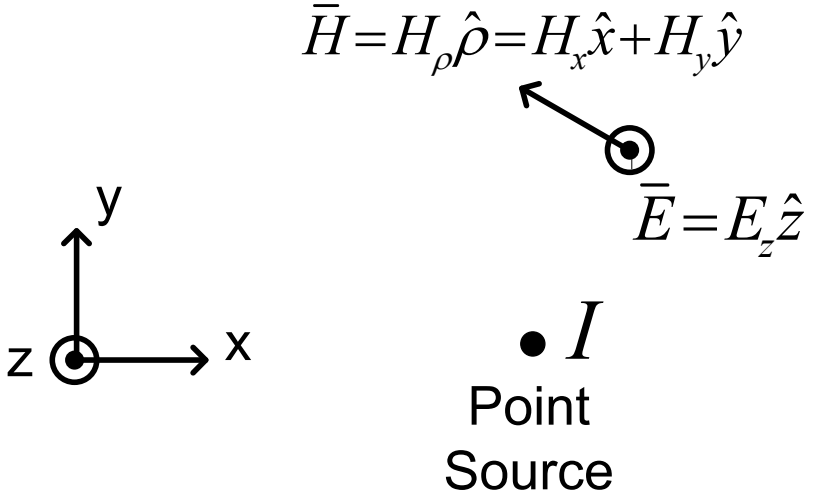

Figure 5.1 Two-dimensional point source model for TM_z configuration

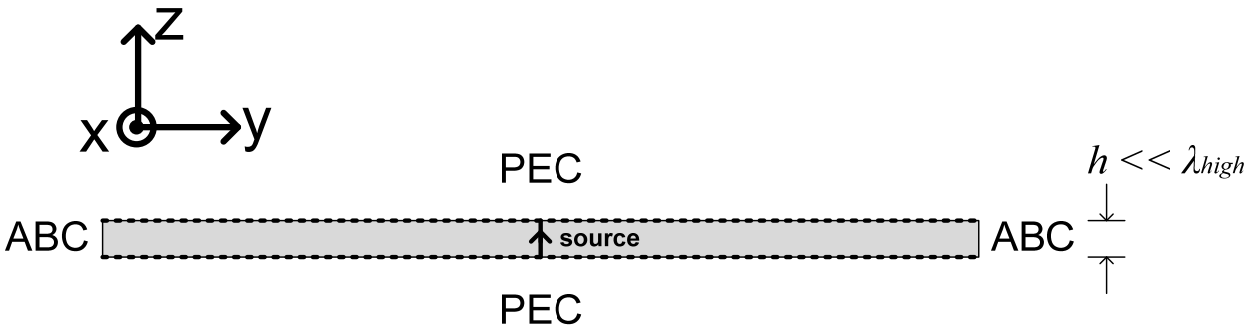

Figure 5.2 Side-view of an effective TM_z 2D point source model created in SEMCAD X®

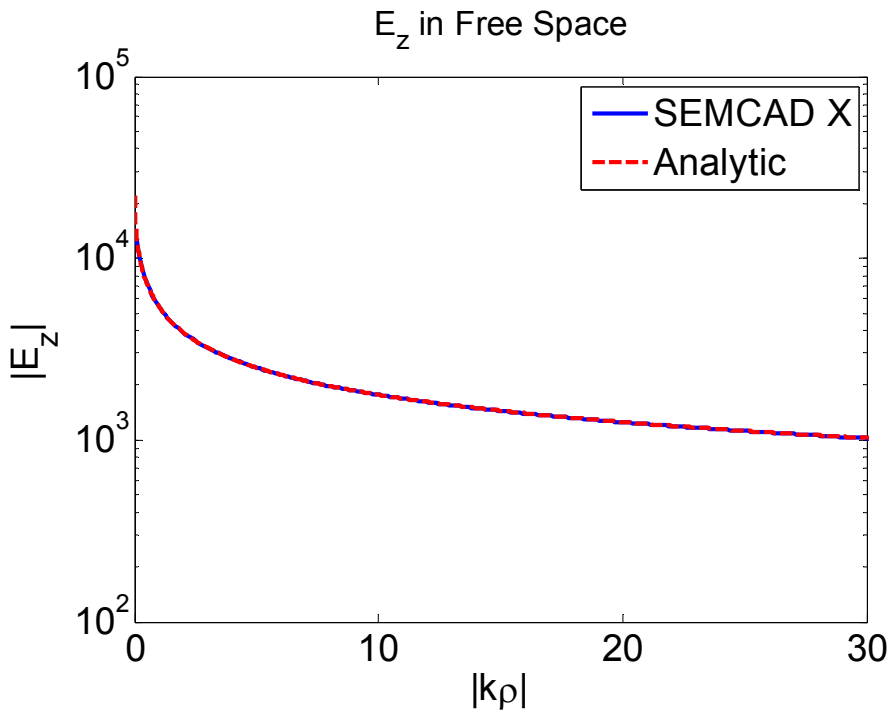

(a)

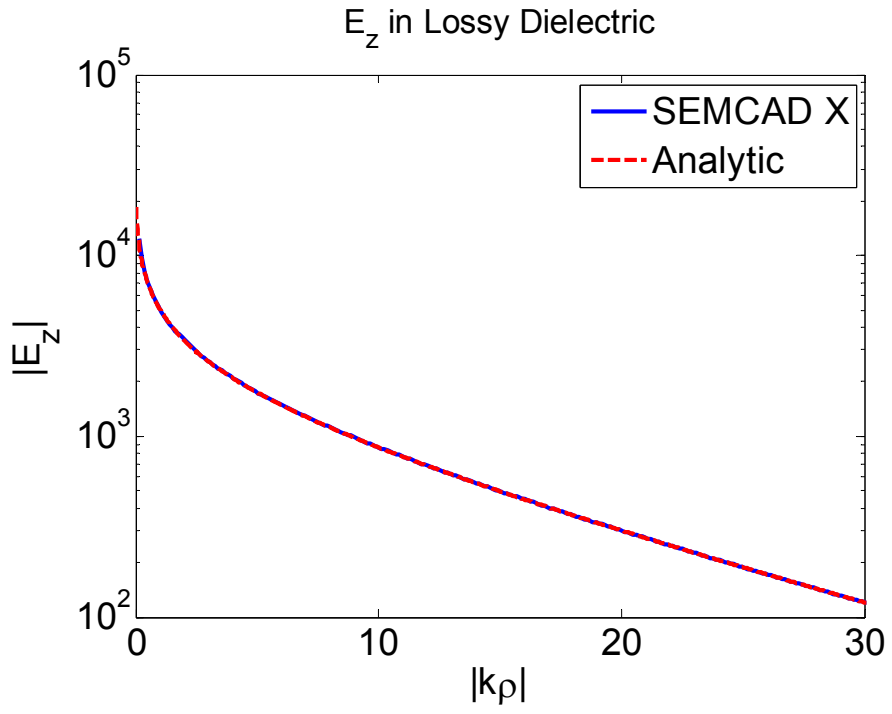

(b)

Figure 5.3 Comparison between the E_z obtained from 2D simulation in SEMCAD X® and analytic solution. The current I at the source is normalized to 1A. The solution in free space is shown in (a) and lossy dielectric ($\varepsilon_r = 5$ and $\sigma_{eff} = 0.2$ S/m) in (b).

5.1.3 Numerical Breast Tumor Models for Simulation

In this study two types of 2D numerical breast models are considered, namely semicircular and circular models, as shown in Figure 5.4. The semicircular model is representative of a supine position configuration or a compressed breast shown in Figures 2.1b and c, while the circular model is representative of a prone position configuration shown in Figure 2.1a. For each model, the diameter of an average size breast is used [14]. Note that the circular model has a smaller diameter than the semicircular model since the prone position has a breast stretched downwards resulting in a smaller diameter, while the supine position or compressed breast will result in a larger diameter. In both models, an array of point sources (TM_z) is used. In the semicircular model, the array consists of 20 elements with 1cm spacing and the elements are placed at 3cm from the breast surface. The array in the circular model has 25 elements with 1.75cm spacing, and located at 2cm away from the breast surface. Arrays in both models are assumed to be in a coupling medium. Both models consist of 1.5mm thick skin layer. All four sides in the computation domain are terminated with absorbing boundary conditions.

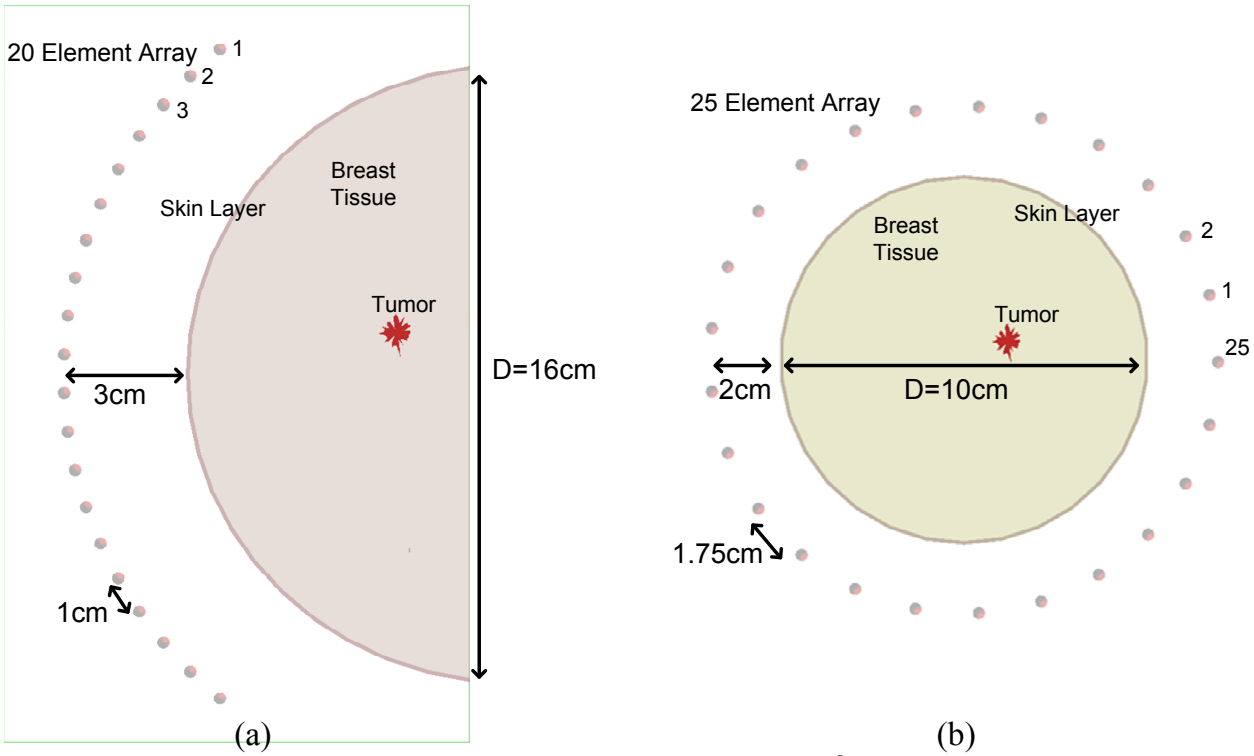

Figure 5.4 Two types of 2D breast models used in SEMCAD X® simulation: a) Semicircular model representing the supine position and compressed plate configuration, and b) Circular model representing the prone position configuration.

5.1.3.1 Tumor Shape Model

As mentioned previously, it have been reported that malignant tumors have distinguishable morphology from benign masses, i.e. malignant tumors tend to have more spiculated, random shape as opposed to smooth, oval shapes of benign tissues [15-17]. Hence, the tumor models used for simulation are generated by applying a random variation to the baseline radius of a circle (which represents a rough size) as follows:

$$r(\phi) = r_{base} + \text{random}[-r_{base}, r_{base}]. \tag{5.2}$$

This approach is similar to that used in the work by Chen et al. [16]. Figure 5.5 shows an example of a tumor model generated from a baseline circle with the radius of 3.5mm. All of the semicircular models are simulated with tumors generated using a 3.5mm radius baseline circle. For the circular models, in addition to the 3.5mm baseline tumors, 6mm and 9mm baseline models are also simulated to investigate the effects of tumor size. A new variation of tumor shape was generated for each size.

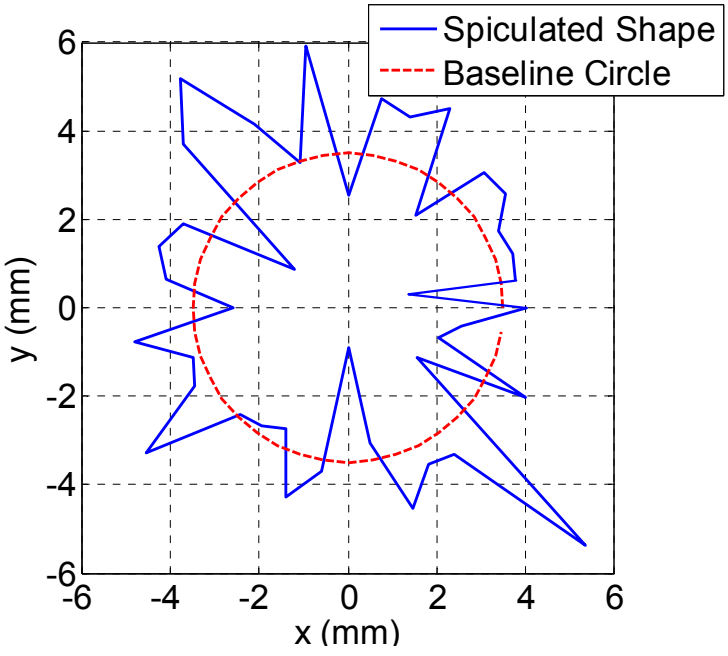

Figure 5.5 Malignant tumor shape model generated using random variation of baseline radius. The example shown here uses 3.5mm radius baseline circle.

5.1.3.2 Material Properties and Tissue Configurations used in Simulation

It is known that breast tissues and tumors have dispersive dielectric properties and the Debye relaxation models have shown to be a suitable choice for modeling breast tissues at microwave frequencies as suggested by Lazebnik et al. [18]. For implementation into FDTD, SEMCAD X® utilizes the multipole Debye model [9, 19],

$$\varepsilon_r = \varepsilon_r^{'} - j\frac{\sigma_{eff}}{\omega\varepsilon_o} \approx \varepsilon_{r\infty} + \sum_{n}^{N} \frac{\left(\varepsilon_{rs\_n} - \varepsilon_{r\infty}\right)}{1 + j\omega\tau_{d\_n}} + \frac{\sigma_s}{j\omega\varepsilon_o} \tag{5.3}$$

where ε_{rs_n} is the static permittivity, $\varepsilon_{r\infty}$ is the permittivity at infinity, σ_s is the electrical conductivity, and σ_{eff} is the effective conductivity. The number of poles, *N*, depends on the material and frequency bandwidth considered. For the simulations carried out in this study, we use the two-pole Debye parameters developed by Lazebnik et al. [18], which are obtained from recent large scale experimental data reported in the work by Lazebnik et al. [20, 21]. The values of these parameters are shown in Table 5.1. Dielectric properties in terms of $\varepsilon_r^{'}$ and σ_{eff} are shown in Figure 5.6. Fatty tissue is the normal low water content breast tissue and medium/low fat tissues are the fibroglandular tissues that have higher water content. The dielectric property plots in Figure 5.6 were also shown and discussed in Chapter 2. As it was mentioned, the dielectric contrast between the malignant tumor and fatty tissue is up to 10:1 depending on the frequency. On the other hand, the contrast between the tumor and fibroglandular tissues is as low as 1.2:1, which could cause a significant clutter problem.

Table 5.1 Debye Model of Tissue Dielectric Properties used for Simulation [18].

Type	$\varepsilon_{r\infty}$	ε_{rs_1}	τ_{d_1} (ps)	ε_{rs_2}	τ_{d_2} (ps)	τ_{d_1} (S/m)
Malignant Tumor	6.75	32.36	7.22	30.66	15.3	0.79
Fatty Tissue	3.14	3.72	8.07	4.23	19.25	0.036
Medium Fat Tissue	5.57	25.21	5.81	19.8	16.49	0.52
Low Fat Tissue	7.82	28.63	7.39	28.64	15.18	0.71
Skin	18.4	40.3	17.5	N/A	N/A	0.74

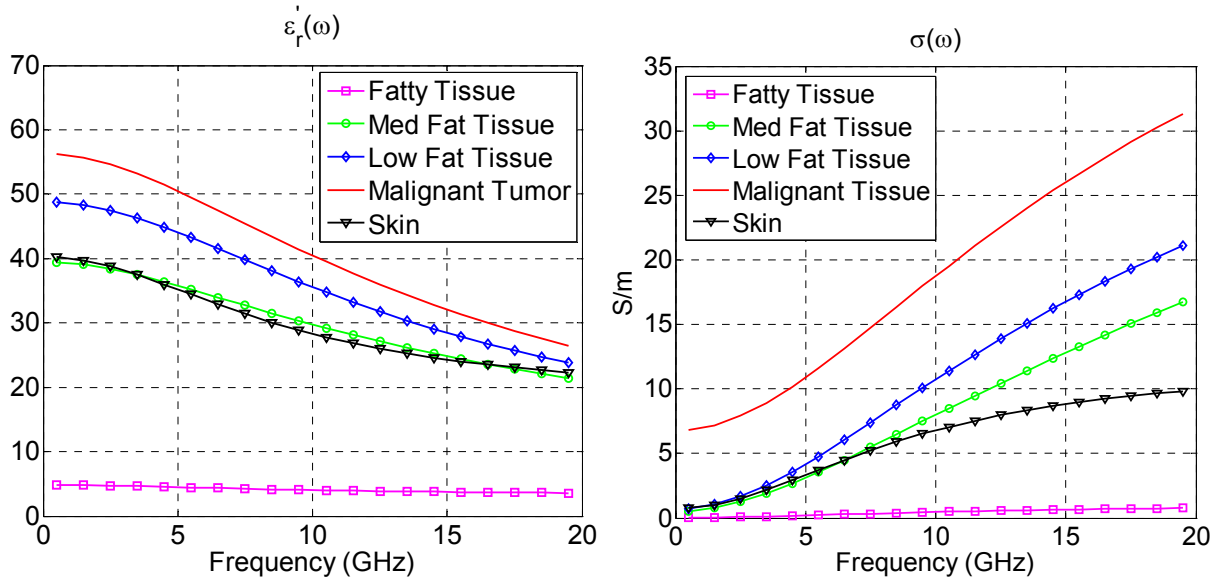

Figure 5.6 Dielectric properties of different tissue types in the breast based on two-pole Debye model [18]: Dielectric constant (real permittivity) is shown on the left, and the effective conductivity (obtained from imaginary permittivity) is shown on the right.

In the simulation, three different tissue configurations are considered for each breast model. The three configurations are: 1) a breast consisting of fatty tissues only (homogeneous), 2) a moderately dense breast with some fibroglandular tissues, and 3) a dense breast with the tumor surrounded by significant portion of fibroglandular tissues. These configurations for both semicircular and circular breast models are shown in Figures 5.7 and 5.8, respectively. The fibroglandular tissues are modeled as clusters of small, smooth circular shapes.

Matching medium, often referred to as coupling medium or bolus liquid, is also used in the simulation to minimize the skin reflection. Different materials have been used by various authors as matching medium, such as deionized water [22] and other types of liquid mixtures such as glycerin/water [23, 24] and paraffin oil/water [25]. It is desired to have a low-loss material to reduce the attenuation in the medium. To minimize numerical error at the absorbing boundaries of the computation domain, the matching medium used in this study is modeled as a constant low-loss dielectric with $\varepsilon_r^{'} = 25$ and $\sigma_{eff} = 0.3\ \mathrm{S/m}$. The choice of constant permittivity matching medium should not affect the qualitative analysis in this study.

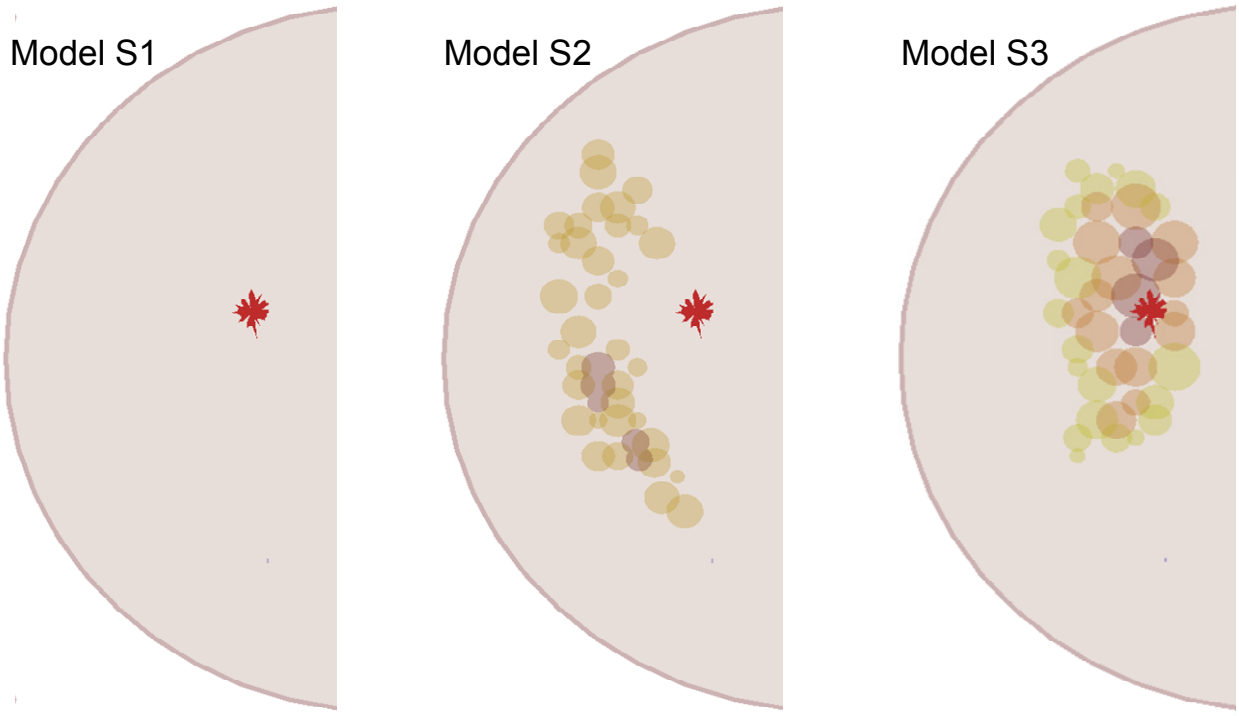

(a) (b) (c)

Figure 5.7 Various tissue configurations used in the semicircular breast model: a) Model S1 - Fatty tissue only, b) Model S2 - Moderately dense breast with some medium/low fat tissues, and c) Model S3 - Dense breast with tumor surrounded by medium/low fat tissues.

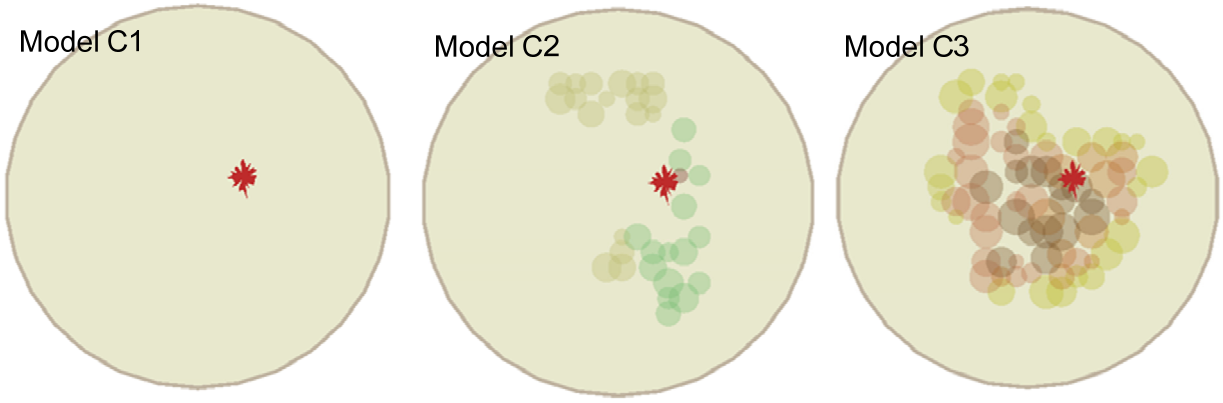

(a) (b) (c)

Figure 5.8 Various tissue configurations used in the circular breast model: a) Model C1 - Fatty tissue only, b) Model C2 - moderately dense breast with some medium/low fat tissues, and c) Model C3 - dense breast with tumor surrounded by medium/low fat tissues.

5.2 Detection Signal Processing for Identifying Tumor Response

Here we consider a multi-element array setup, which provides a set of multistatic responses. This array-based scheme is found typical in microwave breast tumor detection as mentioned in Chapter 2. Considering a setup with K-element array which can be representative of either model in Figure 5.4, the multistatic responses $\mathbf{X}_i(t)$ is

$$\mathbf{X}_i(t) = \begin{bmatrix} x_{i,1}(t) \\ x_{i,2}(t) \\ \vdots \\ x_{i,K}(t) \end{bmatrix} \qquad \text{for} \quad i = 1, 2, \ldots, K \quad , \tag{5.4}$$

where the subscript i denotes the transmit element number and $x_{i,j}(t)$ represents the signal received by j^{th} element with i^{th} element transmitting. In a practical scenario, a full array can be electronically scanned by multiplexing the feeds, or an antenna pair can be mechanically scanned. Figure 5.9 shows the general illustration of a multi-element array setup used in simulation. This multistatic data matrix can be processed to effectively represent different types of scans, i.e. a moving transmit/receive element pair or a fixed transmit with varying receive element. These two scan types are discussed in Section 5.2.2.

Throughout the simulation, the responses are obtained by transmitting a 75ps differentiated Gaussian pulse. The pulsewidth of 75ps (spacing between the bipolar peaks) corresponds to the frequency bandwidth of 16GHz (at 10% points), as shown in Figure 5.10.

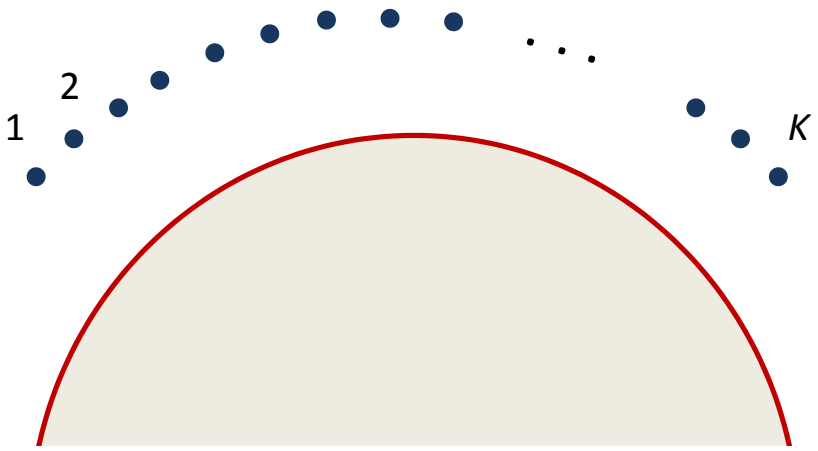

Figure 5.9 General multi-element array setup used in simulation

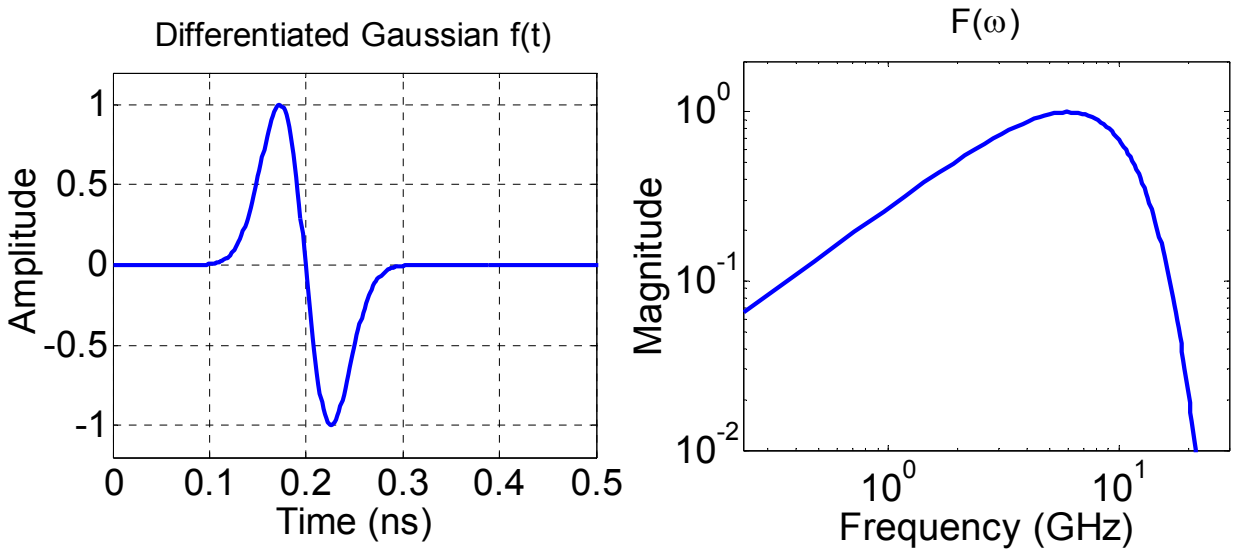

(a) (b)

Figure 5.10 Differentiated Gaussian pulse with 75ps pulsewidth used in the simulation: a) Time-domain plot, and b) Frequency-domain (Fourier transform) plot.

The response data, $\mathbf{X}_i(t)$, represents the raw signals collected by a detection system consisting of a multi-element array. There are indeed prior steps needed in order to obtain the data, but such steps could vary depending on the design, setup and operation mechanism of the system used to collect data, which is out of the scope of the current work based on numerical simulation. Regardless, $\mathbf{X}_i(t)$, should be the starting point of any signal processing carried out for detection of tumor. The general objective of signal processing is to present the data in a format that can be interpreted by an operator or an additional decision making algorithm. As mentioned in Chapter 2, there have been many signal processing approaches proposed by various authors [1-4, 25], which are mostly based on generating a focused image of the breast to detect and locate the physical position of tumor. In this section, a relatively simple approach with minimal processing is presented as a means to gain information sufficient for extracting the resonances and identifying the electrical location. Change detection and the use of contrast enhancing agents are also discussed as schemes to improve detection for heavily cluttered breasts.

5.2.1 Pre-processing

In this subsection, we discuss techniques for removing antenna coupling and direct-transmission between transmit and receive elements. This pre-processing is an important first step towards an accurate extraction of tumor responses.

5.2.1.1 Antenna Coupling

Each row in the multistatic data $\mathbf{X}_i(t)$ represents a bistatic response between j^{th} and i^{th} elements (monostatic when $j=i$), as shown in Equation 5.4. For the bistatic responses between the elements in direct line-of-sight with respect to each other, there will be a significant antenna coupling, which is the incident pulse coupled directly from the transmit element to the receive element. Since a short pulse is used for excitation, a time-gate can be applied to eliminate the antenna coupling. Figure 5.12 shows the bistatic response, $x_{1,3}(t)$, obtained from the semicircular homogeneous breast model (shown in Figure 5.7a). In the response, the antenna coupling is observed before the skin reflection and tumor response. Note that the antenna coupling has amplitude significantly larger than the skin and tumor responses. Also, the received antenna coupling is now the second derivative of a Gaussian pulse, since the radiated electric field is a derivative of the current at the source. Having identified the antenna coupling, one can apply a time-gate (in this case at t=1ns) and the gated signal is shown in Figure 5.12b. Subtracting a calibration (or background) measurement is another way to eliminate the antenna coupling. Calibration response is obtained by measuring $\mathbf{X}_i$ in the absence of breast, with only the array in the matching medium, which generates only the antenna coupling. Therefore when this calibration response is subtracted from the total response, only the skin reflection and the tumor response will remain in the response, resulting in the same type of response in Figure 5.12b.

Once the antenna coupling is eliminated, one is left with the skin reflection and the tumor response (with possible clutter) which can now be further processed for detection.

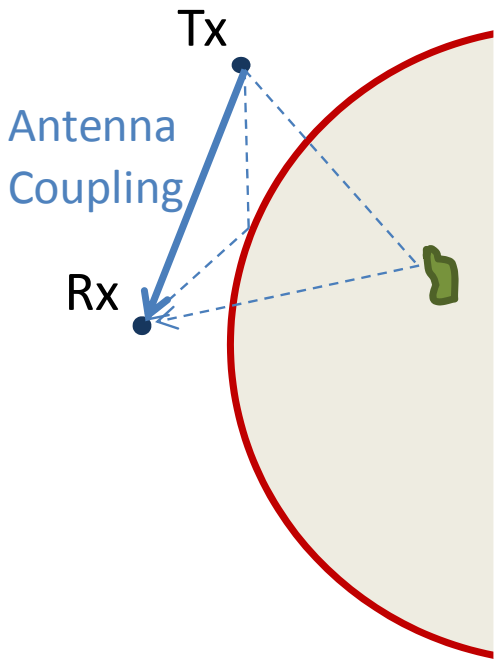

Figure 5.11 Illustration of antenna coupling between transmit and receive elements in direct line-of-sight.

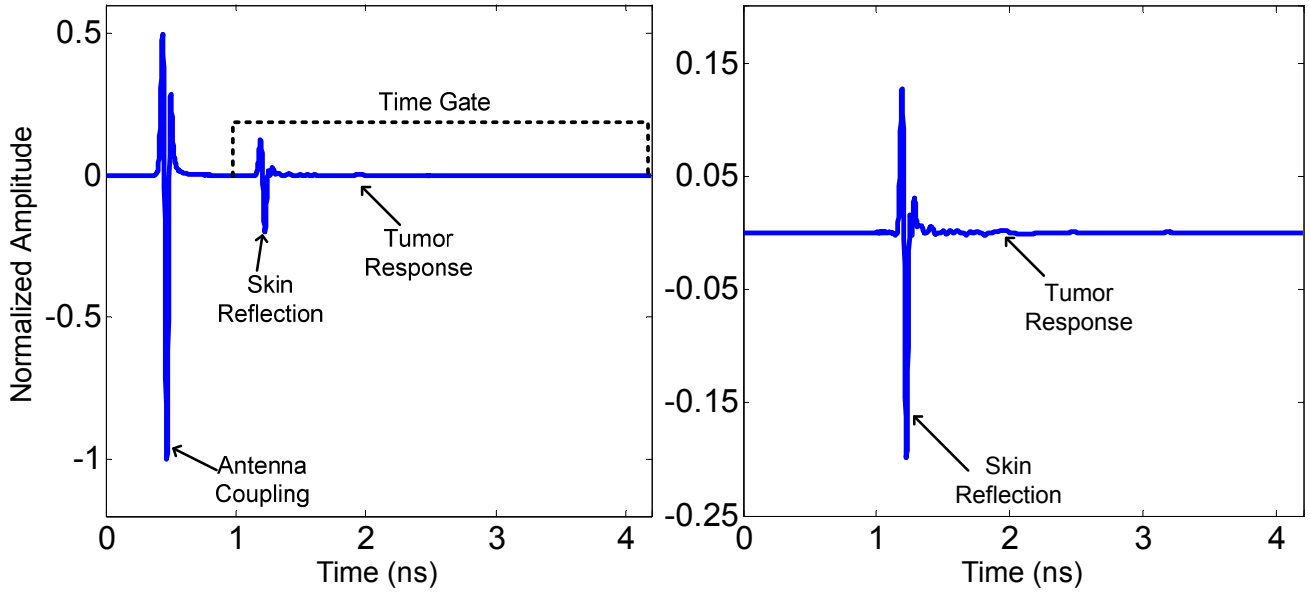

Figure 5.12 Example of antenna coupling in a bistatic response. $x_{1,3}(t)$ from the simulation of semicircular homogeneous breast model is shown: a) Raw signal, and b) signal after time-gating.

5.2.1.2 Direct-Transmission

For bistatic element pairs with no direct line-of-sight, antenna coupling does not exist. Also, there is no skin reflection. However, there is a direct-transmission response corresponding to the incident pulse received through a shortest path between transmit and receive elements as shown in Figure 5.13. This means that the tumor responses will always follow direct-transmission response in time. Hence, if they are separated far enough in time, a time-gate can be applied to suppress the direct-transmission. However, in case of some overlap between the two responses, it is not so clear where to apply the time-gate. Figure 5.14 shows the bistatic response, $x_{7,17}(t)$, obtained from Model C1, the circular homogeneous breast model shown in Figure 5.8a. Here, a wider pulsewidth is observed due to a lower amount of higher frequency content transmitted through the dispersive skin and breast. The highlighted regions in the plot indicate the direct-transmission pulse and the tumor response, and there is an overlap between the two. In such cases, additional processing is required to more clearly determine the tumor response.

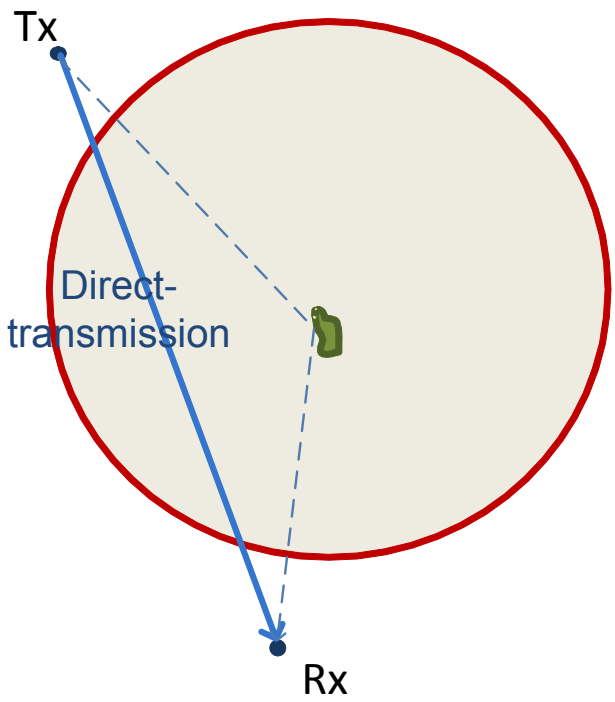

Figure 5.13 Direct-transmission between bistatic elements with no direct line-of-sight.

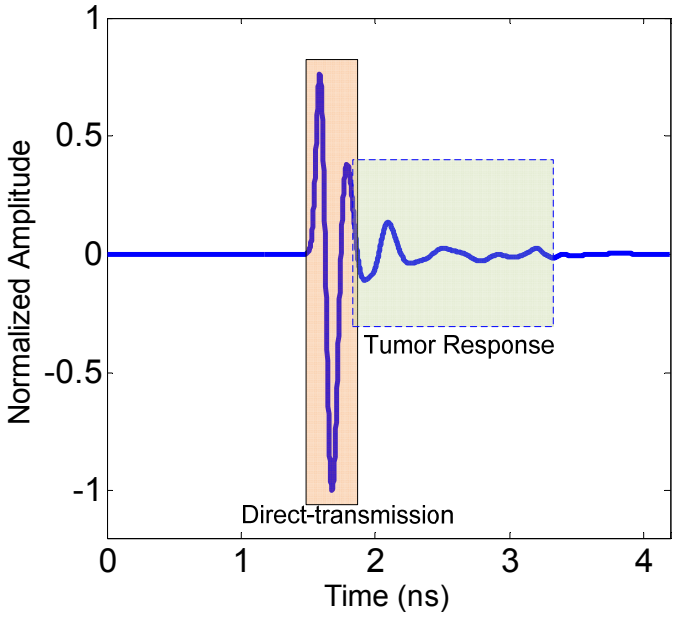

Figure 5.14 Example of a bistatic response between the elements with no direct line-of –sight: $x_{7,17}(t)$ from the simulation of circular homogeneous breast model is shown.

5.2.2 Tumor Response Extraction using GPR-based Scanning Plots

Once the preprocessing is carried out to remove the antenna coupling and some direct-transmission, bistatic signals in $\mathbf{X}_i(t)$ can be represented as

$$x_{i,j}(t) = s_{i,j}(t) + m_{i,j}(t) + c(t) + n(t) \tag{5.5}$$

Where $s_{i,j}(t)$ represents the skin reflection or unresolved direct-transmission, $m_{i,j}(t)$ is the tumor response, $c(t)$ is the clutter due to tissue heterogeneity in the breast, and $n(t)$ represents noise in the received signal. In this subsection, a GPR-type scanning plot is considered as a simple technique for determining and extracting the tumor response, $m_{i,j}(t)$. This is not a technique generating a focused image of breast to locate the physical position of the tumor, such as delay-and-sum based techniques [1, 3, 25], but rather an approach to gaining an insight into the electrical location of the tumor which can be used in focusing the microwave. Since this approach is based on minimal signal processing, it should work fairly well for uncluttered, relatively homogeneous breast. However, it could also work well if used with contrast enhanced

breast or in routine screening scheme where change detection can be performed. This approach can easily be implemented as a precursory step before applying focused imaging.

5.2.2.1 GPR B-scan

A typical GPR (ground penetrating radar) display shows a position-time profile of the responses. As depicted in Figure 5.15a, a bistatic (or monostatic) antenna pair is scanned linearly above a surface below which an object is immersed, and the ensemble of responses collected at different positions during the scan is presented in terms of a position-time plot as illustrated in Figure 5.15b. This type of scan and presentation of data is known as B-scan (C-scan for a planar scan) [26]. It is observed that the reflection from surface occurs consistently at the same point in time since the distance between the antennas and surface remains constant, whereas the response from a finite-size scatterer occurs at different times since the path length changes as the antenna varies its position. For this reason, the peaks from the surface response appear to be a flat line as a function of antenna position in the position-time plot, while the peaks from a finite subsurface object appear as a hyperbolic curve due to relative time delays between the peaks as shown in Figure 5.15b. The prominence of the object response in position-times plot indeed depends on the homogeneity of the medium surrounding the object. The same kind of position-time plot (or B-scan) can be generated using $\mathbf{X}_i(t)$ from the breast model since the configuration is very much similar. A slight difference comes from the fact that the skin boundary is not flat in the breast model, which results in a different curvature profile in the tumor response. However, it should still have a concave curvature with the vertex representing the shortest path length point, except when the tumor is located exactly equidistant (electrically) from all array elements.

The focused image of a breast generated using aforementioned methods such as DAS-based algorithm [1, 3] is in essence a result of further processing of B-scan data, that is, the spatial spreading of wavefront is deconvolved thereby creating a focus at a point corresponding to the location of the scatterer. In other words, the peaks of the target response in the signal at different positions are basically back-projected, such that they will add coherently creating a strong focus. Such approach in GPR is usually known as the migration or synthetic aperture radar (SAR) processing [26]. In order to obtain a well focused image with an accurate estimate of the physical location of scatterer, accurate *a priori* information about the dielectric property of

the propagation medium is required. Highly heterogeneous medium could significantly degrade the performance.

Therefore the B-scan (position-time plot) based approach discussed here is basically a step before applying a focused image, providing only the information regarding relative time-delays between the peaks of the scatter responses, which correspond to the electrical location of the scatterer. For the purpose of detecting and extracting the tumor response to estimate its electrical location and resonances, the position-time plot would provide sufficient information.

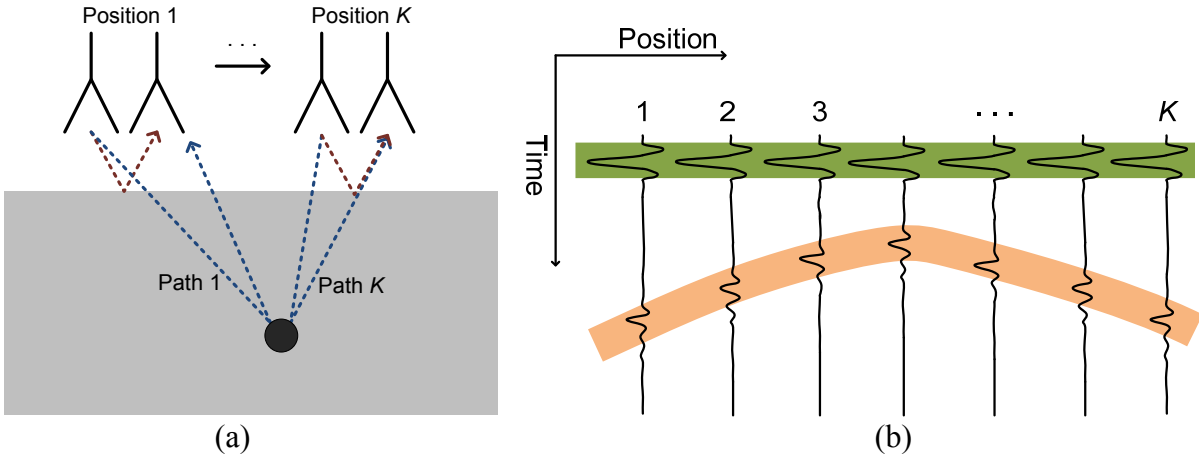

Figure 5.15 Typical position-time scan (B-scan) used in ground penetrating radar: a) Schematic illustration of a linear position scan of bistatic response from sub-surface object, and b) Position-time profile of responses.

5.2.2.2 Scan Type 1: Moving Transmit/Receive Element Pair (B-scan)

Here, the same type of position-time plot as discussed in Figure 5.15b is presented. Since the collection of multistatic data $\mathbf{X}_i$ contains multiple sets of bistatic responses, more than one position-time plots can be generated using the monostatic or bistatic pairs with direct line-of-sight. As illustrated in Figure 5.16, an ensemble of bistatic responses with constant element spacing (i.e. $d\Delta$) at different positions represents a position-time plot,

$$\mathbf{X}_{\mathrm{PT1},d} = \left[\mathbf{x}_{1,1+d} \quad \mathbf{x}_{2,2+d} \quad \cdots \quad \mathbf{x}_{K,K+d}\right] \qquad d = 0,1,\ldots \tag{5.6}$$

where K is the number of array elements and d represents the distance between bistatic elements (d=0 for monostatic responses). This type of scan represent a case where the transmit/receive

pair moves along the skin surface, and is hereafter referred to as Moving Transmit Scan. Here, $\mathbf{x}_{i,j}$ represents the sampled signal such that

$$\mathbf{x}_{ij} = \left[x_{ij}(\Delta_t t) \;\; x_{ij}(2\Delta_t t) \;\ldots\; x_{ij}(M\,\Delta_t t) \right]^T \tag{5.7}$$

where M is the number of samples in the response. The number of possible d values corresponds to the number of position-time plots generated, and is limited by the maximum direct line-of-sight distance between bistatic pairs. It is to be noted that a sliding window average (with window size 1/30 of total sample size) is applied before generating the plot. This was done in an effort to reduce the peak amplitude in the skin reflection as well as some high frequency content. Since the electromagnetic waves at higher frequencies do not penetrate into the breast as well as at lower frequencies, such averaging (in essence a high-pass filter) minimizes the amplitude contrast between the skin and tumor responses without altering the tumor responses.

Figure 5.17a shows the position-time plot generated from the magnitude of monostatic responses, $\left|\mathbf{X}_{\mathrm{PT1},0}\right|$, in Model S1. In much the same way as in Figure 5.15b, the skin reflection is clearly observed as a flat line, while the tumor response peak is shown as a concave down curve with the vertex at position 7, indicating the shortest path length between the tumor and element 7 (in agreement with the model geometry shown in Figure 5.4a). Figure 5.17b shows the same response with the skin reflection removed (time-gated), the lower amplitude late-time response can be seen. The position-time plots (skin reflections removed) generated from the responses with various d values, i.e. d = 0, 1, 2, and 3, are shown in Figures 5.18a, b, c, and d, respectively. The tumor response peaks consistently appear in all four plots. The red dashed curve in each plot is the relative time-delay profile obtained by placing a source at the tumor location in the model, which accurately represents the electrical location of tumor. By placing the curve on the top of the tumor response peak in each plot, it is clear that there is a very close match between the two. Figure 5.19 shows the position-time plots generated from the responses simulated in Model C1. The tumor responses in this case also consistently appear in all four plots, closely matching the time-delay profile shown in red dashed curve. The shortest tumor-antenna path length exists at element 1 (Figure 5.4b) for this model, which can be observed in the position-time plots. A slightly different observation, however, is made in this circular model, that is, the tumor response peak wraps around going from the last position back to the beginning position.

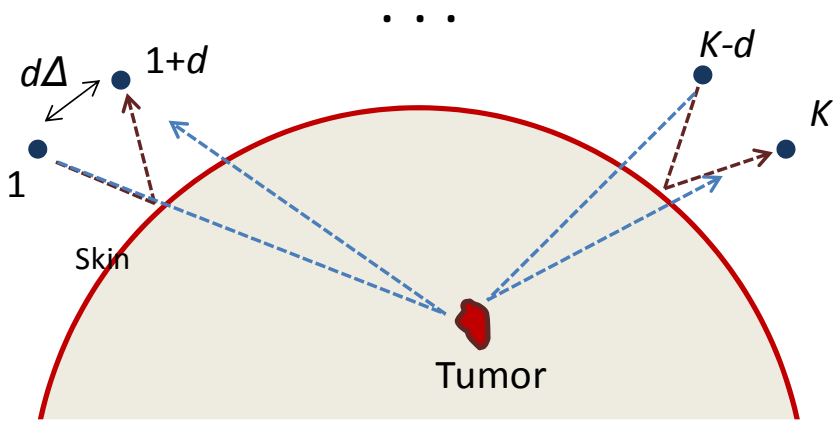

Figure 5.16 Illustration of using element pairs as a function of position to generate position-time (Moving Transmit Scan) plots from breast model. This configuration represent a case where the transmit/receive pair is scanned along the skin surface.

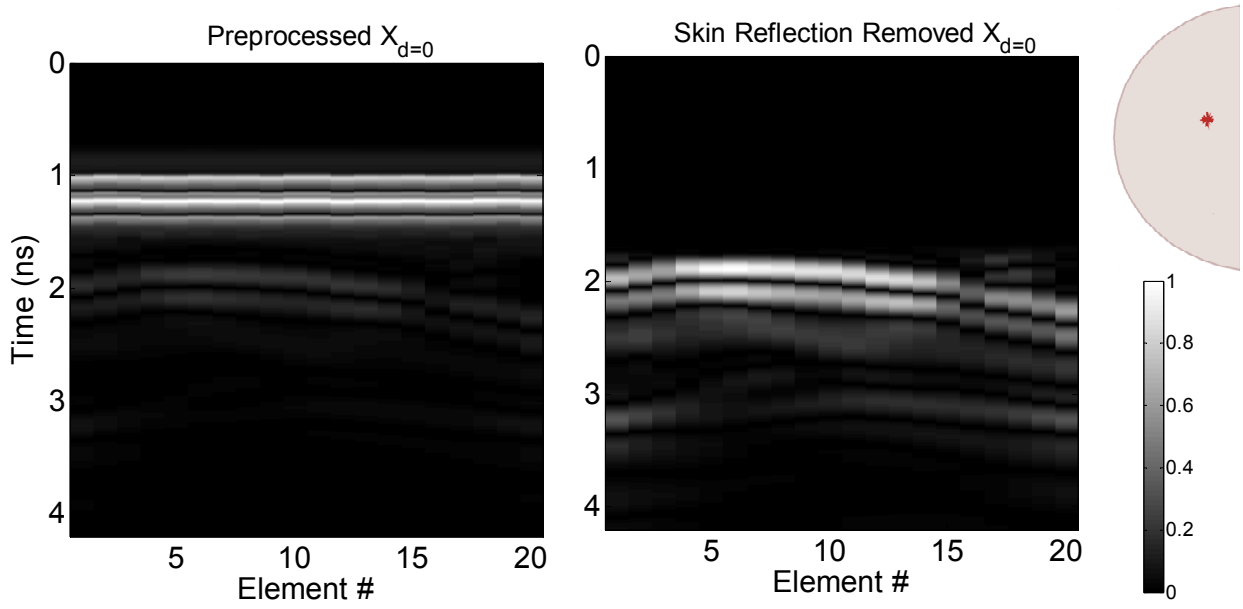

Figure 5.17 Position-time plots generated from monostatic Moving Transmit Scan (d=0) of responses in Model S1: a) with skin reflection after antenna coupling is removed, and b) After skin reflection is removed.

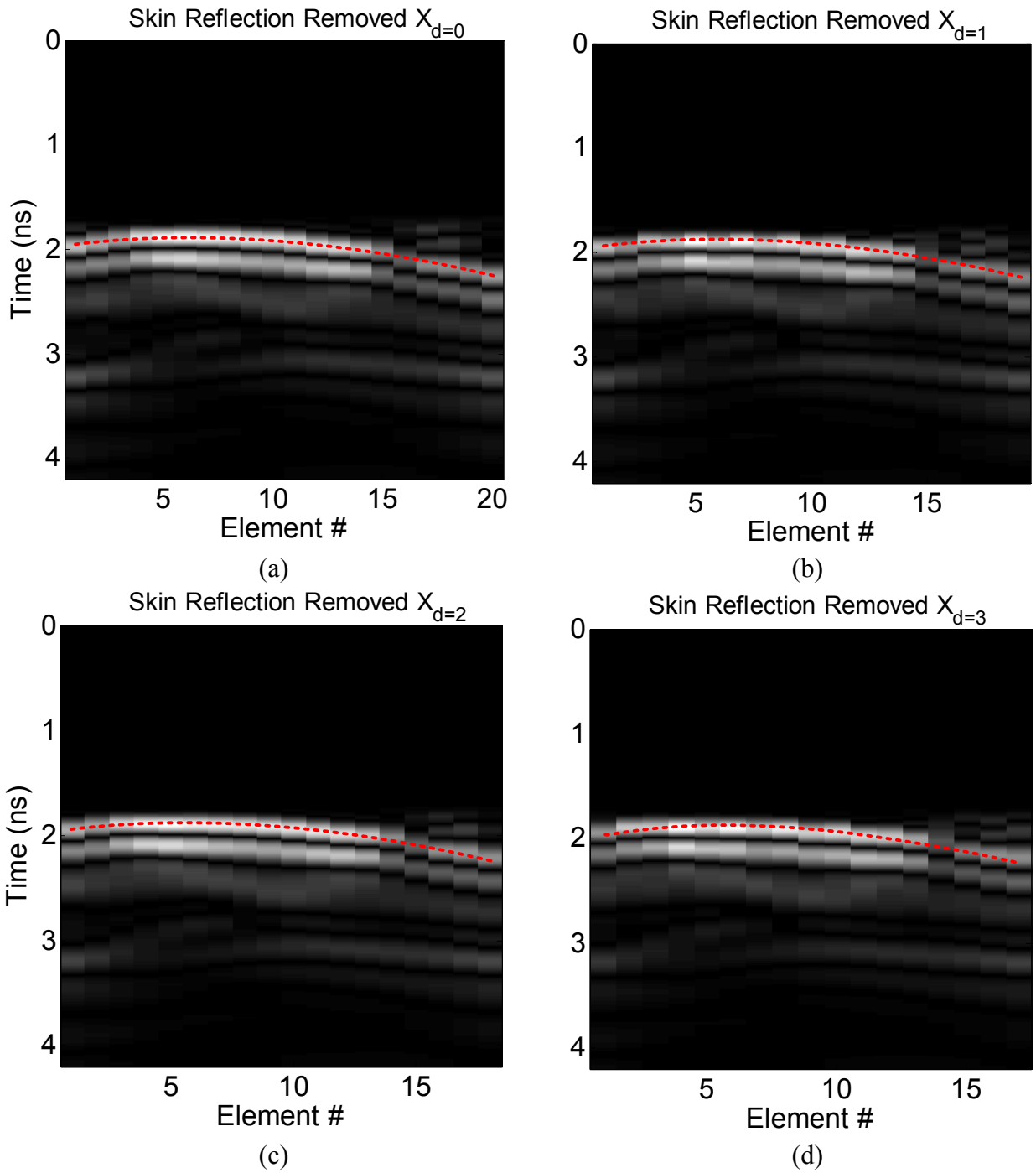

Figure 5.18 Position-time plots (skin reflections removed) generated from Moving Transmit Scan of simulated responses in Model S1 with various *d* values, i.e. *d* = 0, 1, 2, and 3, shown in (a), (b), (c), and (d), respectively. The red dashed curve corresponds to relative time-delay profile that represents the electrical location of tumor.

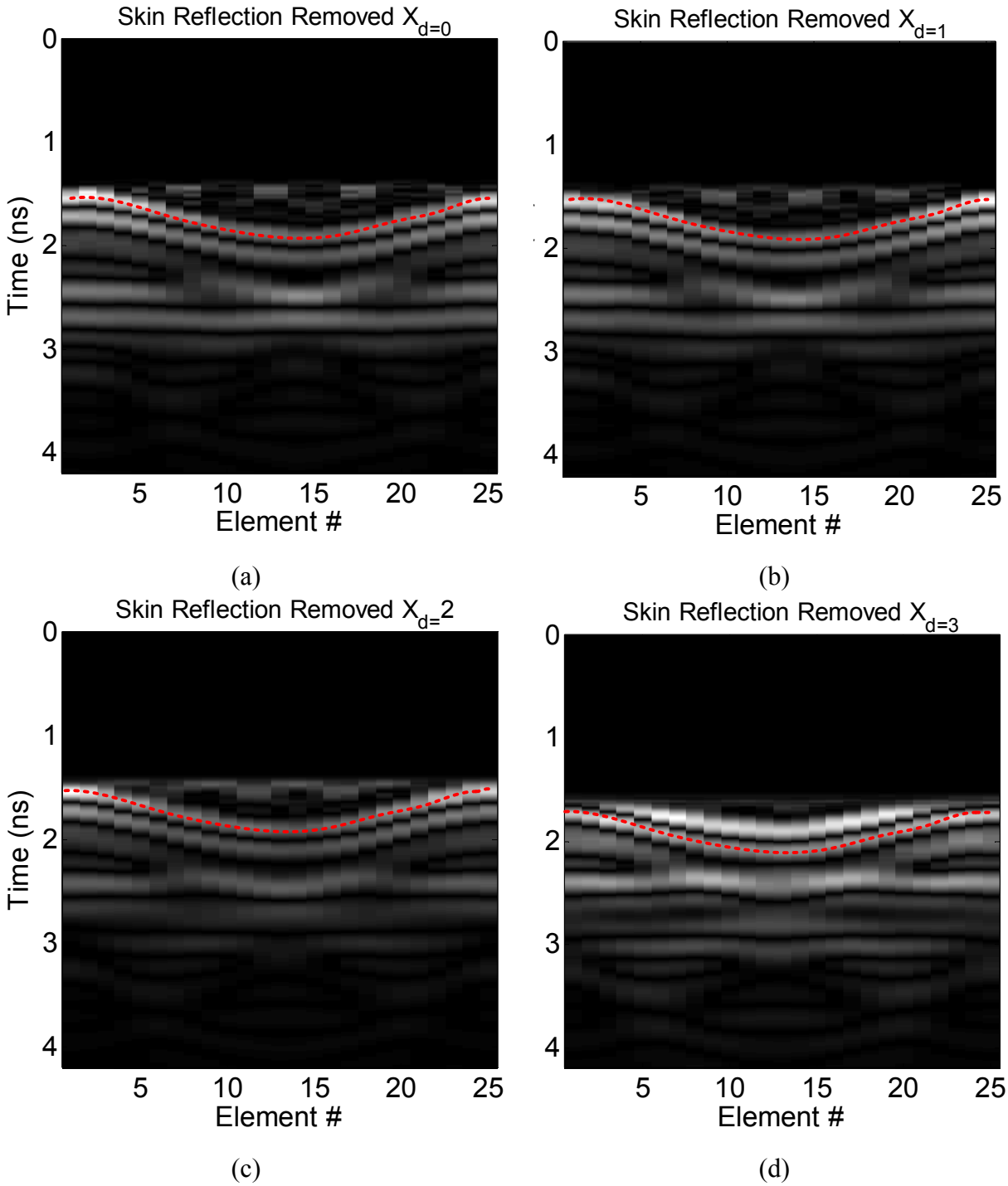

Figure 5.19 Position-time plots (skin reflections removed) generated from Moving Transmit Scan of simulated responses in Model C1 with various *d* values, i.e. *d* = 0, 1, 2, and 3, shown in (a), (b), (c), and (d), respectively. The red dashed curve corresponds to relative time-delay profile that represents the electrical location of tumor.

Based on the results shown in Figures 5.17 through 5.19 for the homogeneous breast models, the position-time plots seem to effectively provide the information needed to extract the tumor response. Using multiple position-time plots generated from the multistatic data, one can monitor the consistency of the tumor response to accurately determine the specular peak locations in time. Once the location of tumor response is identified in the position-time plot, a time-gate can be applied to monostatic responses at each element to extract the tumor responses, as shown in Figure 5.20. The extracted tumor responses are then ready for the SEM analysis to estimate the poles and residues. It should be noted that the extracted tumor responses may include other types of responses such as multiple reflections from inner boundary of the breast (between skin and breast tissues), which could affect the resonance analysis. However, since the interest is in determining the fundamental resonance of the tumor (ringing should be much slower than the reflected signals from inner boundaries), the pole estimation should be fairly robust in estimating such resonances, which is discussed in Section 5.5.

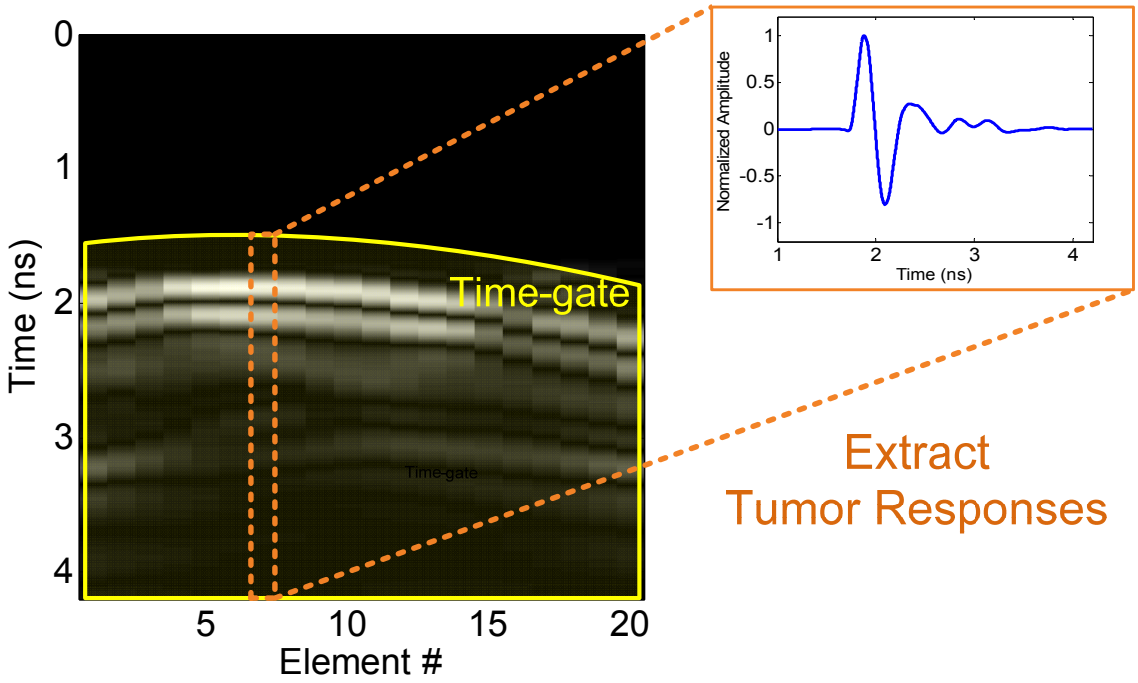

Figure 5.20 Extracting tumor responses from the position-time plot by applying time-gates based on the identified location of the tumor response peaks.

For an inhomogeneous breast containing fibroglandular tissues, identifying the tumor response from the position-time plot becomes significantly more difficult since additional boundary conditions exist due to tissue heterogeneity creating more reflections in the response. Moreover, if the tumor is surrounded by fibroglandular tissues, the lower dielectric contrast could provide significantly lower the scattering intensity. Also, the presence of other tissues may result in inconsistent propagation speed in the breast, causing the tumor response profile in the position-time plot to be deformed from a simple concave curve (with one minimum point) into more complicated shape difficult to estimate. Figures 5.21 and 5.22 show the position-time plots of the simulated responses in Models S2 and C3. In both Figures, the red dashed curves represent the location of the tumor response peaks, and it is indeed very difficult to extract this curve profile out of the position-time plots. The red curve profile is not of a simple concave or hyperbolic curve as expected, especially for the one in Figure 5.21. The tumor response just seems to be embedded in clutter, requiring additional processing to reduce clutter or different data collection scheme to enhance the tumor response.

Inhomogeneous breasts also provide significant limitations in focused imaging approaches. Although some additional processing can be applied to improve focused images of breasts as suggested by Klemm et al. [25] and Yang et al. [27], it still remains a challenge to accurately image a dense inhomogeneous breast for detecting tumors. It is important to have a good estimate of the propagation speed in the medium to accurately generate a focused image, since the coherent addition of the peaks depends on the effective delay based on the estimated propagation speed. Inhomogeneous breast makes it very difficult to estimate the propagation speed in the medium, resulting in a severely degraded focused image. Even with a reasonable estimate of the propagation speed in the breast, clutter in the responses increase more bright spots in the image, making it more difficult to identify tumors. This means that both position-time plot and focused image approaches essentially suffer from the same problem.

Applying additional signal processing alone would limit how well the tumor response can be identified from a heavily cluttered response. Since the tumor responses in such breasts could be very subtle, utilizing measurement schemes such as change detection and differential responses using contrast agents [28-30] could be significantly beneficial in extracting the tumor response. The following Sections (5.3 and 5.4) present how such schemes can be utilized to improve identification of tumor response in position-time plots.

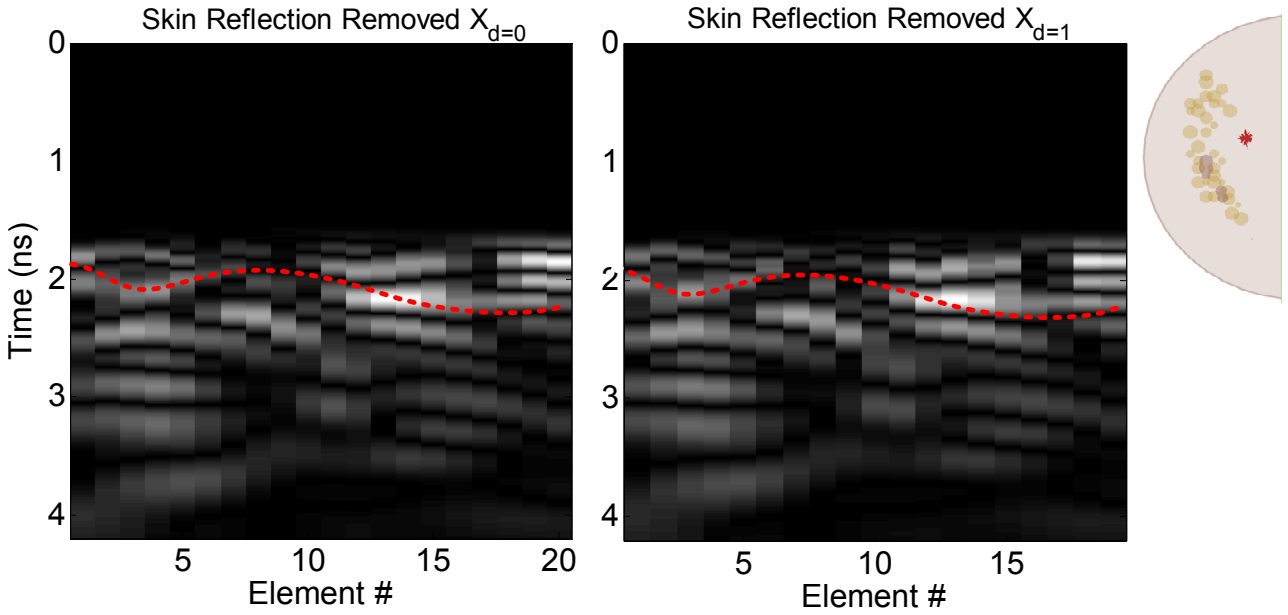

(a) (b)

Figure 5.21 Position-time plots (skin reflections removed) generated from simulated Moving Transmit Scan of responses in Model S2 with $d = 0$ and $d = 1$, shown in (a) and (b), respectively. The red dashed curve corresponds to relative time-delay profile that represents the electrical location of tumor.

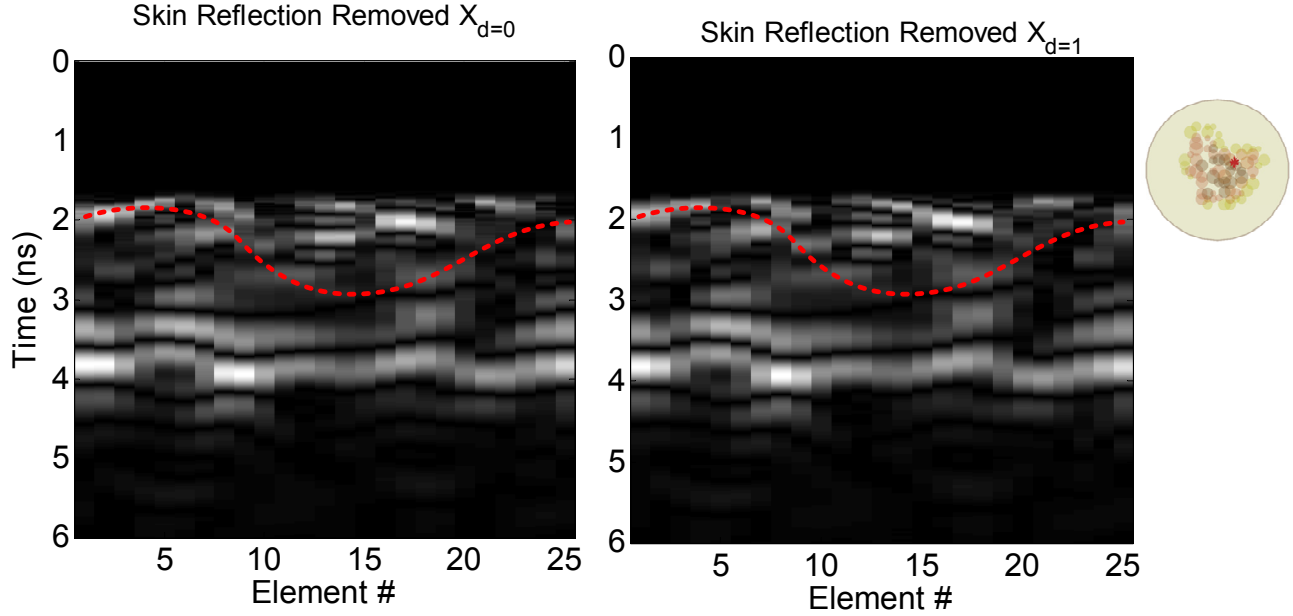

(a) (b)

Figure 5.22 Position-time plots (skin reflections removed) generated from Moving Transmit Scan of simulated responses in Model C3 with $d = 0$ and $d = 1$, shown in (a) and (b), respectively. The red dashed curve corresponds to relative time-delay profile that represents the electrical location of tumor.

5.2.2.3 Scan Type 2: Fixed Tx Element, Varying Rx Element

Another way of generating position-time plots from multistatic data, $\mathbf{X}_i$, is by using an ensemble of the monostatic and bistatic responses collected while transmit element is fixed:

$$\mathbf{X}_{\mathrm{PT2}\_i} = \begin{bmatrix} \mathbf{x}_{i1} & \mathbf{x}_{i2} & \cdots & \mathbf{x}_{iK} \end{bmatrix} \qquad i = 1, 2, ..., K \tag{5.8}$$

where K is the number of array elements. This is a different kind of position-time plot since the path length of skin reflection varies as the receiver location changes, and is hereafter referred to as Fixed Transmit Scan. Figure 5.23 shows the schematic illustration Fixed Transmit Scan.

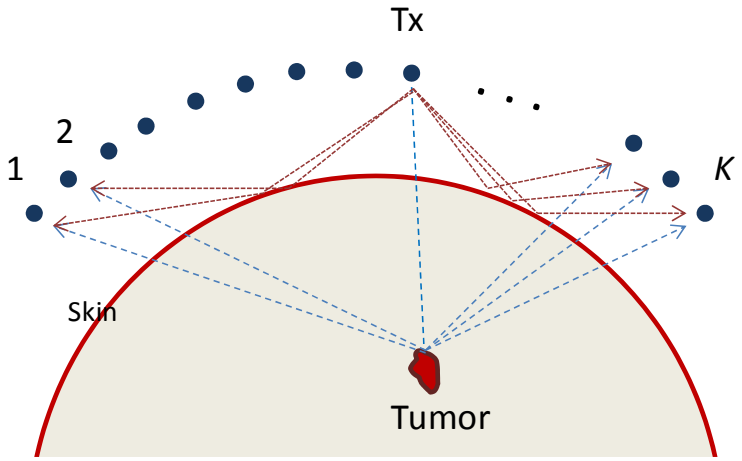

Figure 5.23 Illustration of scanning of the array with fixed transmit element. A position time-plot is generated by ensemble of the monostatic and bistatic responses collected while transmit element is fixed (Fixed Transmit Scan).

In Figure 5.24, the position-time plots generated from Fixed Transmit Scan of the simulated responses, $\left|\mathbf{X}_{\mathrm{PT2},i}\right|$, of Model S1 for i = 3, 7, 9, and 12 are shown. The magnitude of the responses in the plot is shown in a log scale to make the tumor response more visible in the plot. Unlike Moving Transmit Scan (scan type 1), the skin reflection is shown to be a hyperbolic curve, due to the change in path lengths as a function of receiver position. Moreover, the vertex of the curve (shortest path length point) changes as i is varied. The tumor response is still displayed as concave/hyperbolic curve with the vertex at receiver position 7 (shortest path length from tumor) and consistently appear in all four plots. However, the curve is slightly flatter since the relative differences in path lengths exists only in the return path, thereby reducing the relative time-delay

between the elements by half. The red dashed curve here also indicates the relative time-delay profile representing the electrical location of tumor, with which the tumor response peaks in each plot seems to be in close agreement.

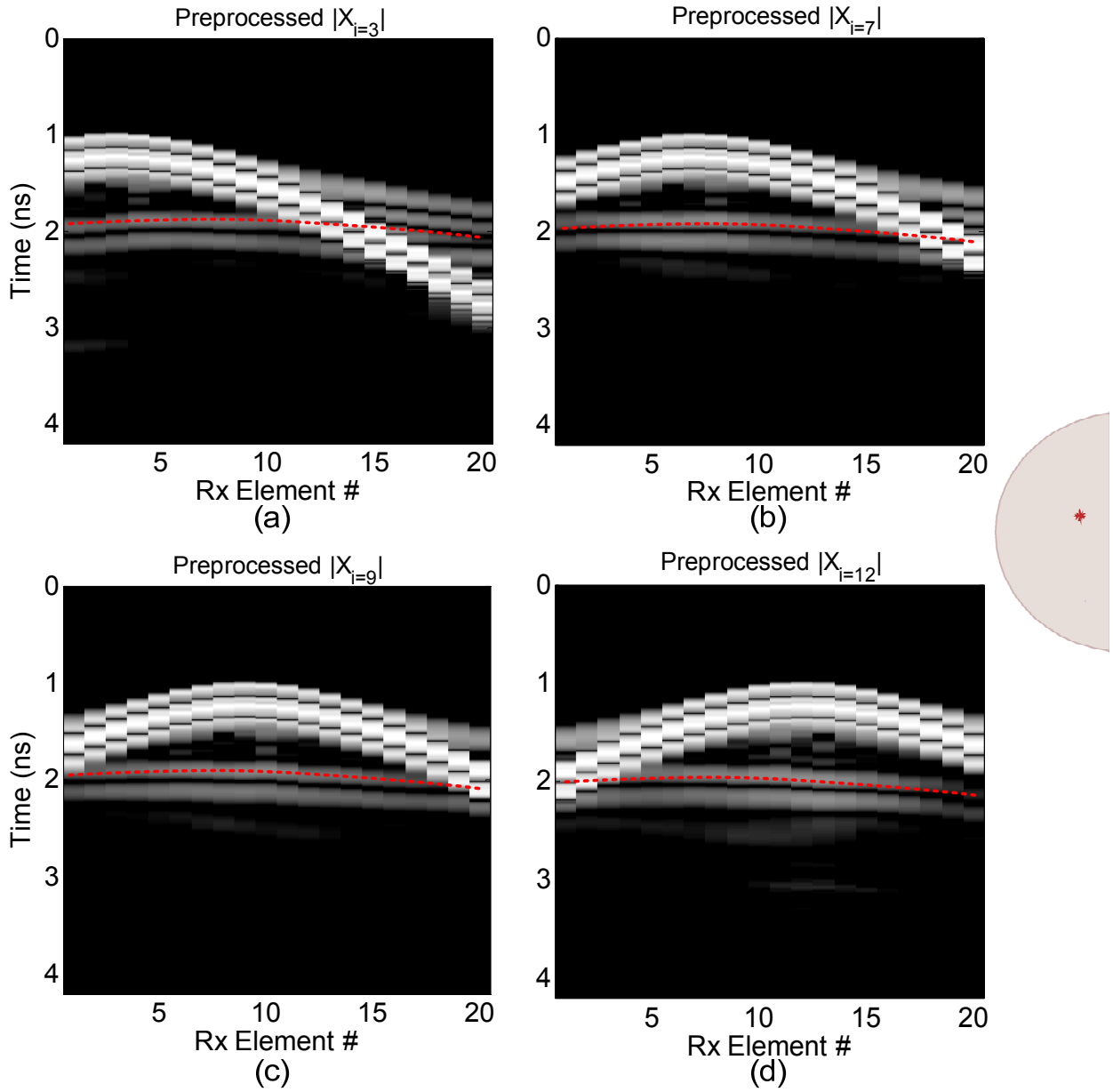

Figure 5.24 Position-time plots generated from Fixed Transmit Scan of simulated responses in Model S1 with various *i* values, i.e. $i = 3$, 7, 9, and 12, shown in (a), (b), (c), and (d), respectively. The magnitude of the responses in the plot is shown in log scale. The red dashed curve corresponds to relative time-delay profile that represents the electrical location of tumor.

Since there is consistency in the position-time profile of the tumor responses with various transmit elements (with slight time delay due to differences in incident path lengths), one can remove the inconsistent skin response by correlating the plots and retaining only the tumor responses, or by time gating the tumor response in the same manner as in Figure 5.20. The extracted tumor responses are then ready for the SEM analysis. The same approach can be taken to extract the tumor response from the Model C1.

This approach also is limited by clutter when the breast consists of tissue heterogeneity. Figure 5.25 shows the position-time plots from Fixed Transmit Scan of the simulated responses in Models S2. It is definitely not obvious which curve profile represents the tumor response, requiring additional procedure or information to identify the tumor response, as discussed in the case of Moving Transmit Scan (Type 1).

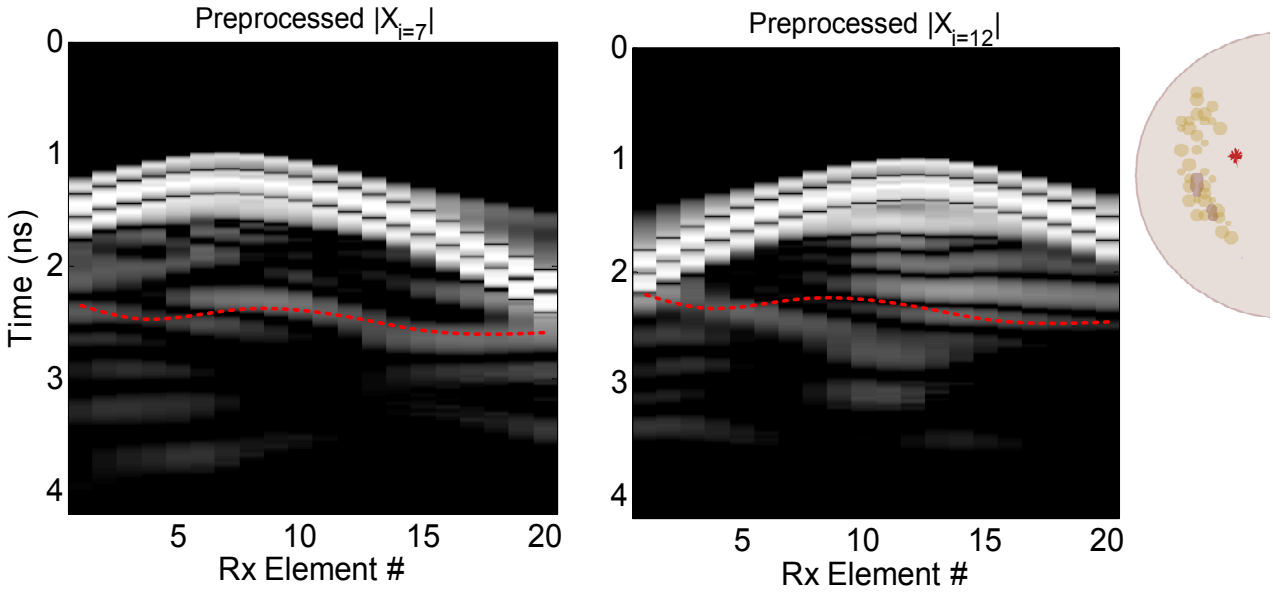

Figure 5.25 Position-time plots generated from Fixed Transmit Scan of simulated responses in Model S2 with $i = 7$ and 12, shown in (a) and (b), respectively. The red dashed curve corresponds to relative time-delay profile that represents the electrical location of tumor.

5.3 Change Detection

A scenario in which the tumor response can be detected and extracted from highly cluttered signal is through change detection. Comparison of responses taken over a period of time through a routine screening would enable one to detect small changes made in the response caused by a tumor. These changes can be caused by a newly developed tumor or a growth in tumor size compared to previous detections. Figure 5.26 illustrates three possible stages at which measurements can be made and produce differences in the responses. Change detection scheme was suggested for mammograms to improve the detection rate and reduce false positives, and was shown to be effective [31]. This makes the change detection scheme an attractive approach for potential combination use of mammogram and microwave systems as previously discussed, thereby increasing the overall robustness of detection. The key to an accurate change detection is the alignment of the responses taken at different times. Since the measurements will have slightly different setup each time, a good calibration procedure is essential to ensure the alignment of responses. Once the responses are properly aligned, the changes in the responses can be detected and extracted. While the alignment of the responses is a very important topic, it is out of the scope of this dissertation and we leave it for possible future discussion. Hence, for the results discussed in this section it is assumed that a proper calibration has taken place to align the responses.

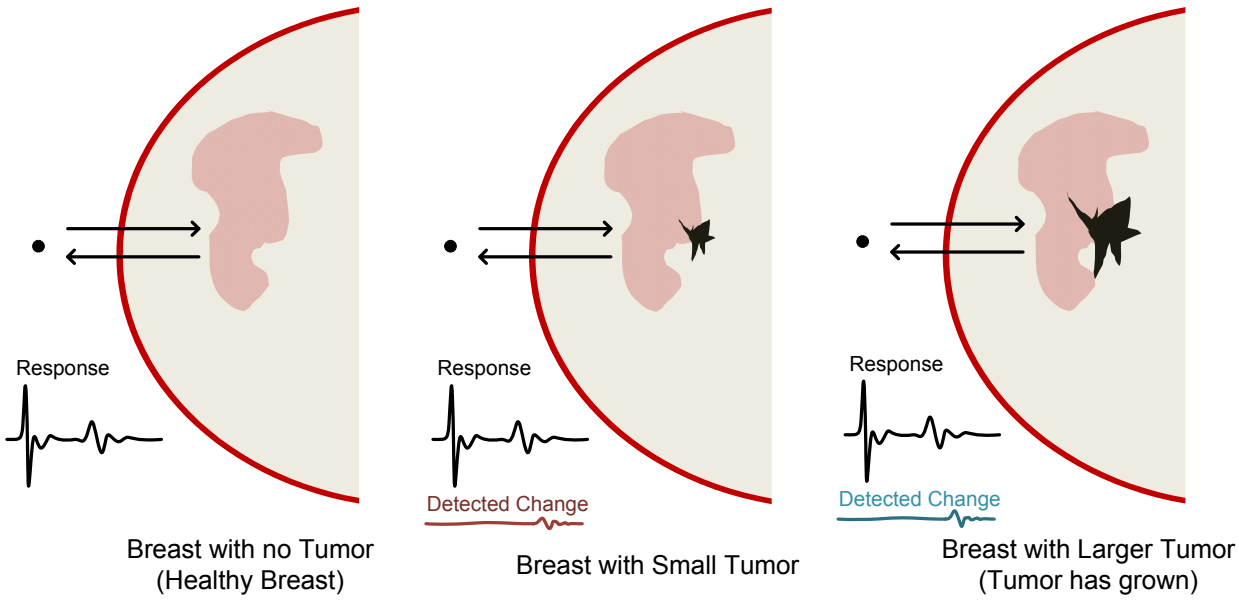

Figure 5.26 Illustration of three breasts at different stages which could provide changes in the UWB response.

Figure 5.27 shows an example of time-domain responses simulated with Model C3, which consists of inhomogeneous breast with fibroglandular tissues surrounding the tumor. In the plot, the bistatic responses, $x_{1,2}(t)$, simulated with and without tumor are shown. Notice a large skin response followed by small responses from inside the breast. A very small difference with respect to the skin reflection is observed in the breast responses, indicating a change in the response due to the tumor. By subtracting the response, a relatively small time domain signal which corresponds to the tumor response is obtained. Applying this subtraction to other responses in the multistatic data, change detection can be made into position-time plots. Figure 5.28 shows the position-time plots from Fixed Transmit Scan (scan Type 2) of Models S2, S3, C2, and C3. For each model, the first and second plots from the left are the preprocessed (antenna coupling removed) responses with and without the tumor shown in log scale. The plot on the right is the subtracted response shown in linear scale. For all four models, it is very hard to visually distinguish any change between the position-time plots since the tumor response is subtle. However, the subtracted response plot clearly shows the change, with the relative time delay between the first peaks in a good agreement with the expected electrical location of the tumor (indicated by red dashed line).

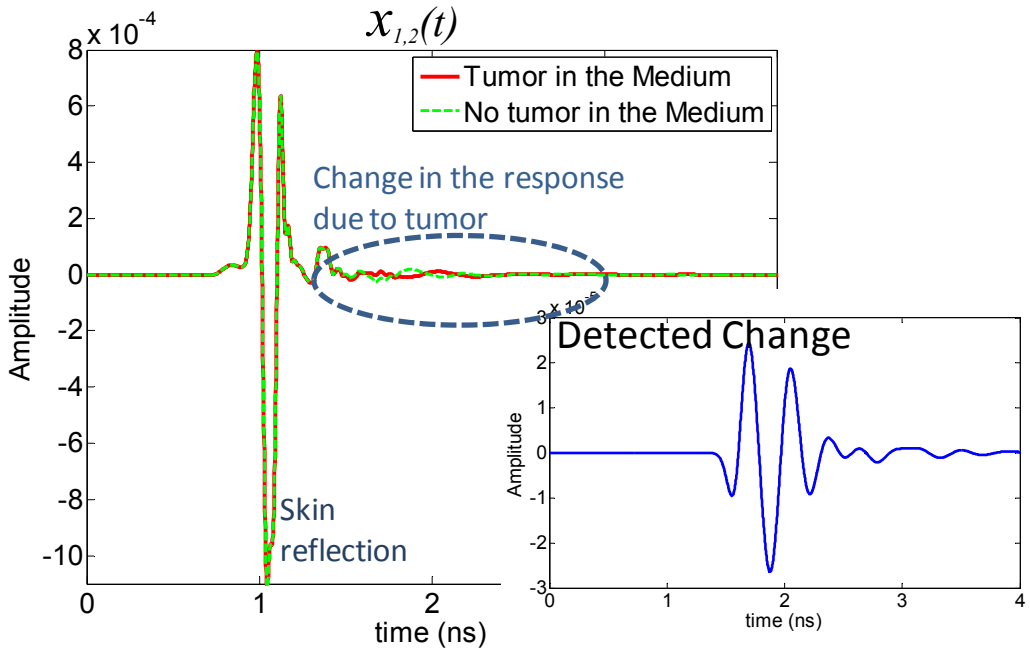

Figure 5.27 Change detection from simulated breast responses from Model C3 through subtraction of the responses with and without the tumor. The response shown in the figure is $x_{1,2}(t)$.

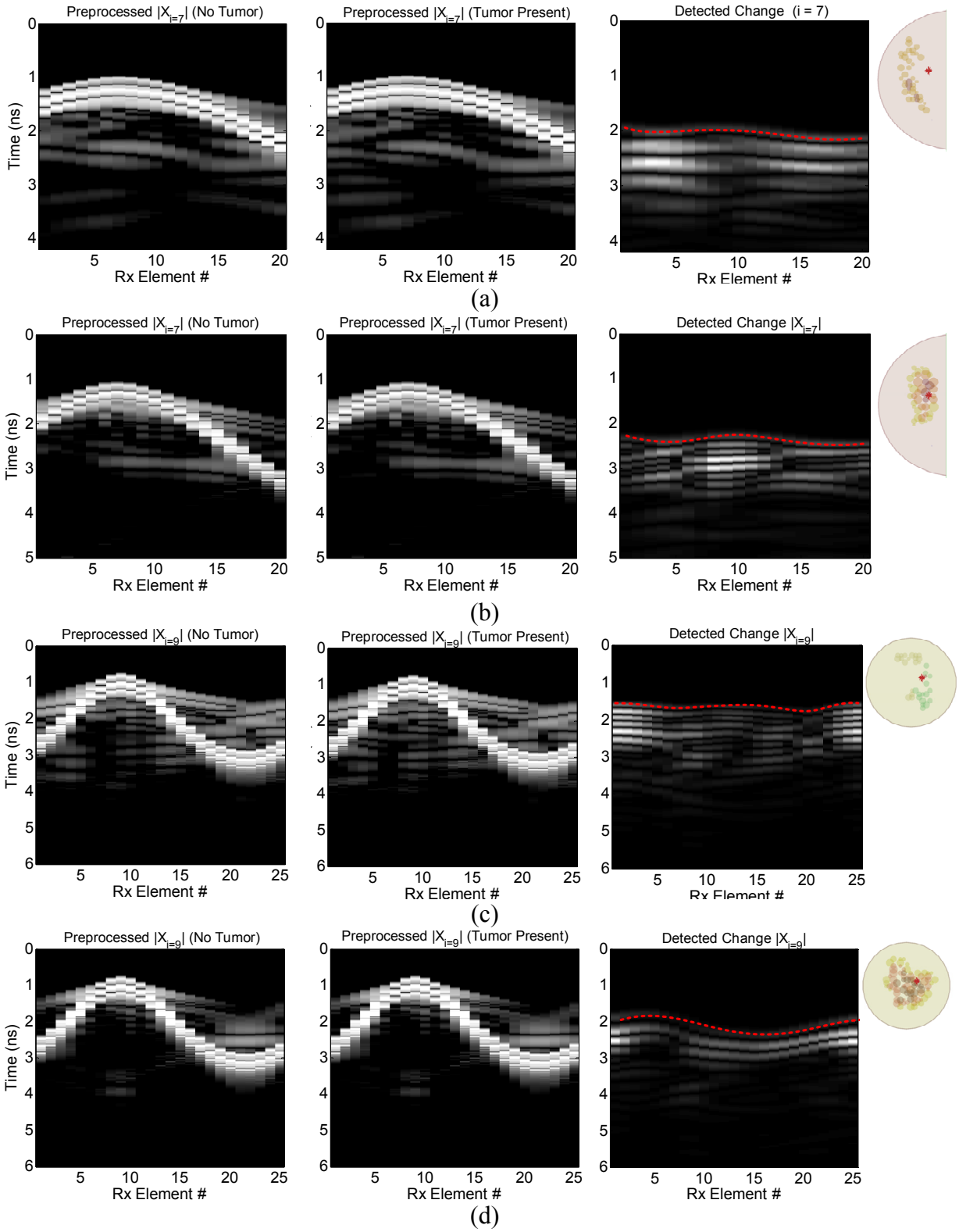

Figure 5.28 Position-time plots from Fixed Transmit Scan of the responses simulated with (center) and without (left) tumor and the subtracted response (right) for: a) Model S2, b) Model S3, c) Model C2, and d) Model C3. The red dashed line indicates the electrical location (peak time delays) of tumor.

Responses measured at different stages of tumor could provide information regarding the changes in size and resonances, which can also be useful. Detected changes between the current measurement and the first measurement (no tumor) should correspond to the absolute response of tumor at current state, which can be used to estimate the tumor resonances for use in hyperthermia treatment. Detected changes between the current and previous measurements correspond to relative changes occurred in the tumor parameters over the screening interval. Monitoring relative changes in the amplitude would be a way to determine any changes in tumor size since a larger size would provide some increase in the scattering amplitude as well as a shift in the resonances. Figure 5.29 shows the detected changes in Moving Transmit Scan plots of the simulated responses of Model C3. In the left plot, the changes between 6mm tumor and no tumor cases is shown. In the center plot the change between 12mm tumor and no tumor cases is shown. These two plots indicate the absolute tumor response at each state since the change is obtained with respect to the tumorless case. The plot on the right shows the change between 12mm tumor and 6mm tumor cases, which corresponds to a relative change between the two cases.

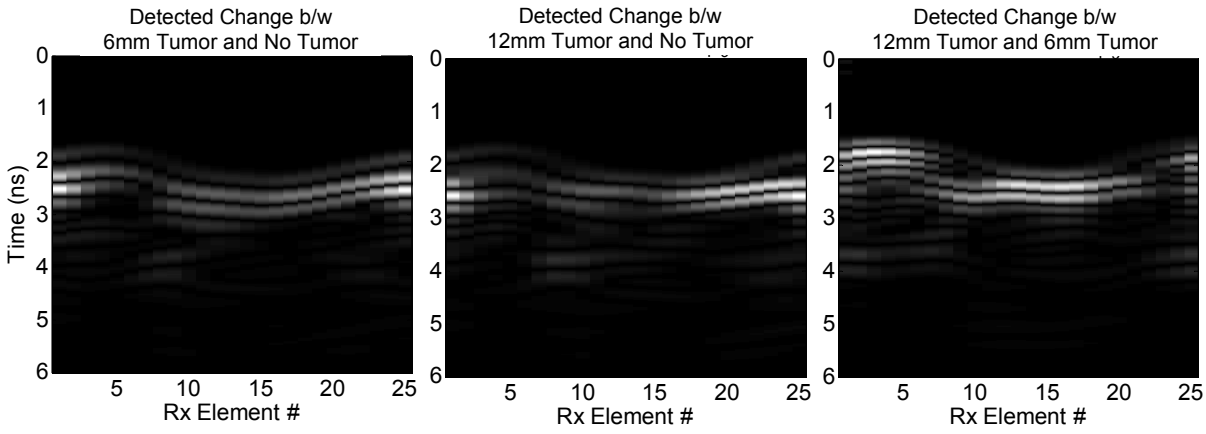

Figure 5.29 Detected changes in position-time plots (Moving Transmit Scan) of simulated responses of Model C3: Change between 6mm tumor and no tumor cases (left), change between 12mm tumor and no tumor cases (center), and change between 12mm tumor and 6mm tumor cases (right).

5.4 Dielectric Contrast Enhancement for Highly Cluttered Breast

Another approach to improve the detection and extraction of tumor responses is by altering the dielectric property of tumor via infusion of contrast agents, which would allow differential responses to be obtained between before and after the contrast agent is applied [28-30]. This is similar to change detection in a sense that they both use differential response between two different states to detect the tumor response. However, this approach does not require measurements taken between long time intervals.

Recent studies have shown that dielectric properties of tumor can be altered in the presence of microbubble or nanoparticles [30, 32]. It was reported that when injected such particles can passively accumulate at the boundary or in the tumor via enhanced permeability and retention effect in tumor blood vessels [30]. Assuming that significant changes are made only at the tumor by such agents, the differential responses obtained between before and after the infusion of contrast agents would only consist of the tumor response. The use of microbubbles seems to reduce the dielectric properties of tumor by 15-30% [28, 32], while the use of single-walled carbon nanotubes (CNTs) increases the dielectric properties of tumor by up to 37% (81% in effective conductivity). For a tumor surrounded by fibroglandular tissues, the use of microbubbles would decrease the tumor dielectric property to a level similar to the surrounding tissues. Hence, the differential response between before and after the infusion of microbubbles would be close to that obtained by subtracting the tumorless response. On the other hand, a differential response obtained by using CNTs indicates relative changes between two different tumor states rather than the response obtained by subtracting the tumorless case. For resonant scattering analysis to obtain tumor resonances, it would be more suitable to use microbubbles that reduce the tumor dielectric values close to surrounding medium. That way, it would provide the background subtracted response corresponding to the absolute tumor response.

Figure 5.30 shows grayscale maps of dielectric constants used in Model C3 at 2GHz as an example. The plot on the left shows the original dielectric property of the tumor based on the value from Table 5.1. Here we assume that microbubbles are used, indicating a decrease in the dielectric property of tumor to a value close to that of surrounding tissues. Hence, the center and the right plots show the tumor dielectric constant reduced to 15% and 30%, respectively. The location of the tumor is indicated by a red circle. Based on this scheme, the tumor responses are simulated using these values and the differential responses are obtained. The change in the tumor

dielectric properties is assumed to be uniform throughout the tumor without any changes in the tumor geometry. Figure 5.31 shows one of the time-domain differential responses obtained from Model C3, in particular $x_{1,23}(t)$. In Figure 5.31a, the responses are shown in relative amplitude scale with respect to the maximum of the three differential responses obtained from: 30% decrease in dielectric, 15% decrease in dielectric, and tumorless responses. The amplitude of the differential response from 15% decrease is very similar to that obtained by subtracting the tumorless response. This is because of the tissues surrounding the tumor are mostly low fat tissues with the dielectric property close to 15% lower than that of the tumor, resulting in a dielectric condition similar to that of the tumorless case. The amplitude of the differential response from 30% decrease is relatively larger, since a 30% decrease in the tumor dielectric would result in a value slightly lower than that of surrounding tissues. This makes some contrast to remain between the tumor and surrounding tissues, resulting in a larger change between the responses. In Figure 5.31b, the same responses are shown in normalized amplitudes. Notice that when the responses are normalized to 1, they are very similar, which indicates that the resonant scattering of tumor is primarily due to the external interaction at the boundary with the surrounding medium. The external resonance phenomena should remain relatively constant as long as the geometry is kept the same and there exists boundary condition as discussed in the previous chapter. Figure 5.32 shows Fixed Transmit Scan plots of differential responses for 30% (left) and 15% (right) decrease in tumor dielectric properties. Both plots are very similar and the relative peak occurrences match closely with the electrical location (red dash) of the tumor.

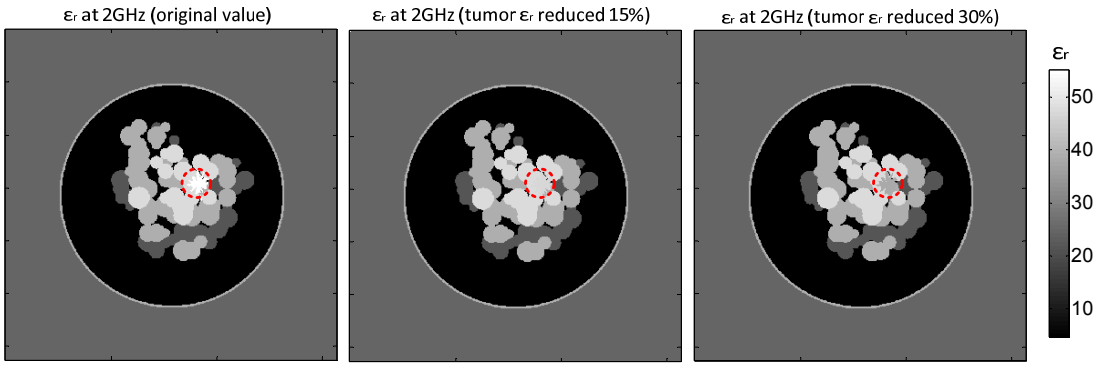

Figure 5.30 Maps of dielectric properties used in Model 3C at 2GHz with altered tumor dielectric constant, assuming the infusion of contrast agents (i.e.microbubbles). From left to right: original tumor dielectric constant, tumor dielectric reduced 15%, and tumor dielectric reduced 30%. The location of tumor is indicated by red circle.

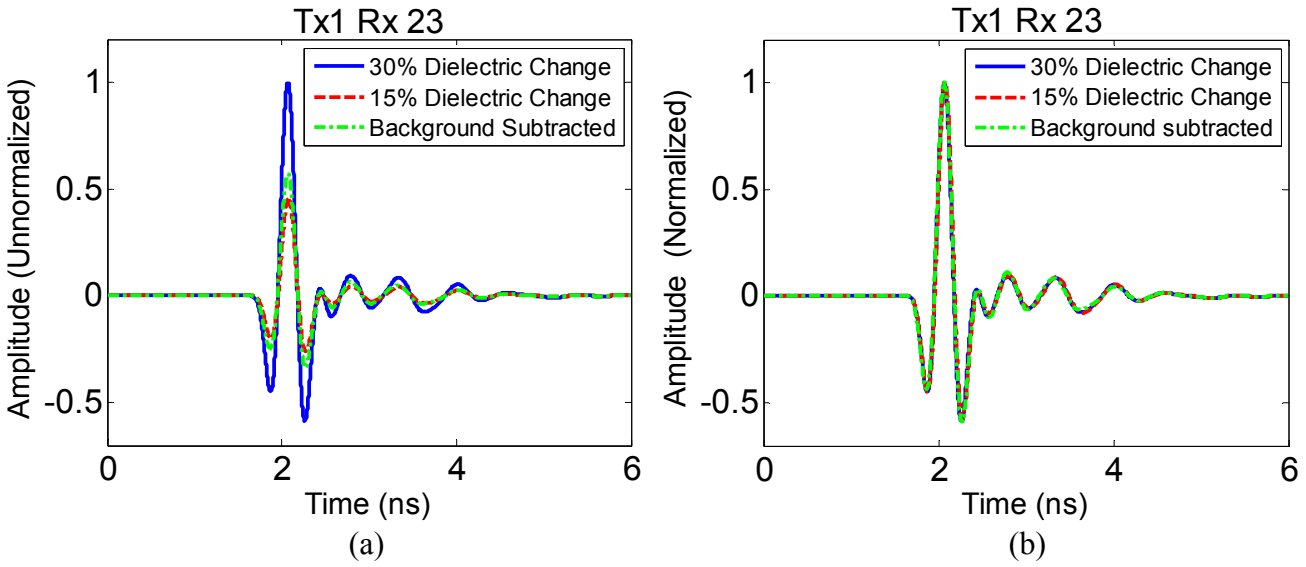

Figure 5.31 Time-domain differential responses obtained from Model C3, in particular $x_{1,23}(t)$, for 30% decrease in dielectric, 15% decrease in dielectric, and tumorless subtracted. Plot on the left shows the responses in relative amplitude scale with respect to the maximum of the three. Plot on the right shows the same responses normalized to 1.

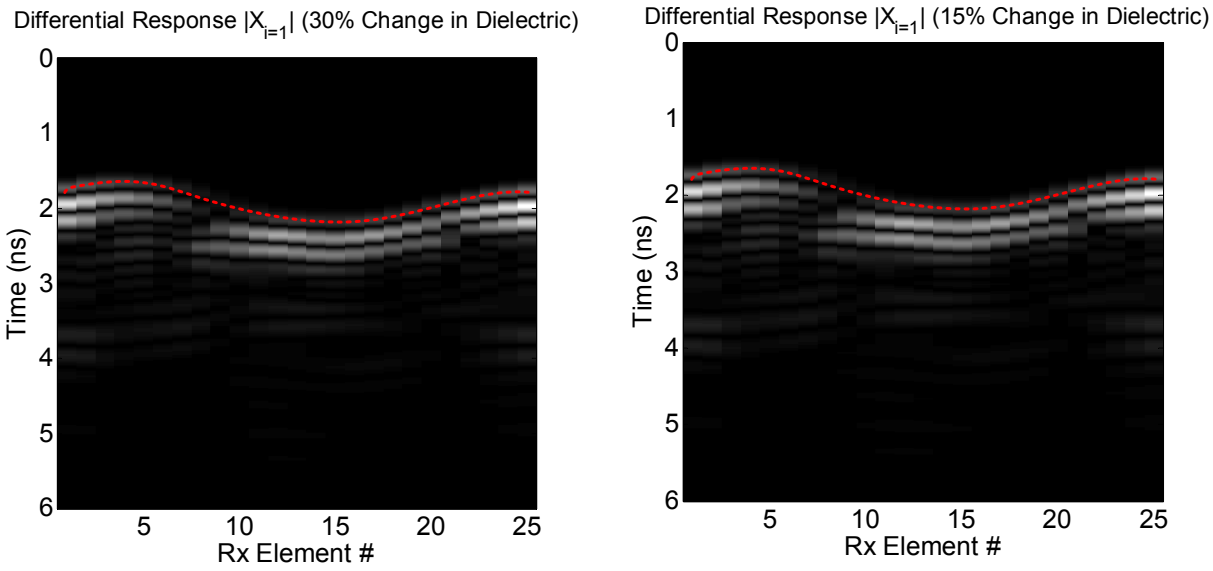

Figure 5.32 Position-time plots (Fixed Transmit Scan) of differential responses (with Tx element 1) in Model C3 simulated with 30% (left) and 15% (right) decrease in tumor dielectric properties.

5.5 Identification of Tumor Resonances and Location

Once the tumor responses are extracted either directly from the original preprocessed data, change detection, or contrast enhanced breast, the tumor-specific resonances and electrical location can be obtained using the approaches discussed in Chapter 4. The tumor resonances are obtained by applying the sliding-window matrix pencil method (MPM). The electrical location of tumor can be obtained either from the phase angle of complex residues or by obtaining the relative time delay between the specular peaks at each antenna location.

5.5.1 Tumor Resonance Extraction

The general procedure for extracting the tumor resonance is illustrated in Figure 5.33. After carrying out necessary preprocessing to remove antenna coupling and other unwanted responses, we assume that the tumor responses are accurately obtained through either one of the techniques discussed in the previous section. Whether directly from original preprocessed data, via change detection or through differential response (of contrast enhanced breast), the resulting multistatic responses can be used to estimate the tumor resonance. For K element array, the full multistatic data contains K^2 responses. While all of these responses can be used to estimate the poles, a set of responses corresponding to type-1 (Moving Transmit) or type-2 (Fixed Transmit) scan can be chosen to be evaluated. That is, one can use either $\mathbf{X}_{\mathrm{PT1}\_d}$ (Equation 5.6) or $\mathbf{X}_{\mathrm{PT2}\_i}$ (Equation 5.8), which are Moving Transmit Scan and Fixed Transmit Scan representations, respectively. Each set (for a given value of d or i) contains K responses that are received at different locations providing sufficient information to extract the resonances and electrical location of the tumor. Here we use the datasets from Fixed Transmit Scan to estimate the tumor resonances from the simulated responses. As shown in Figure 5.33 (results from Model S1 shown), the sliding-window MPM is applied to each of the responses in the data set. As a result N extracted pole sets are obtained. As discussed previously, the temporal presentation of extracted poles allows one to distinguish between the consistent poles that are likely to represent the resonances and the "curve fitting" poles which occur inconsistently as the window location changes. After eliminating some of the insignificant and seemingly spurious poles, the pole sets are then combined to generate an overall set of extracted poles. There can be few locations at which the extracted poles consistently cluster around. These locations should correspond to the tumor resonances, and the dominant (or the lowest) pole typically represents the fundamental resonance. After identifying

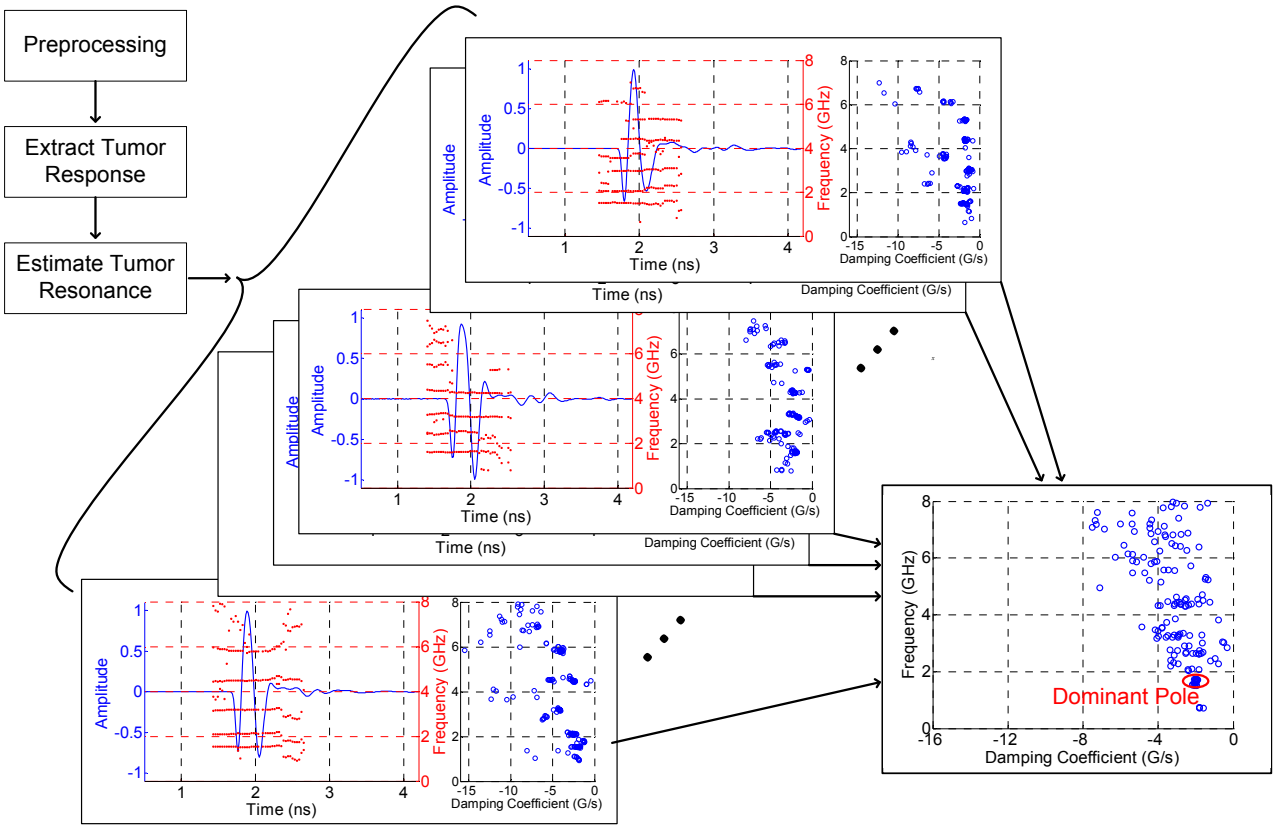

Figure 5.33 Illustration of extracting tumor resonances from multiple time domain responses.

the fundamental pole cluster, the final estimated pole value, s_o, can be obtained by simply taking average of the poles in the cluster.

Figures 5.34 through 5.37 show the extracted poles from the Fixed Transmit Scan data set of the simulated numerical models with various tissue configurations as shown in Figure 5.7 and 5.8. Figure 5.34 shows the pole plots obtained from the tumor responses ($\mathbf{X}_{\text{PT2\_9}}$, Fixed Transmit Scan data with element 9 used as transmit) in Models S1, S2, and S3, where a 3.5mm baseline radius tumor is used. Figure 5.35 shows the pole plots obtained from the responses in Model C1 with different tumor baseline radii, i.e. 3.5mm, 6mm and 9mm. Figures 5.36 and 5.37 show the pole plots obtained from the responses in Models C2 and C3, respectively, with tumor size varied in the same way as in Model C1. For the circular models, poles are extracted from $\mathbf{X}_{\text{PT2\_1}}$. For each model, a new variation of tumor shape was generated. The tumor responses evaluated here are obtained by subtracting the simulated tumorless responses. In the pole estimation

process from each time-domain response, the maximum number of estimated poles, *P*, is set between 20 and 30. The residue energy threshold of 1-5% was also applied to retain only the significant poles. Each pole plot in the figures is the combination of the poles extracted from *K* responses in the data set after eliminating some insignificant and spurious poles. In the plot the vertical axis is shown in GHz (Im{s}/2π), which is more relevant unit for a practical discussion. The horizontal axis is in damping coefficient which is simply Re{s}. The extracted pole generally have larger damping coefficients compared to highly resonant structures such as wires (shown in Figure 4.16), since the tumor and the tissue medium are lossy dielectrics that contribute to a faster damping of energy. This is also evident from the time domain responses shown in figure 5.33 where much of the signal decays shortly after the specular peaks.

In general clustering of poles is observed at several locations, which correspond to the estimated resonances. For each pole cluster, there seems to be more variation in damping coefficient (real axis) while the frequency part remains relatively constant. Such variation in damping constants in this case should be primarily from different amount of additional damping experienced at various aspect angles due to lossy tissue medium, as the amount of additional damping depends on the propagation distance and the effective conductivity in the propagation path. A similar observation was also made in the previous chapter where the poles estimated from multiple shots of noisy response showed more deviation in damping coefficient from the actual pole location than in oscillating frequency. It is also consistent with what was observed in statistical pole model by Joshi [33], where statistical modeling of noisy poles was discussed.

Since the purpose of extracting poles in this study is to use the tumor resonance as an operating frequency for hyperthermia treatment, we are primarily interested in the oscillating frequency rather than the modulus of the complex frequency, $|s_n|$, which is more related to the scatterer geometry. The damping coefficient, σ_o, indicates how fast the oscillation decays in time. If the poles were to be used for other purposes such as tumor classification as suggested by Chen and Yang et al. [16, 34], then σ_o becomes an important parameter since the location of the poles in the Laplace domain is determined by both σ_o and ω_o. In each plot from Figures 5.34-5.37, cluster of lowest order dominant poles are highlighted. These poles are likely to be the fundamental poles of the tumor. The mean values of the poles in the identified clusters are then obtained and used as the tumor-specific resonant frequencies for microwave focusing which is

presented in Chapter 6. In table 5.2, the mean frequency value obtained from the dominant pole cluster in each model is listed. In general the resonant frequency seems to decrease as the breast becomes denser with medium/low fat tissues. For example, in semicircular models S1, S2 and S3 the resonant frequencies obtained for 3.5mm tumor are respectively 1.63 GHz, 1.29 GHz, and 1.0 GHz. For circular models the same general trend is observed for all three tumor sizes simulated. Such behavior is due to a slowdown in wave propagation in the tissues surrounding the tumor as higher dielectric constant is introduced by adding more fibroglandular tissues. As the heterogeneity in the surrounding medium increases, the resonance phenomenon, especially the external resonance, is not only governed by the interaction at the tumor/tissue boundary, but also by other boundary conditions surrounding the tumor due to the tissue heterogeneity. Hence it becomes a "global" resonance rather than a local resonance at the tumor boundary.

To see how the resonant frequency of a spiculated tumor model compares with that of a perfect sphere (circle) model of the same baseline radius, a simulation was run with a 3.5mm circular tumor in Model S1. The dominant pole extracted in the same way described above for this perfect circle model is $\left[-2+j2\pi(1.53)\right]\times10^{9}$. In other words, the damping constant is -2ns^{-1} and the oscillating frequency is 1.53GHz. These values compare closely with the dominant pole of the spiculated 3.5mm tumor in Model S1, which has the damping constant of -2.2ns^{-1} and oscillating frequency of 1.63GHz as shown in Figure 5.34a. A slight shift is possibly due to the change in effective size due to spiculated geometry.

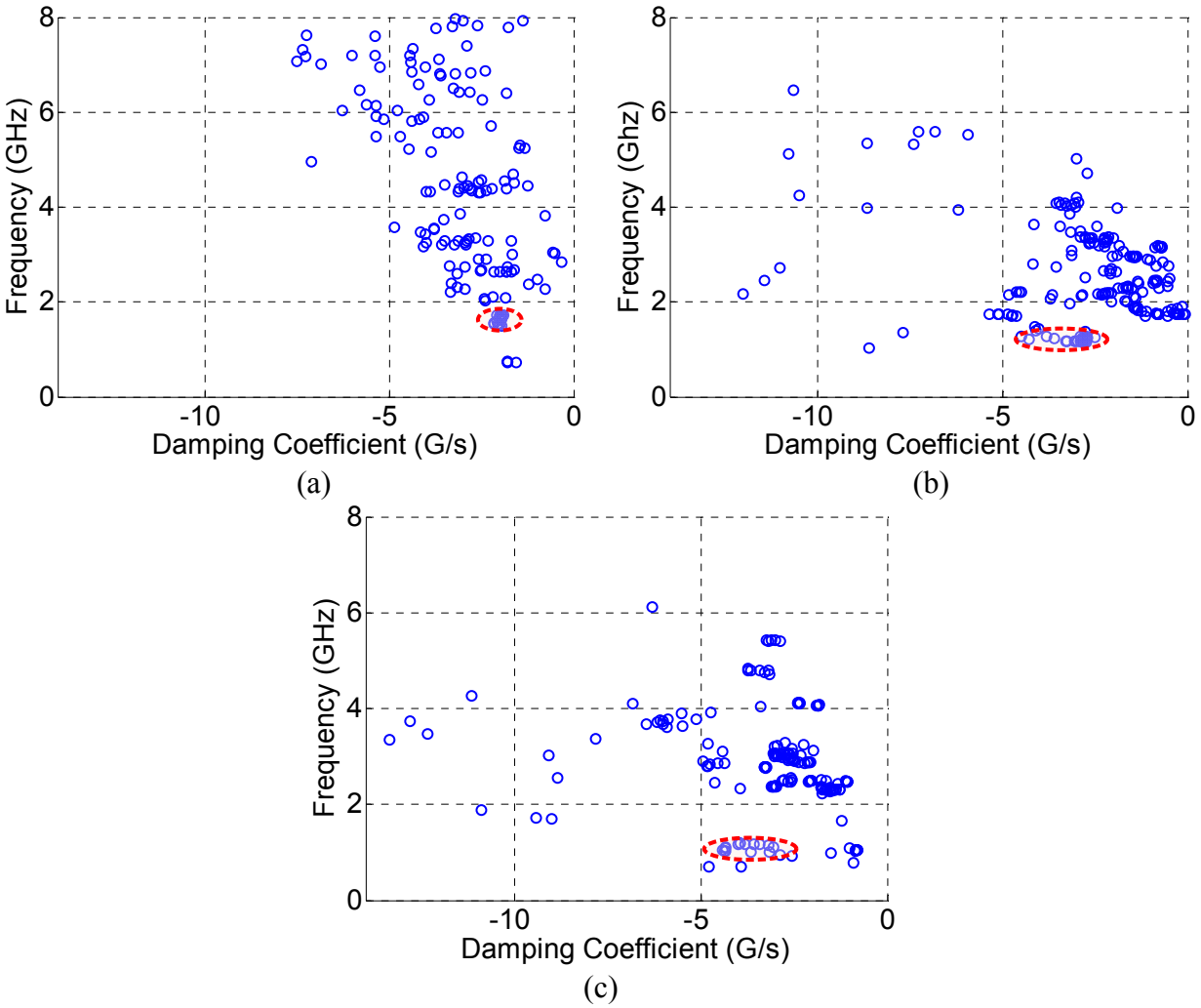

Figure 5.34 Poles extracted from simulated responses of: a) Models S1, b) Model S2, and c) Model S3. Fixed Transmit Scan dataset, $\mathbf{X}_{PT2\_9}$, is used for all three plots. Clusters of dominant poles are highlighted by red dashed ellipse.

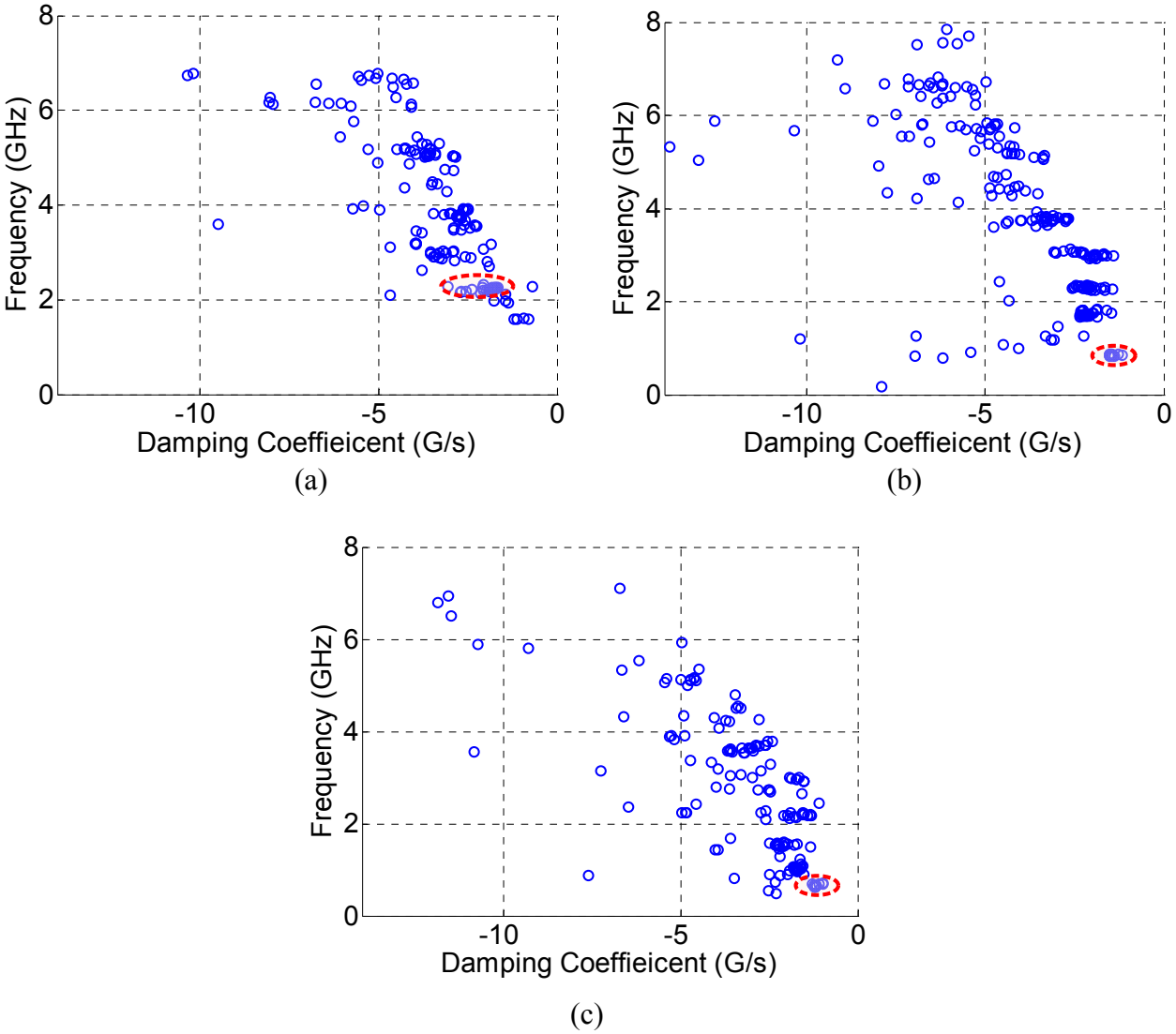

Figure 5.35 Pole extracted from simulated responses in Model C1 with various tumor baseline radii: a) 3.5mm, b) 6mm, and c) 9mm. Fixed Transmit Scan dataset, $\mathbf{X}_{PT2\_1}$, is used for all three plots. Clusters of dominant poles are highlighted by red dashed ellipse.

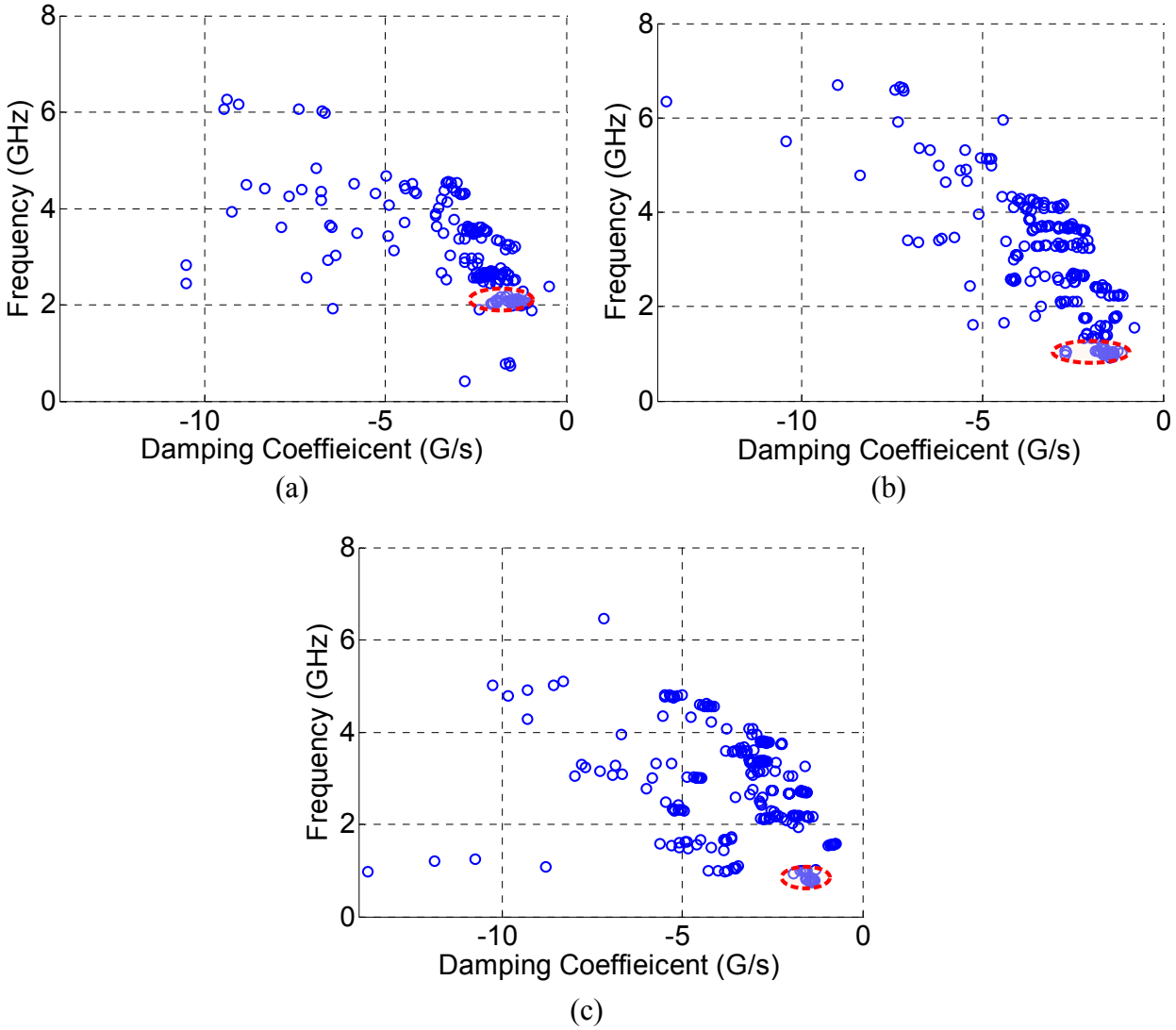

Figure 5.36 Pole extracted from simulated responses in Model C2 with various tumor baseline radii: a) 3.5mm, b) 6mm, and c) 9mm. Fixed Transmit Scan dataset, $\mathbf{X}_{PT2\_1}$, is used for all three plots. Clusters of dominant poles are highlighted by red dashed ellipse.

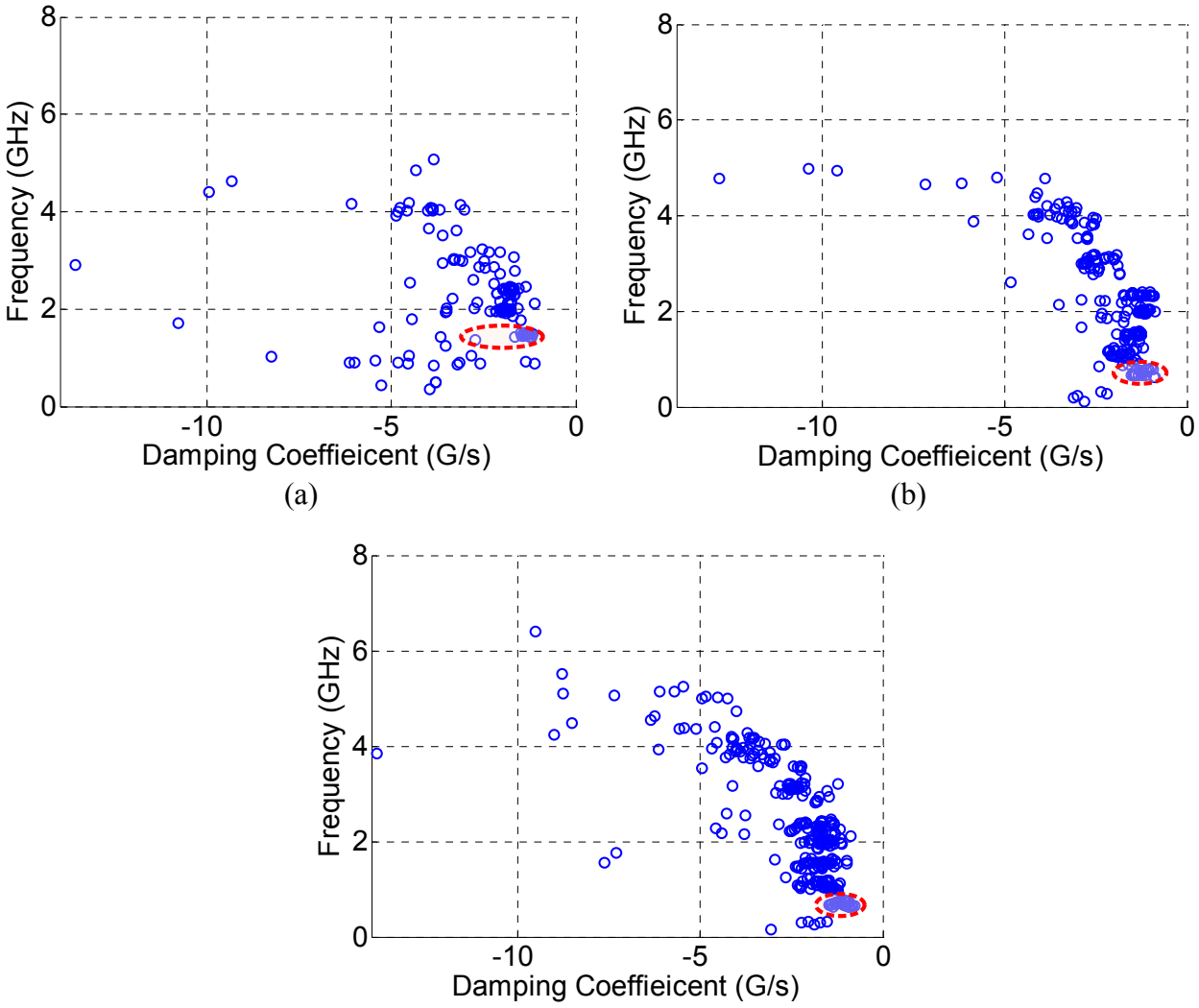

Figure 5.37 Pole extracted from simulated responses in Model C3 with various tumor baseline radii: a) 3.5mm, b) 6mm, and c) 9mm. Fixed Transmit Scan dataset, $\mathbf{X}_{PT2\_1}$, is used for all three plots. Clusters of dominant poles are highlighted by red dashed ellipse.

Table 5.2 Mean frequency value obtained from the dominant pole cluster in each model.

Model	Tumor Baseline Radius (mm)	Dominant Pole: $f_o = \mathrm{Im}\{s_o\}/2\pi$ (GHz)
S1	3.5	1.63
S2	3.5	1.29
S3	3.5	1.0
C1	3.5	2.2
	6	0.9
	9	0.7
C2	3.5	2.2
	6	1.0
	9	0.75
C3	3.5	1.55
	6	0.75
	9	0.7

5.5.2 Tumor Electrical Location

The electrical location of the tumor is the key parameter for microwave focusing. As previously discussed the electrical location basically represents the equivalent time-delay or phase shift at the tumor with respect to the antenna element locations.

Relative time delays between specular peaks in the responses received by elements represent relative differences in the path length from the tumor. Given accurate tumor responses obtained from the previous steps, relative time delays (with respect to the shortest delay), τ_j, are determined. Here the subscript *j* is the receiving element number. The time delays can then be converted into phase shift at frequency f_o determined from the tumor resonance as

$$\phi_j = 360\tau_j f_o \quad \text{(in degrees)}. \tag{5.9}$$

For a large tumor with multiple effective scattering points, the relative time delays could vary depending on the transmit element used, which in turn might result in a shifted focal spot. Limitation in using the pure time delay between the specular peaks also could occur when the responses are not as clean making it difficult to identify the specular reflection from the tumor.

The mechanism of the phase angles of complex residues (of extracted poles), $R_{i,j}$, is similar to that of the relative specular peak delays. As it was discussed in Chapter 4 (Equation 4.49), the phase angle in the complex residues in the SEM representation inherently includes the time delay term. However, since the SEM residues are associated with the resonance "turn on" time which occurs after the full body illumination by the incident wave, in principle the relative phase delays in residues are not affected by scatterer size and number of scattering points. This would also mean that the residue phase angle could still provide an accurate electrical location when the specular peak is not easily identifiable in the response.

Figures 5.38 through 5.41 show the plots comparing the equivalent phase angles (Equation 5.9) obtained from the relative peak time delays and the phase angles of residues of the poles (f_o) obtained from the previous subsection (Table 5.2). The figures and plots are arranged in the same order as in the pole plots from Figures 5.34-5.37. In each plot, the obtained phase angles are shifted to be aligned with each other without loss of any information since we are only interested in the relative phase delays (curve shape), not the absolute phase angle. The effective phase shift from peak time delays are shown in green curves with circles and the

residue phase angles are shown in red curves with squares. In Figure 5.38, which shows the results from semicircular models S1, S2 and S3 with 3.5mm tumor, the two curves in general follow closely with each other indicating both represent well the electrical location of tumor. In Figure 5.39, which show the results from Model C1 with different tumor sizes (3.5, 6, 9mm baseline radii from left to right), the two curves are in good agreement. Notice that the difference between the minimum and maximum phase angle decreases as tumor size increases. This is due to decrease in the tumor resonance frequency which results in a smaller relative phase delay. Figures 5.40 and 5.41 show the plots obtained from the results in Models C2 and C3, respectively, with tumor size varied in the same way as in Model C1. In these figures, the phase angles follow closely for 3.5 and 6mm tumor models. However, for 9mm tumor model, especially for Model C2, there seems to be significant discrepancy between the two curves, which is possibly due to shifted specular peaks from multiple effective scattering points resulting from large tumor as mentioned above. To determine which curve more closely represents the electrical location of the tumor, they are compared with the equivalent phase angles obtained from the relative time delays between the responses simulated by placing a source at the tumor (center point) as shown in Figure 5.43. In the figure the phase angle obtained from the residue follows more closely with the phase shift obtained from the source at the tumor, indicating that the residue phase angle more closely represent the electrical location of the tumor.

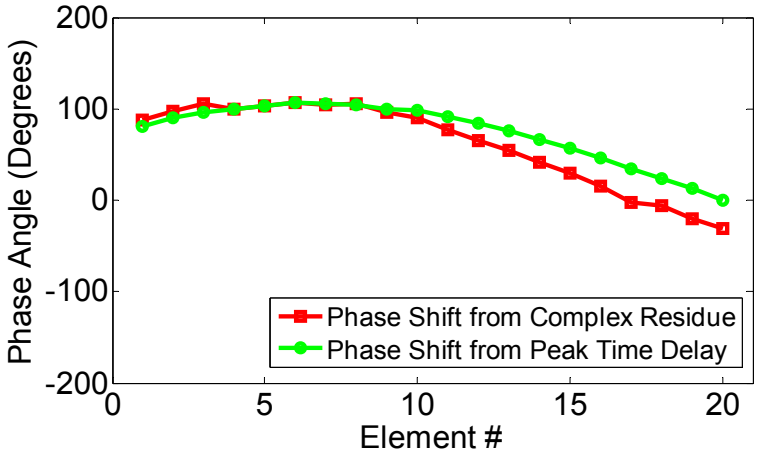

(a)

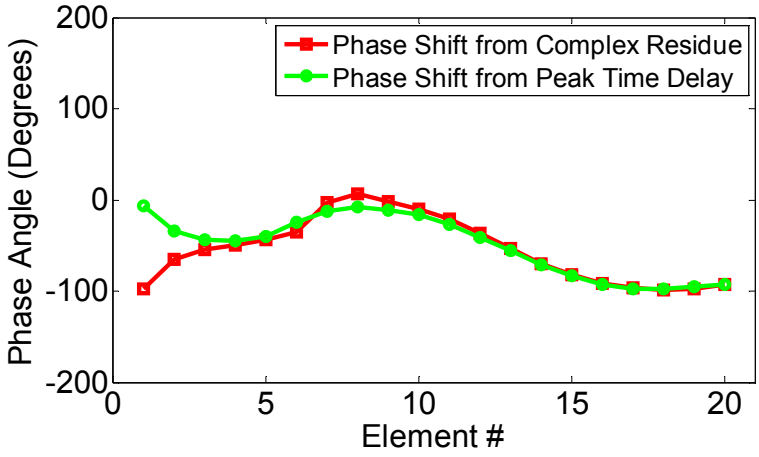

(b)

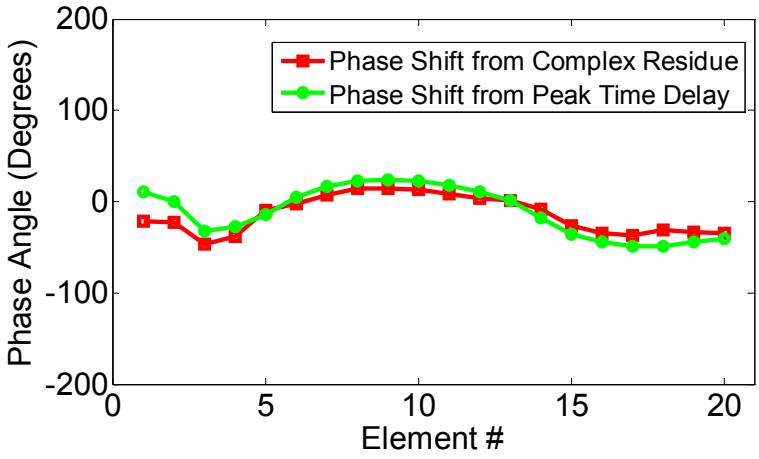

(c)

Figure 5.38 Phase angles obtained from the relative peak time delays and the phase angles of residues of the poles for: a) Model S1 at f_o=1.63GHz, b) Model S2 at f_o=1.29GHz, and c) Model S3at f_o=1.0GHz.

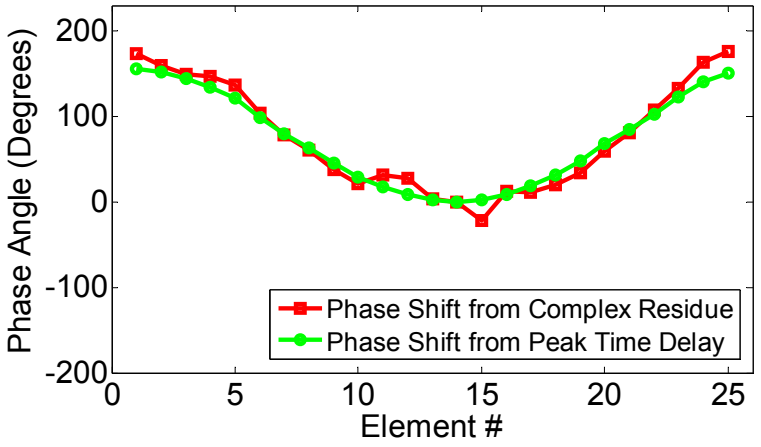

(a)

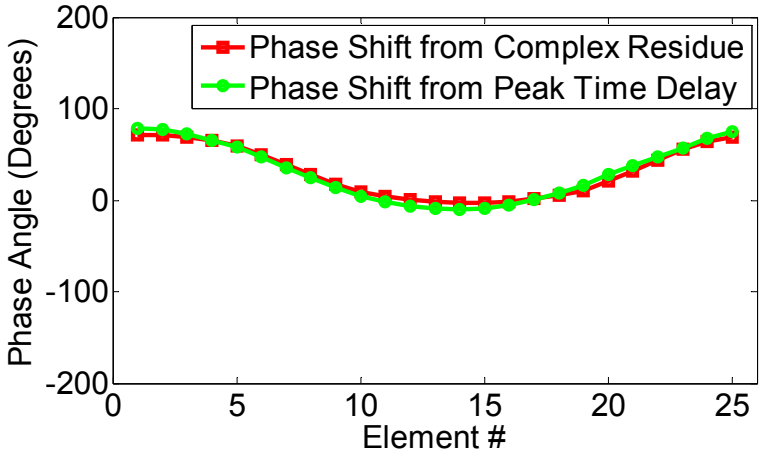

(b)

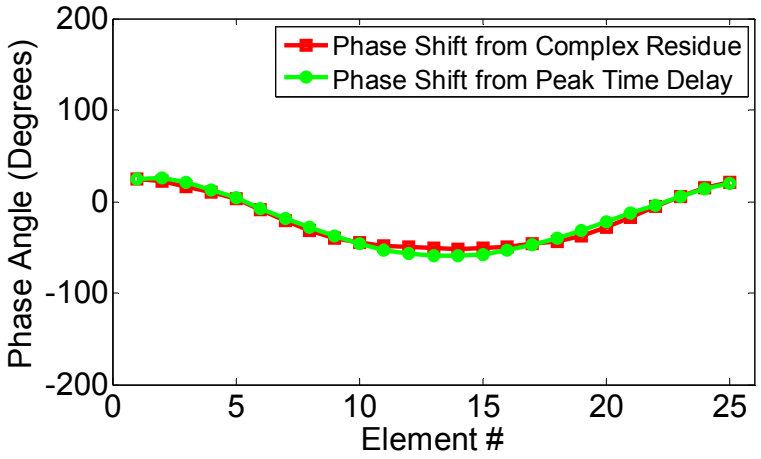

(c)

Figure 5.39 Phase angles obtained from the relative peak time delays and the phase angles of residues of the poles for Model C1 with: a) 3.5mm radius tumor at f_o=2.2GHz, b) 6mm radius tumor at f_o=0.9GHz, and c) 9mm radius tumor at f_o=0.7GHz.

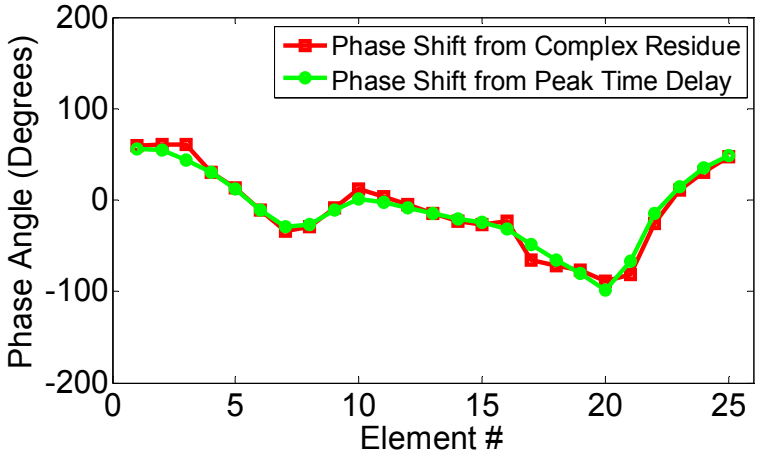

(a)

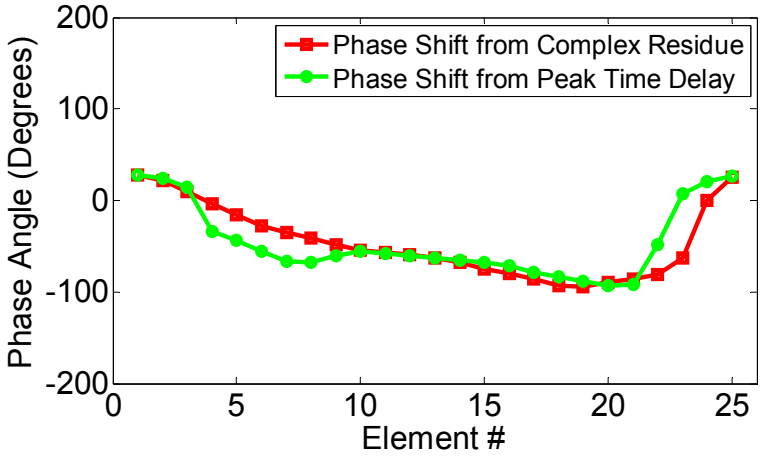

(b)

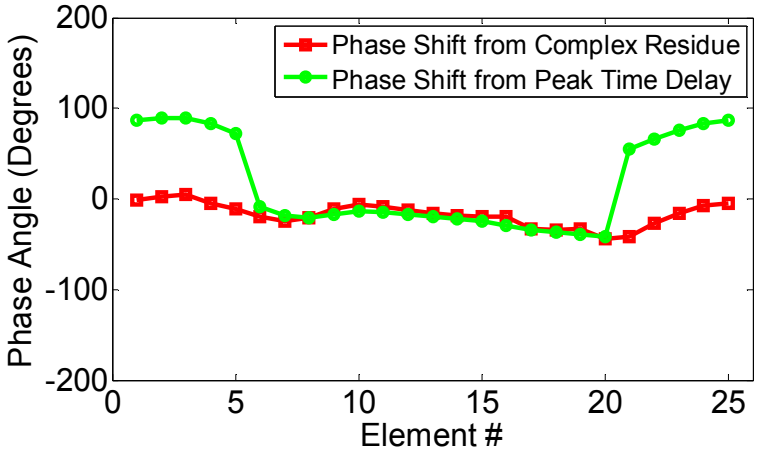

(c)

Figure 5.40 Phase angles obtained from the relative peak time delays and the phase angles of residues of the poles for Model C2 with: a) 3.5mm radius tumor at f_o=2.2GHz, b) 6mm radius tumor at f_o=1.0GHz, and c) 9mm radius tumor at f_o=0.75GHz.

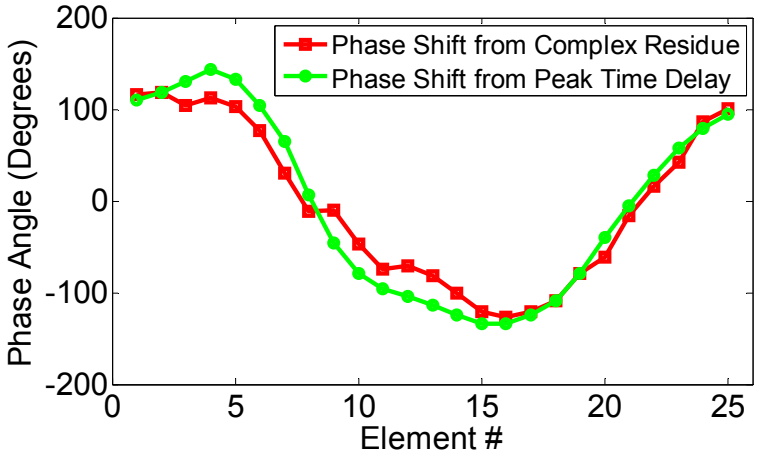

(a)

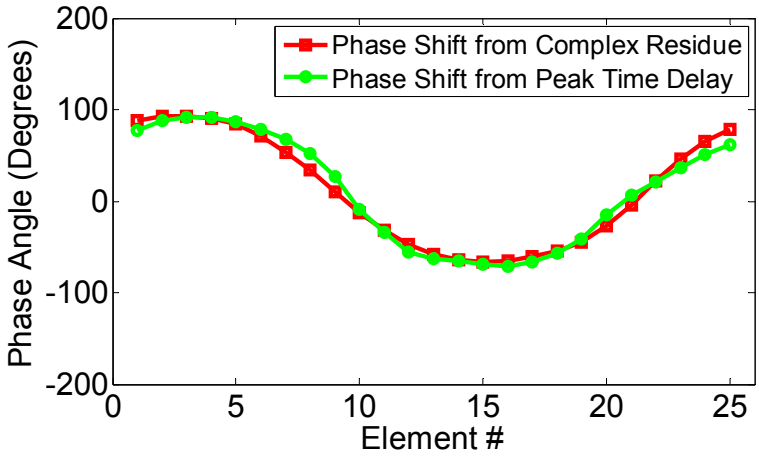

(b)

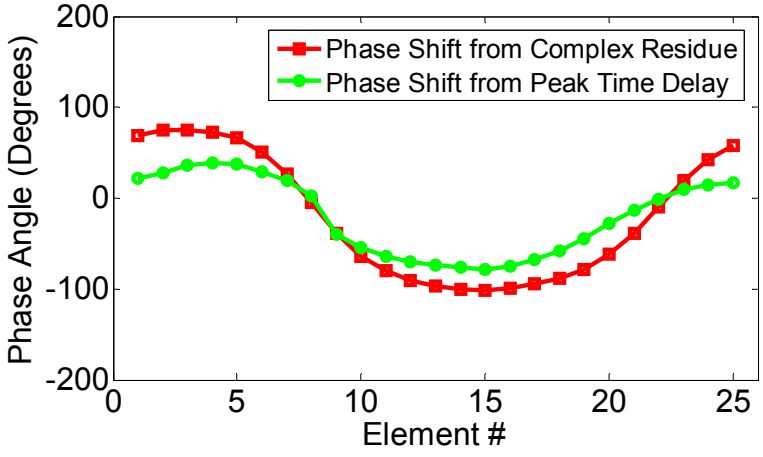

(c)

Figure 5.41 Phase angles obtained from the relative peak time delays and the phase angles of residues of the poles for Model C3 with: a) 3.5mm radius tumor at f_o=1.55GHz, b) 6mm radius tumor at f_o=0.75GHz, and c) 9mm radius tumor at f_o=0.7GHz.

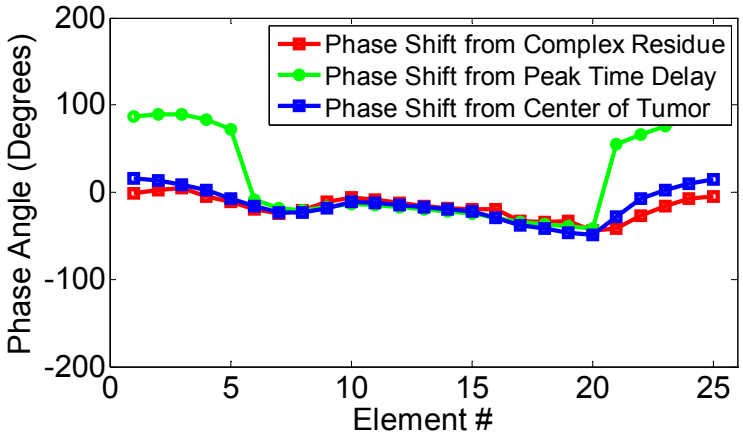

Figure 5.42 Comparison of the phase angles obtained from the relative peak time delays and the phase angles of residues of the poles for Model C2 with 9mm radius tumor with the phase angle obtained from the time delays between the responses simulated by placing a source at the tumor.

5.6 Simplified Experimental Model

A simplified apparatus was designed to carry out an experimental demonstration of the concept. The objective was to perform a 2D-like experiment with homogeneous medium for a simplified demonstration. To this end a setup with electrically small vertical dimension (i.e. less than the wavelength at the highest frequency in the incident spectrum) was built. Figure 5.43 shows an illustration of the experiment. Figure 5.44 shows the dimensions used and the pictures of the setup. As shown in these figures, two aluminum plates were used to create electric walls at the top and bottom in much the same way as the numerical simulation was carried out. In between the plates, four walls of acrylic glass were placed and sealed to contain liquid tissue simulants. A thin rubber gasket (~0.2cm thickness and 5.5cm diameter) was used as the skin simulant. An eight-element monopole array was placed (fed from the bottom plate) around the skin simulant. Four probes were placed (fed from the top plate) between the center and skin simulant to monitor the focusing which will be discussed in the next chapter.

To create a breast tissue simulant, an emulsion of water and liquid paraffin oil was used as suggested in [35] by Leendertz et al. A liquid laundry detergent was used as emulsifying agent. The targeted dielectric constant was the average of the three tissue types from Figure 5.6 to generate an effective homogeneous tissue representing the breast. After a number of trials, a close value was obtained by using the proportion of 30% water, 60% liquid paraffin, and 10%

detergent. The tumor simulant was created using corn flour and water as suggested by Bindu et al. in [36]. The mixture of corn flour and water was heated in oven to generate a dough-like form. The dielectric values close to that of tumor from Table 5.1 (Debye model) was targeted. The key here is to generate significant contrast against the tissue dielectric property. With 35% corn flour and 65% water, a value close to that of Debye model was obtained. The measured dielectric properties of the tissue and tumor simulant are plotted in Figure 5.45 in comparison with those of the average (of three tissue types) and the tumor from the Debye model. In the figure, the dielectric constant and effective conductivity values are shown in the plots on left and right, respectively. Complex dielectric properties are measured using Agilent 85070E dielectric probe connected to Agilent N5230a PNA network analyzer, which determines the dielectric properties from S_{11} responses. Although the dielectric constant of the tumor simulant is not a very close match with that of the Debye model, it still provides significant contrast (up to 5:1) against the tissue simulant, which is sufficient to generate scattering.

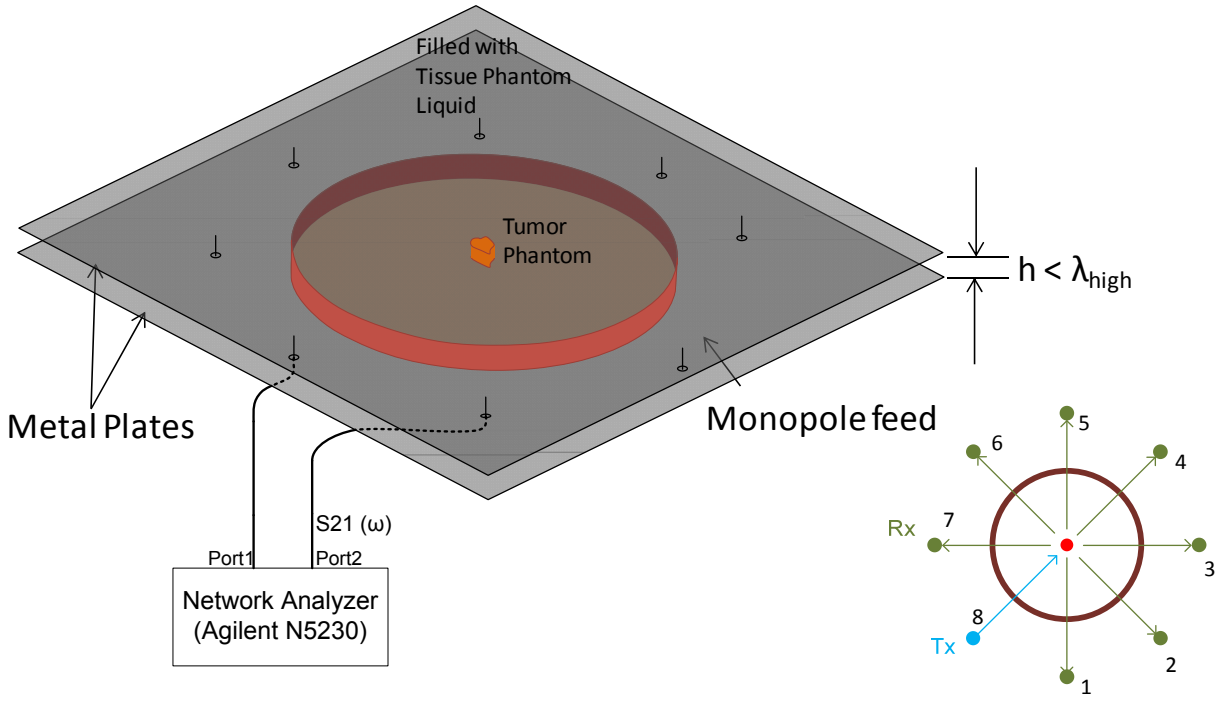

Figure 5.43 Illustration of the simplified experimental setup used.

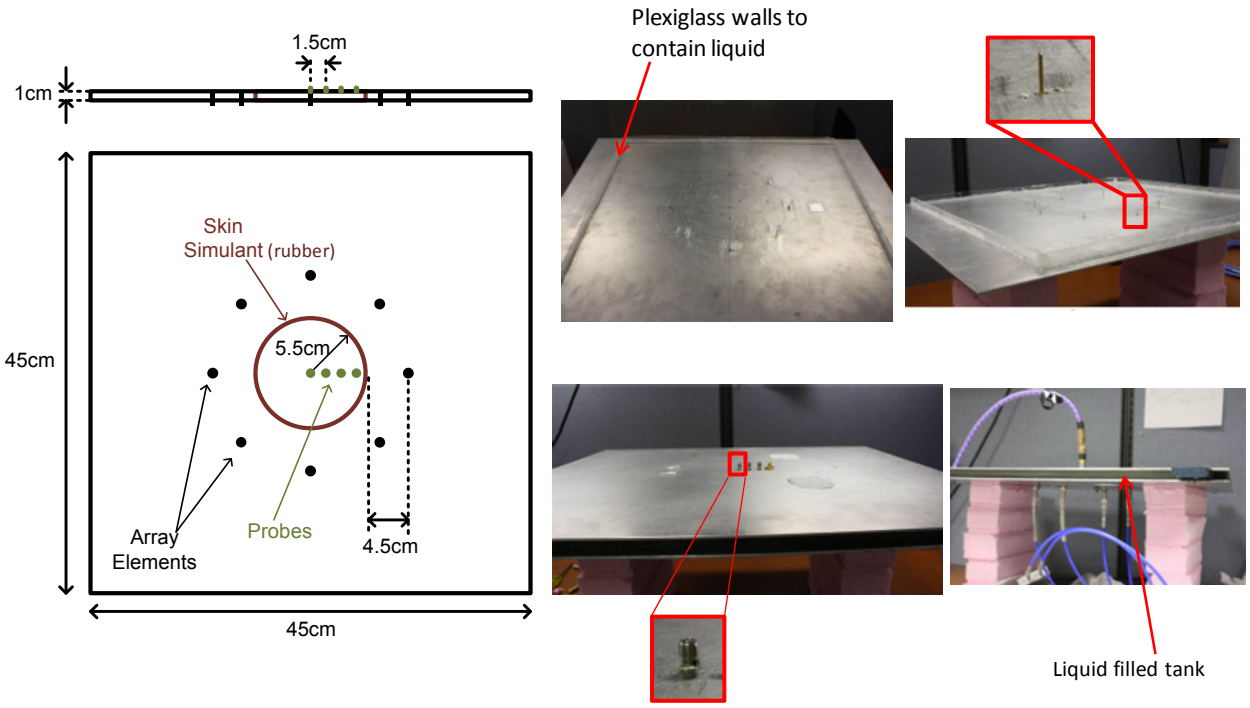

Figure 5.44 Dimensions used in experimental apparatus and pictures of the setup.

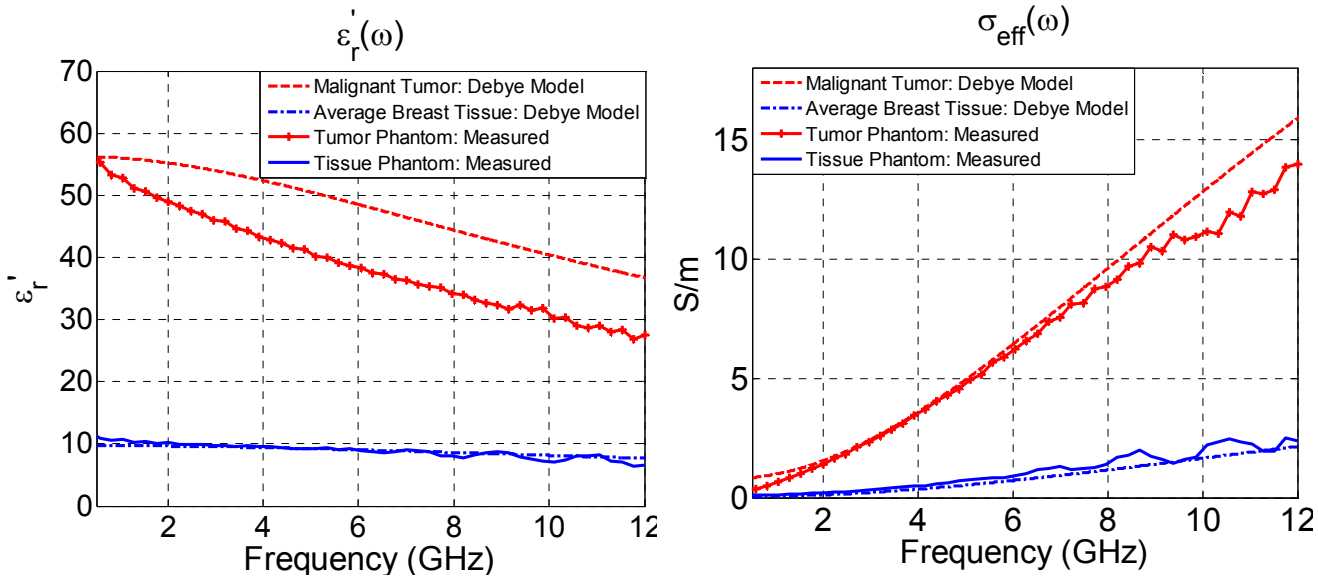

Figure 5.45 Measured dielectric properties of the materials used as tissue and tumor simulants. The values are compared with the Debye model values used in simulation.

The tissue simulant was filled in both inside and outside the skin, representing an ideal case of the coupling medium that perfectly matches the breast tissue medium. The tumor simulant was formed to have about 8mm baseline diameter. An attempt was given to make the shape of the tumor somewhat random rather than a smooth circular shape. Due to limited resources and instrumentation for focusing experiment, the tumor simulant was placed at the center location to eliminate the need for phasing each element. That is, since the tumor location is equidistant from all elements in the array, the focus would take place at the tumor location with the signals transmitted from all elements in phase. Hence the primary objective of the experiment was to demonstrate the tumor resonance extraction and evaluate the effectiveness of using the tumor resonance in comparison with other frequencies.

The tumor responses are measured using Agilent N5230a network analyzer via S_{21} frequency response. By manually switching the receive port, the S_{21} measurement was scanned across the elements in the array. The frequency was stepped from 0.3 to 10GHz at 1601 points. The frequency responses were then converted into time-domain through the inverse Fourier Transform. In order to accurately extract the tumor response, a tumor free measurement was made and subtracted from the response measured with the tumor in place. The responses measured through one of the bistatic pairs, i.e. $x_{8,2}(t)$, with and without the tumor are shown in Figure 5.46a. The points 1, 2 and 3 in the plot indicate the times at which the antenna coupling, skin reflection and tumor response occur, respectively. After subtracting the tumor free response, a time-gating was applied to obtain a clean signal corresponding to the tumor response as shown in Figure 5.46b.

Resonances are extracted using the sliding-window MPM. Temporal presentation of the resonant frequencies obtained at different sliding window location is shown in Figure 5.47a and the Laplace domain plot of the same in complex poles are shown in 5.47b. In this pole extraction process, the maximum number of poles, P, is set to 30 and residue energy threshold of 1-5% was used to retain the significant poles. The dominant resonance frequency, $f_o = \mathrm{Im}\{s_o\}/2\pi$, was obtained to be 1.65GHz. Using this frequency as the identified tumor resonance, focusing experiment was performed to investigate the effectiveness of using the resonant frequency in comparison with other frequencies. The procedure and results of the focusing experiment are presented in Chapter 6.

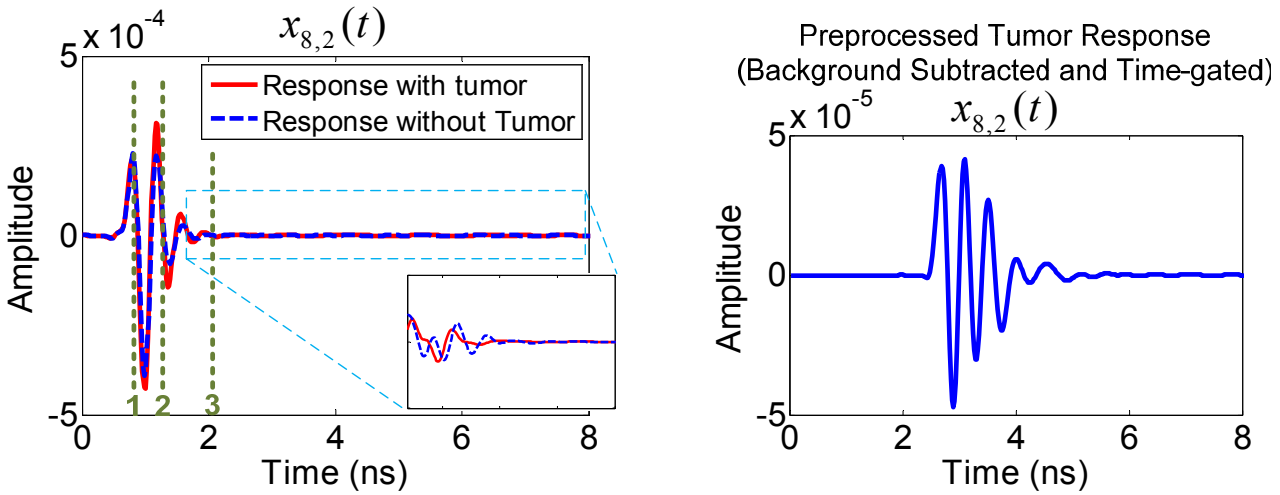

Figure 5.46 a) The equivalent time-domain responses measured through one of the bistatic pairs, i.e. $x_{8,2}(t)$, with and without the tumor, and b) Tumor response obtained after subtracting the tumor free response and time-gating.

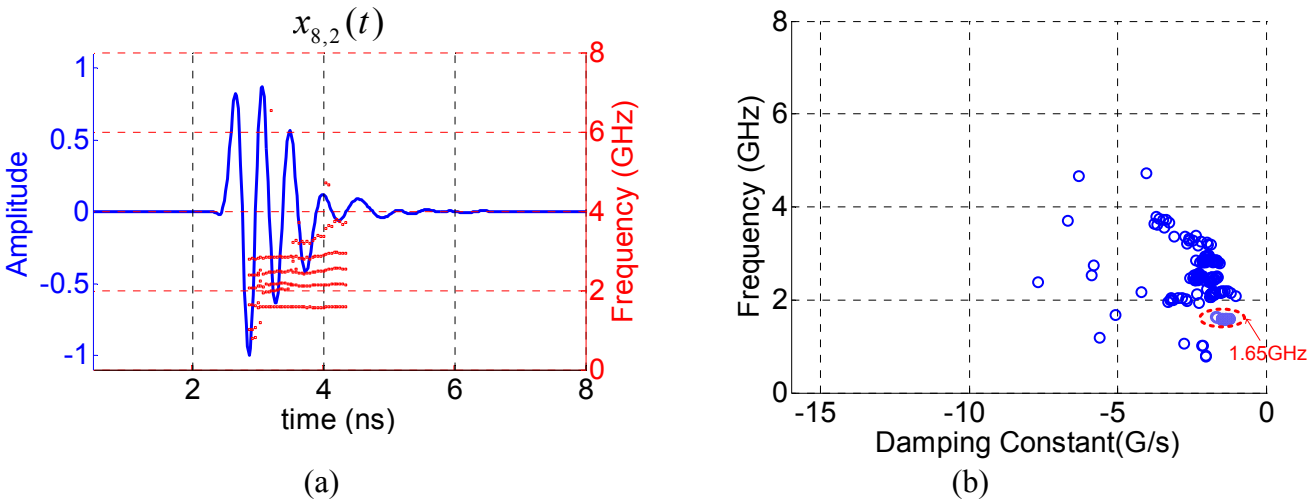

Figure 5.47 a) Temporal presentation of the extracted poles (frequencies) from the response by applying the sliding-window MPM to the tumor response, $x_{8,2}(t)$, and b) Laplace domain plot of the extracted complex poles.

5.7 Practical Considerations and Possible Additional Techniques

Since the objective of this study is to demonstrate the basic concept, the work presented in this chapter considered only two-dimensional models. The results are encouraging and the techniques presented here should be applicable to more realistic three-dimensional cases. However, there is no doubt that realistic cases will be more complicated with some limitations. For this reason, it is important to briefly discuss practical issues that will need to be addressed. Possible techniques to exploit some feature that are only inherent to three dimensional cases are also discussed.

a. Antenna Response

In a realistic three dimensional scenario, the array consists of actual antenna elements. Antennas, as any other finite structures, have their own characteristic responses which might generate some unwanted resonances, hereafter referred to as the antenna ringing. That is, the antenna ringing will be inherently convolved with the measured tumor responses. Hence it is important to mitigate such effects, especially for tumor resonance estimation since the characteristic resonances of antennas might overshadow the tumor resonances.

By properly designing the antennas one can significantly reduce the antenna ringing. TEM horns are known to have an impulsive response with almost no ringing [37]. Vivaldi antenna could also be a good design to use. The response is not as impulsive as that of TEM horns due to its hybrid type of operation between the TEM horn and dipole antenna [37], which means that some ringing is present in the impulse response. However, such ringing can be very low which in turn might not affect the tumor response. Also, modifications to the design can be made to further reduce the ringing. Resistively loaded ultra-wideband antennas are also effective in mitigating the antenna ringing. Resistive loading is equivalent to increasing the resistance value in an RLC circuit to reduce ringing by damping the resonant response. This approach could be useful when there is antenna size limitation. The use of such antennas was demonstrated in [38, 39].

Deconvolution of antenna responses can also be carried out to mitigate the antenna response. Impulse responses of the antennas measured in advance in the same medium used for breast measurements can be deconvolved in the post processing. Deconvolution of antenna impulse responses has shown to be effective in removing the antenna ringing for scatterer characterization [33].

b. Dynamic Range

As shown in the plots throughout this chapter, the tumor response is very small in amplitude. Largely due to loss (conductivity) in the dielectric tissue medium and skin, the incident and scattered waves experience significant amount of attenuation which results in very low amplitude scattered responses. The tumor response amplitudes are observed to be up to 40dB lower than the amplitude of skin reflections. This indicates that the tumor responses could be as low as ~ 80-90dB lower than the incident transmit power. While signal to noise ratio can be significantly improved by averaging multiple shots and adjusting transmit power, dynamic range of a system being used must be large enough to cover the huge ratio between the incident and scattered amplitude.

c. Polarization

In the two-dimensional models presented in this chapter, only one polarization, TM_z (typically representing vertical polarization), was considered. While the results from the two-dimensional models qualitatively represent the problem without loss of generality, limitations exist in polarimetric aspect. Use of two orthogonal polarizations, i.e. vertical and horizontal, would allow one to measure cross-polarized responses. That is, a horizontally polarized scattered response induced by a vertically polarized incident pulse (and vice versa) can be measured. The polarimetric aspect could be important for breast tumors, since malignant tumors are shown to have more spiculated and random shapes, which could enhance cross-polarized scattering. In the work by Davis et al. [17], polarimetric aspect of the tumor responses is considered for use in distinguishing malignant tumors from benign tissues.

d. Statistical Algorithm for Tumor Resonance

In a practical scenario, the goal is to obtain and present the tumor resonance to the operator for detection and use in microwave focusing. As shown in the pole plots above, the extracted pole locations in Laplace domain seem to slightly vary depending on element locations and time-window positions in the sliding MPM. An algorithm based on statistical pole modeling as used by Joshi [33] can be useful in determining the pole clusters. By combining the sliding-MPM with the statistical approach, efficient and robust algorithm can be written for automated resonance extraction.

e. Combination with SEM-based classification

The SEM pole-based classification approaches used by Chen and Yang et al. [16, 34] can be readily combined with the techniques presented in this study. It would only require an extra step in the detection processing since the same poles are used for target classification. For an accurate classification of tumors between benign and malignant using the SEM poles, an extensive investigation is required to generate a robust library of pole data or trend data based on variety of tumor and tissue models.

5.8 Chapter Summary and Conclusions

With the primary goal of extracting the tumor resonance and electrical location, use of GPR-inspired position-time scans to detect tumor responses was introduced. Unlike other imaging techniques the position-time scan does not provide a focused image representing the physical location of the tumor, but rather presents a time-delay profile of the tumor responses at each receiver location in the array. The position-time scan could provide sufficient information for detection of tumor response after preprocessing. Change detection and the use of dielectric contrast agents were also discussed as alternative schemes to improve detection for heavily cluttered breasts. Both approaches seem to be effective in detecting tumor responses in cluttered breast tissues. However, since both schemes are based on obtaining differences between measurements, the key is the alignment of the responses taken at different times. A good calibration procedure and additional processing would be required for successful change detection and contrast response. Since it applies minimal processing, the position-time scan could potentially be used as a simple presentation of data similar to GPR B-scan displays, which is widely used in mine detection applications. Also, the position-time scan can easily be implemented as a precursory step before generating a focused image.

The tumor resonance extraction was presented using the sliding-window Matrix Pencil Approach. The temporal information of the extracted poles definitely contributes to a better extraction of the resonant poles of a tumor as opposed to the spurious poles. By combining the sliding-window MPM with a statistical approach, efficient and robust algorithm could be developed for an automated resonance extraction.

Determining the electrical location of a detected tumor was presented. Results have shown that both the complex residue phase angles and the relative time delays between specular

peaks in general effectively represent the tumor electrical location. In case of large tumor, residue phase angle seems to more closely represent the electrical location of the tumor.

In the following chapter, microwave focusing using the extracted resonance frequencies is presented. The performance of these tumor-specific resonances in dielectric-heating of the tumor in comparison to other frequencies is presented.

5.9 References

[1] X. Li and S. Hagness, "A Confocal Microwave Imaging Algorithm for Breast Cancer Detection," *IEEE Microwave and Wireless Components Letters,* vol. 11, no. 3, pp. 130-132, Mar. 2001.

[2] E. C. Fear, X. Li, and S. C. Hagness, "Confocal microwave imaging for breast tumor detection: localization of tumors in three dimensions," *IEEE Transactions on Biomedical Engineering,* vol. 49, no. 8, pp. 812-822, Aug. 2002.

[3] E. J. Bond, X. Li, S. C. Hagness, and B. D. Van Veen, "Microwave imaging via space-time beamforming for early detection of breast cancer," *IEEE Transaction on Antennas and Propagation,* vol. 51, no. 8, pp. 1690-1705, Aug 2003.

[4] P. Kosmas and C. Rappaport, "Time Reversal With the FDTD Method for Microwave Breast Cancer Detection," *IEEE Transaction on Microwave Theory and Techniques,* vol. 53, no. 7, pp. 2317-2323, Jul. 2005.

[5] SEMCAD X. EM Simulation Platform,. http://www.semcad.com

[6] J. L. Volakis, A. Chatterjee, and L. C. Kempel, *Finite Element Method for Electromagnetics*. New York, NY: Wiley-IEEE Press, 1998.

[7] R. F. Harrington, *Field Computation by Moment Methods*. New York, NY: Wiley-IEEE Press, 1993.

[8] K. S. Yee, "Numerical solution of initial boundary value problems involving Maxwell's equations in isotropic media," *IEEE Transactions on Antennas and Propagation,* vol. 14, no. 3, pp. 302-307, May 1966.

[9] A. Taflove and S. Hagness, Eds., *Computational Electrodynamics: The Finite Difference Time Domain Method*. Artech House, 2005.

[10] J. Berenger, "Perfectly Matched Layer for the FDTD Solution of Wave-Structure Interaction Problems," *IEEE Transaction on Antennas and Propagation,* vol. 44, no. 1, pp. 110-117, Jan. 1996.

[11] S. D. Gedney, "An Anisotropic Perfectly Matched Layer-Absorbing Medium for the Truncation of FDTD Lattices," *IEEE Transaction on Antennas and Propagation,* vol. 44, no. 12, pp. 1630-1639, Dec. 1996.

[12] J. A. Roden and S. D. Gedney, "Convolutional PML (CPML): An Efficient FDTD Implementation of the CFS-PML for Arbitrary Media," *Microwave and Optical Technology Letters,* vol. 27, no. pp. 334-339, Jun. 2000.

[13] R. F. Harrington, *Time-Harmonic Electromagnetic Fields*. New York, NY: Wiley-IEEE Press, 2001.

[14] M. Sonka and J. M. Fitzpatrick, Eds., *Handbook of Medical Imaging, Volum 2. Medical Image Processing and Analysis*. 2000.

[15] R. M. Rangayyan, N. M. El-Faramawy, J. E. L. Desautels, and O. A. Alim, "Measures of actuance and shape for classification of breast tumors," *IEEE Transactions on Medical Imaging,* vol. 16, no. 6, pp. 799-810, Dec. 1997.

[16] Y. Chen, E. Gunawan, K. S. Low, S. Wang, C. B. Soh, and T. C. Putti, "Effect of Lesion Morphology on Microwave Signature in 2-D Ultra-Wideband Breast Imaging," *IEEE Transaction on Biomedical Engineering,* vol. 55, no. 8, pp. 22011-2021, Aug. 2008.

[17] S. K. Davis, B. D. Van Veen, S. C. Hagness, and F. Kelcz, "Breast Tumor Characterization Based on Ultrawideband Microwvave Backscatter," *IEEE Transaction on Biomedical Engineering,* vol. 55, no. 1, Jan. 2008.

[18] M. Lazebnik, M. Okoniewski, J. Booske, and S. C. Hagness, "Highly Accurate Debye Models for Normal and Malignant Breast Tissue Dielectric Properties at Microwave Frequencies," *IEEE Microwave and Wireless Components Letters,* vol. 17, no. 12, pp. 822-824, Dec. 2007.

[19] M. Okoniewski, M. Mrozowski, and M. A. Stuchly, "Simple Treatment of Multi-Term Dispersion in FDTD," *IEEE MIcrowave and Guided Wave Letters,* vol. 7, no. 5, pp. 121-123, May 1997.

[20] M. Lazebnik, L. McCartney, D. Popovic, C. Watkin, M. Lindstrom, J. Harter, S. Sewall, A. Magliocco, J. Booske, M. Okoniewski, and S. Hagness, "A large-scale study of the ultrawideband microwave dielectric properties of normal breast tissue obtained from reduction surgeries," *Physics in Medicine and Biology,* vol. 52, no. pp. 2637-2656, 2007.

[21] M. Lazebnik, L. McCartney, D. Popovic, C. Watkin, M. Lindstrom, J. Harter, S. Sewall, A. Magliocco, J. Booske, M. Okoniewski, and S. Hagness, "A large-scale study of the ultrawideband microwave dielectric properties of normal, benign and malignant breast tissues obtained from cancer surgeries," *Physics in Medicine and Biology,* vol. 52, no. pp. 6093-6115, 2007.

[22] M. C. Converse, E. J. Bond, S. C. Hagness, and B. D. Van Veen, "Ultrawide-band microwave space-time beamforming for hyperthermia treatment of breast cancer. A computational feasibility study," *IEEE Transactions on Microwave Theory and Techniques,* vol. 52, no. 8, pp. 1876-1889, Aug. 2004.

[23] C. Rappaport, "Determination of Bolus Dielectric Constant for Optimum Coupling of Microwaves through Skin for Breast Cancer Imaging," *International Journal of Antennas and Propagation,* vol. 2008, no. pp. 1-5, 2008.

[24] E. C. Fear, P. M. Meaney, and M. A. Stuchly, "Microwaves for breast tumor detection?," *IEEE Potentials,* vol. 22, no. 1, pp. 12-18, Feb.-Mar. 2003.

[25] I. J. Klemm, J. A. Craddock, J. A. Leendertz, A. Preece, and R. Benjamin, "Improved Delay-and-Sum Beamforming Algorithm for Breast Cancer Detection," *International Journal of Antennas and Propagation,* vol. 2008, no. pp. 1-9, 2008.

[26] D. J. Daniels, Ed., *Ground Penetrating Radar*. London: IET, 2004.

[27] F. Yang and A. S. Mohan, "EM techniques for the detection of breast cancer," in *IEEE Antennas and Propagation Society International Symposium (APSURSI)*, Toronto, ON, 2010.

[28] J. D. Shea, P. Kosmas, S. Hagness, and B. D. Van Veen, "Contrast-Enhanced Microwave Breast Imaging," in *13th International Symposium on Antenna Technology and Applied Electromagnetics and the Canadian Radio Sciences Meeting*, Toronto, ON, 2009.

[29] Y. Chen, I. J. Craddock, and P. Kosmas, "Feasibility Study of Lesion Classification via Contrast-Agent-Aided UWB Breast Imaging," *IEEE Transaction on Biomedical Engineering,* vol. 57, no. 5, pp. 1003-1007, May 2010.

[30] A. Mashal, B. Sitharaman, X. Li, P. K. Avti, A. V. Sahakian, J. H. Booske, and S. C. Hagness, "Toward Carbon-Nanotube-Based Theranostic Agents for Microwave Detection and Treatment of Breast Cancer: Enhanced Dielectric and Heating Response of Tissue-Mimicking Materials," *IEEE Transaction on Biomedical Engineering,* vol. 55, no. 8, pp. 1831-1834, Aug. 2010.

[31] S. Grant and P. C. Oleson, "Breast Cancer Detection Research: Dual Use of Intelligence Technologies," *Studies in Intelligence,* vol. Semiannual Edition, no. 1, pp. 27-34, 1997.

[32] A. Mashal, J. H. Booske, and S. Hagness, "Toward contrast-enhanced microwave-induced thermoacoustic imaging of breast cancer: An experimental study of the effects of microbubbles on simple thermoacoustic targets," *Physics in Medicine and Biology,* vol. 54, no. pp. 641-650, 2009.

[33] G. Joshi, "Ultra-wideband Channel Modeling using Singularity Expansion Method," Ph.D. Dissertation, Virginia Tech, Blacksburg, VA, 2006.

[34] F. Yang and A. S. Mogan, "Complex natural resonances for breast tissues with complex morphology," in *IEEE International Symposium on Antennas and Propagation*, Spokane, WA, 2011, pp. 699-702.

[35] J. A. Leendertz, A. Preece, R. Nilavalan, I. J. Craddock, and R. Benjamin, "A liquid phantom medium for microwave breast imaging," in *Proceedings of 6th Congress of European Bioelectromagnetics Association*, Budapest, Hungary, 2003, p. 232.

[36] G. Bindu, A. Lonappan, V. Thomas, C. K. Aanandan, and K. T. Mathew, "Dielectric Studies of Corn Syrup for Applications in Microwave Breast Imaging," *Progress In Electromagnetic Research,* vol. 59, no. pp. 175-186, 2006.

[37] S. Licul, "Ultra-Wideband Antenna Characterization and Measurements," Ph.D. Dissertation, Electrical Engineering, Virginia Polytechnic Institute and State University, Blacksburg, VA, 2004.

[38] X. Li, S. Hagness, M. K. Choi, and B. D. Van Veen, "Numerical and Experimental Investigation of an Ultrawideband Ridged Pyramidal Horn AntennaWith Curved Launching Plane for Pulse Radiation," *IEEE Antennas and Wireless Propatation Letters,* vol. 2, no. pp. 259-262, 2003.

[39] M. Klemm, I. J. Craddock, A. Preece, J. Leendertz, and R. Benjamin, "Evaluation of a hemi-spherical wideband antenna array for breast cancer imaging " *Radio Science,* vol. 43, no. RS6S06, 2008.

Chapter 6 Microwave Focusing using Tumor-Specific Resonances

In this chapter, microwave focusing using the tumor resonance frequencies and electrical locations obtained in the previous chapter is demonstrated. Using the same numerical models from Chapter 5, focusing is simulated at the identified resonance frequencies as well as other frequencies for comparison. Measure of dielectric heating is evaluated via the power absorption density calculated using the simulated electric field (probed voltage for measurement). The results are analyzed by comparing the power absorption values in various ways to evaluate the performance. The results suggest that the tumor-specific resonance frequencies provide optimal performance. This would correspond to a faster temperature rise at the tumor resonances while minimizing the heating in other regions in the breast, indicating that more efficient microwave thermotherapy (hyperthermia) could potentially be achieved.

6.1 Microwave Focusing using Tumor Resonances and Electrical Locations

As previously mentioned, the key to an effective focusing of microwaves in the tumor is in phasing of the array. The phase shift at each element must accurately correspond to the electrical location of tumor. The extraction of the tumor resonance and the electrical location from the SEM parameters was demonstrated in the previous chapter. Using the tumor resonance (f_o) and phase angles (ϕ_n) obtained from the poles and residues (or peak-time-delay), microwave signals for each element can be generated. The signals fed into an array of *K* elements is represented in phasor form as

$$\mathbf{S} = \begin{bmatrix} |S_1| e^{j\phi_1} \\ |S_2| e^{j\phi_2} \\ \vdots \\ |S_K| e^{j\phi_K} \end{bmatrix} \tag{6.1}$$

where $|S_n|$ is the magnitude and ϕ_n is the phase shift at each element. The phase shifts are the conjugate angles of those corresponding to the electrical location. The amplitudes can be chosen to be uniform or weighted to compensate for the path loss and attenuation that could vary for each element location. Uniform amplitude versus weighted amplitude is discussed in Section 6.3. Figure 6.1 illustrates the general case of microwave focusing at the tumor. The time-domain form of the continuous-wave signal in Equation 6.1 is represented as

$$\mathbf{S} = \begin{bmatrix} s_1(t) \\ s_2(t) \\ \vdots \\ s_N(t) \end{bmatrix}, \qquad s_n(t) = A_n \sin\left(\omega_o (t - \tau_n)\right) \tag{6.2}$$

where $\omega_o = 2\pi f_o$ and $\tau_n = \phi_n / \omega_o$. The microwave signals can be pulsed, such that by adjusting the pulse parameters, i.e. pulse repetition rate (PRF) and pulsewidth (PW), the average power (P_{avg}) can be controlled given a peak power (P_{peak}) level as follows:

$$P_{avg} = P_{peak} \times PW \times PRF\,. \tag{6.3}$$

Since the measure of dielectric heating is determined by the average power, adjusting the pulse parameters provides an additional power control other than directly from the source. Ability to control microwave power is essential since the power level needs to be adaptively adjusted to ensure a desired therapeutic temperature level at the tumor. Phase control is also essential for adaptively adjusting the focus in case of a slight offset in the original electrical location used.

6.2 Measure of Dielectric Heating

As it was discussed in Chapter 2 the effective conductivity, σ_{eff}, determines the electromagnetic heating of dielectric tissues. The effective conductivity is related to the imaginary part of the complex permittivity (shown in Equation 2.1) as

$$\sigma_{eff} = \omega \,\mathrm{Im}\{\varepsilon\} = \omega \varepsilon_o \varepsilon_r^{"}\,. \tag{6.4}$$

One way to evaluate the dielectric heating in tissues is by examining the power absorption density (PAD). Here we consider a time-harmonic problem since a narrowband microwave focusing is used. At a given frequency, PAD represents the power absorbed (or dissipated) due to incident electric field acting upon the material and is directly proportional to σ_{eff} as follows:

$$\text{PAD} = \frac{\sigma_{eff} \left| E\left(\vec{r}\right) \right|^2}{2} \qquad \left(\frac{\text{W}}{\text{m}^3} \right), \tag{6.5}$$

where $E\left(\vec{r}\right)$ is the electric field. Note that PAD in the above equation is expressed in terms of time-averaged power. PAD is related to the specific absorption rate (SAR) as

$$\text{SAR} = \frac{\text{PAD}}{\rho} \qquad \left(\frac{\text{W}}{\text{kg}} \right), \tag{6.6}$$

where ρ is the density of the material. This shows that PAD and SAR essentially represent the same quality in different ways, i.e. PAD is the power absorption per unit volume and SAR is the power absorption per unit mass. The level of PAD values indicates the amount of temperature rise in the dielectric material [1]:

$$\text{PAD} = \rho \text{SAR} \sim \text{c}\rho \frac{dT}{dt}, \tag{6.7}$$

where c is the specific heat capacity and T is the temperature. We use PAD to evaluate the performance of dielectric heating in this work. PAD is an appropriate measure of performance as we are interested in a relatively straightforward measure of performance at the current stage of the research.

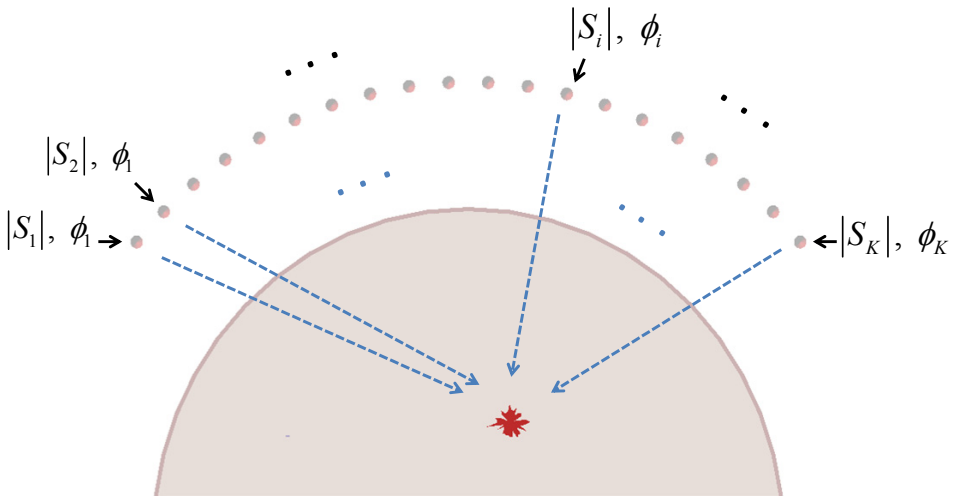

Figure 6.1 Illustration of the general case of microwave focusing at the tumor.

6.3 Results and Discussion

6.3.1 Numerical Simulation

Microwave focusing is investigated using the identified tumor resonance frequencies and other selected frequencies for comparison of performances in the heating of the tumor and focusing quality. The results in this subsection are simulated using uniform amplitudes fed into the array while the entire array elements are used (i.e. 20 elements for semicircular models and 25 elements for circular models). The same source power is used for all frequencies. After obtaining the electric field values from simulation, PAD values are calculated using Equation 6.5. For two-dimensional (TM_z) models considered here, Equation 6.5 becomes

$$\mathrm{PAD}(x,y)=\frac{\sigma_{eff}(x,y)\left|E_z(x,y)\right|^2}{2}, \tag{6.8}$$

where the quantities only vary in x and y and the electric field has only z component. Figure 6.2 illustrates the process of obtaining $\mathrm{PAD}(x,y)$.

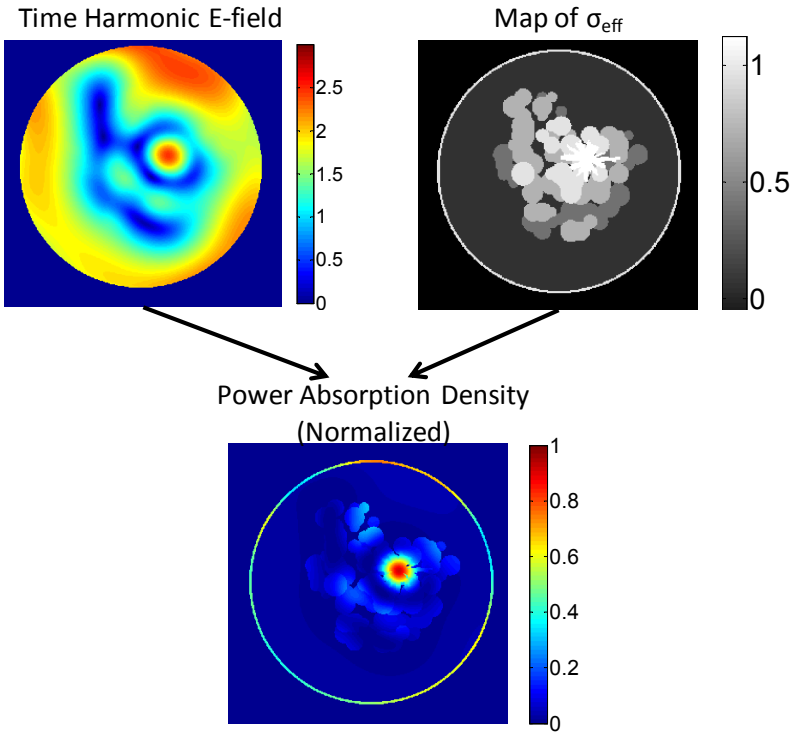

Figure 6.2 Procedure for obtaining the power absorption density (PAD) values from the simulated electric field values in the numerical breast models.

6.3.1.1 Performance Indicators

The calculated PAD values can be analyzed in various ways to evaluate the relative performance at the tumor resonance frequency. Here we use five different indicators. The first indictor is the normalized PAD values:

$$\mathrm{PAD}_{\mathrm{norm}}(x,y)=\frac{\mathrm{PAD}(x,y)}{\mathrm{PAD}_{\mathrm{max\_}f_o}}, \tag{6.9}$$

where $\mathrm{PAD}_{\mathrm{max\_}f_o}$ is the maximum PAD value in the tumor when the resonance frequency, f_o, is used. This indicator provides a map of relative PAD values in the simulated breast model, which allows for a visual comparison of the heating and focusing performance. The second indicator is the average $\mathrm{PAD}_{\mathrm{norm}}$ in the tumor,

$$\overline{\mathrm{PAD}_{\mathrm{norm}}}(x_{\mathrm{t}},y_{\mathrm{t}}), \tag{6.10}$$

where (x_t, y_t) are the coordinates corresponding to the tumor in the model and the bar, $\overline{\cdot}$, denotes the average. This indicator provides a relative measure of overall heating in the tumor. The third indicator is the ratio between the average PAD values outside and inside the tumor:

$$\overline{\mathrm{PADR}}=\frac{\overline{\mathrm{PAD}}(x_{\mathrm{b}},y_{\mathrm{b}})}{\overline{\mathrm{PAD}}(x_{\mathrm{t}},y_{\mathrm{t}})}, \tag{6.11}$$

where (x_b, y_b) indicate the coordinates corresponding to the region outside the tumor in the breast. This indicator provides a quantitative insight into the focusing of power in the tumor relative to the overall region outside the tumor. The skin layer is not included in the calculation of $\overline{\mathrm{PADR}}$. The fourth indicator is the maximum $\mathrm{PAD}_{\mathrm{norm}}$ in the tumor:

$$\max\left\{\mathrm{PAD}_{\mathrm{norm}}(x_{\mathrm{t}},y_{\mathrm{t}})\right\}. \tag{6.12}$$

Finally the fifth indicator is the ratio between the maximum $\mathrm{PAD}_{\mathrm{norm}}$ values outside the tumor and the average PAD values in the tumor:

$$\mathrm{PADR}_{\mathrm{max}}=\frac{\max\left\{\mathrm{PAD}(x_{\mathrm{b}},y_{\mathrm{b}})\right\}}{\overline{\mathrm{PAD}}(x_{\mathrm{t}},y_{\mathrm{t}})}, \tag{6.13}$$

which provides information regarding possible "hot spots" in other regions in the breast. A similar approach using the PAD-based performance indicators can be found in the work by Trefina et al. [2]. Table 6.1 summarizes the abovementioned indicators. Indicators 2 to 5 in

essence are the parameters interpreting the PAD map given by Indicator 1. By evaluating these quantities, it helps determine the relative performance of tumor-specific resonances in terms of selective heating of the tumor and the focusing quality.

Table 6.1 Various performance indicators calculated using power absorption density

Indicator 1	$\mathrm{PAD}_{\mathrm{norm}}(x,y)=\dfrac{\mathrm{PAD}(x,y)}{\mathrm{PAD}_{\max\_f_o}}$	Overall map of relative PAD w.r.t. the maximum PAD value at f_o (identified tumor resonance frequency)
Indicator 2	$\overline{\mathrm{PAD}_{\mathrm{norm}}}(x_{\mathrm{t}},y_{\mathrm{t}})$	Average $\mathrm{PAD}_{\mathrm{norm}}$ value in the tumor
Indicator 3	$\overline{\mathrm{PADR}}=\dfrac{\overline{\mathrm{PAD}}(x_{\mathrm{b}},y_{\mathrm{b}})}{\overline{\mathrm{PAD}}(x_{\mathrm{t}},y_{\mathrm{t}})}$	Ratio between average $\mathrm{PAD}_{\mathrm{norm}}$ values in other regions in the breast and tumor
Indicator 4	$\max\{\mathrm{PAD}_{\mathrm{norm}}(x_{\mathrm{t}},y_{\mathrm{t}})\}$	Maximum $\mathrm{PAD}_{\mathrm{norm}}$ value in the tumor
Indicator 5	$\mathrm{PADR}_{\max}=\dfrac{\max\{\mathrm{PAD}(x_{\mathrm{b}},y_{\mathrm{b}})\}}{\max\{\mathrm{PAD}(x_{\mathrm{t}},y_{\mathrm{t}})\}}$	Ratio between maximum $\mathrm{PAD}_{\mathrm{norm}}$ values outside and inside the tumor

6.3.1.2 Simulation Results

Using the same breast models introduced in the previous chapter, microwave focusing is simulated. The PAD-based indicators discussed above are obtained for each model at the identified tumor resonances and other frequencies selected for performance comparison. Six different frequencies including f_o are used for comparison. The frequencies for comparison are selected to have about 20-35% increment. In general, the use of tumor-specific resonances seems to provide an optimal performance among the frequencies considered. A detailed discussion of the results is provided in the following.

A. 3.5mm Radius Tumor - Semicircular Model 1 (S1)

In this homogeneous semicircular breast model (see Figure 5.7a), the identified tumor resonance, f_o, is 1.63GHz. Note that the frequency is the imaginary part of the pole, which is the

oscillating frequency. This frequency typically corresponds to the fundamental resonance of the tumor. As mentioned previously the natural resonances of the tumor is determined not only by the properties of the tumor, but also by the properties and complexity of the surrounding medium. Also note that the region outside the breast corresponding to the matching medium is not evaluated here.

Figure 6.3 shows the simulated electric field intensity maps, $|\mathrm{E}_z(x,y)|$, at various frequencies including f_o. In each plot, the tumor location is indicated by a black dotted circle. For all frequencies considered, a focus occurs at the tumor location, indicating that the phase angles used in the array accurately correspond to the electrical location of the tumor. The size of the focal spot, however, decreases as a function of frequency. This is due to the focal size being closely related to the classical diffraction limit as mentioned in Chapter 5. Outside the focal spot, there are other lobes with significant field intensity. Size of these lobes also depends on the wavelength.

The field intensity values are now used to calculate the PAD values using Equation 6.8 as well as the PAD-based performance indicators in Table 6.1. Figure 6.4 shows the map of the normalized PAD values, $\mathrm{PAD}_{\mathrm{norm}}(x,y)$. Notice that the power absorption plots are notably different from the field intensity plots, with much of the hot spots outside the tumor significantly reduced. Since this model consists only of homogeneous fatty tissue, relatively low effective tissue conductivity allows for a much less dielectric heating in the tissue. Table 6.2 summarizes Indicators 2-5 defined in Table 6.1 obtained for this model. It is apparent that the optimal power absorption in the tumor occurs at f_o, the identified tumor resonance frequency. Although the $\max\left\{\mathrm{PAD}_{\mathrm{norm}}(x_{\mathrm{t}},y_{\mathrm{t}})\right\}$ values are higher at 2, 3 and 4 GHz with respect to f_o, $\overline{\mathrm{PAD}_{\mathrm{norm}}}(x_{\mathrm{t}},y_{\mathrm{t}})$ is maximum at f_o. This indicates a more effective dielectric heating in the overall tumor volume taking place at f_o. In contrast, the power absorption is high only over a portion of the tumor at 2, 3 and 4 GHz . This phenomenon is also related to the size of the focal spot generate at the tumor. As the wavelength at the tumor resonance frequency is closely related to the physical dimensions of the tumor, so too should the size of the focal spot. Both $\mathrm{PADR}_{\mathrm{avg}}$ and $\mathrm{PADR}_{\mathrm{max}}$ are low (i.e. << 1) for all frequencies since no significant heating (power absorption) takes place outside

the tumor. Significant power absorption is observed in the skin layer. However, much of the skin heating can be mitigated by means of cooling the temperature in the matching medium.

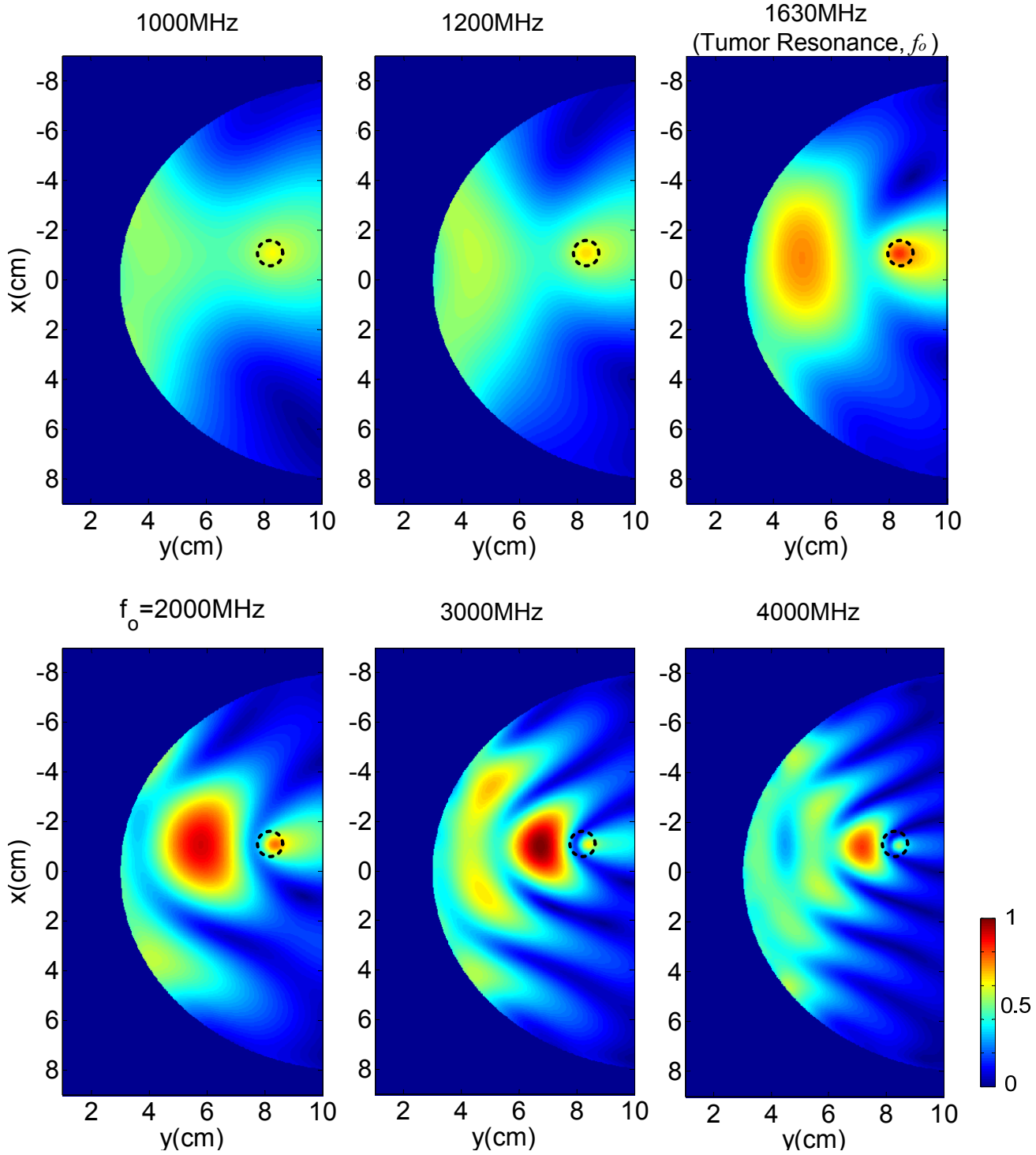

Figure 6.3 Simulated electric field distributions in Model S1 with 3.5mm (baseline radius) tumor at various frequencies. The tumor location is indicated by a black circle.

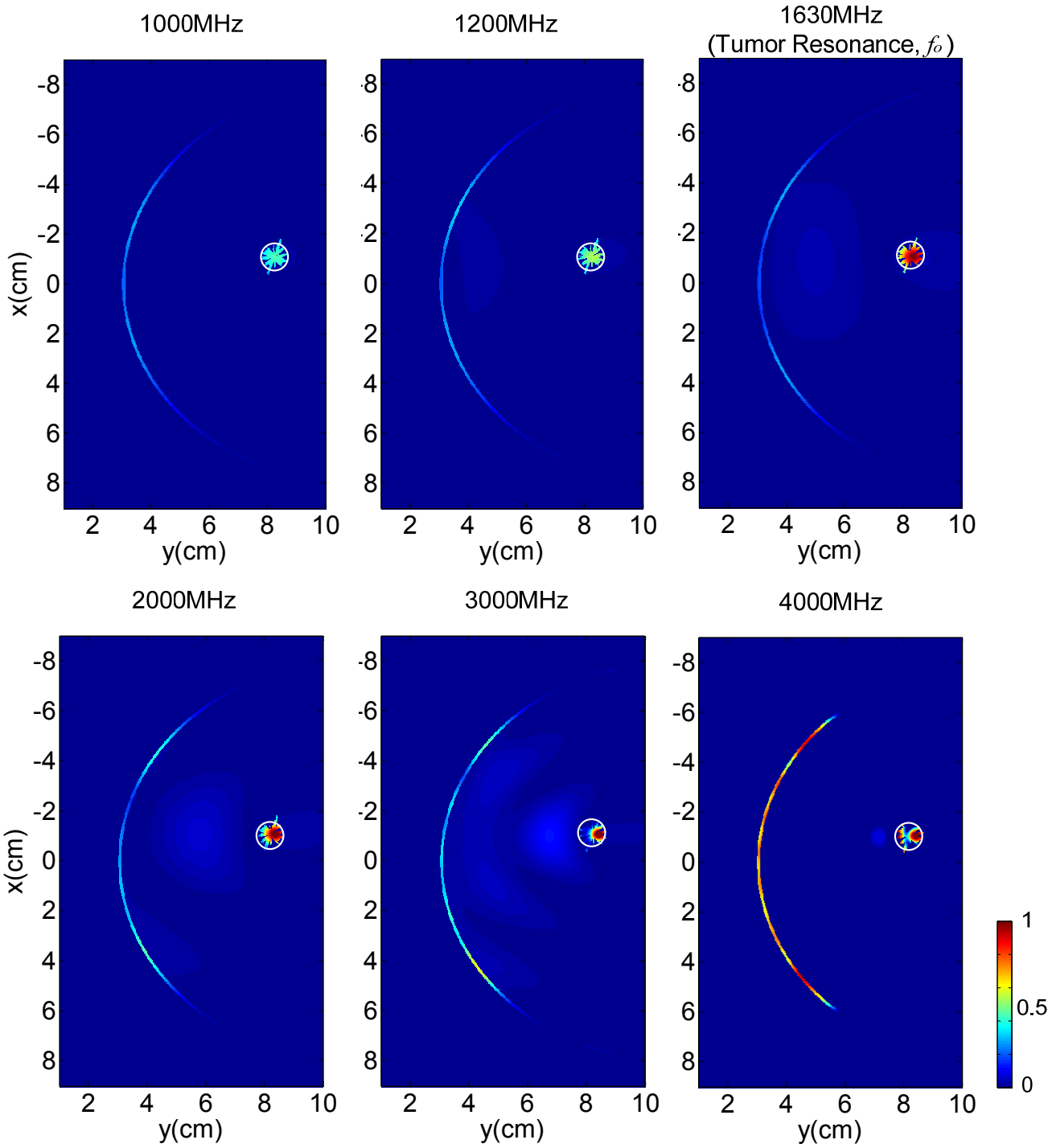

Figure 6.4 Normalized power absorption density (PAD) values obtained from the simulated electric field distribution in Model S1 with 3.5mm (baseline radius) tumor at various frequencies. The tumor location is indicated by a white circle.

Table 6.2 PAD-based performance indicators for Model S1 with 3.5mm (baseline radius) tumor at various frequencies. The tumor resonance frequency, f_o, is in bold.

Frequency (GHz)	$\overline{\mathrm{PAD}_{\mathrm{norm}}}(x_t, y_t)$	$\mathrm{PADR}_{\mathrm{avg}}$	$\max\{\mathrm{PAD}_{\mathrm{norm}}(x_t, y_t)\}$	$\mathrm{PADR}_{\mathrm{max}}$
1	0.519	0.015	0.441	0.049
1.2	0.604	0.015	0.540	0.051
1.63	**1**	**0.013**	**1**	**0.056**
2	0.866	0.017	1.05	0.105
3	0.577	0.039	1.1	0.296
4	0.548	0.040	1.2	0.280

B. 3.5mm Radius Tumor - Semicircular Model 2 (S2)

Model S2 shares the same breast geometry as that in Model S1, but consists of some fibroglandular (medium/low fat content) tissues in the breast as shown in Figure 5.7b. The tumor resonance, f_o, for this model is identified to be 1.29GHz. The shift in the resonance is mostly due to tissue heterogeneity introduced by the fibroglandular tissues affecting the overall electromagnetic interaction with the tumor.

Figure 6.5 shows the simulated electric field intensity maps at various frequencies including f_o. Fairly different field distributions compared to that in Model S1 are observed. A focus still takes place in each plot at the tumor location indicated by a white circle. However, the relative field intensity at the focus for 3 and 4 GHz is significantly smaller compared to that from Model S1.

Figure 6.6 shows the $\mathrm{PAD}_{\mathrm{norm}}(x, y)$ plots. Unlike Model S1, there are regions outside the tumor with relatively higher power absorption, especially in the region where the fibroglandular tissues are located, due to the higher effective conductivity values of such tissues. Table 6.3 shows the other indicators obtained. As it can be seen from the plots and indicators, the dielectric heating seems to be optimal at f_o, where $\overline{\mathrm{PAD}_{\mathrm{norm}}}(x_t, y_t)$ is fairly uniform at values close to 1 with no significant hot spots outside the tumor. At other frequencies, the power absorption in the tumor is less, and more significant hot spots seem to occur outside the tumor. The minimum $\mathrm{PADR}_{\mathrm{max}}$ value at f_o shows that hot spots are most effectively avoided at this frequency.

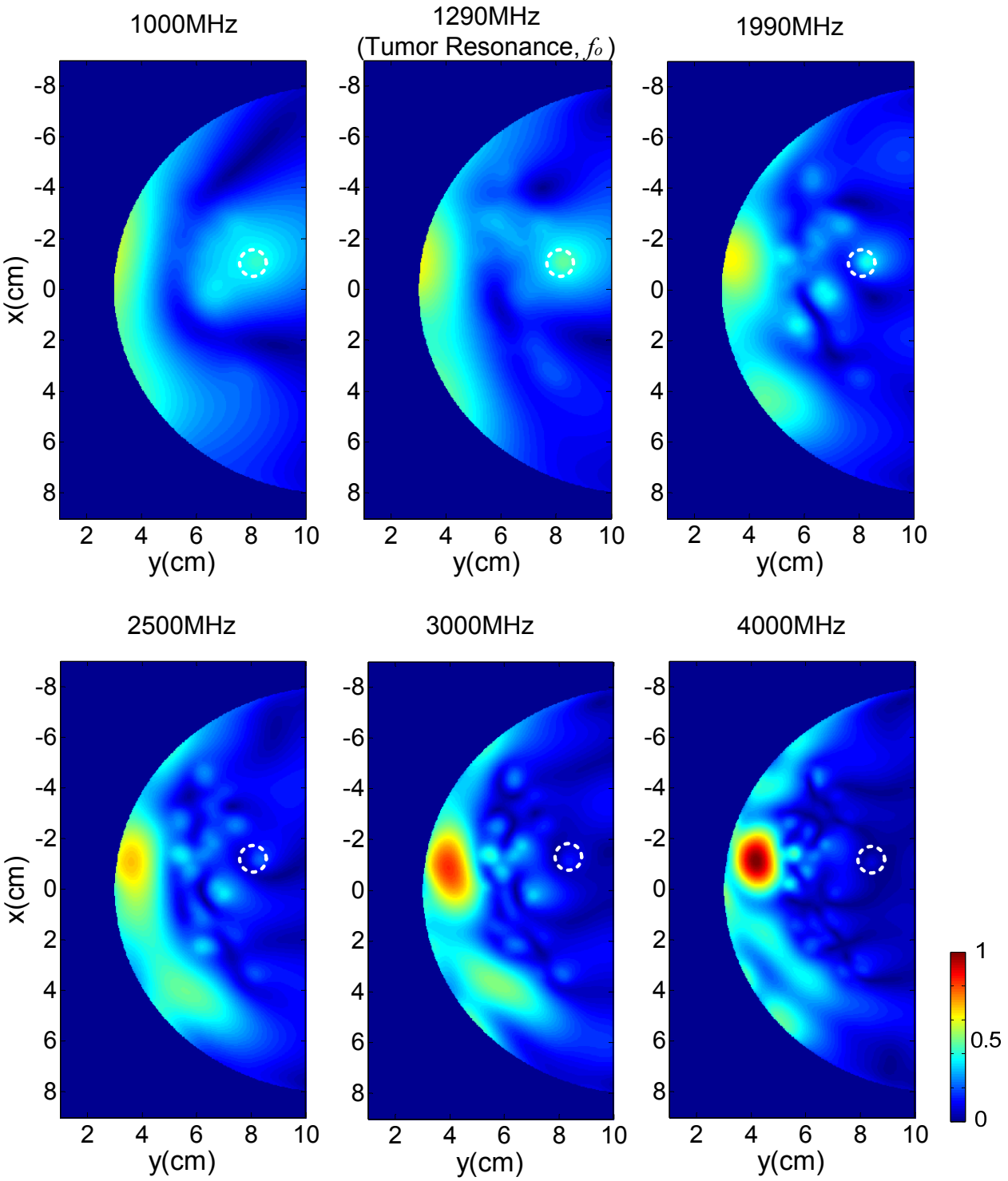

Figure 6.5 Simulated electric field distributions in Model S2 with 3.5mm (baseline radius) tumor at various frequencies. The tumor location is indicated by a white circle.

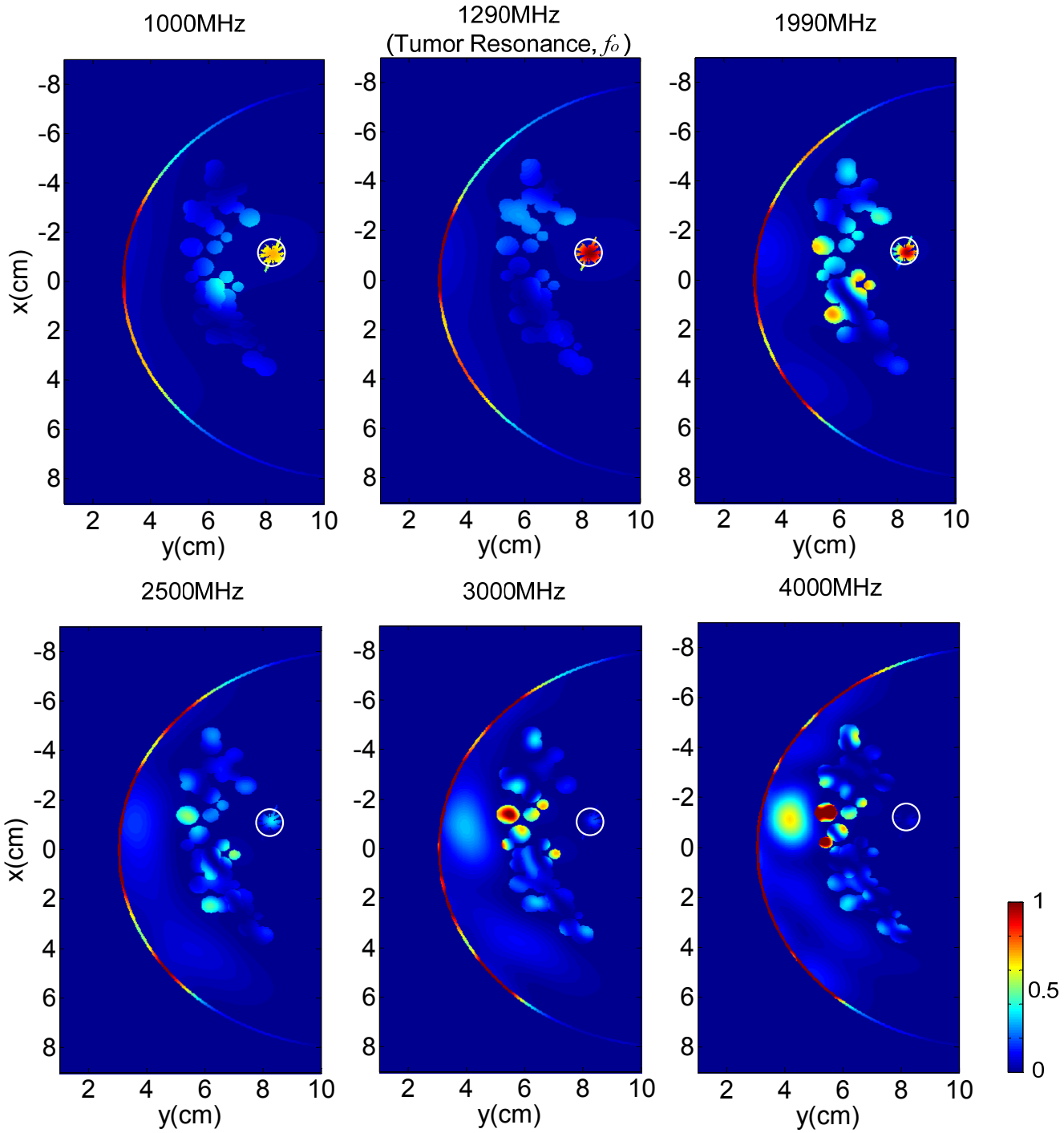

Figure 6.6 Normalized PAD values obtained from the simulated electric field distribution in Model S2 with 3.5mm (baseline radius) tumor at various frequencies. The tumor location is indicated by a white circle.

Table 6.3 PAD-based performance indicators for Model S2 with 3.5mm (baseline radius) tumor at various frequencies. The tumor resonance frequency, f_o, is in bold.

Frequency (GHz)	$\overline{\mathrm{PAD}_{\mathrm{norm}}}(x_t, y_t)$	$\mathrm{PADR}_{\mathrm{avg}}$	$\max\{\mathrm{PAD}_{\mathrm{norm}}(x_t, y_t)\}$	$\mathrm{PADR}_{\mathrm{max}}$
1	0.751	0.038	0.697	0.663
1.29	**1**	**0.031**	**1**	**0.351**
1.99	0.763	0.066	0.98	1.152
2.5	0.227	0.202	0.36	2.730
3	0.102	0.582	0.194	12.38
4	0.044	1.566	0.127	48.82

C. 3.5mm Radius Tumor - Semicircular Model 3 (S3)

Model S3 consists of a larger portion of fibroglandular tissues by which the tumor is surrounded, as shown in Figure 5.7c. The tumor resonance, f_o, for this model is identified to be 1GHz. The shift in the resonance should be mainly due to the fibroglandular tissues with higher dielectric constant surrounding the tumor, changing the effective electrical size of the tumor.

The simulated electric field intensity maps are shown in Figure 6.7. Again, different field distributions compared that of Models S1 and S2 are observed, as well as a focus still taking place in at the corresponding tumor location indicated by a white circle. Also, the field intensity at the focus diminishes at higher frequencies (2.6 and 3.5 GHz).

The $\mathrm{PAD}_{\mathrm{norm}}(x, y)$ plots are shown in Figure 6.8 and the other PAD-based indicators are summarized in Table 6.4. The tumor resonance frequency in this model also provides the optimal results with highest $\overline{\mathrm{PAD}_{\mathrm{norm}}}(x_t, y_t)$ and $\max\{\mathrm{PAD}_{\mathrm{norm}}(x_t, y_t)\}$ values. The $\mathrm{PADR}_{\mathrm{avg}}$ and $\mathrm{PADR}_{\mathrm{max}}$ values are also among the lowest at f_o. Put differently, at f_o the maximum dielectric heating takes place in the tumor while effectively avoiding other hot spots in the breast.

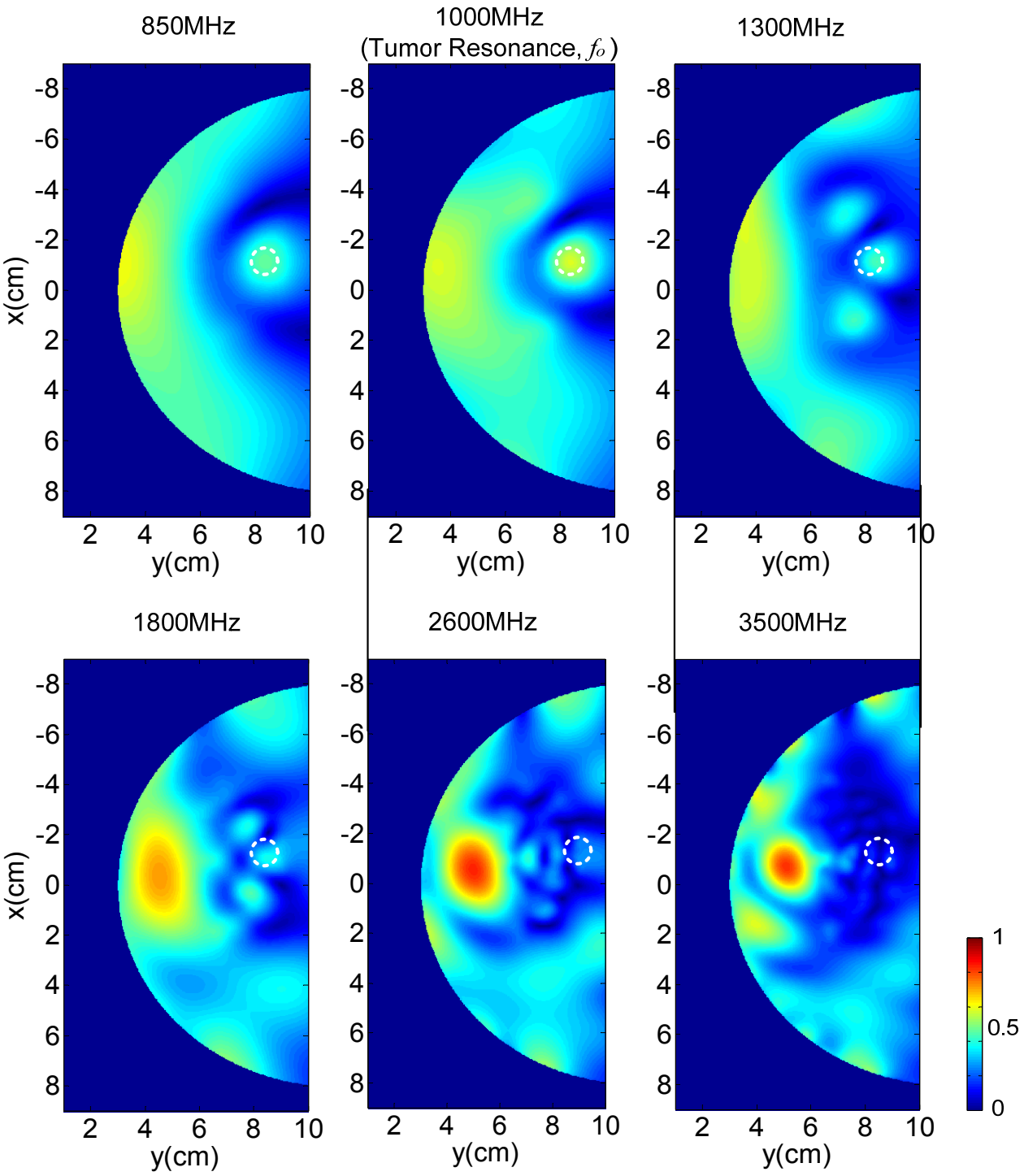

Figure 6.7 Simulated electric field distributions in Model S3 with 3.5mm (baseline radius) tumor at various frequencies. The tumor location is indicated by a white circle.

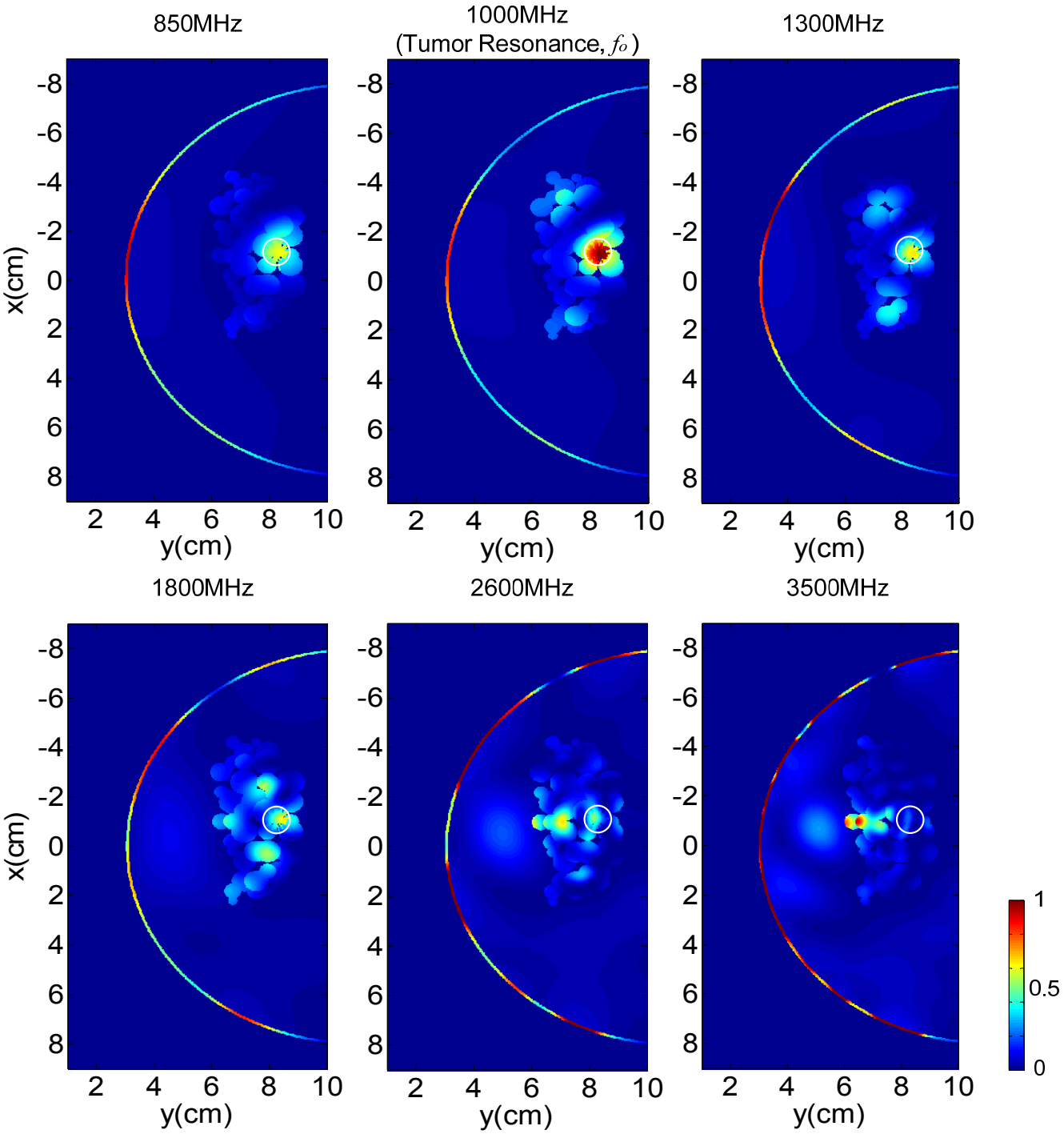

Figure 6.8 Normalized PAD values obtained from the simulated electric field distribution in Model S3 with 3.5mm (baseline radius) tumor at various frequencies. The tumor location is indicated by a white circle.

Table 6.4 PAD-based performance indicators for Model S3 with 3.5mm (baseline radius) tumor at various frequencies. The tumor resonance frequency, f_o, is in bold.

Frequency (GHz)	$\overline{\mathrm{PAD}_{\mathrm{norm}}}(x_t, y_t)$	$\mathrm{PADR}_{\mathrm{avg}}$	$\max\{\mathrm{PAD}_{\mathrm{norm}}(x_t, y_t)\}$	$\mathrm{PADR}_{\mathrm{max}}$
0.85	0.636	0.062	0.607	0.803
1	**1**	**0.056**	**1**	**0.724**
1.3	0.578	0.077	0.642	0.790
1.8	0.469	0.126	0.6383	1.346
2.6	0.339	0.177	0.506	2.224
3.5	0.238	0.259	0.263	8.043

D. 3.5mm Radius Tumor - Circular Model 1 (C1)

Model C1 is a circular breast model consisting only of fatty tissue, as shown in Figure 5.8a. For this homogeneous model, the identified tumor resonance, f_o, is 2.2GHz. Figure 6.9 shows the simulated electric field intensity maps at various frequencies including f_o. In each plot, the tumor location is indicated by a black dotted circle. A focal spot also talks place at the tumor location. The size of the focal spot, in the same manner as in the abovementioned models, decreases as a function of frequency.

The $\mathrm{PAD}_{\mathrm{norm}}(x, y)$ plots are shown in Figure 6.10 and the other PAD-based indicators are summarized in Table 6.5. The tumor resonance frequency in this model also provides the best performance overall with highest $\overline{\mathrm{PAD}_{\mathrm{norm}}}(x_t, y_t)$ and $\max\{\mathrm{PAD}_{\mathrm{norm}}(x_t, y_t)\}$ values. Since this is a homogeneous fatty tissue model, the $\mathrm{PADR}_{\mathrm{avg}}$ and $\mathrm{PADR}_{\mathrm{max}}$ values are very low in general with no significant hot spots outside the tumor at any frequencies considered.

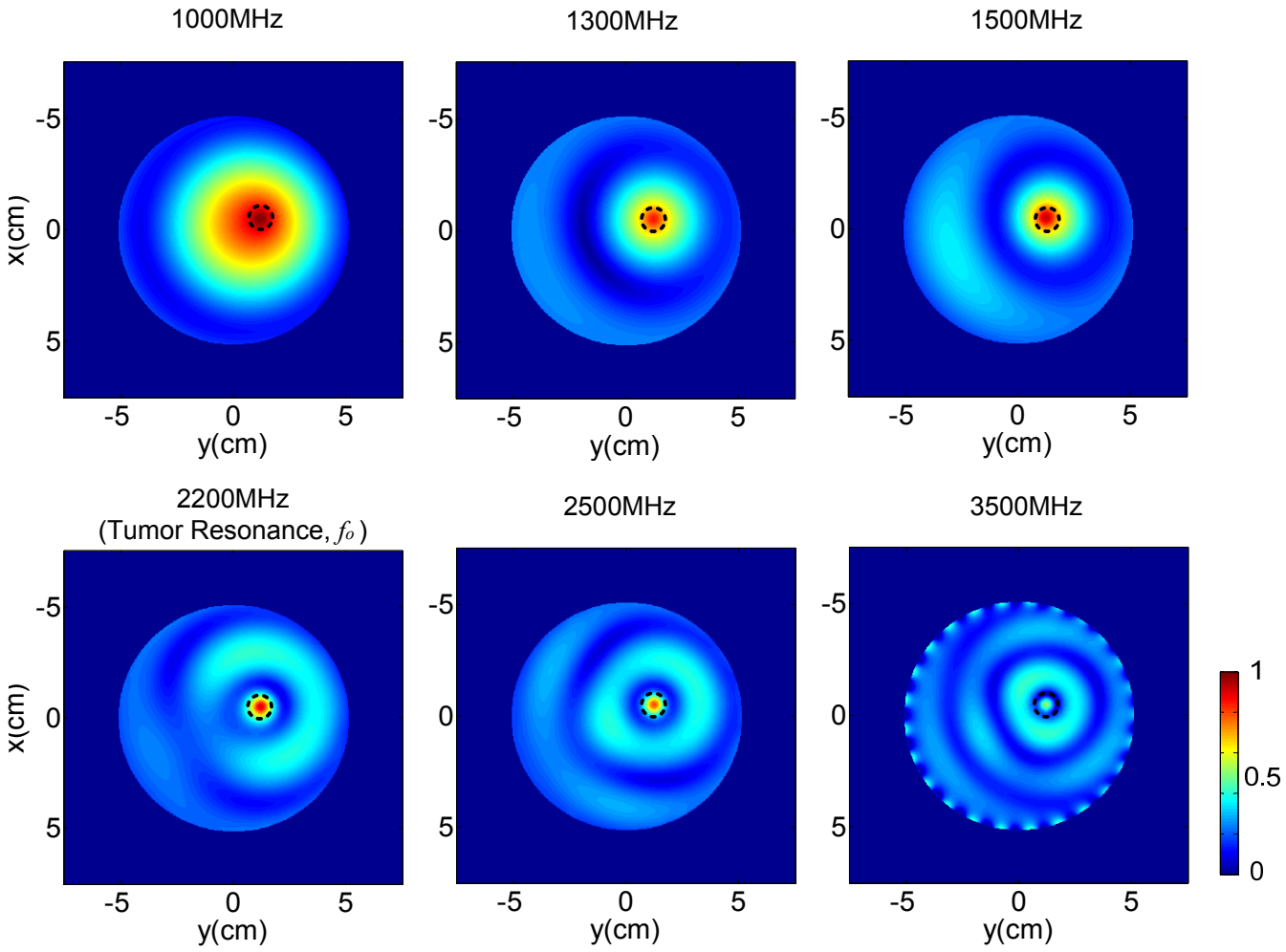

Figure 6.9 Simulated electric field distributions in Model C1 with 3.5mm (baseline radius) tumor at various frequencies. The tumor location is indicated by a black circle.

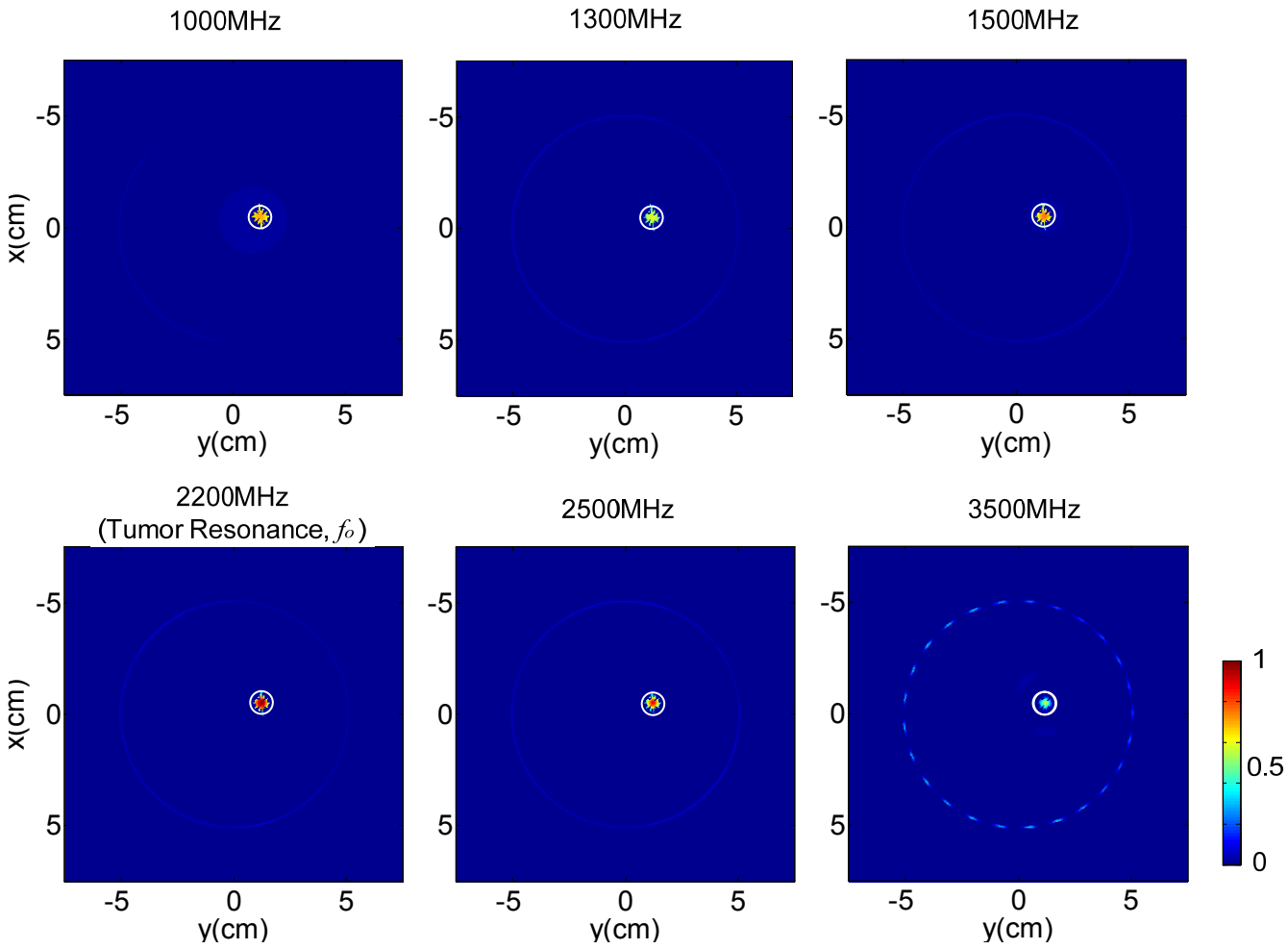

Figure 6.10 Normalized PAD values obtained from the simulated electric field distribution in Model C1 with 3.5mm (baseline radius) tumor at various frequencies. The tumor location is indicated by a white circle.

Table 6.5 PAD-based performance indicators for Model C1 with 3.5mm (baseline radius) tumor at various frequencies. The tumor resonance frequency, f_o, is in bold.

Frequency (GHz)	$\overline{\mathrm{PAD}_{\mathrm{norm}}}(x_t, y_t)$	$\mathrm{PADR}_{\mathrm{avg}}$	$\max\{\mathrm{PAD}_{\mathrm{norm}}(x_t, y_t)\}$	$\mathrm{PADR}_{\mathrm{max}}$
1.0	0.94	0.0082	0.69	0.049
1.3	0.806	0.0049	0.585	0.053
1.5	0.834	0.0056	0.751	0.063
2.2	**1**	**0.0059**	**1**	**0.065**
2.5	0.771	0.0086	0.879	0.071
3.5	0.322	0.027	0.564	0.089

E. 3.5mm Radius Tumor - Circular Model 2 (C2)

Model C2 a shares the same breast geometry as that in Model C1, but consists of some fibroglandular tissues in the breast as shown in Figure 5.8b. The identified tumor resonance, f_o, is 2.2GHz. Notice that the resonance remained the same, although the electric field distribution is different from that in Model C1. The focal spot takes place in each plot at the tumor location indicated by a black circle as shown in Figure 6.11.

The $\mathrm{PAD}_{\mathrm{norm}}(x,y)$ plots are shown in Figure 6.12 and the performance indicators are summarized in Table 6.6. Overall, the tumor resonance provides the optimal performance. Although the $\overline{\mathrm{PAD}_{\mathrm{norm}}}(x_{\mathrm{t}},y_{\mathrm{t}})$ and $\max\{\mathrm{PAD}_{\mathrm{norm}}(x_{\mathrm{t}},y_{\mathrm{t}})\}$ values at 2.5GHz are slightly larger than that at f_o, the $\mathrm{PADR}_{\mathrm{max}}$ value is greater by nearly a factor of two, indicating that hot spots exist outside the tumor with power absorption exceeding that in the tumor.

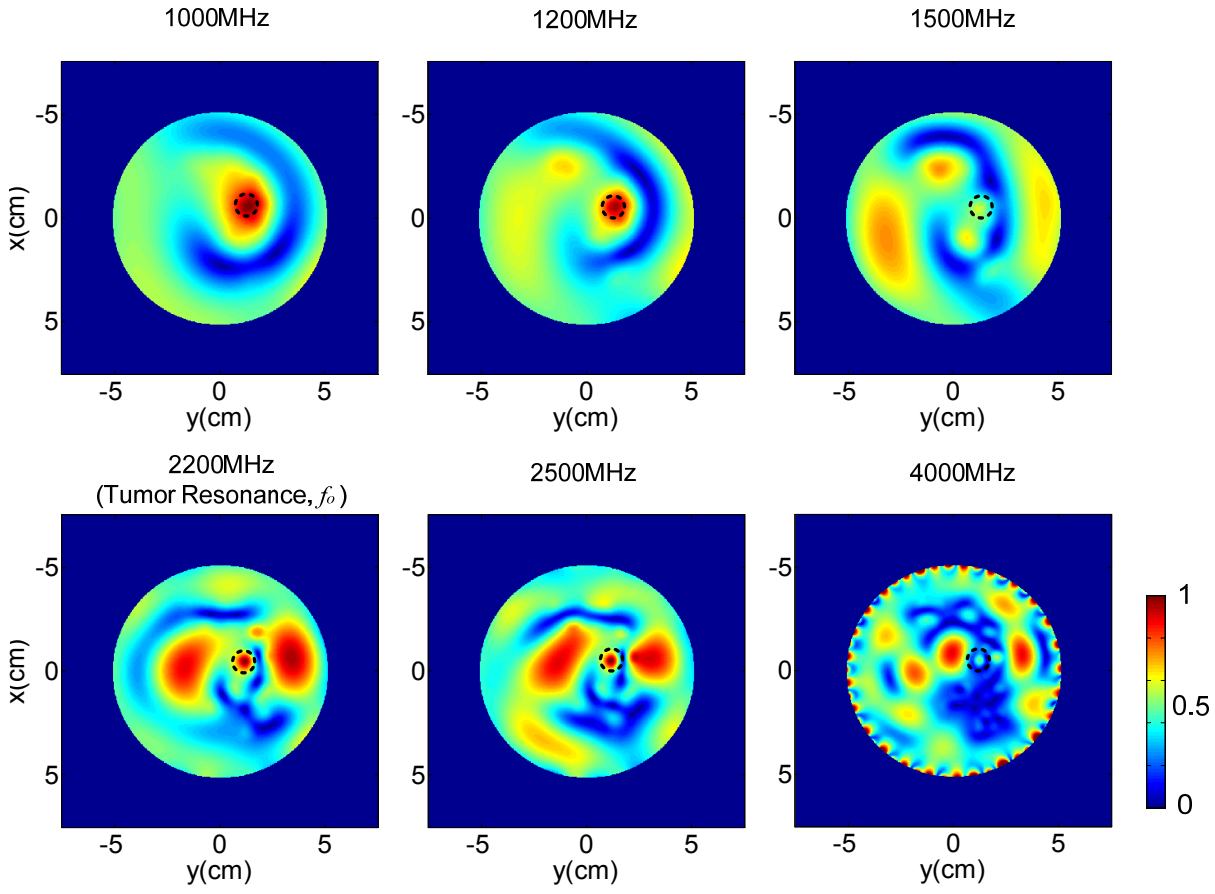

Figure 6.11 Simulated electric field distributions in Model C2 with 3.5mm (baseline radius) tumor at various frequencies. The tumor location is indicated by a black circle.

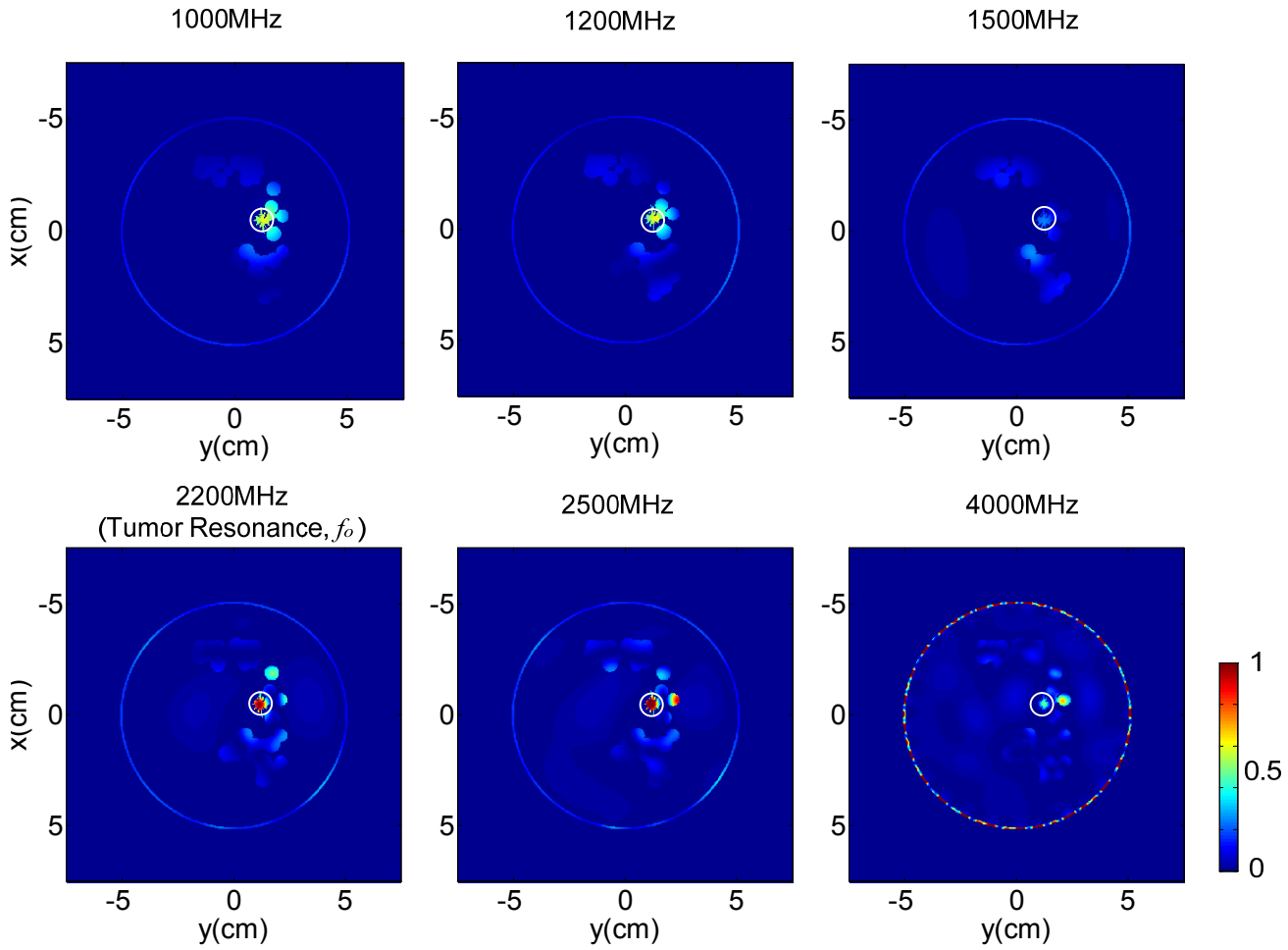

Figure 6.12 Normalized PAD values obtained from the simulated electric field distribution in Model C2 with 3.5mm (baseline radius) tumor at various frequencies. The tumor location is indicated by a white circle.

Table 6.6 PAD-based performance indicators for Model C2 with 3.5mm (baseline radius) tumor at various frequencies. The tumor resonance frequency, f_o, is in bold.

Frequency (GHz)	$\overline{\mathrm{PAD}_{\mathrm{norm}}}(x_t, y_t)$	$\mathrm{PADR}_{\mathrm{avg}}$	$\max\{\mathrm{PAD}_{\mathrm{norm}}(x_t, y_t)\}$	$\mathrm{PADR}_{\mathrm{max}}$
1.0	0.867	0.029	0.596	0.998
1.2	0.826	0.031	0.606	1.059
1.5	0.318	0.082	0.242	1.343
2.2	**1**	**0.032**	**1**	**0.792**
2.5	1.20	0.036	1.1	1.419
4.0	0.274	0.149	0.504	4.21

F. 3.5mm Radius Tumor - Circular Model 3 (C3)

Model C3 consists of a larger portion of fibroglandular tissues in the breast surrounding the tumor as shown in Figure 5.8c. The identified tumor resonance, f_o, is shifted to 1.55GHz. Similar to Model S3, this shift should be caused by a change in the effective electrical size of the tumor caused by the surrounding tissues. The E-field intensity plots are shown in Figure 6.13.

The $\mathrm{PAD}_{\mathrm{norm}}(x,y)$ plots and the PAD-based indicators for this model are shown in Figure 6.14 and Table 6.7, respectively. The tumor resonance frequency provides the optimal performance in this model as well. The $\overline{\mathrm{PAD}_{\mathrm{norm}}}(x_t,y_t)$ and $\max\{\mathrm{PAD}_{\mathrm{norm}}(x_t,y_t)\}$ values are the highest at f_o, and the $\mathrm{PADR}_{\mathrm{max}}$ value is the lowest among the frequencies considered. $\mathrm{PADR}_{\mathrm{avg}}$ are generally very low for frequencies below 3GHz and moderately low otherwise. A similar trend for $\mathrm{PADR}_{\mathrm{avg}}$ can be found in other models as well, since $\mathrm{PADR}_{\mathrm{avg}}$ uses the average power absorption in the overall breast outside the tumor.

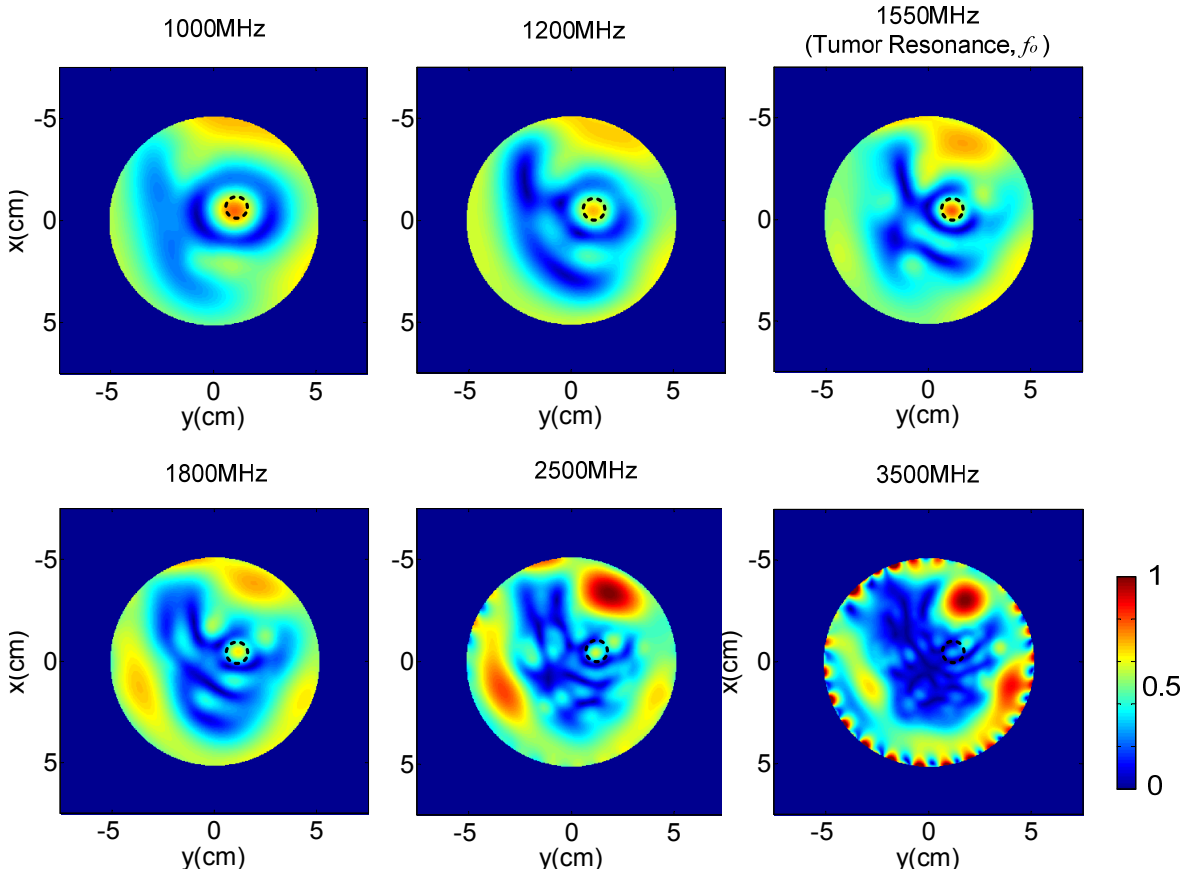

Figure 6.13 Simulated electric field distributions in Model C3 with 3.5mm (baseline radius) tumor at various frequencies. The tumor location is indicated by a black circle.

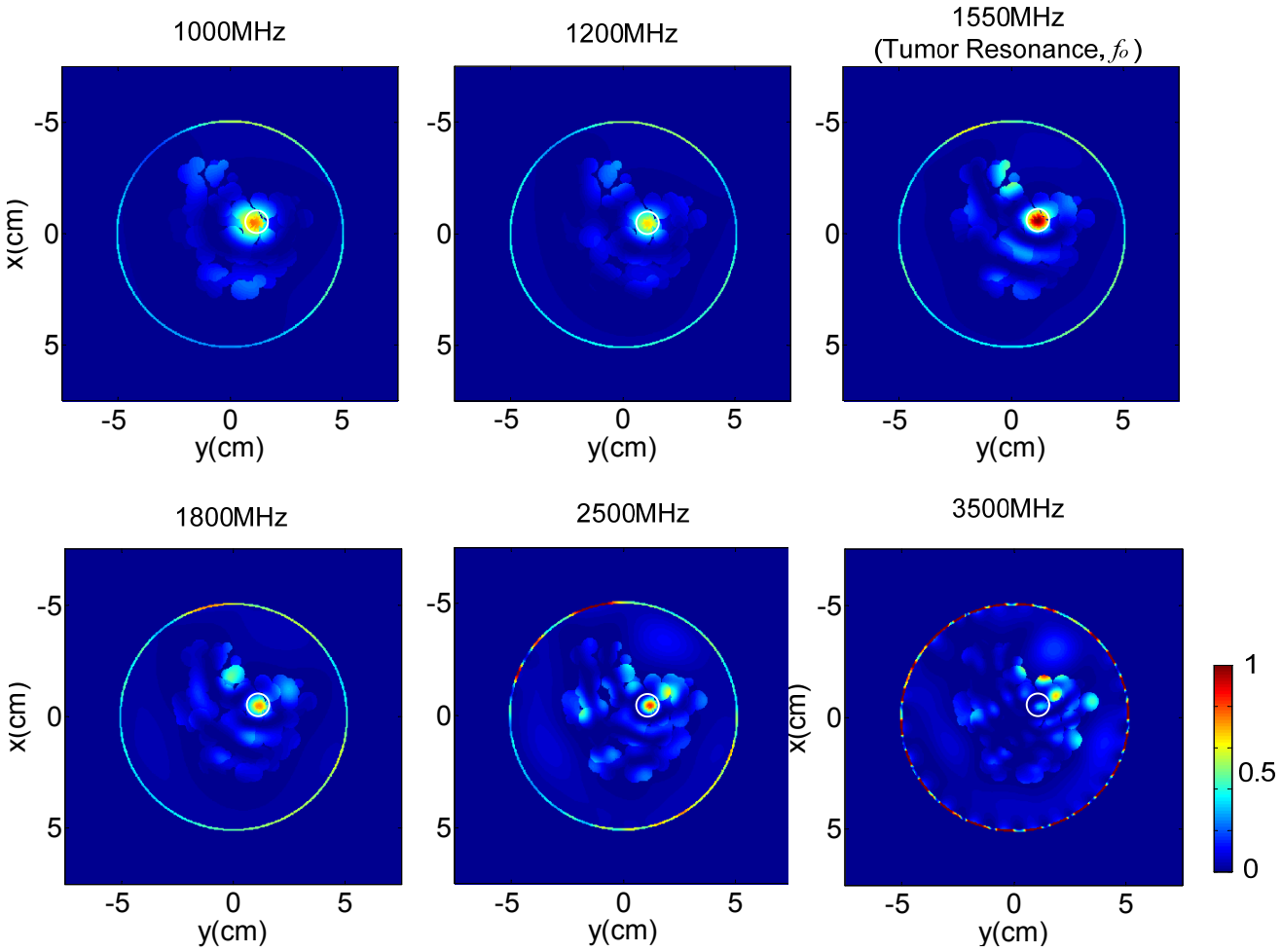

Figure 6.14 Normalized PAD values obtained from the simulated electric field distribution in Model C3 with 3.5mm (baseline radius) tumor at various frequencies. The tumor location is indicated by a white circle.

Table 6.7 PAD-based performance indicators for Model C3 with 3.5mm (baseline radius) tumor at various frequencies. The tumor resonance frequency, f_o, is in bold.

Frequency (GHz)	$\overline{\mathrm{PAD}_{\mathrm{norm}}}(x_t, y_t)$	$\mathrm{PADR}_{\mathrm{avg}}$	$\max\{\mathrm{PAD}_{\mathrm{norm}}(x_t, y_t)\}$	$\mathrm{PADR}_{\mathrm{max}}$
1.0	0.885	0.063	0.763	0.910
1.2	0.731	0.063	0.655	0.848
1.55	**1**	**0.060**	**1**	**0.601**
1.8	0.691	0.082	0.737	0.939
2.5	0.609	0.125	0.837	1.415
3.5	0.223	0.344	0.446	5.311

G. 6mm Radius Tumor - Circular Model 1 (C1)

In this model the tumor baseline radius is increased to 6mm. The tumor shape is generated in the same way that the 3.5mm radius tumor was generated, i.e. by applying a random variation to a baseline circle as discussed in Chapter 5. The identified resonance, f_o, in this model is 0.9 GHz, which is lower compared to that of the 3.5mm tumor in the same model, due to the increased overall tumor size. The E-field intensity plots are not shown for this model and the ones discussed hereafter, as they are similar to that obtained from the circular models with 3.5mm radius tumor discussed above. The $\mathrm{PAD}_{\mathrm{norm}}(x,y)$ plots in Figure 6.15 and the indicators summarized in Table 6.8 show that the tumor resonance frequency provides the optimal power absorption in the tumor. Both $\overline{\mathrm{PAD}_{\mathrm{norm}}}(x_t,y_t)$ and $\max\{\mathrm{PAD}_{\mathrm{norm}}(x_t,y_t)\}$ values are highest for f_o. Similar to the 3.5mm radius tumor case, the $\mathrm{PADR}_{\mathrm{avg}}$ and $\mathrm{PADR}_{\mathrm{max}}$ values are very low in general with no significant hot spots outside the tumor at any frequencies considered.

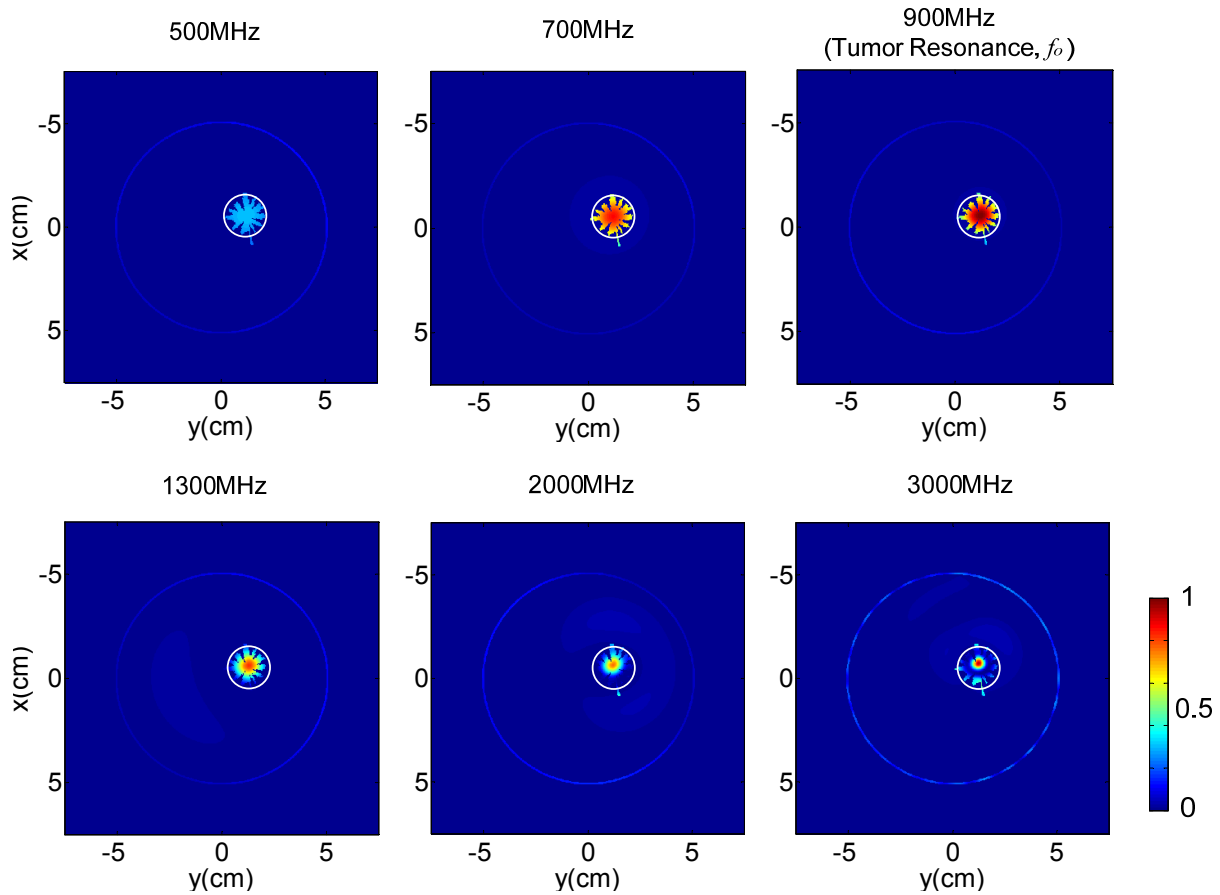

Figure 6.15 Normalized PAD values obtained from the simulated E-field distribution in Model C1 with 6mm radius tumor at various frequencies. The tumor location is indicated by a white circle.

Table 6.8 PAD-based performance indicators for Model C1 with 6mm (baseline radius) tumor at various frequencies. The tumor resonance frequency, f_o, is in bold.

Frequency (GHz)	$\overline{\mathrm{PAD}_{\mathrm{norm}}}(x_t, y_t)$	$\mathrm{PADR}_{\mathrm{avg}}$	$\max\{\mathrm{PAD}_{\mathrm{norm}}(x_t, y_t)\}$	$\mathrm{PADR}_{\mathrm{max}}$
0.5	0.387	0.023	0.312	0.050
0.7	0.974	0.011	0.863	0.053
0.9	**1**	**0.006**	**1**	**0.058**
1.3	0.5734	0.020	0.816	0.077
2.0	0.357	0.042	0.757	0.139
3.0	0.311	0.051	0.933	0.186

H. 6mm Radius Tumor - Circular Model 2 (C2)

For Model C2 with 6mm baseline radius tumor, the identified resonance, f_o, is 1 GHz, which seems to have shifted up slightly. As previously mentioned a shift in the resonance should mainly come from tissue heterogeneity introduced the fibroglandular tissues affecting the overall electromagnetic interaction with the tumor. In this model, however, it is likely that the change in the spiculated geometry from random model is also a contributing factor to the resonance shift, a larger tumor baseline circle would allow for a larger effective change in overall geometry. Furthermore, since the fibroglandular tissues do not completely surround the tumor in this model, the effective electrical size of the tumor may not have necessarily decreased, which would be one of the reasons that the resonance is shifted up slightly from that in Model C1.

The $\mathrm{PAD}_{\mathrm{norm}}(x, y)$ plots are shown in Figure 6.16 and the PAD-based indicators are summarized in Table 6.9. Although $\overline{\mathrm{PAD}_{\mathrm{norm}}}(x_t, y_t)$ for 0.5GHz exceeds that for f_o, the $\mathrm{PADR}_{\mathrm{max}}$ value is greater for 0.5GHz. That is, more significant hot spots exist outside the tumor at 0.5GHz than at f_o, which is also evident from the power absorption plots in Figure 6.16. The power absorption in the tumor at other frequencies is significantly lower, and the $\mathrm{PADR}_{\mathrm{max}}$ values are significantly higher. Hence, it can be said that the use tumor resonance provides the optimal performance in the heating of the tumor among the frequencies considered.

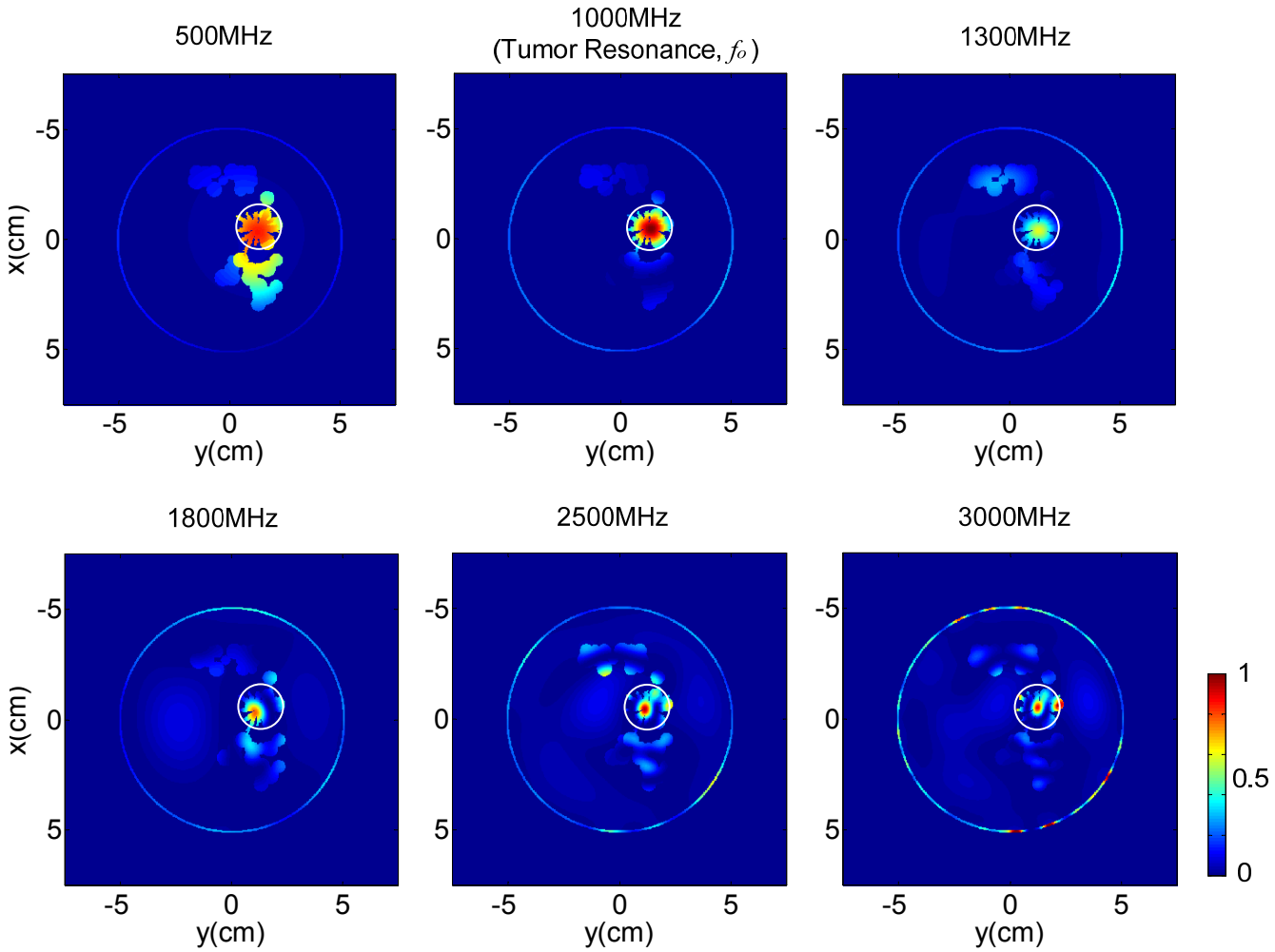

Figure 6.16 Normalized PAD values obtained from the simulated electric field distribution in Model C2 with 6mm (baseline radius) tumor at various frequencies. The tumor location is indicated by a white circle.

Table 6.9 PAD-based performance indicators for Model C2 with 6mm (baseline radius) tumor at various frequencies. The tumor resonance frequency, f_o, is in bold.

Frequency (GHz)	$\overline{\mathrm{PAD}_{\mathrm{norm}}}(x_t, y_t)$	$\mathrm{PADR}_{\mathrm{avg}}$	$\max\{\mathrm{PAD}_{\mathrm{norm}}(x_t, y_t)\}$	$\mathrm{PADR}_{\mathrm{max}}$
0.5	1.14	0.056	0.847	0.639
1.0	**1**	**0.025**	**1**	**0.303**
1.3	0.491	0.068	0.592	1.055
1.8	0.421	0.106	0.773	1.603
2.5	0.445	0.125	0.949	2.105
3.0	0.419	0.114	1	3.234

I. 6mm Radius Tumor - Circular Model 3 (C3)

For Model C3 with 6mm baseline radius tumor, the identified resonance, f_o, is 0.75GHz, which is slightly lower from the resonances in Models C1 and C2. As in the case of 3.5mm radius tumor, the shift should be mainly caused by an increase in the effective electrical size of the tumor due to the surrounding glandular tissues. Figure 6.17 shows the $\mathrm{PAD}_{\mathrm{norm}}(x,y)$ plots for various frequencies including f_o. The optimal power performance takes place at the resonance frequency, f_o ,in terms of both the relative amount of power absorption and the level of other hot spots in the breast, as indicated by the values of $\overline{\mathrm{PAD}_{\mathrm{norm}}}(x_{\mathrm{t}},y_{\mathrm{t}})$, $\max\{\mathrm{PAD}_{\mathrm{norm}}(x_{\mathrm{t}},y_{\mathrm{t}})\}$, and $\mathrm{PADR}_{\mathrm{max}}$ summarized in Table 6.10.

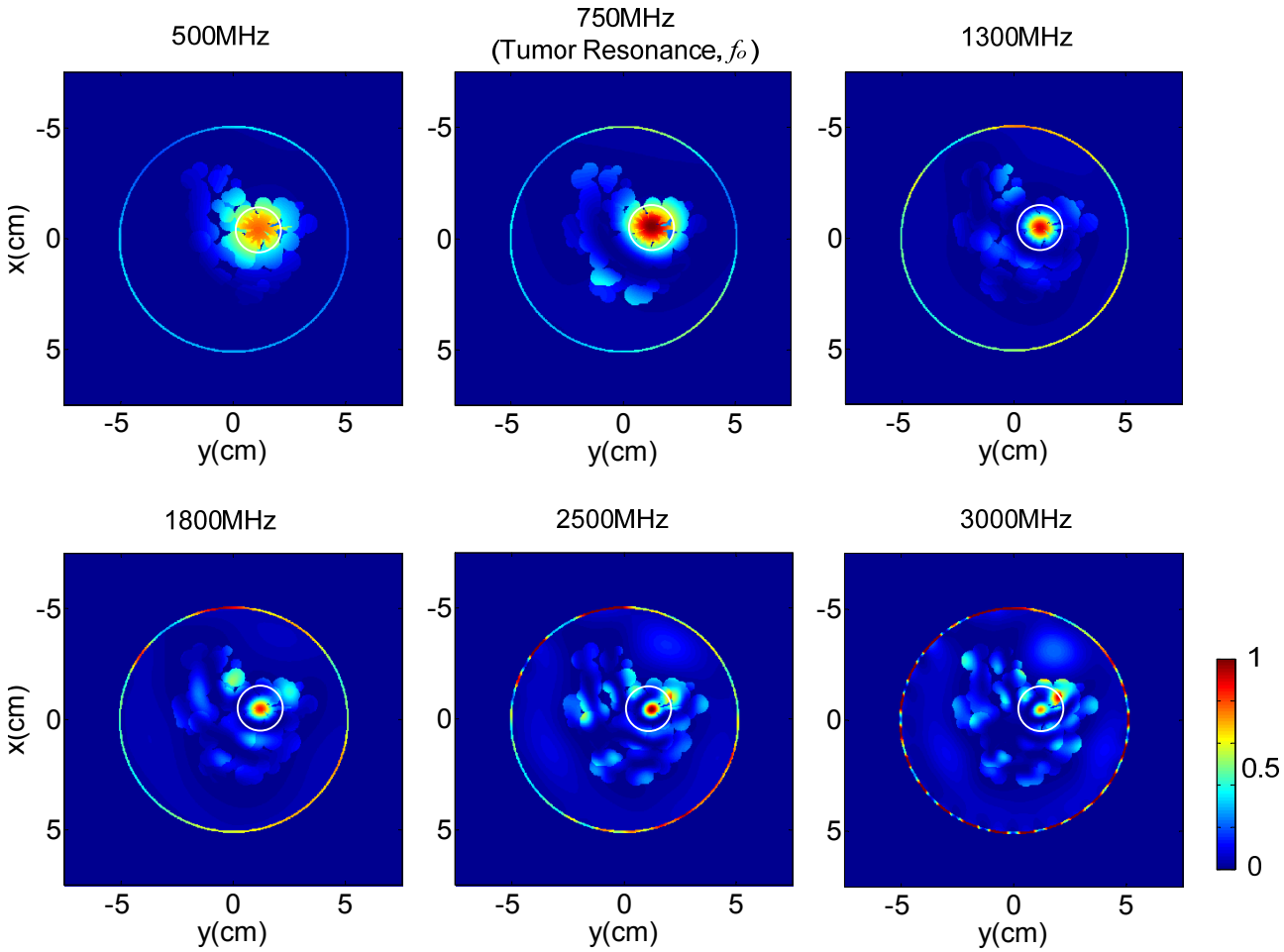

Figure 6.17 Normalized PAD values obtained from the simulated electric field distribution in Model C3 with 6mm (baseline radius) tumor at various frequencies. The tumor location is indicated by a white circle.

Table 6.10 PAD-based performance indicators for Model C3 with 6mm (baseline radius) tumor at various frequencies. The tumor resonance frequency, f_o, is in bold.

Frequency (GHz)	$\overline{\mathrm{PAD}_{\mathrm{norm}}}(x_t, y_t)$	$\mathrm{PADR}_{\mathrm{avg}}$	$\max\{\mathrm{PAD}_{\mathrm{norm}}(x_t, y_t)\}$	$\mathrm{PADR}_{\mathrm{max}}$
0.5	0.876	0.083	0.771	0.779
0.75	**1**	**0.063**	**1**	**0.602**
1.3	0.633	0.078	0.913	0.620
1.8	0.422	0.146	0.854	1.486
2.5	0.356	0.242	1.02	2.786
3.0	0.254	0.368	0.765	4.482

J. Circular Model 1 (C1) with 9mm tumor baseline radius

The tumor baseline radius used here is 9mm. The tumor shape is generated in the same way that the 3.5mm and 6mm radius tumor models are generated as discussed in Chapter 5. For this homogeneous tissue model (Model C1), the identified tumor resonance, f_o, is 0.7 GHz. As expected, a decrease in the resonance frequency occurs due to an increased overall tumor size. The $\mathrm{PAD}_{\mathrm{norm}}(x, y)$ plots are shown in Figure 6.18 and the indicators are summarized in Table 6.11. The tumor resonance frequency seems to provide the optimal dielectric heating in the tumor, as indicated by the maximum $\overline{\mathrm{PAD}_{\mathrm{norm}}}(x_t, y_t)$ and $\max\{\mathrm{PAD}_{\mathrm{norm}}(x_t, y_t)\}$ values taking place at f_o among the frequencies considered. Similar to the cases of 3.5mm and 6mm tumors in the same breast model, $\mathrm{PADR}_{\mathrm{max}}$ values are very low in general with no significant hot spots outside the tumor, due to the low effective conductivity of the surrounding fatty tissues. The $\mathrm{PADR}_{\mathrm{avg}}$ values are also very low as the average power absorption in the overall breast outside the tumor is very small.

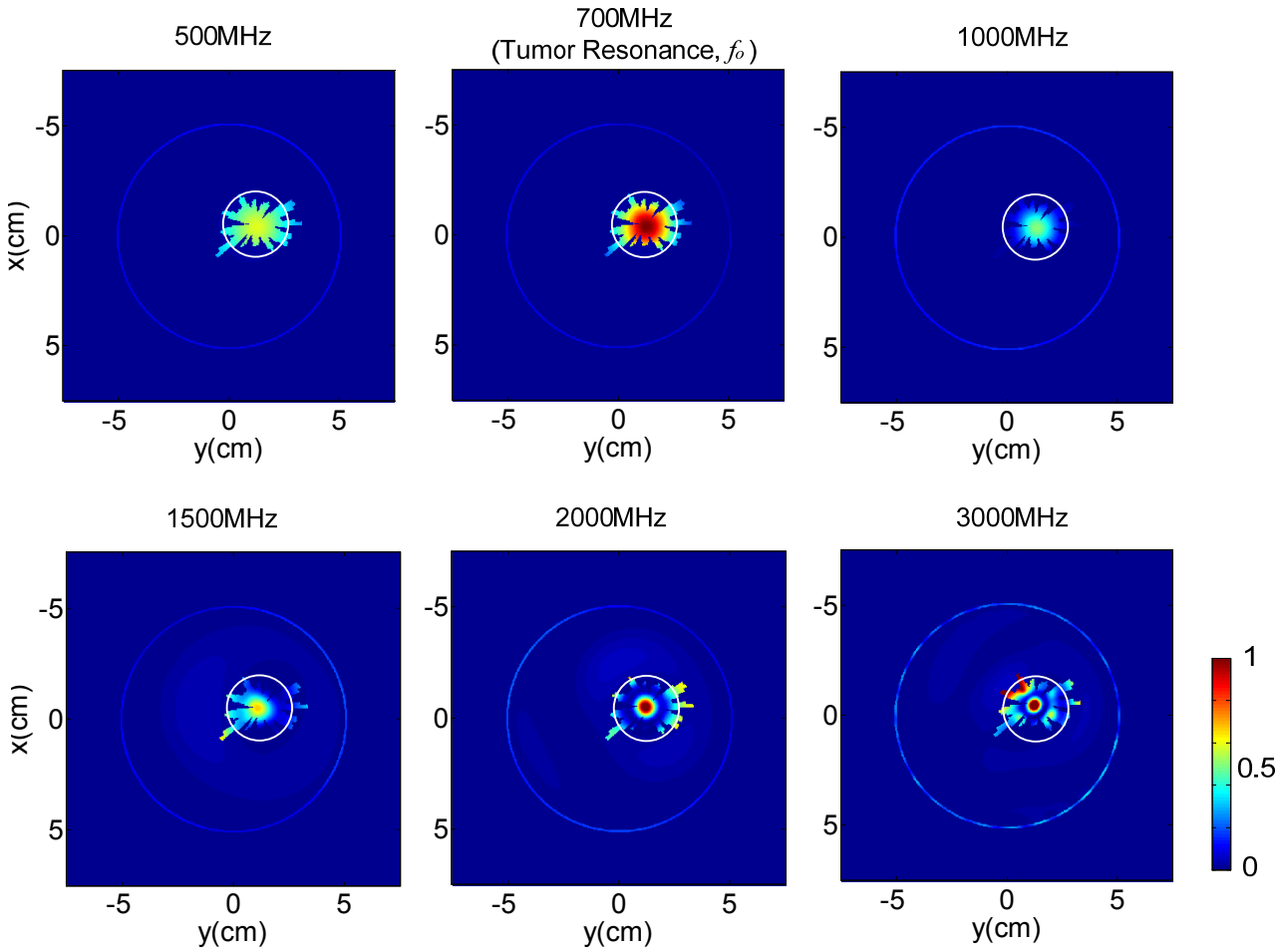

Figure 6.18 Normalized PAD values obtained from the simulated electric field distribution in Model C1 with 9mm (baseline radius) tumor at various frequencies. The tumor location is indicated by a white circle.

Table 6.11 PAD-based performance indicators for Model C1 with 9mm (baseline radius) tumor at various frequencies. The tumor resonance frequency, f_o, is in bold.

Frequency (GHz)	$\overline{\mathrm{PAD}_{\mathrm{norm}}}(x_t, y_t)$	$\mathrm{PADR}_{\mathrm{avg}}$	$\max\{\mathrm{PAD}_{\mathrm{norm}}(x_t, y_t)\}$	$\mathrm{PADR}_{\mathrm{max}}$
0.5	0.746	0.019	0.586	0.038
0.7	**1**	**0.009**	**1**	**0.018**
1.0	0.325	0.030	0.504	0.020
1.5	0.421	0.033	0.672	0.180
2.0	0.503	0.043	1.13	0.186
3.0	0.482	0.050	1.4	0.140

K. Circular Model 2 (C2) with 9mm tumor baseline radius

For Model C2 with 9mm tumor baseline radius, the identified resonance, f_o, is 0.75GHz. Similar to the case of 6mm radius tumor in the same model, the resonance frequency seems to have shifted up slightly, most likely for the same reason. The $\mathrm{PAD}_{\mathrm{norm}}(x, y)$ plots and the PAD-based indicators are in Figure 6.19 and Table 6.12, respectively. In this model, the use of the tumor resonance frequency seems to provide better performance than any other frequencies considered except for 0.5GHz. The power absorption in the tumor is greater at 0.5GHz than at f_o in terms of both $\overline{\mathrm{PAD}_{\mathrm{norm}}}(x_{\mathrm{t}}, y_{\mathrm{t}})$ and $\max\{\mathrm{PAD}_{\mathrm{norm}}(x_{\mathrm{t}}, y_{\mathrm{t}})\}$ values. One disadvantage, however, for 0.5GHz would be more hot spots outside the tumor taking place compared to f_o. The amount of hot spots outside the tumor is an important factor for performance evaluation. Nevertheless, considering a moderate difference between the $\mathrm{PADR}_{\mathrm{max}}$ values at 0.5GHz and f_o, it is appropriate to conclude that 0.5GHz works just as well as f_o in this model. However, it still puts f_o among the better frequencies to use for more effective dielectric heating.

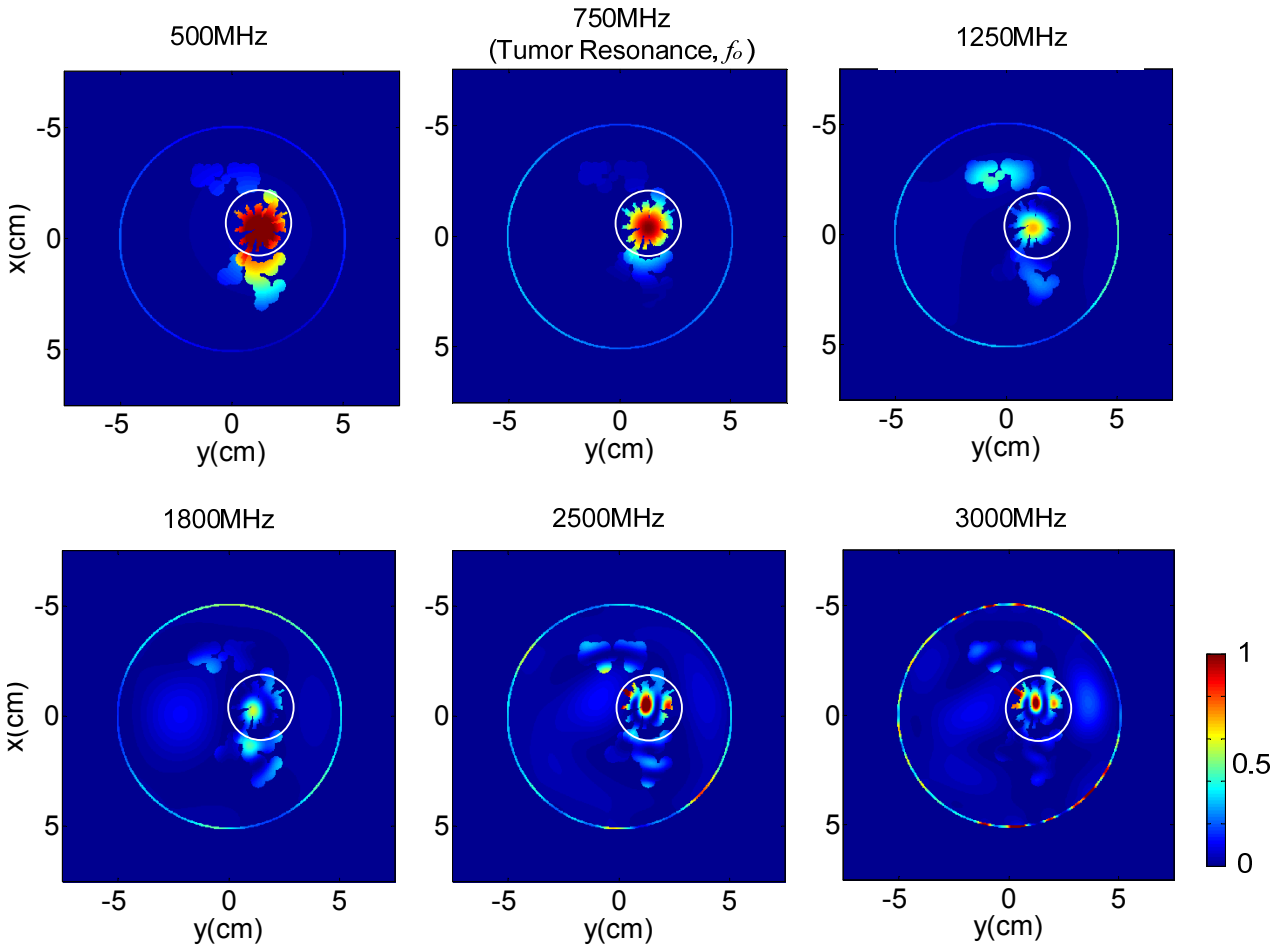

Figure 6.19 Normalized PAD values obtained from the simulated electric field distribution in Model C2 with 9mm (baseline radius) tumor at various frequencies. The tumor location is indicated by a white circle.

Table 6.12 PAD-based performance indicators for Model C2 with 9mm (baseline radius) tumor at various frequencies. The tumor resonance frequency, f_o, is in bold.

Frequency (GHz)	$\overline{\mathrm{PAD}_{\mathrm{norm}}}(x_t, y_t)$	$\mathrm{PADR}_{\mathrm{avg}}$	$\max\{\mathrm{PAD}_{\mathrm{norm}}(x_t, y_t)\}$	$\mathrm{PADR}_{\mathrm{max}}$
0.5	1.40	0.046	1.14	0.489
0.75	**1**	**0.026**	**1**	**0.345**
1.25	0.428	0.112	0.678	1.479
1.8	0.282	0.189	0.581	2.336
2.5	0.589	0.108	1.5	1.778
3.0	0.504	0.116	1.18	1.725

L. Circular Model 3 (C3) with 9mm tumor baseline radius

The identified resonance, f_o, for this model is 0.7GHz. Notice that f_o is the same as that of the 9mm radius tumor used in Model C1. There are two possible reasons for no effective change in the resonance between Model C1 and C3. First, as previously discussed a change in the spiculated geometry from random model brings about a larger effective change in overall geometry due to a larger tumor baseline circle. Second, the overall tumor size is significantly larger and the tumor is not completely surrounded by the medium/low fat tissues anymore, hence there is no significant change in the effective electrical size of the tumor.

Figure 6.20 shows the $\mathrm{PAD}_{\mathrm{norm}}(x,y)$ plots for the frequencies evaluated including f_o. The PAD-based indicators are summarized in Table 6.13. For this model, the optimal power absorption in the tumor takes place at f_o among the frequencies considered. The $\overline{\mathrm{PAD}_{\mathrm{norm}}}(x_{\mathrm{t}},y_{\mathrm{t}})$ value at 0.5GHz is on par with that at f_o. However, all other indicators suggest that f_o provides a better overall performance, particularly in terms of reduced hot spots outside the tumor as indicated by the $\mathrm{PADR}_{\mathrm{max}}$ values and the power absorption plots in Figure 6.20.

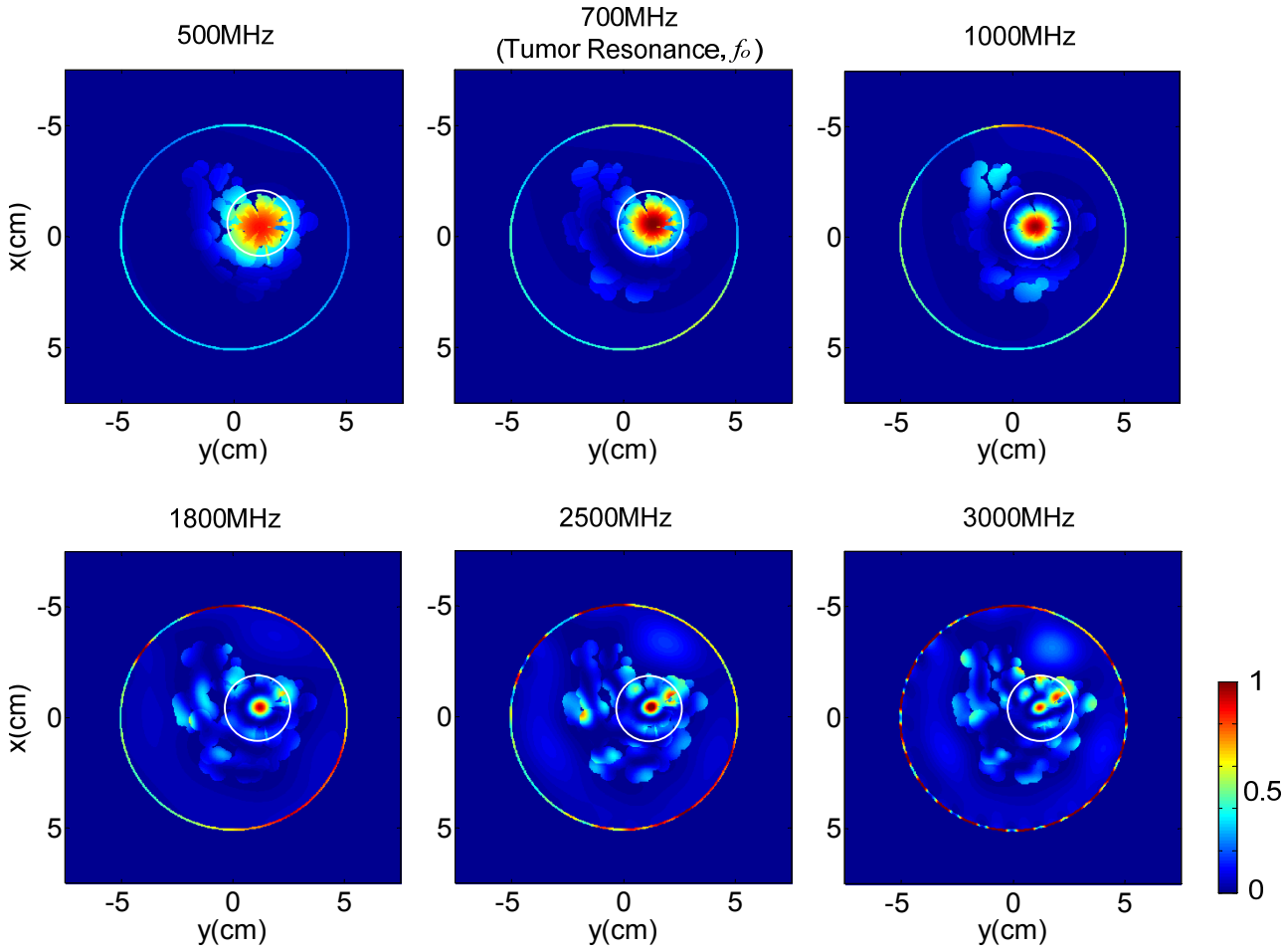

Figure 6.20 Normalized PAD values obtained from the simulated electric field distribution in Model C3 with 9mm (baseline radius) tumor at various frequencies. The tumor location is indicated by a white circle.

Table 6.13 PAD-based performance indicators for Model C3 with 9mm (baseline radius) tumor at various frequencies. The tumor resonance frequency, f_o, is in bold.

Frequency (GHz)	$\overline{\mathrm{PAD}_{\mathrm{norm}}}(x_t, y_t)$	$\mathrm{PADR}_{\mathrm{avg}}$	$\max\{\mathrm{PAD}_{\mathrm{norm}}(x_t, y_t)\}$	$\mathrm{PADR}_{\mathrm{max}}$
0.5	1	0.075	0.859	0.852
0.7	**1**	**0.061**	**1**	**0.354**
1.0	0.685	0.092	0.974	0.783
1.8	0.378	0.203	0.944	1.585
2.5	0.416	0.255	1.18	2.320
3.0	0.386	0.295	0.883	2.827

6.3.1.3 Uniform vs. Weighted Amplitude

While the location of the focus depends on the phasing of the array, the focusing quality could depend on the amplitude of the signal fed into each element. Since the propagation path between the tumor and each array element have different length and medium properties (in case of inhomogeneous tissues), the amount of attenuation each path experiences could vary. Hence we investigate the use of uniform amplitudes versus weighted amplitudes. Amplitude weights are determined by multiplying the inverse proportion of the received peak amplitude at each element with respect to the maximum peak amplitude. This would compensate for the loss related to $1/r$ spread (where r represents the path length between the transmit element, target, and receive element) as well as the loss due to the effective conductivity in the medium.

Here we consider two representative configurations, namely Models S2 and C3, a semicircular breast model with moderate proportion of fibroglandular tissues and a circular breast model with larger proportion of fibroglandular tissues, respectively. For both models, 3.5mm radius tumor is used. The identified tumor resonance frequencies (1.29GHz for S2 and 1.55GHz for C3) and the phase angles are used as the source signal.

Figure 6.21 shows the simulated electric field intensity plots for Model S2 are shown. The field distribution from uniform amplitudes is shown on the left, and the field distribution from weighted amplitudes is shown on the right. Note that each plot is normalized by scaling with its own maximum value, unlike the previous plots for frequency comparison. The overall shape of the distribution is similar in both plots, but the relative intensity between the focal spot at the tumor location and the major lobe outside the tumor is higher when weighted amplitudes are used. This implies relatively stronger hot spots outside the tumor for weighed amplitudes, which is apparent in the power absorption density (PAD) plots in Figure 6.22. Each PAD plot in Figure 6.22 is also normalized using it own maximum value, so as to provide a relative PAD level with respect to the value at the tumor. Relatively higher power absorption takes place for weighted amplitudes in regions outside the tumor, particularly in the surrounding fibroglandular tissues. This observation is quantified by the $\mathrm{PADR}_{\mathrm{avg}}$ values, which are 0.35 for uniform amplitudes and 0.58 for weighted amplitudes. The power absorption in the skin is greater for uniform amplitudes. However, much of the heating in the skin can be mitigated by means of cooling the temperature of the matching medium.

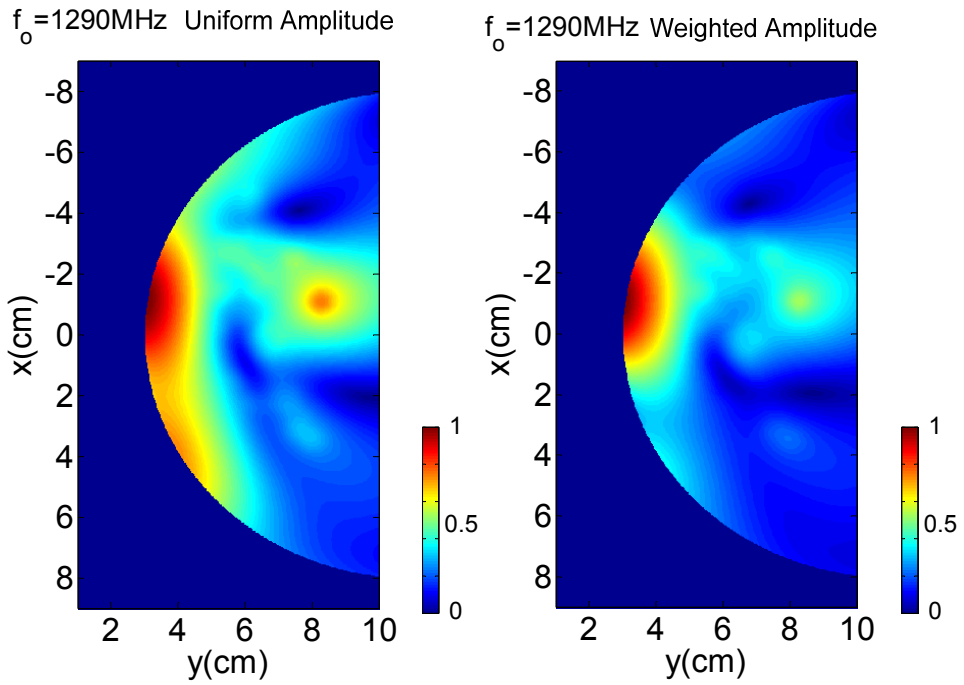

Figure 6.21 Simulated electric field distributions in Model S2 with 3.5mm (baseline radius) tumor at the resonance frequency (1.29GHz) for uniform amplitudes (left) and weighted amplitudes (right) in the array. Note that the electric field intensity values in each map are normalized using its own maximum value.

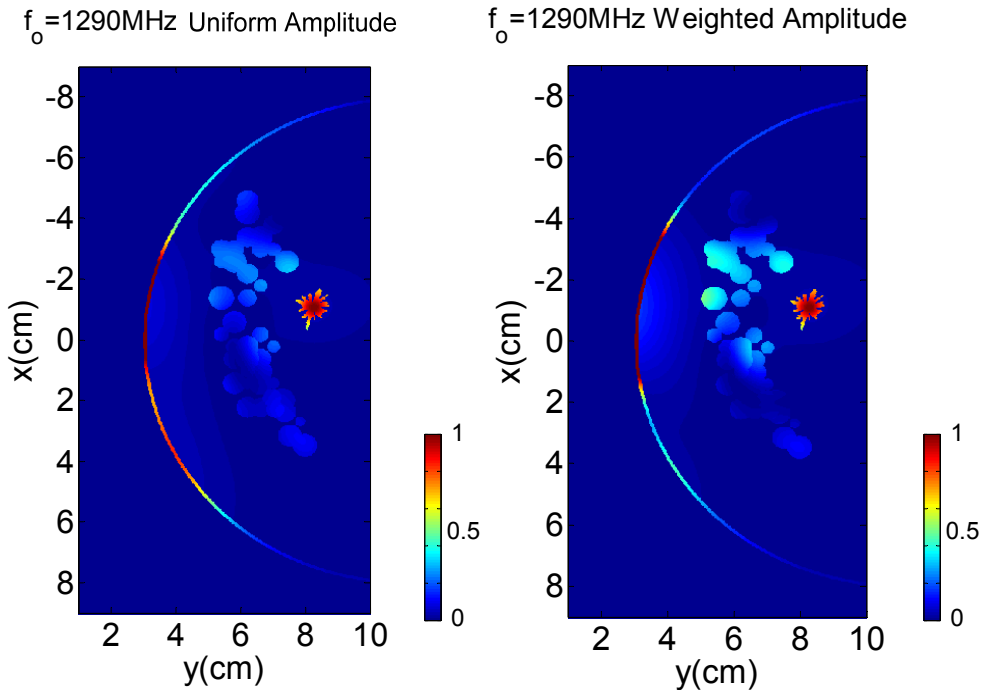

Figure 6.22 Normalized PAD maps obtained from the simulated electric field distribution in Model S2 with 3.5mm (baseline radius) tumor at the resonance frequency for uniform amplitudes (left) and weighted amplitudes (right) in the array. Note that the PAD values in each map are normalized using its own maximum value in the tumor.

Similar observations can be made with Model C3. Figure 6.23 shows the simulated electric field intensity plots for uniform (left) and weighted (right) amplitudes. While the overall shape of the distribution is similar, the relative intensity between the focal spot at the tumor location and the major lobe outside the tumor is higher for weighted amplitudes. As a result relatively stronger hot spots outside the tumor take place for weighed amplitudes in the PAD plots in Figure 6.24. A strong hot spot with PAD values exceeding that in the tumor takes place outside the tumor for weighted amplitude model. The $PADR_{avg}$ values are 0.6 for uniform amplitudes and 1.56 for weighted amplitudes. For this model, the relative power absorption in the skin is greater for weighted amplitudes.

The results from both models suggest that using uniform amplitudes in the array provides better selective heating at the tumor with reduced hot spots compared to using weighted amplitudes. Although only two models were considered, the results still provide a qualitative insight into the effect of feed amplitudes in the array, and can serve as a guideline in potential practical scenario.

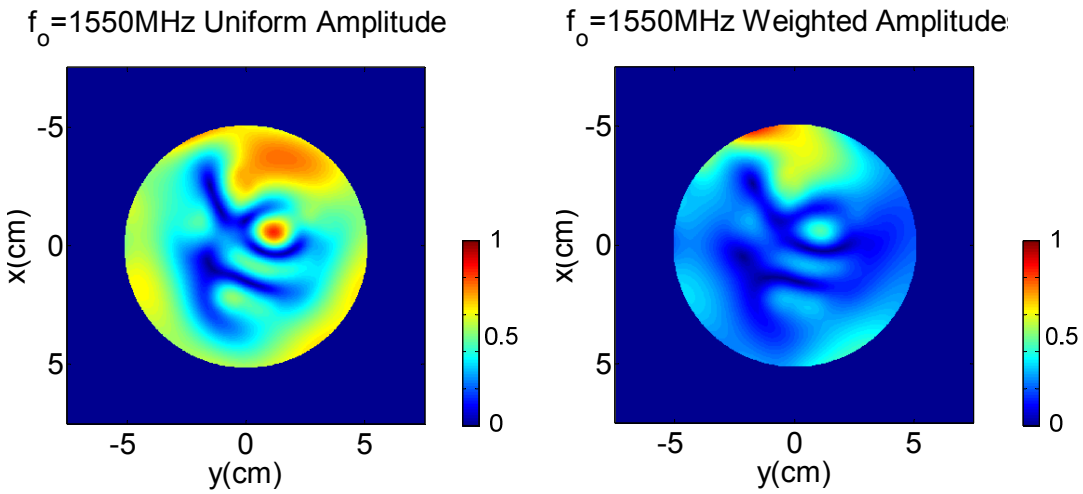

Figure 6.23 Simulated electric field distributions in Model C3 with 3.5mm (baseline radius) tumor at the resonance frequency (1.55GHz) for uniform amplitudes (left) and weighted amplitudes (right) in the array.

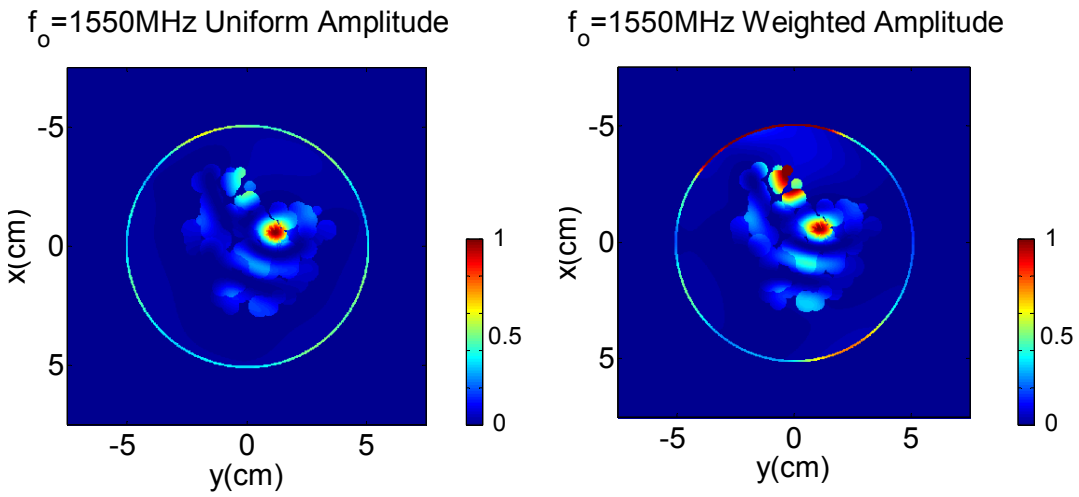

Figure 6.24 Normalized PAD maps obtained from the simulated electric field distribution in Model C3 with 3.5mm (baseline radius) tumor at the resonance frequency (1.29GHz) for uniform amplitudes (left) and weighted amplitudes (right) in the array.

6.3.1.4 Number of Elements

Focusing quality could also depend on the number of array element used to transmit microwave signals. Here the interest is in the effects due to changes in the number of elements while the overall array size remains constant, in which case the element spacing increases as the number of elements decreases. Hence we investigate such effects using the same models considered above, namely Models S2 and C3 with 3.5mm radius tumor. The identified tumor resonance frequencies are also used here. Model S2 is simulated using 20, 10, and 5 elements. Model C3 is simulated using 25, 12, and 5 elements. For both models, uniform amplitudes are used to feed the array.

Figure 6.25 shows the simulated electric field intensity plots of Model S2. The field distribution from 20, 10 and 5 elements are shown on the left, center and right, respectively. Each plot is normalized by scaling with its own maximum value. The absolute intensity at the focus would be lower with fewer elements used, since the coherent addition of fields would be proportional to the number of elements. However, since we are only interested in a relative level with respect to the intensity at the focal spot, a normalized plot is more suitable for comparison. The overall shape of the distribution for 20 and 10 elements are very similar. The field distribution for 5 elements is also similar, but with a slightly larger focal spot and some higher intensity near the skin. The PAD plots are shown in Figure 6.26 in the same order from left to

right as in Figure 6.25. Each PAD plot is also normalized using its own maximum value in the tumor. All three PAD plots are similar. Only a slight increase in the relative PAD values in the hot spots outside the tumor is observed. PAD levels in the skin seem to differ between each case, but heating in the skin is not of a great concern as mentioned previously. The $PADR_{max}$ values for 20, 10 and 5 element models are 0.37, 0.39 and 0.41, respectively, showing only a slight increase.

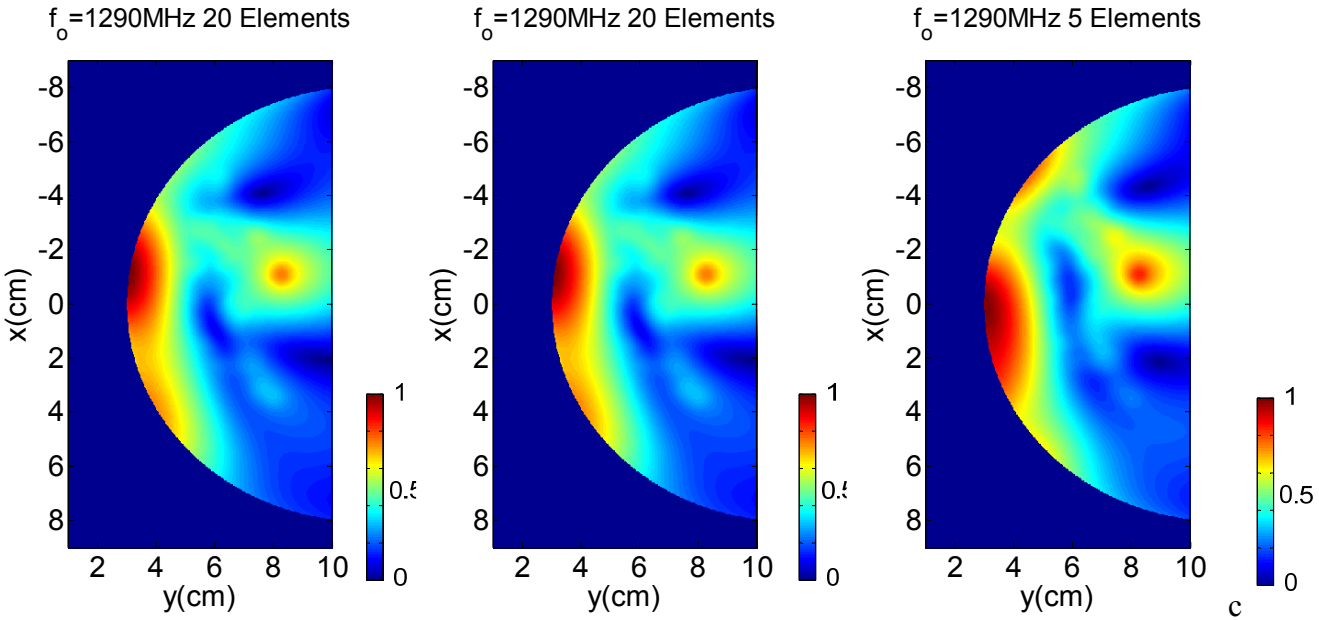

Figure 6.25 Simulated electric field distributions in Model S2 with 3.5mm (baseline radius) tumor at the resonance frequency (1.29GHz) for 20 (left), 10 (center), and 5 (right) array elements used for transmit. Note that the electric field intensity values in each map are normalized using its own maximum value.

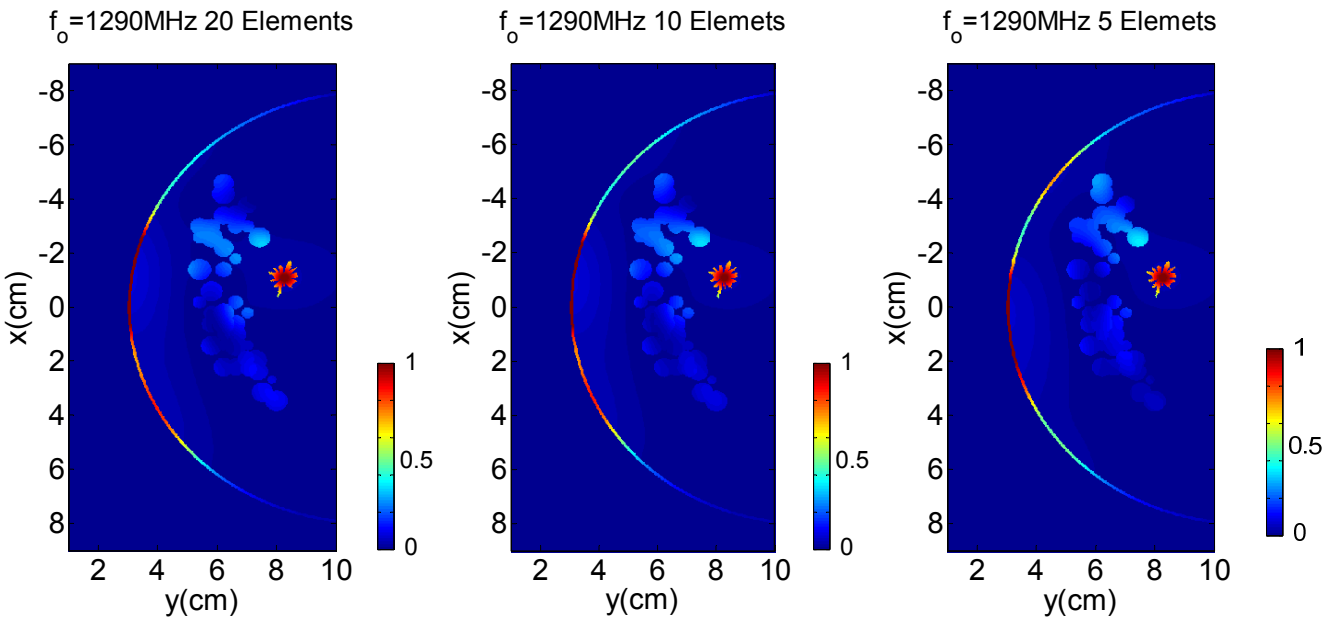

Figure 6.26 Normalized PAD maps obtained from the simulated electric field distribution in Model S2 with 3.5mm (baseline radius) tumor at the resonance frequency (1.29GHz) for 20 (left), 10 (center), and 5 (right) array elements used for transmit. Note that the PAD values in each map are normalized using its own maximum value.

Figure 6.27 shows the simulated electric field intensity plots for Model C3 with 25 (left), 12 (center) and 5 (right) elements used. For this model, the field distribution varies between each plot. Higher field intensity near the skin is observed for 12 and 5 elements. However, the relative intensity at the focal spot with respect to that in the inner region does not seem to vary as much. Figure 6.28 shows the PAD plots in the same order as in Figure 6.27. As expected, the amount of power absorption in the skin is greater for 12 and 5 elements. In the inner region, there seems to be a slight increase in hot spots outside the tumor as fewer elements are used. The $PADR_{max}$ values for 20, 12 and 5 element models are 0.64, 0.73 and 0.77, respectively.

The number of element seems to affect, although not significantly, the focusing quality. As the element spacing increases due to a decrease in the number of elements, more hot spots are generated affecting the quality of selective heating. The decrease in performance caused by fewer elements is more noticeable in the circular model. It would be desirable to use minimal number of elements in a practical system. This type of study could help determine the optimal number that reduces the system complexity with a minimum compromise on the performance.

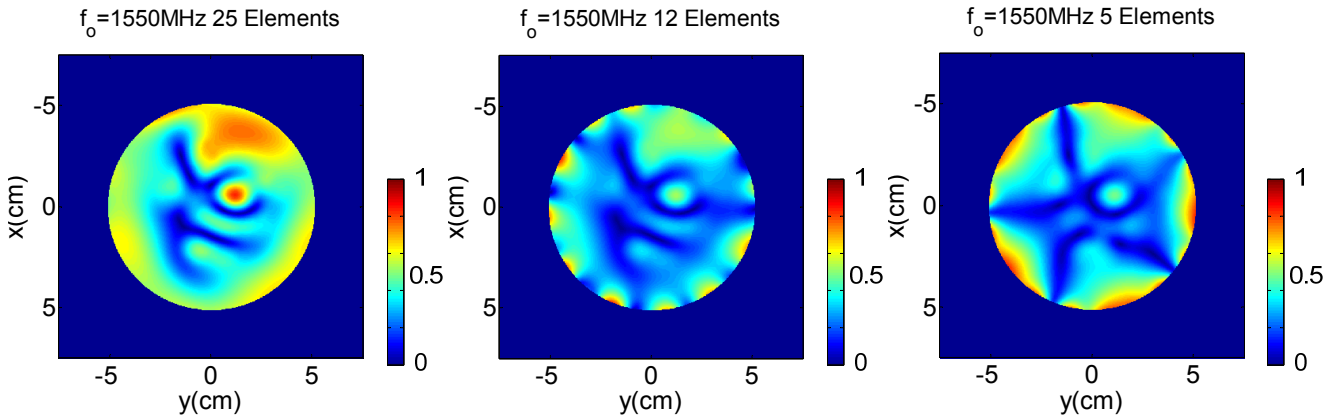

Figure 6.27 Simulated electric field distributions in Model C3 with 3.5mm (baseline radius) tumor at the resonance frequency (1.55GHz) for 25 (left), 12 (center), and 5 (right) array elements used for transmit.

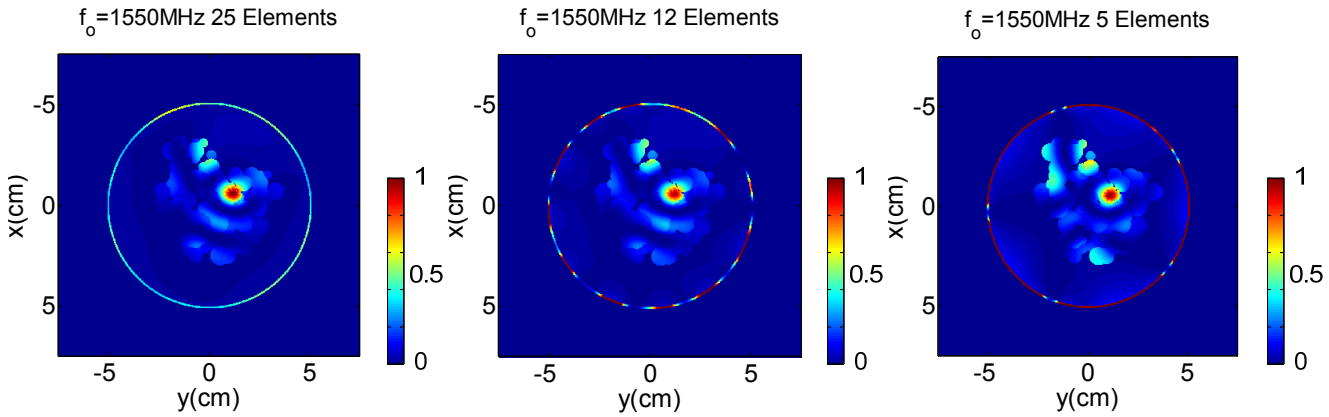

Figure 6.28 Normalized PAD maps obtained from the simulated electric field distribution in Model C3 with 3.5mm (baseline radius) tumor at the resonance frequency (1.55GHz) for 25 (left), 12 (center), and 5 (right) array elements used for transmit.

6.3.2 Simplified Experiment

Using the same apparatus presented in Chapter 5, a simplified experiment was carried out to evaluate the performance of the tumor resonance frequency. As described previously, the apparatus has a 2D-like setup with homogeneous tissue simulant for a simplified demonstration. The setup consists of a circular array of eight coaxial feed elements spaced uniformly. The tumor simulant was placed at the center of the circular breast model to eliminate the need for phasing the array. The tumor resonance, f_o, is identified to be 1.65GHz.

As shown in Figure 6.29, the experiment was carried out using Agilent N5230a network analyzer by measuring S_{21} responses. Using Port 1 of the network analyzer as a source, RF power dividers were used to equally divide the source power into the array. The cables connected to the feeds had the same length to ensure the focal point at the center where the tumor was located. Responses were measured by connecting Port 2 of the network analyzer to each of the four probes and switching them manually. Due to an axially symmetric configuration, the power level measured at the probes should also generally represent the power at the same radial distance from the center.

In order to evaluate the performance, a relative level of dielectric heating was estimated using the measured S_{21} magnitude at selected frequencies. The S_{21} values represent relative voltage levels, which are proportional to the electric field at the corresponding probe:

$$S_{21} \to v_i \sim E_i \ , \tag{6.14}$$

Since PAD is proportional to the magnitude of the electric field squared, it should also be proportional to the magnitude of the voltage squared:

$$\text{PAD} \ \sim \ \sigma \left| E_i \right|^2 \sim \sigma \left| v_i \right|^2 . \tag{6.15}$$

Hence, using the S_{21} values and the measured effective conductivity values of the tissue and tumor simulants, values that are proportional to PAD can be obtained, which indicate the level of power absorption.

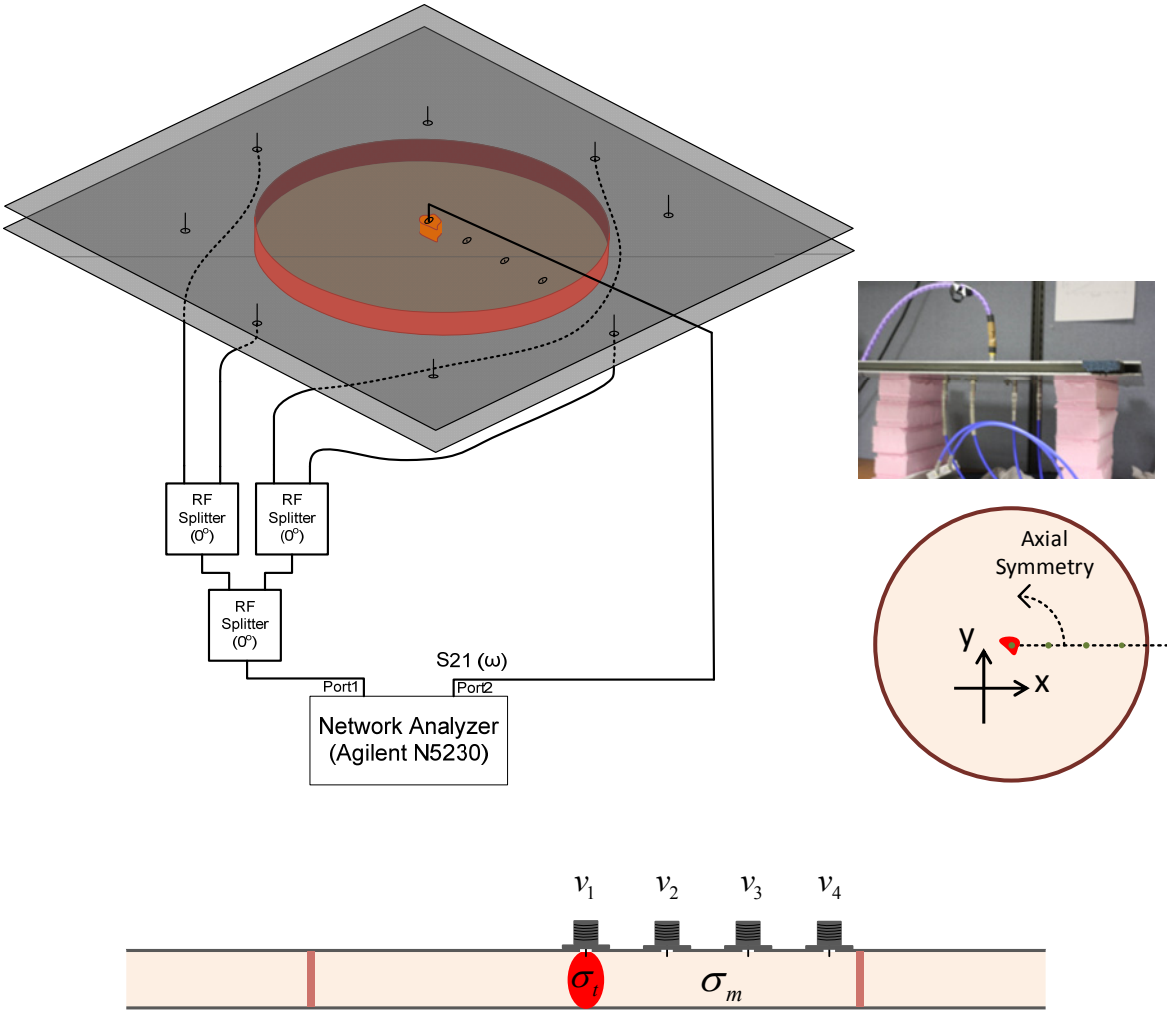

Figure 6.29 Diagram of the simplified setup used for microwave focusing experiment.

Figures 6.30 to 6.32 show the estimated power absorption at selected frequencies including f_o using three different transmit element configurations. The first configuration uses all eight elements to transmit, as shown in Figure 6.30. The second configuration uses four symmetrical elements and the third configuration uses four adjacent elements to transmit as shown in Figures 6.31 and 6.32, respectively. Note that the PAD values are normalized by scaling with respect to the value at f_o (1.65GHz) as follows:

$$\mathrm{PAD}_{norm\_i} = \frac{\sigma_{eff}\left|v_i\right|^2}{\sigma_{eff}\left|v_i\right|^2\Big|_{f_o}}. \qquad (6.16)$$

The normalized PAD value for probe 1 corresponds to the estimated power absorption in the tumor, while the values for other probes correspond to the power absorption in the breast tissues outside the tumor. In all three transmit element configurations the estimated power absorption at the tumor is the highest among the frequencies considered. Since the model only consists of fatty tissue simulants, the estimated power absorption for probes 2-4 are in general significantly lower than that in the tumor. However the PAD values from probes 2-4 increase, although slightly, for both four-element transmit configuration, indicating an increase in hot spots outside the tumor. This phenomenon is consistent with the results from numerical simulations discussed in the previous subsection.

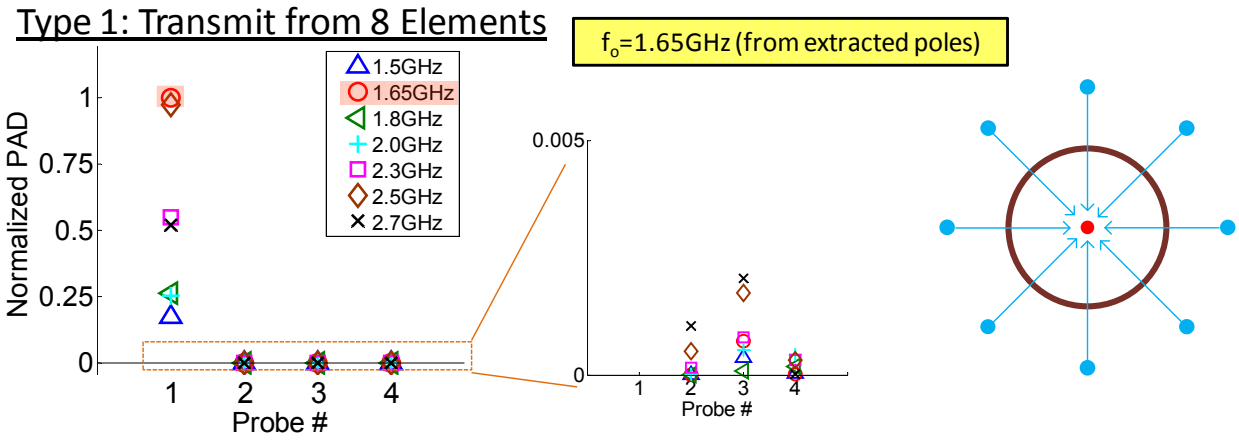

Figure 6.30 Normalized PAD values obtained from the measured S21 (voltage) at the probes located in the breast simulant when all eight elements were used for transmit. Probe #1 corresponds to the location of the tumor.

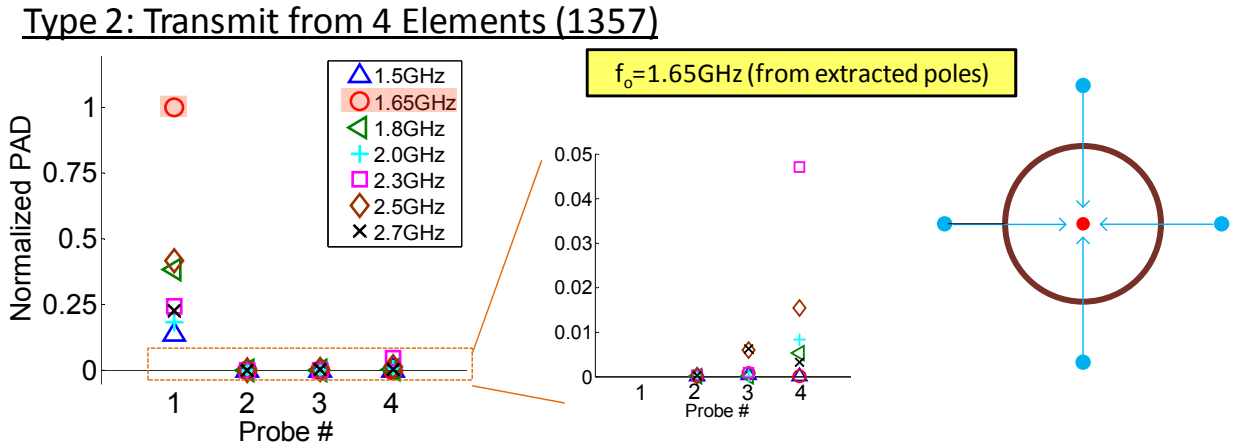

Figure 6.31 Normalized PAD values obtained from the measured S21 (voltage) at the probes located in the breast simulant when four symmetrical elements were used for transmit. Probe #1 corresponds to the location of the tumor.

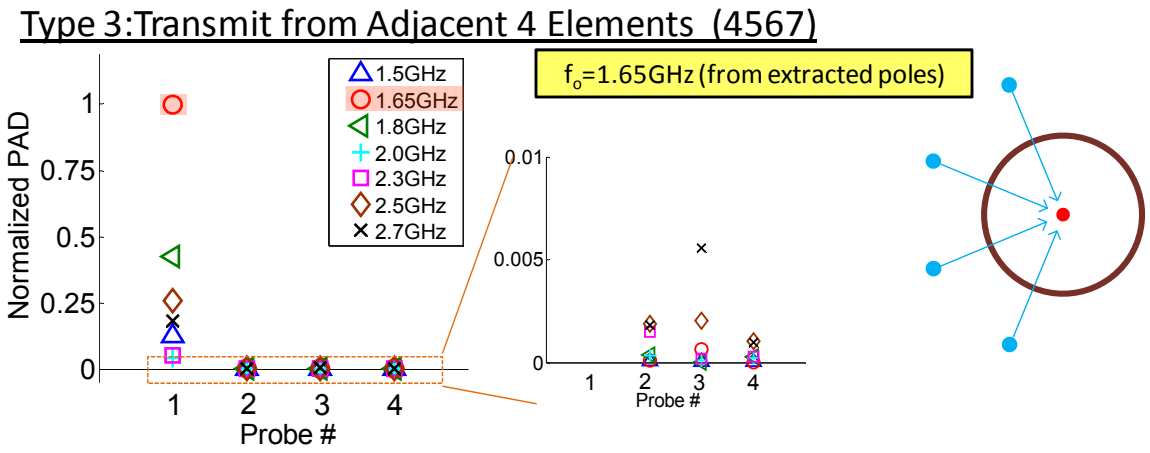

Figure 6.32 Normalized PAD values obtained from the measured S21 (voltage) at the probes located in the breast simulant when four adjacent elements were used for transmit. Probe #1 corresponds to the location of the tumor.

6.4 Chapter Summary and Conclusions

In this chapter, focusing of microwaves using the tumor-specific resonance frequencies was demonstrated. Using the tumor resonances and electrical locations identified from the SEM parameters obtained in Chapter 5, dielectric heating in the tumor and the focusing quality were evaluated via the relative power absorption density obtained from the simulated electric fields for the numerical models and the measured probe voltage for the experiment. Performance was evaluated at various frequencies for comparison. The results from numerical simulations with various tissue configurations and a simplified experiment show that the power absorption in the tumor is optimal at the identified tumor-specific resonance frequencies. Moreover, the relative levels in other hot spots in the breast are shown to be lower when the tumor resonance frequencies are used. Since the power absorption is directly proportional to the temperature rise and the level of hot spots correspond to the focusing quality, the optimal performances shown at the tumor-specific resonances indicate a more efficient thermotherapy (hyperthermia). That is, the therapeutic temperature level in the tumor can be achieved faster using the resonance frequencies, while maintaining lower temperature levels outside the tumor. In a potential practical scenario, the operating frequency can be adaptively adjusted to the identified tumor-specific resonance frequency to achieve more efficient hyperthermia.

Also presented in this chapter was a brief study based on the use of uniform amplitudes versus weighted amplitudes in the array. The amplitude weights were determined from the inverse proportion of the received peak amplitude in efforts to compensate for the spherical spreading of the wavefront and any propagation loss experienced in the path due to the conductivity in the medium. The results from two representative cases suggest that using uniform amplitudes in the array provides better selective heating in the tumor with reduced hot spots. Although only two models were considered, the results still provide a qualitative insight into the effect of feed amplitudes in the array, and can serve as a guideline in potential practical scenario.

Effects on focusing quality due to the number of array elements used were also investigated. A brief study carried out with two numerical models suggests that the number of element seems to affect the focusing quality. As the element spacing increases due to a decrease in the number of elements, more hot spots were generated in other regions in the breast. The decrease in performance caused by fewer elements was more noticeable in the circular model. Since it would be desirable to use minimal number of elements in a practical system, this type of study could help determine the optimal number that reduces the system complexity with a minimum compromise on the performance.

6.5 References

[1] A. J. Fenn, *Breast Cancer Treatment by Focused Microwave Thermotherapy*. Sudbury, MA: Jones and Bartlett Publishers, 2007.

[2] H. D. Trefna, J. Vrba, and M. Persson, "Time-reversal focusing in microwave hyperthermia for deep-seated tumors," *Physics in Medicine and Biology,* vol. 55, no. pp. 2167-2185, 2010.

This page intentionally left blank.

Chapter 7 Summary and Conclusions

An adaptive use of resonant scattering parameters has been presented for microwave breast cancer detection and thermotherapy. This new concept is based on the idea that the absorption (or coupling) of power in a tumor would be optimal if the natural resonance of the tumor is used. Increased power absorption results in a faster temperature rise in the tumor, which indicates that a more efficient thermotherapy (or hyperthermia) could be possible using the tumor-specific resonances. This dissertation demonstrated the adaptive approach in three general steps: 1) identify the electrical location of the tumor, 2) determine the tumor-specific resonance frequency, and 3) apply focused microwave treatment using the identified tumor resonance and the electrical location.

The results obtained through various numerical breast models and a simplified experiment show that the optimal power absorption takes place in the tumor when the tumor-specific resonance frequency is used. This approach can easily be implemented into an existing UWB microwave detection scheme, since it only requires minimal extra processing for obtaining the resonance parameters (pole/residue). This approach could also possibly implemented as a combination technique with mammography. For hyperthermia, a tunable source can be implemented that can adaptively adjust the frequency based on the identified tumor-specific resonance, improving the overall efficiency with minimal complexity added to a single frequency system.

7.1 Dissertation Summary

This dissertation started with a discussion of the motivation behind the research and the significance of the proposed concept for the breast tumor problem in Chapter 1. In Chapter 2, a brief overview of the microwave-based breast cancer problem was provided and a summary of previous efforts and published work in microwave breast tumor detection and thermotherapy was presented. Also discussed in Chapter 2 were current modalities that are clinically used for breast cancer detection/imaging and treatment.

Chapter 3 discussed a general overview of the proposed concept. A flow diagram was presented to explain the overall process. Potential scenarios for the proposed approach as a stand-alone system or more preferably as a combination technique with other modalities such as mammography or microwave imaging system were discussed.

In Chapter 4, an overview of resonant scattering and the Singularity Expansion Method (SEM) representation was given. The parameters used in the SEM representation, particularly the poles and residues, were described. Resonant scattering in a lossy medium was also discussed. Techniques for extracting poles and residues, i.e. Prony's method and the Matrix Pencil Method (MPM) were described. Then a new way of applying the Matrix Pencil Method, namely the sliding window MPM, for improved pole estimation was presented. The sliding window MPM has shown to be an effective approach to more accurately determine the poles without requiring *a priori* knowledge or an initial guess of the late-time.

The use of residue phase angle as the electrical location of scatterer was also introduced in Chapter 4. It was shown that relative phase between the complex residues of a pole obtained at different receiving elements in the array accurately represent the relative time-delay between the responses, which directly corresponds to the scatterer location with respect to the array. This suggests that the SEM analysis of multistatic scattering data, which contain the responses from multiple aspects, could efficiently provide necessary information (electrical location and resonance) to perform adaptive focusing. Relevance of conjugated residue phase approach to the time reversal operation was also discussed.

In Chapter 5, the techniques presented in Chapter 4 were used to obtain the tumor-specific resonances and their electrical locations from the simulated responses of two dimensional numerical breast models of various tissue configurations. A simplified experiment

was also performed. The identified tumor resonances and the electrical locations were used in Chapter 6 for microwave focusing.

Also presented in Chapter 5 was the use of ground penetrating radar-inspired position-time scan as a means to generate a relatively simple presentation of the responses. Since the interest was in determining the electrical location, a time-delay profile of the tumor responses presented by the position-time plots would provide sufficient information without generating a focused image for determining the physical location of the tumor. Chapter 5 also discussed challenges associated with the cluttered breast having high fibroglandular tissue content, which makes detection much more difficult due to tissue heterogeneity. Change detection and the use of dielectric contrast agents were discussed as potential schemes to improve detection for heavily cluttered breasts. Both approaches are shown to be effective in detecting tumor responses in a cluttered breast. Since both schemes are based on obtaining differential responses, an accurate alignment of the responses taken at different times is very important.

In Chapter 6, focusing of microwaves using the tumor-specific resonance frequencies was demonstrated. Using the tumor resonances and electrical locations identified from the SEM parameters obtained in Chapter 5, dielectric heating in the tumor and the focusing quality were evaluated via the relative power absorption density. Performance was evaluated at various frequencies for comparison and the results show that in general the power absorption in the tumor is optimal at the identified tumor-specific resonance frequencies. Moreover, reduced hot spots outside the tumor were observed at the tumor resonance frequencies. Since the power absorption is directly proportional to the temperature rise and the level of hot spots correspond to the focusing quality, the optimal performances shown at the tumor-specific resonances indicate a more efficient hyperthermia. That is, the therapeutic temperature level in the tumor can be achieved faster using the resonance frequencies, while maintaining lower temperature levels outside the tumor.

Also presented in Chapter 6 was a brief study based on the use of uniform amplitudes versus weighted amplitudes in the array. The amplitude weights were determined from the inverse proportion of the received peak amplitudes. The results from two representative cases suggest that uniform amplitudes provide better selective heating in the tumor with reduced hot spots. This provides a qualitative insight into the effect of feed amplitudes in the array, and can serve as a guideline implementing a potential practical system.

Effects on focusing quality due to the number of array elements used were also investigated in Chapter 6. A brief study carried out suggests that the number of elements seems to affect the focusing quality. As the element spacing increases due to a decrease in the number of elements, more hot spots were generated in other regions in the breast. Since it would be desirable to use minimal number of elements in a practical system, this type of study could help determine the optimal number that reduces the system complexity with a minimum compromise on the performance.

7.2 Summary of Contributions

The main original contribution in this dissertation is the introduction of an adaptive approach for breast tumor applications, where one could utilize the SEM parameters to identify the tumor-specific resonances and the electrical location, and use them for more efficient focused microwave hyperthermia. This concept was demonstrated by studying various two-dimensional numerical breast models, as well as a simplified experiment. It was shown that microwave focusing performed at the tumor-specific resonance frequencies generally provides the optimal performance in the heating of the tumor [1, 2]. That is, the therapeutic temperature level in the tumor can be achieved faster using the resonance frequencies, indicating a more efficient hyperthermia. In the process of demonstrating this approach, several original contributions were made as discussed in the following.

The sliding-window Matrix Pencil approach was an original contribution. This is a new scheme of applying the Matrix Pencil Method for improved pole estimation. Use of the sliding-window allows for a temporal presentation of the estimated poles, from which one can determine a stable set of poles that are likely to represent the actual resonance of the scatterer [3]. This approach is very useful for determining the resonant poles without *a priori* knowledge or an initial guess of the late-time and be less of a simple curve fit.

Another original contribution was the use of relative phase between the complex residues of the corresponding poles obtained at different receiving elements in the array. It was shown that the relative residue phase angles closely correspond to the relative time delays between the responses obtained by the array elements. Phasing the array with the conjugated residue phase angles results in focused microwave at the tumor. This suggests that one can obtain the necessary

information (electrical location and resonance) to perform adaptive focusing from reduced SEM parameters.

The GPR-inspired position-time scan as a means to generate a relatively simple presentation of the responses was presented as original contribution. Since the interest was in determining the electrical location of the tumor, a time-delay profile of the responses presented by the position-time plots would provide sufficient information without having to generate a focused image. Since only a minimal signal processing is required to generate position-time plots, this approach can easily be implemented as a precursory step before applying computationally expensive focused imaging.

The success of the proposed adaptive approach relies on accurate extraction of the tumor response, which could be very challenging for breasts with tissue heterogeneity caused by high fibroglandular tissue content. Tissue heterogeneity is not problematic only for the proposed approach, but also for any microwave-based detection approach in general. A minor contribution was made by discussing possible schemes to mitigate the effects of clutter in the response due to tissues heterogeneity. Change detection via routine screening was discussed, as well as the use of contrast enhancing agents for obtaining differential responses. Simple numerical examples were given to demonstrate the feasibility. Since both schemes are based on obtaining some kind of differential responses, the key is in the alignment of the responses taken at different times.

7.3 Future Work

With this dissertation having demonstrated the basic concept of the proposed resonance-based adaptive approach for more efficient breast tumor hyperthermia, the research can be further extended into investigating more complex and practical configurations and addressing some practical challenges. Possible future work could include:

- Study full three-dimensional numerical breast models of various tissue configurations.
- Design an array with antenna elements that provides desired ultra-wide bandwidth.
- Explore the use of polarization diversity and possible additional features from polarimetric measurements for improved detection and treatment.
- Build realistic physical phantoms and array system for experimental demonstration.

- Apply a statistical pole model for more robust and automated resonance extraction.
- Develop good calibration procedures for alignment of the responses of successful change detection and contrast response.
- Upon successful demonstration of the practical apparatus, a potential clinical study can be performed to investigate the effectiveness of the concept.

As mentioned in Chapter 1, the proposed adaptive concept in general is a “smart” way of directing electromagnetic energy onto a desired target, since the source frequency is adaptively selected based on the resonant frequency of the target to more efficiently deliver the energy. A very interesting potential area to utilize this concept would be high power microwave (HPM) attack of remote electronic systems, where one can impulsively ping a target of interest with an ultra wideband signal and obtain the target resonance through the SEM parameters, and adaptively tune the HPM source to the identified resonance of the target for more effective upset or damage of the target.

7.4 References

[1] S. K. Hong and W. A. Davis, "Use of Tumor-specific Resonance in Microwave Hyperthermia of Breast Tumor," *presented at the IEEE International Symposium on Antenna and Propagation and USNC-URSI National Radio Science Meeting*, Chicago, IL, 2012.

[2] S. K. Hong and W. A. Davis, "Use of Tumor-specific Resonances for More Efficient Hyperthermia of Breast Cancer," *Microwave and Optical Technology Letters,* under preparation and to be submitted.

[3] S. K. Hong, W. S. Wall, T. D. Andreadis, and W. A. Davis, "Practical Implications of Pole Series Convergence and the Early-time in Transient Backscatter," *NRL Memorandum Report*, NRL/MR/5740--12-9411, Apr. 2012.